Study of the Origins of the σ^o Blooms

Albert Garcia

Thesis submitted to the Faculty of the
Virginia Polytechnic Institute and State University
in partial fulfillment of the requirements for the degree of

Master of Science
in
Electrical and Computer Engineering

Gary S. Brown, Chair
Ahmad Safaai-Jazi
Timothy Pratt

June, 1999
Blacksburg, Virginia

Keywords: σ^o blooms, TOPEX, radar altimetry

Study of the Origins of the σ^o Blooms

Albert Garcia

Professor Gary Brown, Chair

(ABSTRACT)

The TOPEX/POSEIDON Project is a joint U.S. and French mission to develop and operate an Earth orbiting satellite capable of making accurate measurements of the mean sea level in a way that allows the study of ocean dynamics. The understanding of ocean dynamics is very important in order to study events such as El Niño. Soon after the launch of the TOPEX satellite, some unusually high, but localized, values of the ocean's radar cross section, σ^o, were observed by scientists at the NASA Goddard Space Flight Center. These phenomena have been referred to as σ^o blooms, and are accompanied by an increase in noise in the significant wave height (SWH) and altitude measurements. Since approximately 5% of all data recorded by the satellite contains σ^o blooms, it is important to understand their causes so that corrective measures can be taken by NASA. This thesis investigates two possible origins of the σ^o blooms: a surface containing a step discontinuity in σ^o, and a surface containing slick or calm areas. Models corresponding to the theoretical returns from these two types of surfaces are developed and studied.

Dedication and Acknowledgments

I would like to thank my advisor, Dr. Gary Brown, for the invaluable support, patience, and guidance he has provided me during my research. I would also like to thank my committee members, Dr. Ahmad Safaai-Jazi and Dr. Timothy Pratt, for reviewing this thesis and providing the necessary edits.

I am extremely grateful to Dr. George S. Hayne from the NASA Goddard Space Flight Center for without his knowledge and support this thesis would not have been completed.

I wish to deeply thank my family, especially my wife Greta, and my friends Bill and Deb for all their support and guidance over the years. I would also like to thank Brad, Bryan, Jakov, Ra'id, and Rob for their patience and friendship through graduate school; I will miss you guys.

Contents

List of Figures

List of Tables

Chapter 1

Introduction and Problem Statement

1.1 Introduction

The TOPEX/POSEIDON Project is a joint U.S. and French mission to develop and operate an Earth orbiting satellite capable of making accurate measurements of the mean sea level. The mission objective is to measure the mean sea level in a way that allows the study of ocean dynamics, including the calculation of the mean variable surface geostrophic currents and the tides of the world's oceans which will help understand global climatology and meteorology. One result of measuring ocean circulation patterns and monitoring climatic change is the detection and mapping of the annual phytoplancton bloom in the North Atlantic (Dobson et al., 1992). This bloom is vital to the Earth's biogeochemical cycle, and its existance is dependent on mesoscale circulation patterns (Dobson et al., 1992).

One way to measure ocean circulation patterns is to use ocean surface height measurements provided by a spaceborne radar altimeter. Ocean water movements are manifested by changes in mean sea level. These changes vary from a 1 meter increase in 100 kilometers over the Gulf Stream to a 10 centimeter change in 1000 kilometers for an El Niño event. Using the amplitude of these changes in the ocean surface height, the magnitude and direction of the ocean's water movement can be estimated. That is, the sea height measurements from

the altimeter can be used to determine more than just surface elevation (Marth et al., 1993). The TOPEX satellite is a low earth orbiting satellite operating at an altitude of 1334 Km with an orbital period of 112 minutes that repeats its ground tracks approximately every 10 days. The NASA Radar Altimeter (NRA) on board the TOPEX satellite is the first dual frequency altimeter on board a low earth orbit measurement satellite; it operates at 5.3 and 13.6 GHz, C- and Ku-band, respectively. By using two frequencies, ionospheric path delays can be corrected and greater accuracy can be achieved. The NRA will measure the local height of the ocean's surface to a precission of about 2 cm over a 3 second average of data (Zieger et al., 1991). Parameters such as the ocean's radar cross section and wind speed can be calculated from the data obtained by the NRA .

Soon after the launch of the TOPEX satellite, scientists at the NASA Goddard Space Flight Center began observing some unusually high, but localized, values of the ocean's radar cross section, $\sigma^o(0^o)$ at normal incidence or just σ^o. These phenomena have been referred to as σ^o blooms. A more detailed explanation of the σ^o blooms phenomena is given in the problem statement of this chapter. However, the σ^o blooms have a significant effect on the precision of the altitude data produced by the altimeter. Consequently, it is very important that NASA understand the source of these blooms so that appropriate corrective action can be initiated.

Therefore, the purpose of this thesis is to study the origins of the σ^o blooms. We will consider two possible causes for these blooms: a surface containing a σ^o step discontinuity, and a surface containing slick areas with a radar cross section σ_n^o larger than the background's radar cross section σ_b^o. We will begin by deriving and exercising a model for the average power returned from a surface containing a σ^o step discontinuity. We will then derive another model for the average power returned from a surface containing calm water or slick areas with a radar cross section σ_n^o larger than the background's radar cross section σ_b^o against which we will fit some actual waveform data obtained from the NASA Goddard Space Flight Center. Appendix A provides the parameters of both the TOPEX satellite and the NASA radar altimeter.

1.2 Radar Altimetry Background

The purpose of this section is to provide the reader with a brief overview of the operation principles of a radar altimeter. A radar altimeter works by transmitting a pulse of microwave energy downward and measuring the reflected energy from the surface. There are two main measurements that the altimeter makes: the distance between the altimeter's antenna and the mean ocean surface, and the level of the returned pulse from the surface as a function of time.

The distance h between the altimeter's antenna and the mean sea level is determined from the total propagation time, 2h/c, where c corresponds to the speed of light. Delays such as ionospheric path delays must be accounted for and can be determined by using a dual frequency altimeter.

The transmitted pulse is backscattered by the multiple facets of the ocean surface that it illuminates. The altimeter receives and samples these backscattered pulses. In order to interpret these returned pulses, several of them must be averaged. From the amplitue of the mean received signal or waveform, the ocean's radar cross section at normal incidence, σ^o, can be determined. The radar cross section of an object is defined as 'the equivalent area that would intercept that amount of incident power in order to produce the same scattered power density at the receiver site if the object scattered uniformly in all directions (Cheng, 1992)' and it is a measure of the object's radar detectability. In the case of the ocean, smoother seas produce larger values of σ^o. The ocean's near surface wind speed can then be calculated from σ^o. From the shape of each mean waveform estimates of parameters such as wave heights can be determined by fitting the computed mean waveform to a model for the average returned power from a rough surface such as the one derived in Brown, 1977. For more information regarding the basic altimeter operation principle refer to Chelton et al., 1989.

1.3 Problem Statement

σ^o blooms can be described as spatially localized increases in the ocean's surface radar cross section, σ^o, exceding 12 dB for Ku-band and 16 dB for C-band. The blooms persist for hundreds of kilometers and occur most often for significant wave heights, (SWH) defined as four times the surface's rms height, of less than 1 or 2 meters but some have been observed for SWH of up to 4 m. In some cases, waveform derived attitude angles (usually below 0.1 degrees) increase to a default limit of 2.55 degrees which often occurs when the altimeter's waveform plateau decays too rapidly (Hayne, 1997). σ^o bloom occurrences produce an increase in the noise of both the SWH and altitude data generated by the NRA. Since high precision of these two measurements and approximately 5% of the data obtained from the satellite appears to be affected by σ^o blooms it is very important to understand their origins. It is also frequently the case that most data surrounding the bloom regions is designated as 'contaminated' by the altimeter internal error flags. This makes studying the σ^o blooms difficult at times.

Figure 1.1 shows NASA processed altimeter data corresponding to Cycle 137, Pass 058 of the TOPEX satellite. These data were developed on the ground from the data sent by the radar altimeter. We are most concerned with the third, fourth and fifth graphs from the top of Figure 1.1. The third plot shows σ^o for both Ku- and C-band, the fourth plot shows SWH, and the fifth plot shows the off-nadir or antenna pointing angle as obtained from the radar altimeter waveform data. Four regions denoted by A, B, C, and D, contain σ^o blooms. The blooms are marked with yellow dots. We can see that there is no specific pattern to the blooms and that some have larger magnitudes while others seem to last longer. In most cases the increase in σ^o is quite sudden, regardless of the magnitude of the increase. Also worth noting is the increase in off-nadir angle when the blooms occur. More detailed plots of σ^o and pointing angles will be given in Chapter 5 when the blooms in regions A, B, C, and D are studied in detail. Figure 1.2 shows waveforms from the second bloom marked in region A. These waveforms are shown in 0.1 second increments and end at the peak of the

σ^o bloom. The magnitude of the shown waveforms is given in counts, an engineering unit linearly related to watts used by the NASA radar altimeter. The waveforms shown in Figure 1.2 are typical for a bloom, showing an increase in the level of the waveforms as we enter the bloom up to the peak of the bloom. It is also typical that the waveforms do not exhibit any distinguishable features as the peak of the bloom is reached (other than their amplitude increase).

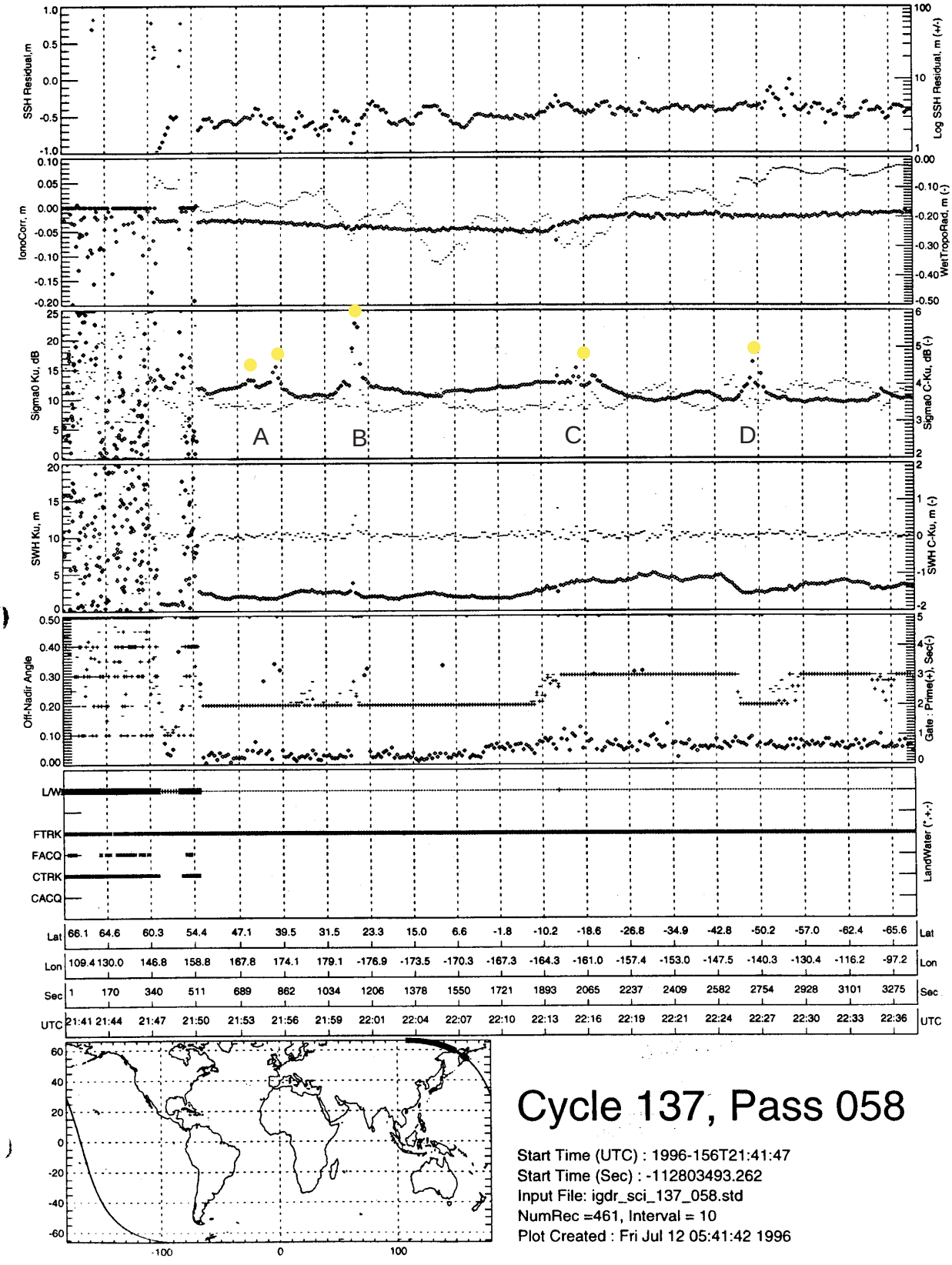

Figure 1.1. NASA TOPEX data corresponding to Cycle 137, Pass 058 (Hayne, 1997)

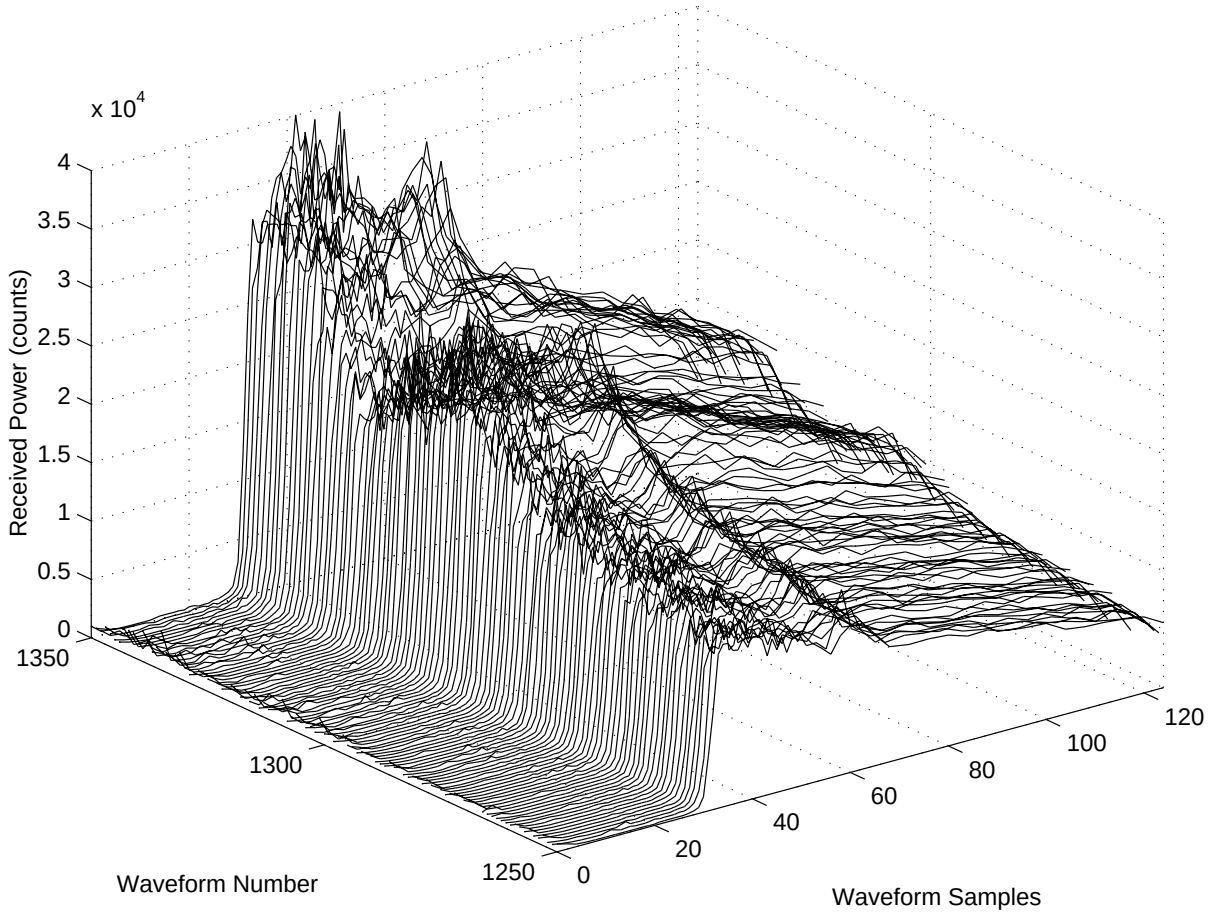

Figure 1.2. Example of σ^o blooms from region A of Cycle 137, Pass 058

Chapter 2

Derivation of the Average Power Returned from a Surface Containing a σ^O Step Discontinuity

2.1 Introduction

It was initially suspected that the σ^o blooms might have originated from a near step change in the normalized radar cross section of the ocean's surface, σ^o. In order to investigate this, a model for the average returned power from a surface containing a σ^o step discontinuity had to be derived. Figure 2.1 shows a surface containing a σ^o step discontinuity where d is the distance between the radar's nadir point and the boundary and α is the approach angle to the boundary. In this chapter we follow the approach used by Brown, 1977 as adapted to a surface containing a σ^o discontinuity. The average power returned, $P_r(t)$, from a rough surface is given by the convolution

$$P_r(t) = P_{FS}(t) * q_s(t) * p_\tau(t) \tag{2.1}$$

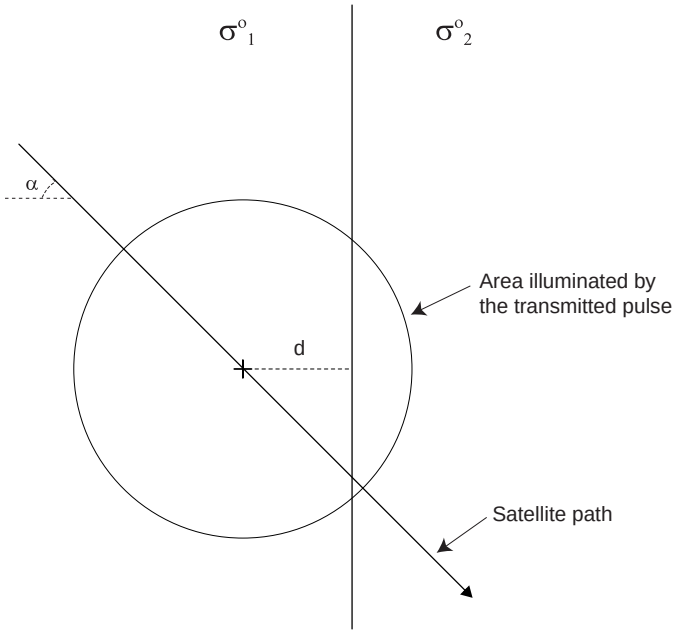

Figure 2.1. Surface containing a σ^o step discontinuity

where $P_{FS}(t)$ is the flat surface impulse response, $q_s(t)$ is the surface roughness height probability density function, and $p_\tau(t)$ is the system point target response (Brown, 1977). For a typical short pulse radar altimeter such as that on board the TOPEX satellite, $p_\tau(t)$ can be represented by a Gaussian function with known parameters (Brown, 1977). The surface height probability density function of the ocean's surface can also be approximated by a Gaussian function which depends on the rms height of the surface roughness. Thus, apart from the rms surface roughness, the only unknown in Equation 2.1 is the the flat surface impulse response $P_{FS}(t)$.

In this chapter we will derive the flat surface impulse response, $P_{FS}(t)$, and the average power returned, $P_r(t)$, from a surface containing a σ^o discontinuity. We will then provide two examples by simulating $P_r(t)$ for several scenarios.

2.2 Derivation of the Flat Surface Impulse Response $P_{FS}(t)$

The flat surface impulse response, $P_{FS}(t)$, represents the average power returned from a mean flat surface with small roughness and with the same radar cross section, σ^o, as the ocean's surface when illuminated by an impulse. $P_{FS}(t)$ is defined as

$$P_{FS}(t) = \frac{\lambda^2}{(4\pi)^3\, L_p} \int\limits_{IlluminatedArea} \frac{\delta(t - \frac{2r}{c})\, G^2(\theta,\omega)\, \sigma^o(\Psi,\phi)}{r^4}\, dA \tag{2.2}$$

where λ is the radar carrier wavelength, L_p is two-way propagation loss over and above the free space loss, $G(\theta,\omega)$ is the gain of the radar antenna, and r is range from the radar to the elemental scattering area dA on the surface (Brown, 1977). We will assume that σ^o is independent of ϕ, and its dependence on the incidence angle Ψ is neglegible. The geometry corresponding to this problem is shown in Figure 2.2.

If we assume the antenna gain to be Gaussian such that

$$G(\theta) \approx G_o\, e^{-(2/\gamma)\sin^2(\theta)}, \tag{2.3}$$

where γ is a parameter dependent on the antenna beamwidth, then Equation 2.2 becomes

$$P_{FS}(t) = \frac{G_o^2\, \lambda^2}{(4\pi)^3\, L_p\, h^4} \int\limits_{IlluminatedArea} \frac{\delta(t - \frac{2h}{c}\sqrt{1+\varepsilon^2})}{[1+\varepsilon^2]^2}\, \sigma^o(\Psi) \cdot \exp\left\{ -\frac{4}{\gamma}\left[1 - \frac{\cos^2\xi}{1+\varepsilon^2}\right] + b + a\,\cos(\tilde{\phi}-\phi) - b\,\sin^2(\tilde{\phi}-\phi)\right\}\, dA \tag{2.4}$$

where

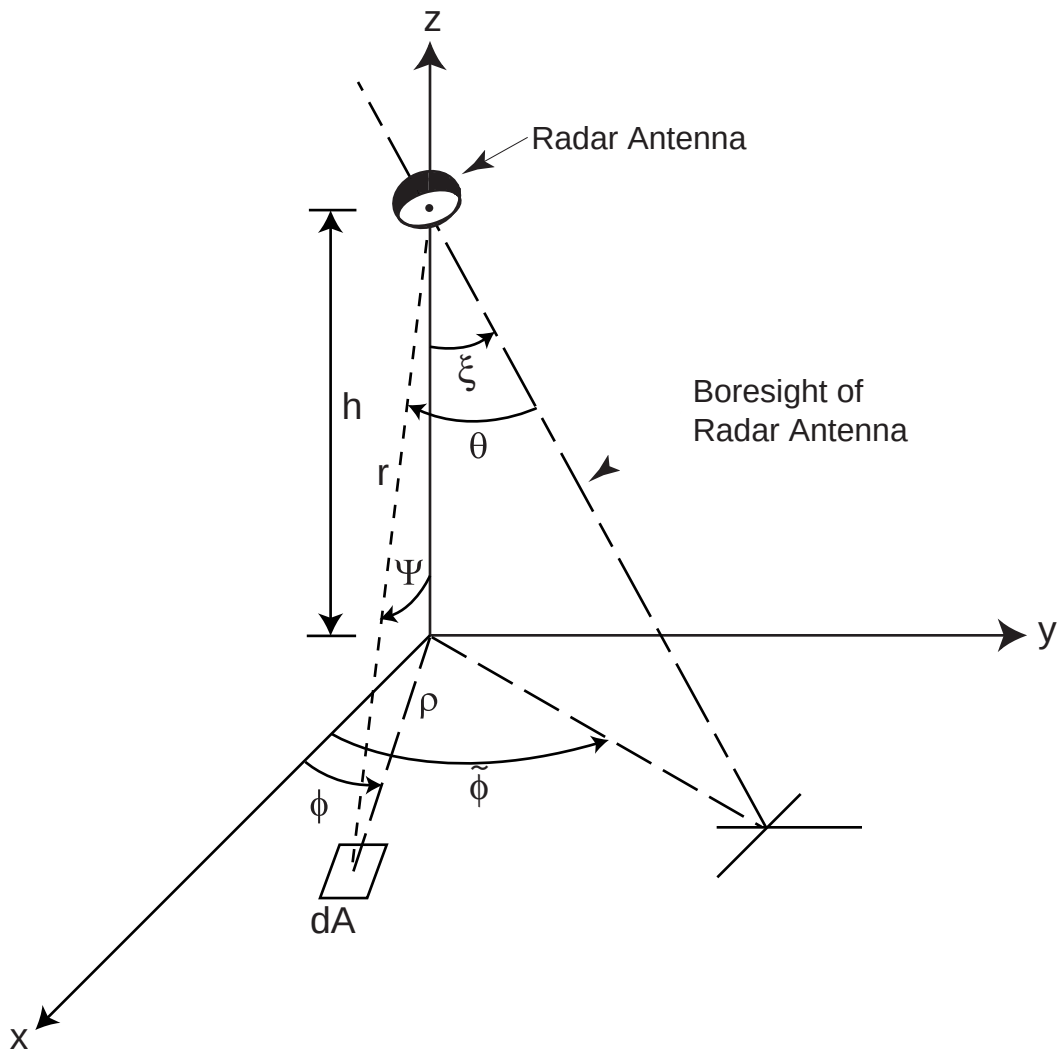

Figure 2.2. Problem geometry for flat surface impulse response.

$$\begin{aligned} \varepsilon &= \frac{\rho}{h} \\ a &= \frac{4\,\varepsilon}{\gamma}\,\frac{\sin(2\xi)}{1+\varepsilon^2} \\ b &= \frac{4\,\varepsilon^2}{\gamma}\,\frac{\sin^2(\xi)}{1+\varepsilon^2}\,. \end{aligned} \tag{2.5}$$

In order to compute the flat surface impulse response, $P_{FS}(t)$, for a surface containing a σ^o boundary, we could divide $P_{FS}(t)$ into two components where each component is found by integrating over the area containing σ_1^o and σ_2^o respectively. However, this approach produces very complicated integrals since the limits will both be ρ- and ϕ-dependent.
A simple way to compute $P_{FS}(t)$ is to divide it into two parts such as

$$P_{FS}(t) = \tilde{P}_{FS}(t) + \hat{P}_{FS}(t) \tag{2.6}$$

where

$$\begin{aligned} \tilde{P}_{FS}(t) = \frac{G_o^2\,\lambda^2}{(4\pi)^3\,L_p\,h^4} \int_0^{\infty}\int_0^{2\pi} \frac{\delta(t-\frac{2h}{c}\sqrt{1+\varepsilon^2})}{[1+\varepsilon^2]^2}\,\sigma_1^o \\ .\exp\left\{-\frac{4}{\gamma}\left[1-\frac{\cos^2\xi}{1+\varepsilon^2}\right]+b+a\,\cos(\tilde{\phi}-\phi)-b\,\sin^2(\tilde{\phi}-\phi)\right\}\,d\phi\,\rho\,d\rho \end{aligned} \tag{2.7}$$

and

$$\begin{aligned}
\hat{P}_{FS}(t) &= \frac{G_o^2\,\lambda^2}{(4\pi)^3\,L_p\,h^4}\int_d^{\infty}\int_{-\arccos(d/\rho)}^{\arccos(d/\rho)} \frac{\delta(t-\frac{2h}{c}\sqrt{1+\varepsilon^2})}{[1+\varepsilon^2]^2}\,\sigma_2^o \\
&\quad .\exp\left\{-\frac{4}{\gamma}\left[1-\frac{\cos^2\xi}{1+\varepsilon^2}\right]+b+a\,\cos(\tilde{\phi}-\phi)-b\,\sin^2(\tilde{\phi}-\phi)\right\}\,d\phi\,\rho\,d\rho \\
&\quad -\frac{G_o^2\,\lambda^2}{(4\pi)^3\,L_p\,h^4}\int_d^{\infty}\int_{-\arccos(d/\rho)}^{\arccos(d/\rho)} \frac{\delta(t-\frac{2h}{c}\sqrt{1+\varepsilon^2})}{[1+\varepsilon^2]^2}\,\sigma_1^o \\
&\quad .\exp\left\{-\frac{4}{\gamma}\left[1-\frac{\cos^2\xi}{1+\varepsilon^2}\right]+b+a\,\cos(\tilde{\phi}-\phi)-b\,\sin^2(\tilde{\phi}-\phi)\right\}\,d\phi\,\rho\,d\rho \\
&= \frac{G_o^2\,\lambda^2}{(4\pi)^3\,L_p\,h^4}\int_d^{\infty}\int_{-\arccos(d/\rho)}^{\arccos(d/\rho)} \frac{\delta(t-\frac{2h}{c}\sqrt{1+\varepsilon^2})}{[1+\varepsilon^2]^2}\,(\sigma_2^o-\sigma_1^o) \\
&\quad .\exp\left\{-\frac{4}{\gamma}\left[1-\frac{\cos^2\xi}{1+\varepsilon^2}\right]+b+a\,\cos(\tilde{\phi}-\phi)-b\,\sin^2(\tilde{\phi}-\phi)\right\}\,d\phi\,\rho\,d\rho \qquad (2.8)
\end{aligned}$$

$\tilde{P}_{FS}(t)$ corresponds to the flat surface impulse response for a surface with a constant radar cross section σ_1^o as if in Figure 2.1 σ_2^o was equal to σ_1^o. $\hat{P}_{FS}(t)$ corresponds to the flat surface impulse response for the area to the right of the boundary, as shown in Figure 2.1, with a radar cross section σ_2^o minus the flat surface impulse reponse for the same area with a radar cross section σ_1^o. By dividing the computation of $P_{FS}(t)$ in this manner, we only have to compute the solution to Equation 2.8 since the solution to Equation 2.7 is known.

The solution to $\tilde{P}_{FS}(t)$ when $\frac{c\tau}{h} \ll 1$ and $\sqrt{\frac{c\tau}{h}}\,tan\xi \ll 1$, which is true for our problem, is well known to be

$$\tilde{P}_{FS}(\tau) \approx \frac{c\,G_o^2\,\lambda^2\,\sigma_1^o}{4(4\pi)^2\,L_p\,h^3}\exp\{-\frac{4}{\gamma}[\sin^2\xi+\frac{c}{h}\tau\cos 2\xi]\}I_o\left(\frac{4}{\gamma}\sqrt{\frac{c\,\tau}{h}}\sin 2\xi\right) \quad \text{for } \tau \geq 0 \qquad (2.9)$$

where $\tau = t - 2h/c$ represents the two-way incremental ranging time (Brown, 1977).

In solving for $\hat{P}_{FS}(t)$ in Equation 2.8, we can restrict the integration over ρ to

$d < \rho < 10^5$ m. This simplification is possible due to the facts that the maximum two-way incremental ranging time, τ_{max}, received by the NASA radar altimter is $\tau_{max} = 400$ ns and ρ is related to τ by $\rho = \sqrt{hc\tau}$. Hence $\rho_{max} = 1.3 * 10^4 < 10^5$ m. For this range in ρ, the parameter b in Equation 2.8 becomes neglegible since b is ρ dependent (Equation 2.5). This yields

$$\hat{P}_{FS}(t) \approx \frac{G_o^2\,\lambda^2}{(4\pi)^3\,L_p\,h^4} \int_d^{10^5} \frac{\delta(t - \frac{2h}{c}\sqrt{1+\varepsilon^2})}{[1+\varepsilon^2]^2}\,(\sigma_2^o - \sigma_1^o)\,\exp\left\{-\frac{4}{\gamma}\left[1 - \frac{\cos^2\xi}{1+\varepsilon^2}\right]\right\} \cdot \int_{-\arccos(d/\rho)}^{\arccos(d/\rho)} \exp\{a\,\cos(\tilde{\phi} - \phi)\}\,d\phi\,\rho\,d\rho. \tag{2.10}$$

After a change of variables such that $\alpha = \tilde{\phi} - \phi$, we have

$$\hat{P}_{FS}(t) = \frac{G_o^2\,\lambda^2}{(4\pi)^3\,L_p\,h^4} \int_d^{10^5} \frac{\delta(t - \frac{2h}{c}\sqrt{1+\varepsilon^2})}{[1+\varepsilon^2]^2}\,(\sigma_2^o - \sigma_1^o)\,\exp\left\{-\frac{4}{\gamma}\left[1 - \frac{\cos^2\xi}{1+\varepsilon^2}\right]\right\} \cdot \int_{\tilde{\phi}-\arccos(d/\rho)}^{\tilde{\phi}+\arccos(d/\rho)} \exp\{a\,\cos(\alpha)\}\;d\alpha\,\rho\,d\rho. \tag{2.11}$$

We know that

$$\exp\{a\,\cos(\alpha)\} = I_o(a) + 2\,\sum_{k=1}^{\infty} I_k(a)\,\cos(k\,\alpha).$$

where $I_n(.)$ corresponds to the modified Bessel function of the first kind. Substituting the above expression into Equation 2.11 we obtain

$$\hat{P}_{FS}(t) = \frac{G_o^2\,\lambda^2}{(4\pi)^3\,L_p\,h^4}\int_d^{10^5}\frac{\delta(t-\frac{2h}{c}\sqrt{1+\varepsilon^2})}{[1+\varepsilon^2]^2}\,(\sigma_2^o-\sigma_1^o)\;\exp\left\{-\frac{4}{\gamma}\left[1-\frac{\cos^2\xi}{1+\varepsilon^2}\right]\right\}$$
$$\cdot\int_{\tilde{\phi}-\arccos(d/\rho)}^{\tilde{\phi}+\arccos(d/\rho)}\left(I_o(a)+2\;\sum_{k=1}^{\infty}I_k(a)\;\cos(k\,\alpha)\right)\;d\alpha\,\rho\,d\rho$$
$$=\frac{G_o^2\,\lambda^2}{(4\pi)^3\,L_p\,h^4}\int_d^{10^5}\frac{\delta(t-\frac{2h}{c}\sqrt{1+\varepsilon^2})}{[1+\varepsilon^2]^2}\,(\sigma_2^o-\sigma_1^o)\;\exp\left\{-\frac{4}{\gamma}\left[1-\frac{cos^2\xi}{1+\varepsilon^2}\right]\right\}$$
$$2\left\{I_o(a)\arccos(d/\rho)+\sum_{k=1}^{\infty}(1/k)I_k(a)[\sin(k(\tilde{\phi}+\arccos(d/\rho)))-\sin(k(\tilde{\phi}-\arccos(d/\rho)))]\right\}\;\rho d\rho. \tag{2.12}$$

Since

$$\sin(a+b)-\sin(a-b)=2\;\cos(a)\;\sin(b),$$

Equation 2.12 can be simplified to be

$$\hat{P}_{FS}(t) = \frac{G_o^2\,\lambda^2}{(4\pi)^3\,L_p\,h^4}\int_d^{10^5}\frac{\delta(t-\frac{2h}{c}\sqrt{1+\varepsilon^2})}{[1+\varepsilon^2]^2}\,(\sigma_2^o-\sigma_1^o)\;\exp\left\{-\frac{4}{\gamma}\left[1-\frac{\cos^2\xi}{1+\varepsilon^2}\right]\right\}$$
$$\cdot\left\{2\,I_o(a)\;\arccos(d/\rho)+4\sum_{k=1}^{\infty}(1/k)I_k(a)\cos(k\tilde{\phi})\sin(k\arccos(d/\rho))\right\}\;\rho\,d\rho. \tag{2.13}$$

After a change of variables such that $x=\frac{2h}{c}\sqrt{1+\varepsilon^2}$, Equation 2.13 becomes

$$\hat{P}_{FS}(t) = \frac{G_o^2\,\lambda^2\,(\sigma_2^o - \sigma_1^o)}{(4\pi)^3\,L_p\,h^4} \int\limits_{\frac{2h}{c}\sqrt{1+(\frac{d}{h})^2}}^{\frac{2h}{c}\sqrt{1+(\frac{10^5}{h})^2}} \frac{\delta(t-x)}{(\frac{x\,c}{2h})^4} \exp\left\{-\frac{4}{\gamma}\left[1 - \frac{\cos^2\xi}{(\frac{x\,c}{2h})^2}\right]\right\} \left(\frac{x\,c^2}{4}\right)$$
$$\cdot \left\{ 2\,I_o\left(\frac{4}{\gamma}\frac{\sqrt{(\frac{x\,c}{2h})^2 - 1}}{(\frac{x\,c}{2h})^2}\sin 2\xi\right) \arccos\left(\frac{d}{h\,\sqrt{(\frac{x\,c}{2h})^2 - 1}}\right) \right.$$
$$\left. +4\sum_{k=1}^{\infty}(1/k) I_k\left(\frac{4}{\gamma}\frac{\sqrt{(\frac{x\,c}{2h})^2 - 1}}{(\frac{x\,c}{2h})^2}\sin 2\xi\right)\cos(k\tilde{\phi})\sin\left(k\arccos\left(\frac{d}{h\sqrt{(\frac{x\,c}{2h})^2 - 1}}\right)\right)\right\} dx. \tag{2.14}$$

Evaluating the integral, we have

$$\hat{P}_{FS}(t) = \frac{G_o^2\,\lambda^2\,(\sigma_2^o - \sigma_1^o)}{(4\pi)^3\,L_p\,h^4} \exp\left\{-\frac{4}{\gamma}\left[1 - \frac{\cos^2\xi}{(\frac{c\,t}{2h})^2}\right]\right\} \left(\frac{c\,h}{2}\right)\left(\frac{2h}{c\,t}\right)^3$$
$$\cdot \left\{ 2\,I_o\left(\frac{4}{\gamma}\frac{\sqrt{(\frac{c\,t}{2h})^2 - 1}}{(\frac{c\,t}{2h})^2}\sin 2\xi\right) \arccos\left(\frac{d}{h\,\sqrt{(\frac{c\,t}{2h})^2 - 1}}\right) \right.$$
$$\left. +4\sum_{k=1}^{\infty}(1/k) I_k\left(\frac{4}{\gamma}\frac{\sqrt{(\frac{c\,t}{2h})^2 - 1}}{(\frac{c\,t}{2h})^2}\sin 2\xi\right)\cos(k\tilde{\phi})\sin\left(k\arccos\left(\frac{d}{h\sqrt{(\frac{c\,t}{2h})^2 - 1}}\right)\right)\right\} \tag{2.15}$$

for $\frac{2h}{c}\sqrt{1+(\frac{d}{h})^2} \le t \le \frac{2h}{c}\sqrt{1+(\frac{10^5}{h})^2}$.

We can further simplify Equation 2.15 by converting to the two-way incremental ranging time through $\tau = t - 2h/c$. For our problem $\frac{c\tau}{h} \ll 1$, so we have

$$\hat{P}_{FS}(\tau) \approx \frac{c\,G_o^2\,\lambda^2\,(\sigma_2^o - \sigma_1^o)}{(4\pi)^3\,L_p\,h^3} \exp\left\{-\frac{4}{\gamma}\left[1 - \cos^2\xi\right]\right\}$$
$$\cdot \left\{ I_o\left(\frac{4}{\gamma}\sqrt{\frac{c\,\tau}{h}}\sin 2\xi\right)\arccos\left(\frac{d}{\sqrt{c\,h\,\tau}}\right) + 2\sum_{k=1}^{\infty}(1/k) I_k\left(\frac{4}{\gamma}\sqrt{\frac{c\,\tau}{h}}\sin 2\xi\right)\right.$$
$$\left. \cos(k\tilde{\phi})\sin\left(k\arccos\left(\frac{d}{\sqrt{c\,h\,\tau}}\right)\right)\right\} \tag{2.16}$$

for $\tau \geq \frac{2h}{c}\left(\sqrt{1+(\frac{d}{h})^2}-1\right)$.

We have neglected the upper limit of the time constraint since such a time limit would be out of range for the altimeter in question.

For the purposes of this paper, the infinite series can be reduced to the sum of the first 20 terms with no significant loss in accuracy. Thus, the final formula for $P_{FS}(\tau)$ is

$$P_{FS}(\tau) \approx \begin{cases} \frac{c\,G_o^2\,\lambda^2\,\sigma_1^o}{4(4\pi)^2\,L_p\,h^3}\exp\{-\frac{4}{\gamma}[\sin^2\xi+\frac{c}{h}\tau\cos 2\xi]\}I_o\left(\frac{4}{\gamma}\sqrt{\frac{c\,\tau}{h}}\sin 2\xi\right) & \text{for } 0\leq\tau<\tau_o \\ \frac{c\,G_o^2\,\lambda^2\,\sigma_1^o}{4(4\pi)^2\,L_p\,h^3}\exp\{-\frac{4}{\gamma}[\sin^2\xi+\frac{c}{h}\tau\cos 2\xi]\}I_o\left(\frac{4}{\gamma}\sqrt{\frac{c\,\tau}{h}}\sin 2\xi\right)+ & \\ \frac{c\,G_o^2\,\lambda^2\,(\sigma_2^o-\sigma_1^o)}{(4\pi)^3\,L_p\,h^3}\exp\{-\frac{4}{\gamma}(\sin^2\xi)\}\{I_o\left(\frac{4}{\gamma}\sqrt{\frac{c\,\tau}{h}}\sin 2\xi\right)\arccos\left(\frac{d}{\sqrt{c\,h\,\tau}}\right) & \\ \quad +2\sum_{k=1}^{20}(1/k)I_k\left(\frac{4}{\gamma}\sqrt{\frac{c\,\tau}{h}}\sin 2\xi\right)\cos(k\tilde{\phi})\sin\left(k\arccos\left(\frac{d}{\sqrt{c\,h\,\tau}}\right)\right)\} & \text{for } \tau\geq\tau_o \end{cases} \tag{2.17}$$

where $\tau_o = \frac{2h}{c}\left(\sqrt{1+(\frac{d}{h})^2}-1\right)$.

2.3 Derivation of the Average Returned Power $P_r(\tau)$

If we assume the system point target response, $p_\tau(t)$, is well represented by a Gaussian function, and the ocean's surface height probability density function can also be represented by a Gaussian function, then the average returned power defined by a convolution in Equation 2.1 can be simplified to

$$P_r(\tau) \approx \eta P_T P_{FS}(\tau)\sqrt{2.\pi}\sigma_p\left[1+erf\left(\frac{\tau}{\sqrt{2}\sigma_c}\right)\right]/2 \qquad \text{for } \tau\geq 0 \tag{2.18}$$

where η is the pulse compression ratio, P_T is the peak transmitted power, σ_p is related to

the point target 3dB width (T) by

$$\sigma_p = 0.425T \tag{2.19}$$

and

$$\sigma_c = \sqrt{\sigma_p^2 + \left(\frac{2\sigma_s}{c}\right)^2} \tag{2.20}$$

where σ_s is the rms sea height (Brown, 1977). Throughout this thesis, we will use the significant wave height (SWH) of the sea which is defined as 4 times σ_s. In order to account for the curvature of the earth we will replace the altimeter's height h by h/0.826 in Equation 2.17 (Hayne, 1998).

2.4 Examples

In order to provide the reader with a more meaningful idea of the effects of a surface containing a σ^o discontinuity on the average power returned waveforms of the altimeter on board the TOPEX satellite, we will simulate several Ku-band waveform returns computed from Equation 4.22. We will simulate the waveform returns from a surface with an increasing and decreasing net radar cross section discontinuity, $\Delta\sigma = \sigma_2^o - \sigma_1^o$, as well as when there is no discontinuity, for different distances d to the discontinuity and antenna pointing angles ξ.

Figure 2.3 shows the average power returned waveforms corresponding to a surface containing a 3 dB increasing σ^o discontinuity when the satellite's nadir point is 8 Km away from the discontinuity and $\sigma_1^o = 10$ dB for antenna pointing angles of 0^o, 0.1^o and 0.2^o. When compared to the plot corresponding to a surface with no discontinuity ($\Delta\sigma = 0$) we can see the positive contributions from the σ_2^o part of the surface. Also noticeable are the changes inflicted in the trailing edge of the waveforms by the different antenna pointing angles. As the pointing angle increases so does the slope of the trailing edge of the waveform.

Figure 2.4 shows the average power returned waveforms corresponding to a surface containing a 3 dB decreasing σ^o discontinuity when the satellite's nadir point is 10 Km away from the discontinuity and $\sigma_1^o = 13$ dB for antenna pointing angles of 0^o, 0.1^o and 0.2^o. When compared to the plot corresponding to a surface with no discontinuity ($\Delta\sigma = 0$) we can see the negative contributions from the σ_2^o part of the surface. Also noticeable are the changes inflicted in the trailing edge of the waveforms by the different antenna pointing angles. In this case, as the pointing angle increases the slope of the trailing edge of the waveform decreases. Although compared to Figure 2.3 we can see that the pointing angle effects on these waveforms are less significant.

More detailed simulations are shown in Chapter 3.

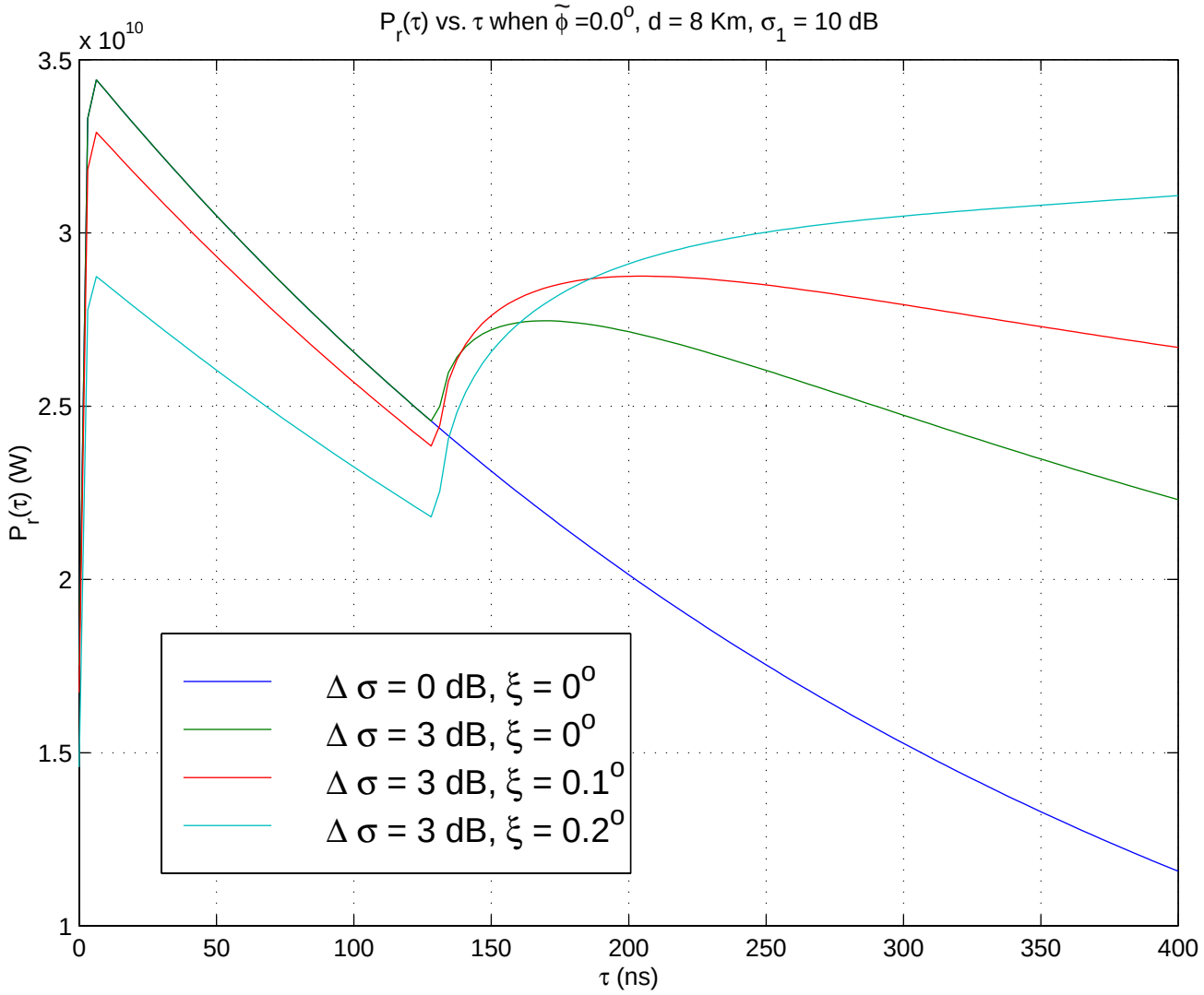

Figure 2.3. Examples of the average power returned from a surface containing an increasing σ^o step discontinuity.

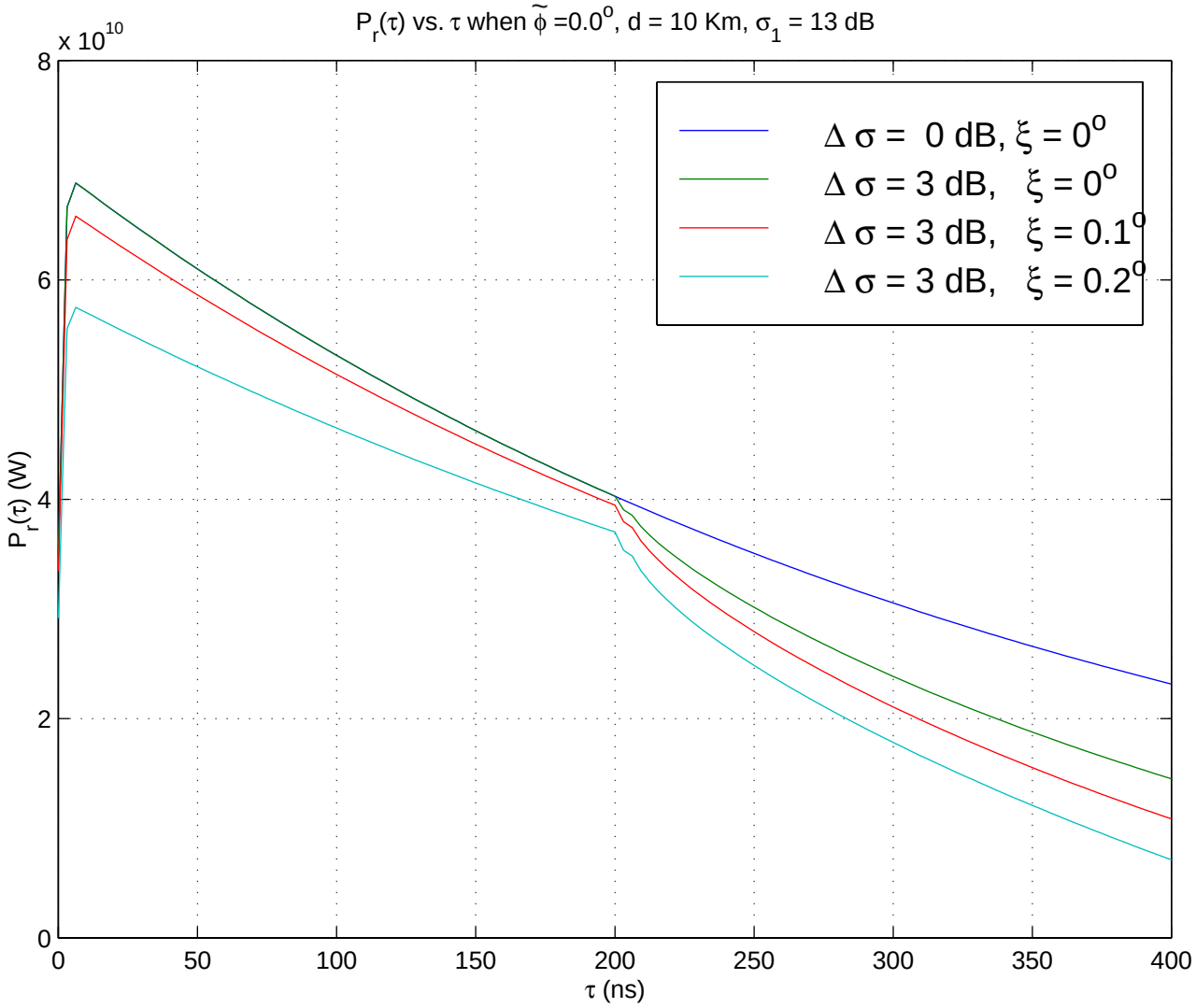

Figure 2.4. Examples of the average power returned from a surface containing a decreasing σ^o step discontinuity.

Chapter 3

The Effect of a Surface Containing a Step Discontinuity in σ^O

3.1 Introduction

In this chapter we will investigate whether a surface containing a σ^o step discontinutity could be the cause of the σ^o blooms. We will do this by studying the effects of such surfaces on the Automatic Gain Control (AGC) system on the NASA radar altimeter (NRA) aboard the TOPEX/POSEIDON satellite.

Initially, the σ^o blooms were called AGC blooms because the blooms were observed in the values of the AGC produced by the radar altimeter. The AGC is actually the way the radar altimeter measures the surface scattered power level. One must go through a calibration curve and the radar range equation to get σ^o from AGC values. We will reverse the process and simulate the response of the AGC system to different step changes in σ^o discontinuity such as shown in Figure 2.1.

We will concentrate on surface situations and pointing angles that yield a higher ocurrance of the σ^o blooms, that is, these surfaces often have small significant wave heights and the pointing angles are frequently out of range. This means that the altimeter waveform's

plateau decays too rapidly, at a rate faster than possible even for a 0.0 attitude angle. We will show that this occurrence is typical on a surface containing a decreasing σ^o boundary when observed with a small pointing angle.

We will start by providing a brief explanation of how the data is acquired by the satellite. We will then simulate and study the returns from surfaces containing both increasing and decreasing σ^o discontinuities, as well as the effects of those returns on the AGC and waveform tracker of the radar altimeter on board the TOPEX satellite.

3.2 Data Acquisition

Transmissions from the radar altimeter occur in bursts. Each burst consists of 38 Ku-band pulses and 10 C-band pulses, with a pulse duration of 102.4 μs and a pulse spacing of 112.4 μs (Ku-band) and 713.84 μs (C-band). Pulses are linearly (decreasing) frequency modulated with center frequencies of 13.9 GHz (Ku-band) and 5.3 GHz (C-band). The interval between bursts is variable and depends on the satellite's altitude. Each surface scattered radar pulse is then downconverted, filtered and pre-processed. The resulting waveform is sampled by 128 samplers evenly spaced at 3.125 ns as shown in Figure 3.1. In order to obtain meaningful results, several of the received waveforms must be averaged to form a mean waveform. Six bursts are grouped to form a 'track interval' corresponding to approximately 50 ms of data (228 Ku-band pulses and 60 C-band pulses). A track interval is the smallest time scale on which the signal processor interprets the averaged waveform.

The mean waveform corresponding to each track interval actually comprises 128 discrete samples spaced by 3.125 ns. The power inside a series of gates will be calculated from the mean waveform in order to obtain information about the ocean's surface. A gate is defined to be the arithmetic average of a number of time-adjacent waveform samples.

Five types of gates will be considered: Early, Middle, Late, AGC and Noise gates. The location and width of these gates with respect to the track point (sample 32.5) is shown in Figure 3.1. The Noise gate is the average of samples 5 through 8 and is used to estimate

the noise floor of the waveform. The AGC gate is the average of samples 17 through 48. The AGC and the radar cross section σ^o are related by a calibration curb and the range equation. Combined with the Noise gate, the AGC gate is used to estimate the signal level of the waveform and thus the radar cross section σ^o of the surface. The AGC gate also determines the setting of the attenuator in the receiver so that the peak level of the received waveforms remains constant. There are five possible Middle gates. The samples comprising each Middle gate are shown in Figure 3.1. The Middle gates assist in tracking the waveform as it is stretched by large surface roughness. The Early and Late gates assist in selecting the radar waveform track point and computing the significant wave height. The samples required for their calculation are also shown in Figure 3.1.

3.3 Waveform Tracking and AGC Computation

Once a waveform has been received and sampled, the signal processor in the radar altimeter attempts to maintain the waveform in a fixed relative time position. The signal processor maintains a fixed gate position of the waveforms by always positioning the waveform's leading edge at sample 32.5 (the track point). The signal processor will position the track point so that the following equation holds true,

$$(S_i * AGC_{gate} - M_i) = 0 \tag{3.1}$$

where S_i is a parameter with value near unity, and AGC_{gate} and M_i correspond to the AGC and Middle gates respectively. The gate index i that will determine the particular Middle gate and S value used depends on the significant wave height. Lower siginificant wave heights will require lower gate indexes. The Ku-band values for S obtained from the Johns Hopkins University Advanced Physics Laboratory flight software are shown in Table 3.1 (Hayne, 1998).

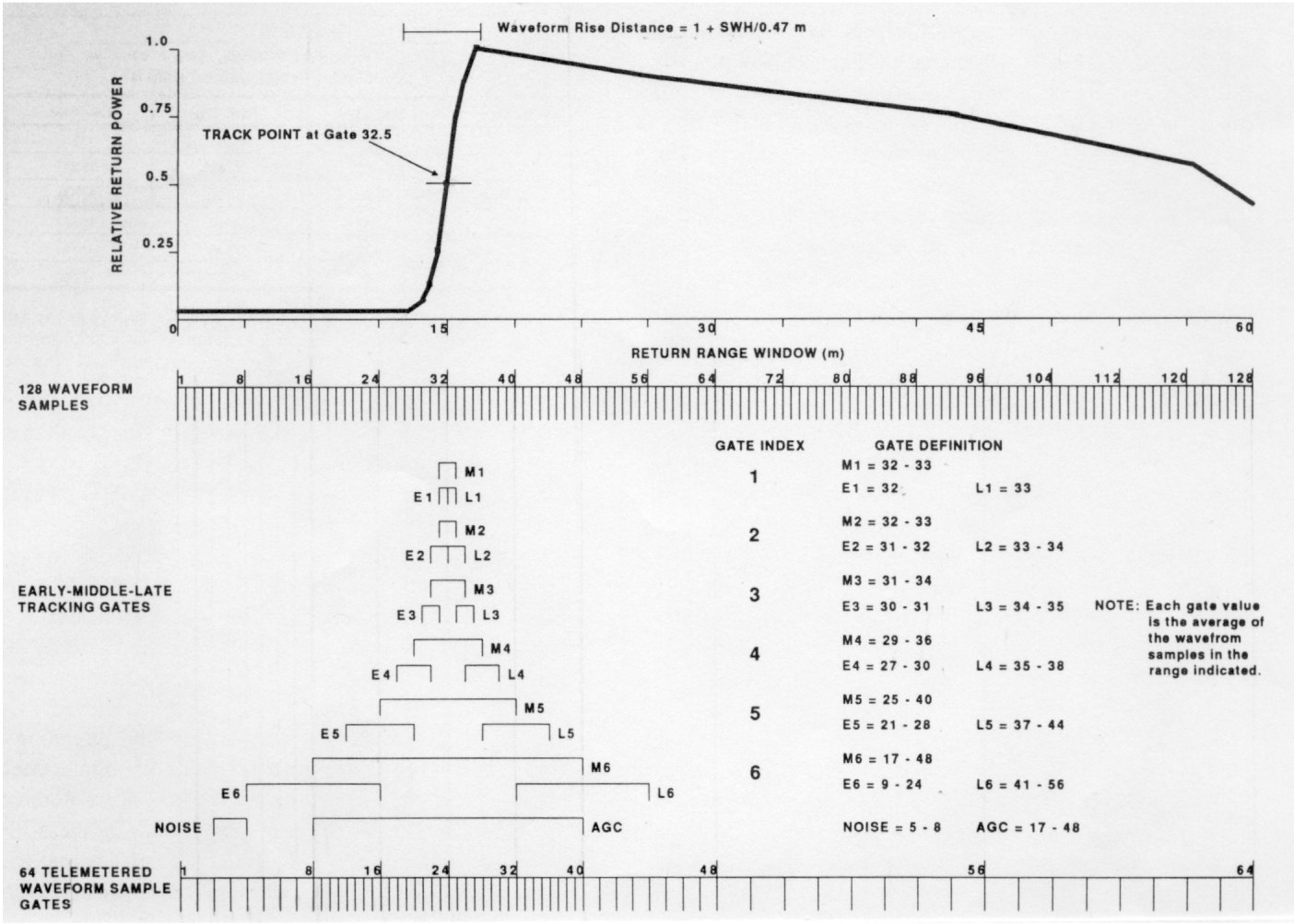

Figure 3.1. Waveform Samples and Gates (Marth et al., 1993)

i	S_i
1	1.02105935
2	1.02105935
3	1.02269096
4	1.02171137
5	1.01651842

Table 3.1. Values for AGC parameter S (Hayne, 1998)

Since we are only concerned with situations where the significant wave height SWH is small, we will use the lowest gate index i = 1 in our simulations.
Once the waveform has been shifted in time and Equation 3.1 holds true, the value of the AGC (AGC_{new}) is calculated every 0.05 seconds from Equation 3.2. By making the value of the AGC (AGC_{new}) dependent on its previous value (AGC_{old}) as well as on the AGC gate (AGC_{gate}), the change in the AGC for very large values of the AGC gate is limited.

$$AGC_{new} = \alpha * AGC_{gate} + (1 - \alpha) * AGC_{old} \tag{3.2}$$

where $\alpha = 1/8$ (Hayne, 1998). The value of the AGC_{new} is what the attenuator in the RF receiver will use to maintain the peak level of the received waveforms constant.

3.4 Simulations

Using the model for the average returned power derived in Chapter 2 we will simulate the returns from a surface containing a σ^o step discontitnuity such as shown in Figure 2.1 as the satellite approaches the discontinuity at a ground speed of 7 Km/sec at an angle α to the boundary. We will start our simulations when the satellite's nadir point is 14 Km away

from the σ^o boundary (d = 14 Km) on the σ_1^o part of the surface. At this distance the contributions from the part of the surface with σ_2^o just begin to become apparent. We will stop our simulations when the satellite's nadir point is 1.5 Km away from the boundary but still over the σ_1^o surface. This distance (1.5 Km) was chosen to simplify the simulations since we do not want to simulate the satellite's nadir point crossing over the boundary. Simulating the satellite's nadir point crossing over and away from the boundary would add complexity to the simulation of our model while not providing any new data. In other words, the waveforms obtained by simulating the the satellite's nadir point beyond the boundary partially duplicates the waveforms (only in a reversed order with different amplitudes) generated by the inverse of this boundary. We will assume that the surface has a significant wave height of 1 m so a gate index of 1 is required. Starting with d = 14 Km we will simulate waveforms every 0.05 seconds until d = 1.5 Km. We will initially only simulate the waveforms corresponding to Ku-band in order to test our hypothesis that a surface containing a σ^o step discontinuity could be the cause of the σ^o blooms.

We simulate surfaces with a net radar cross section discontinuity $\Delta\sigma = \sigma_2 - \sigma_1$ equal to +3, +6, -10 and -7 dB and approaching at α angles of 0, 30 and 45 degrees, with antenna pointing angles of 0.01, 0.05 and 0.1 degrees. In Equation 4.22 we found that the magnitude of the contribution from the σ_2 part of the surface was also dependent on $\tilde{\phi}$, the angle of the satellite's nadir point with respect to the x-axis (see Figure 2.2). Throughout our simulations we will assume that $\tilde{\phi}$ does not change in time. Furthermore, to simplify our simulations we choose $\tilde{\phi} = 0^o$.

For each position increment we will compute its corresponding mean waveform using Equation 2.18. The AGC and first Middle gate will then be computed for the waveform and the result of $S_i * AGC_{gate} - M_i$ (Equation 3.1) will be calculated. The waveform will then be shifted in time one sample and this process will be repeated until the left hand side of Equation 3.1 is minimized and its corresponding AGC gate will be recorded. This simulates the iterative or tracking process that the tracker on the radar altimeter follows.

The value to be used by the attenuator is then computed using Equation 3.2. This whole

process is then repeated for the next waveform. Through our simulations we will show the waveforms computed from the model (Equation 2.18), the AGC, the tracker induced shift, and the attenuated waveforms. For two of the four cases we will study both the attenuated and shifted waveforms. For simplicity, the AGC will be shown normalized and the waveforms will be attenuated with respect to an AGC reference of 0.75.

3.4.1 Simulation for a surface with $\Delta\sigma = +3$ dB

We first simulated the average returned power waveforms from a surface with a net radar cross section step discontinuity of $\Delta\sigma = +3$ dB with $\sigma_1 = 10$ dB, an antenna pointing angle ξ of 0.01^o, and an approach angle α of 0^o. Figure 3.2 shows the average returned power waveforms as computed from Equation 2.18 for 0.05 second increments as the satellite approaches the σ^o discontinuity. These waveforms do not include the normalizing effect of the AGC nor the tracker induced shift. We can see how the contribution from the σ_2 part of the surface appears toward the end of the first waveform (n = 1) and move to an earlier time in the waveform increasing its level until the final waveform (n = 36).

The normalized AGC calculated from Equation 3.2 and the tracker induced shift derived from Equation 3.1 corresponding to each waveform are shown in Figure 3.3. As expected, the AGC remains unchanged for the first 21 waveforms since the contribution from the σ_2 part of the surface does not enter the region of the AGC gate. From this point on, as more of this contribution enters the AGC gate, the value of the AGC will increase accordingly. Similarly, for the first 21 waveforms, the tracker seems to be stabilized shifting the waveforms 16 samples or 50 ns. However, once the contribution from the σ_2 part of the surface begins to enter the AGC gate, the tracker becomes confused and loses track of the waveforms. Near to the final waveforms of this set, the tracker appears to recover and starts tracking the waveforms.

Figure 3.4 shows the attenuated waveforms corresponding to this surface. These waveforms behave as expected since they are all attenuated as their AGC was larger than the reference

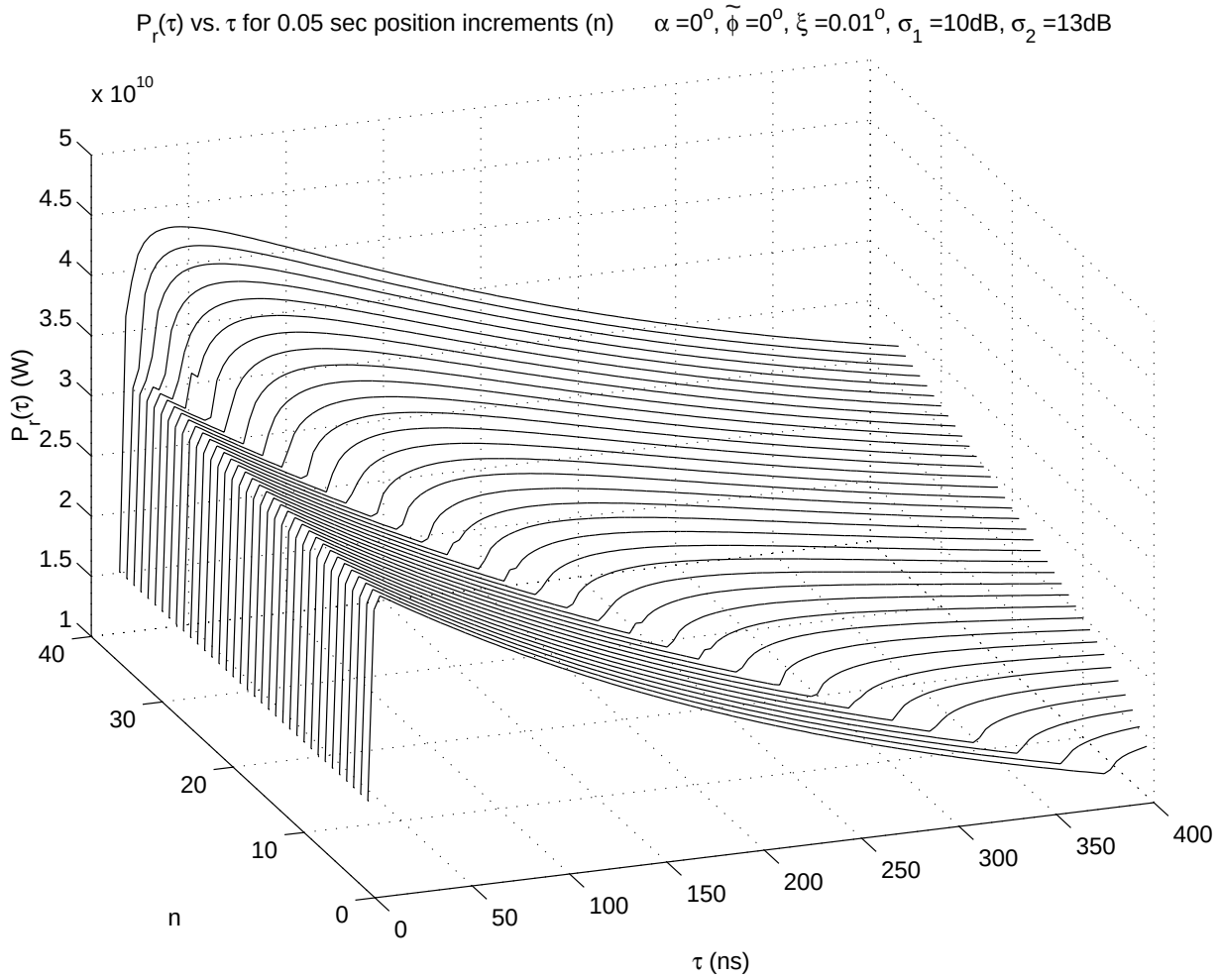

Figure 3.2. Simulated waveforms for $\Delta\sigma = +3$ dB without AGC effects or tracker induced shift

AGC of 0.75, especially towards the end of the set where the waveforms had higher AGC values. We can also see that the level of all the waveforms is more uniform. That is, in the last half of the waveforms in the set their peak level does not appear to increase at the same rate as those in Figure 3.2.

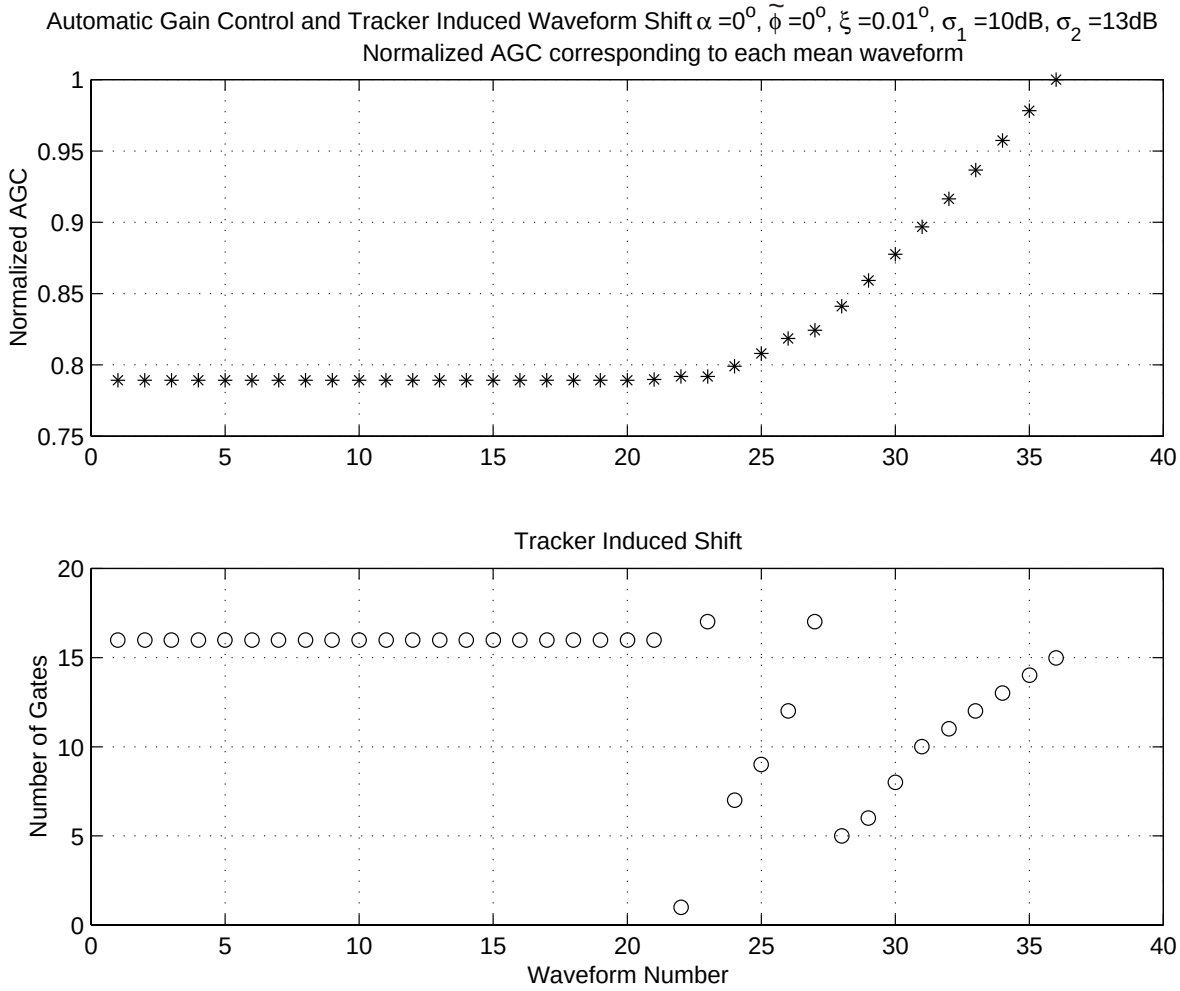

Figure 3.3. Normalized AGC and tracker induced shift for $\Delta\sigma = +3$ dB

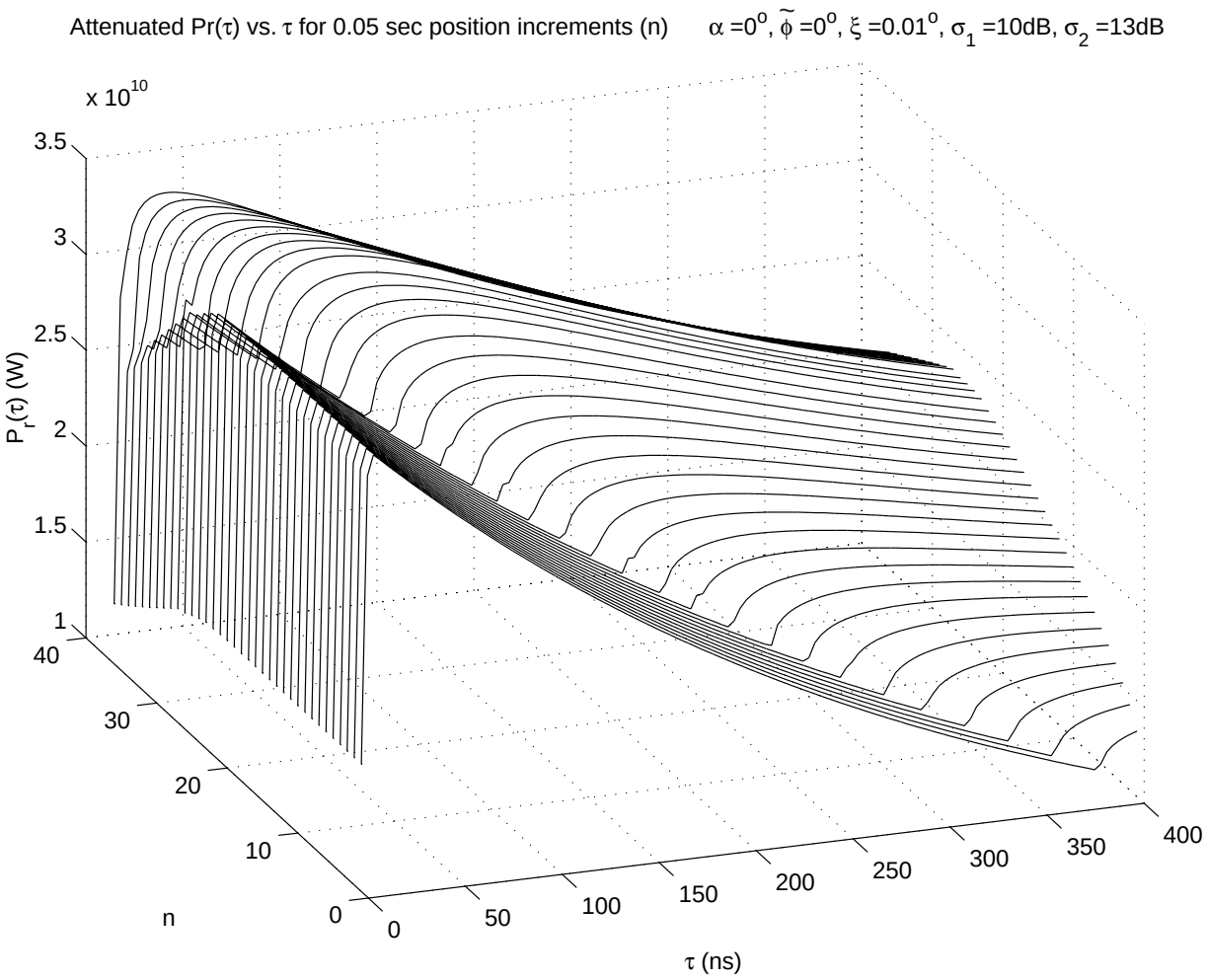

Figure 3.4. Attenuated waveforms for $\Delta\sigma = +3$ dB

3.4.2 Simulation for a surface with $\Delta\sigma = +6$ dB

We next simulate the average returned power from a surface with a net radar cross section discontinutity $\Delta\sigma = +6$ dB with $\sigma_1 = 12$ dB, an antenna pointing angle ξ of 0.1^o and an approach angle α of 30^o.

Figure 3.5 shows the average returned power waveforms as computed from Equation 2.18 without the effects of the AGC or the tracker induced shift. As in the previous simulation we can see how the contributions from the σ_2 part of the surface move through the waveforms as we get closer to the discontinutity; only in this case, these contributions are much more noticeable since the discontinuity is twice as large. Also noticeable is that there are more waveforms in this simulation than in the previous one, 42 versus 36. This is caused by the increase in the approach angle, 30^o versus 0^o.

Figure 3.6 shows the normalized AGC and the tracker induced shift corresponding to this surface. The AGC remains unchanged for the first 27 waveforms and starts increasing as the contributions from the σ_2 part of the surface begin to enter the AGC gate. However, the AGC corresponding to waveform 39 actually drops and then continues to increase for the next waveform. This unexpected drop in the AGC ocurred due to the malfunction of the tracker. If we look at the tracker induced shift corresponding to waveform 39, we can see that the tracker loses track of this waveform. With this exception, the tracker behaves very much as in the previous simulation getting slightly confused as the contributions from the σ_2 part of the surface begin to enter the AGC gate but recovering soon thereafter.

Figure 3.7, 3.8, and 3.9 show the individual mean waveforms from Figure 3.5 with the AGC effects and tracker induced shift included. We note that these waveforms have been normalized by a factor of 10^{-9}. In these figures it is easier to observe both the contributions from the σ_2 part of the surface and the effects of the tracker. Note the sudden tracker induced shift in waveform 39 (n = 39).

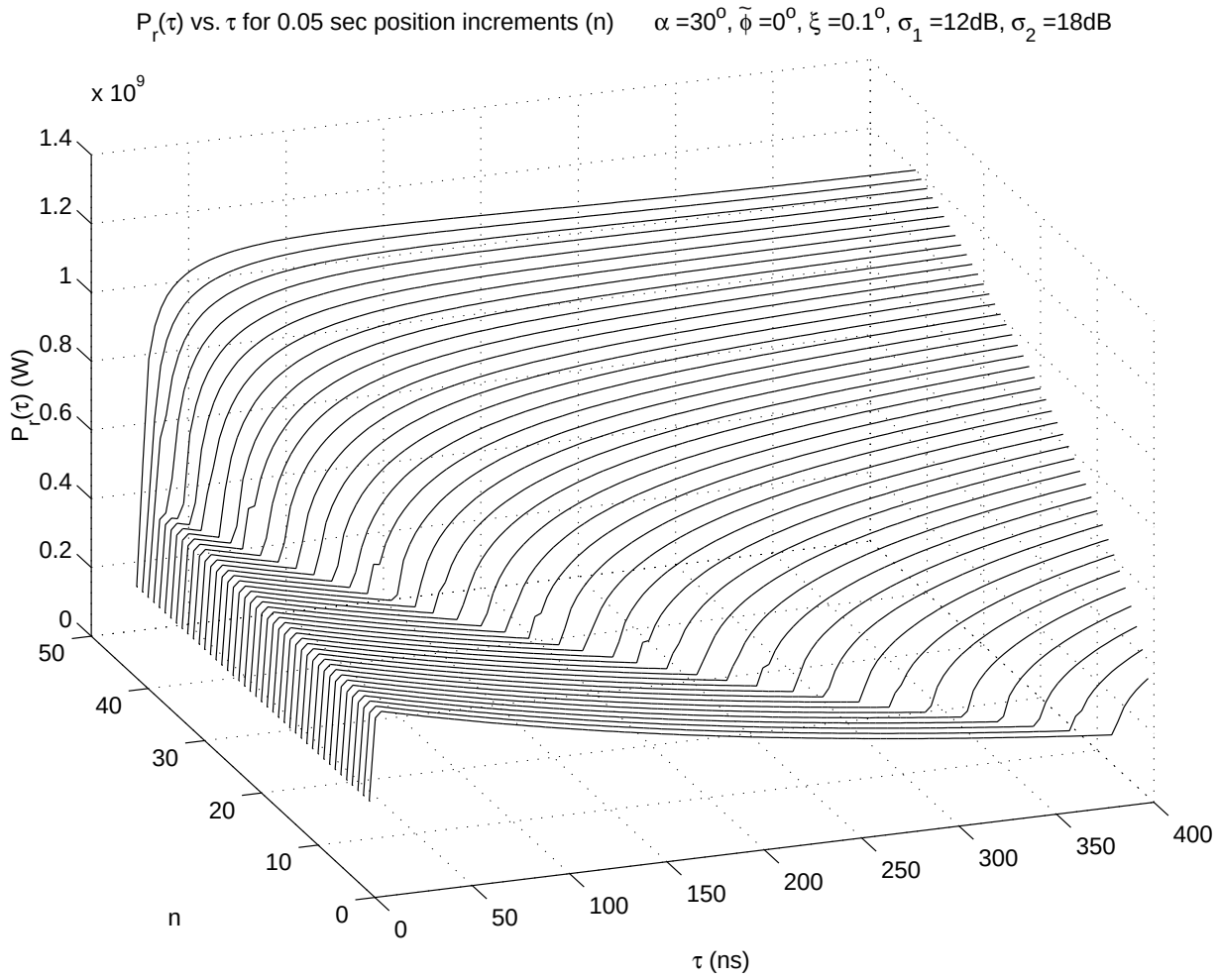

Figure 3.5. Simulated waveforms for $\Delta\sigma = +6$ dB without AGC effects or tracker induced shift

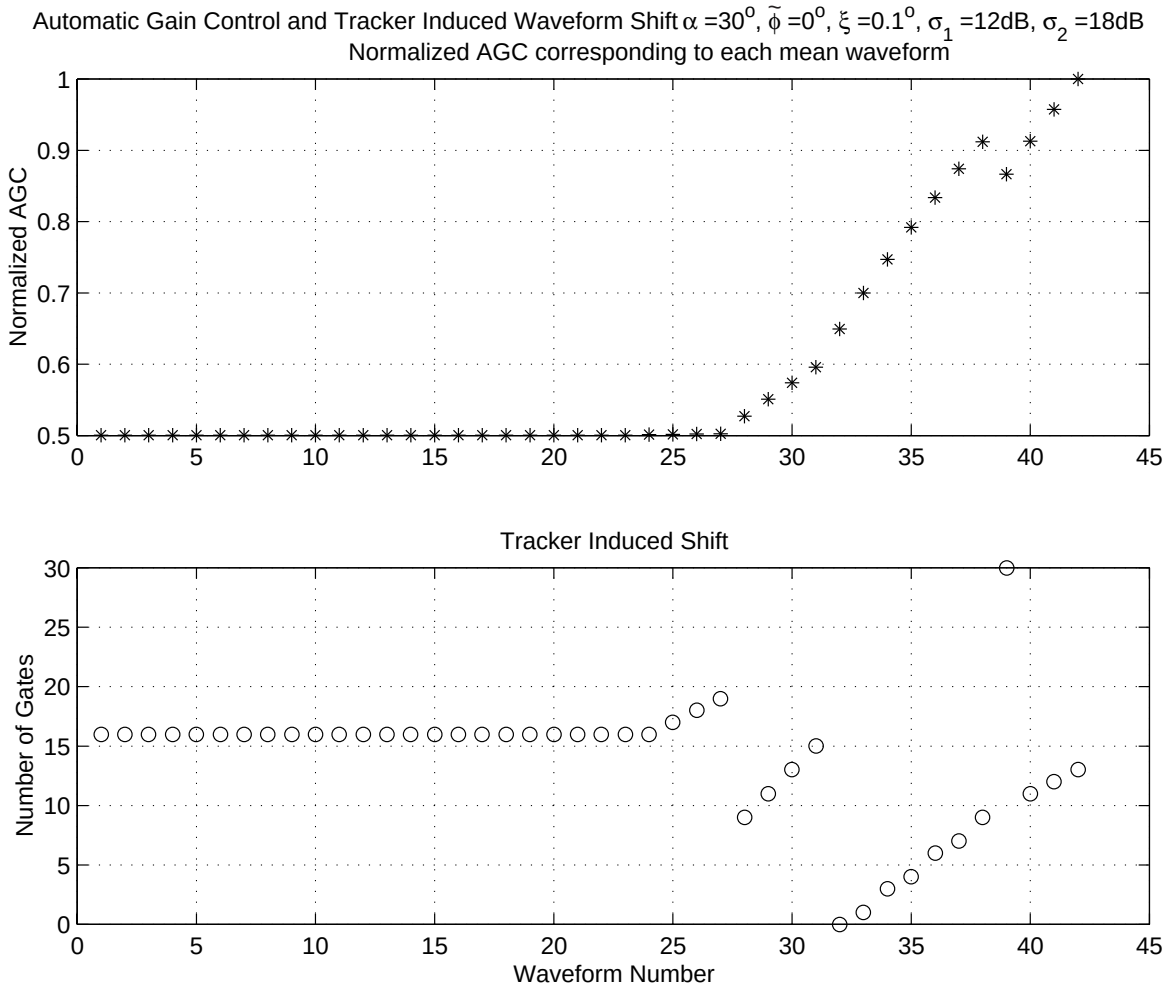

Figure 3.6. Normalized AGC and tracker induced shift for $\Delta\sigma = +6$ dB

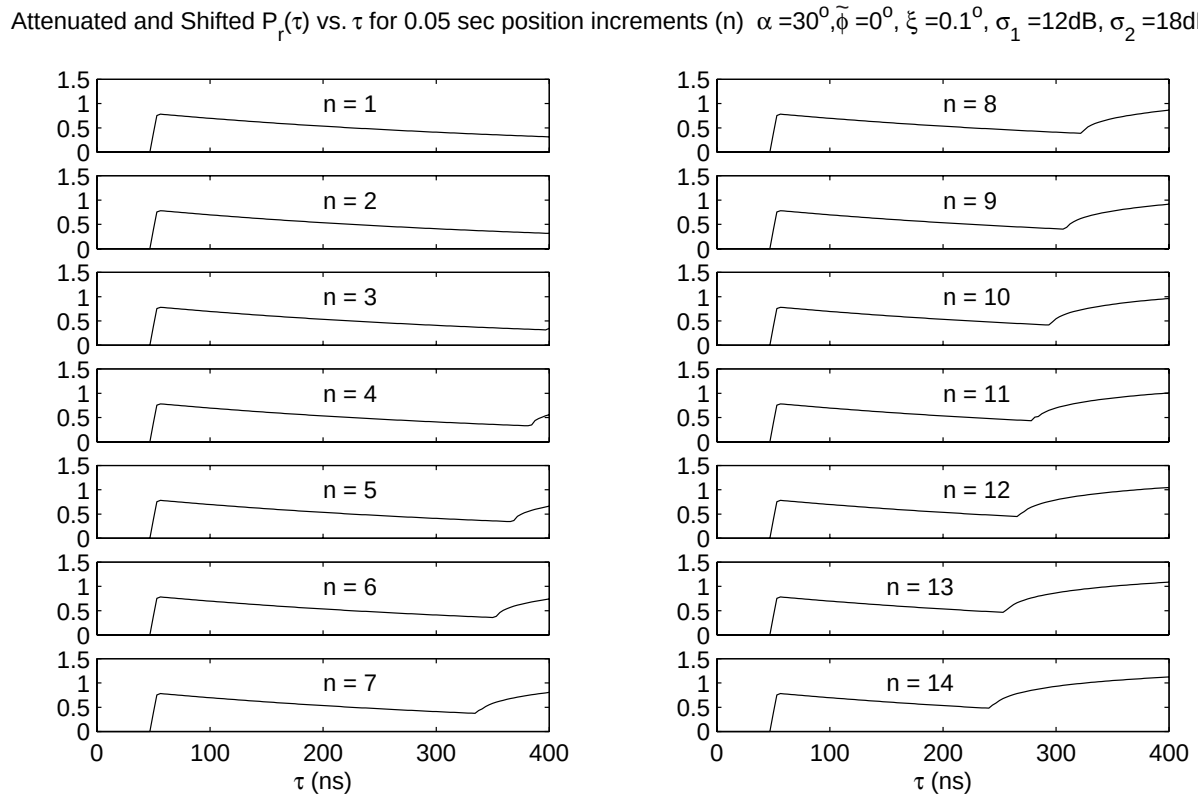

Figure 3.7. Attenuated and shifted waveforms for $\Delta\sigma = +6$ dB (1 - 14)

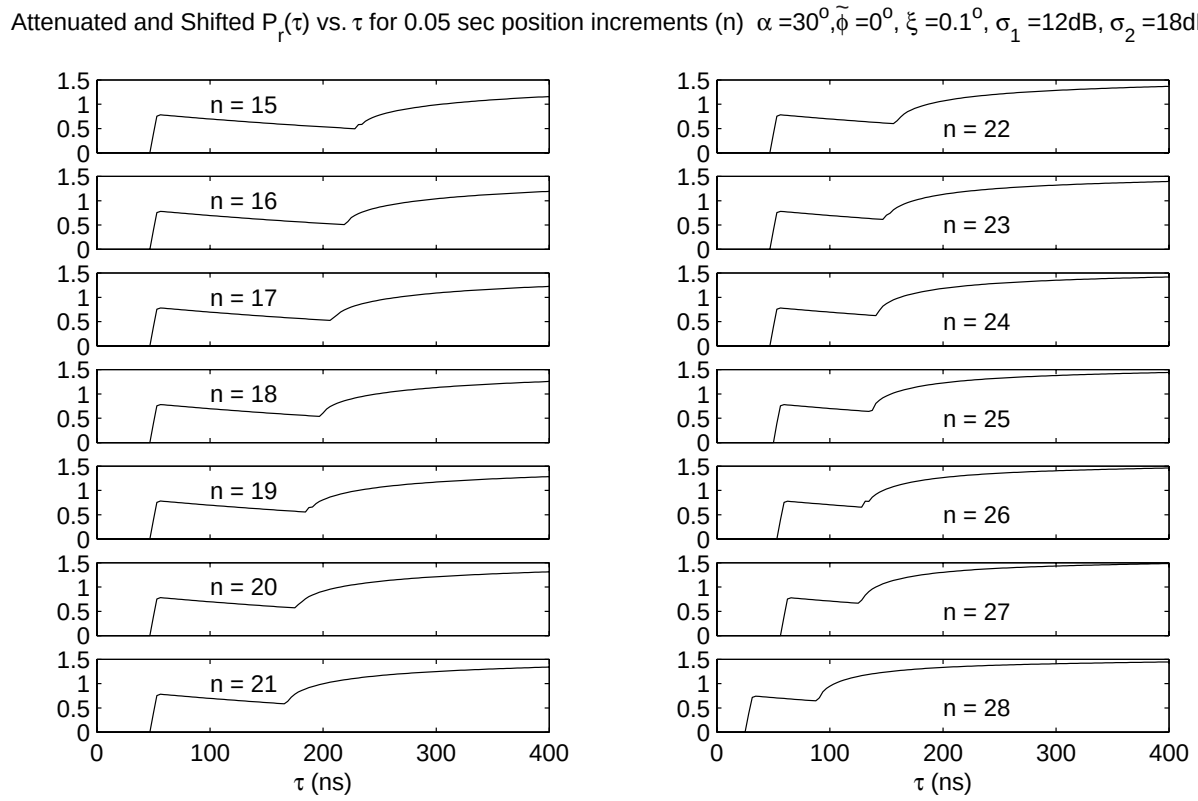

Figure 3.8. Attenuated and shifted waveforms for $\Delta\sigma = +6$ dB (15 - 28)

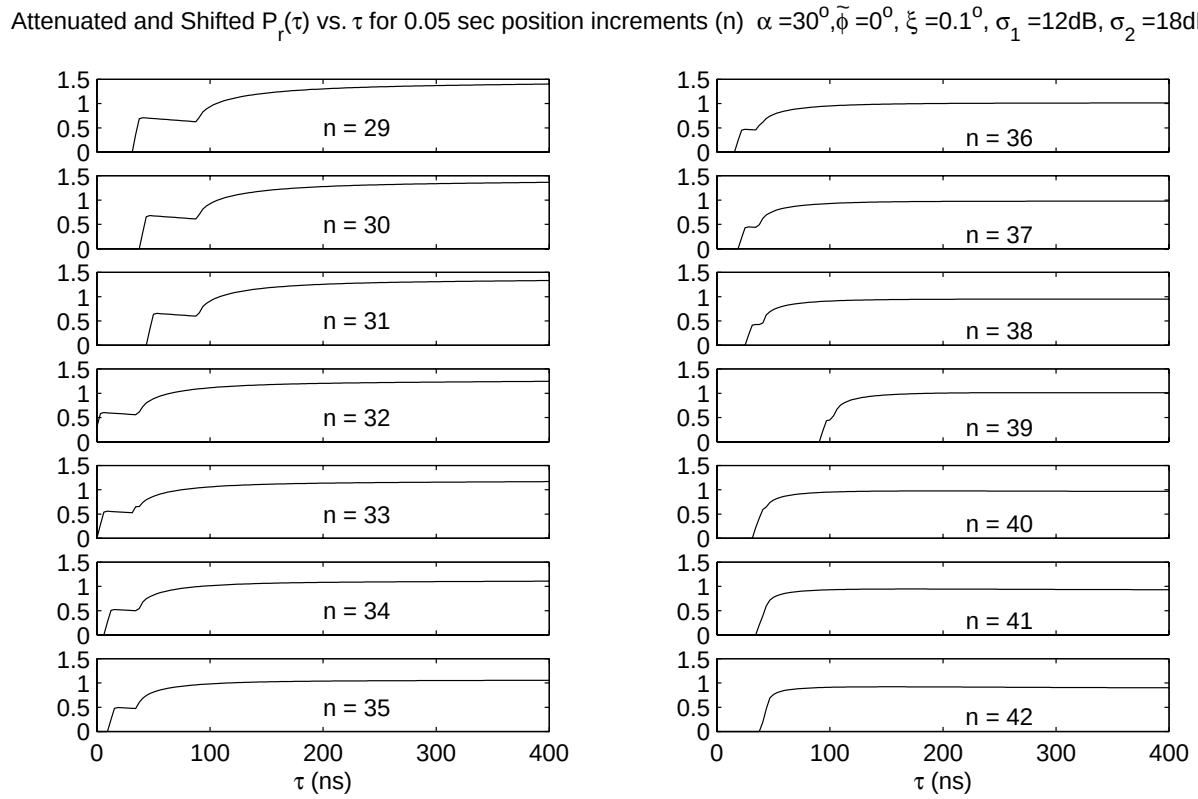

Figure 3.9. Attenuated and shifted waveforms for $\Delta\sigma = +6$d B (29 - 42)

3.4.3 Simulation for a surface with $\Delta\sigma = -10$ dB

We next simulate the average returned power waveforms from a surface with a net radar cross section discontinutity $\Delta\sigma = -10$ dB with $\sigma_1 = 20$ dB, an antenna pointing angle ξ of 0.05^o and an approach angle α of 45^o. Figure 3.10 shows the average returned power waveforms as computed from Equation 2.18 without the effects of the AGC or the tracker induced shift. We reversed the viewing angle so that the waveform changes are more obvious. As in the previous simulations we note how the contributions from the σ_2 part of the surface move through the waveforms as the nadir point angle gets closer to the discontinutity. However, in this case, since the dicontinuity is decreasing the contribution from the σ_2 part of the surface is a negative one and produces a depression in the shape of the waveform. Again, due to the larger approach angle there are more waveforms in this simulation than in the previous examples, ie., 51 versus 42 and 36 waveforms.

Figure 3.11 shows the normalized AGC and the tracker induced shift corresponding to this surface. The AGC remains unchanged for the first 24 waveforms and begins to decrease as the contributions from the σ_2 part of the surface begin to enter the AGC gate. We expected the normalized AGC corresponding to waveforms 25 to 51 to decrease smoothly. However, the normalized AGC appears to decrease in two steps. The first step (n = 26 to 30) corresponds to the tracker being confused, while the second step (n = 31 to 52) corresponds to when the tracker starts to regain stability. This tracker behavior is the same we have seen in the two previous simulations. Figures 3.12, 3.13, 3.14, and 3.15 show the individual waveforms from Figure 3.10 with the AGC effects and tracker induced shift included. We note that these waveforms have also been normalized by a factor of 10^{-9}. In these figures it is easier to see both the negative contributions from the σ_2 part of the surface and the effects of the tracker, as well as how once the depression in the waveforms caused by the σ_2 part of the surface fills the AGC gate completely the waveforms progressively return to a normal track point in time. If we look closely at the waveforms we can see how in a decreasing discontinuity the plateu region of the waveform could appear to decrease at a rate faster than usual thus confusing the altimeter when computing the pointing angle from similar waveforms.

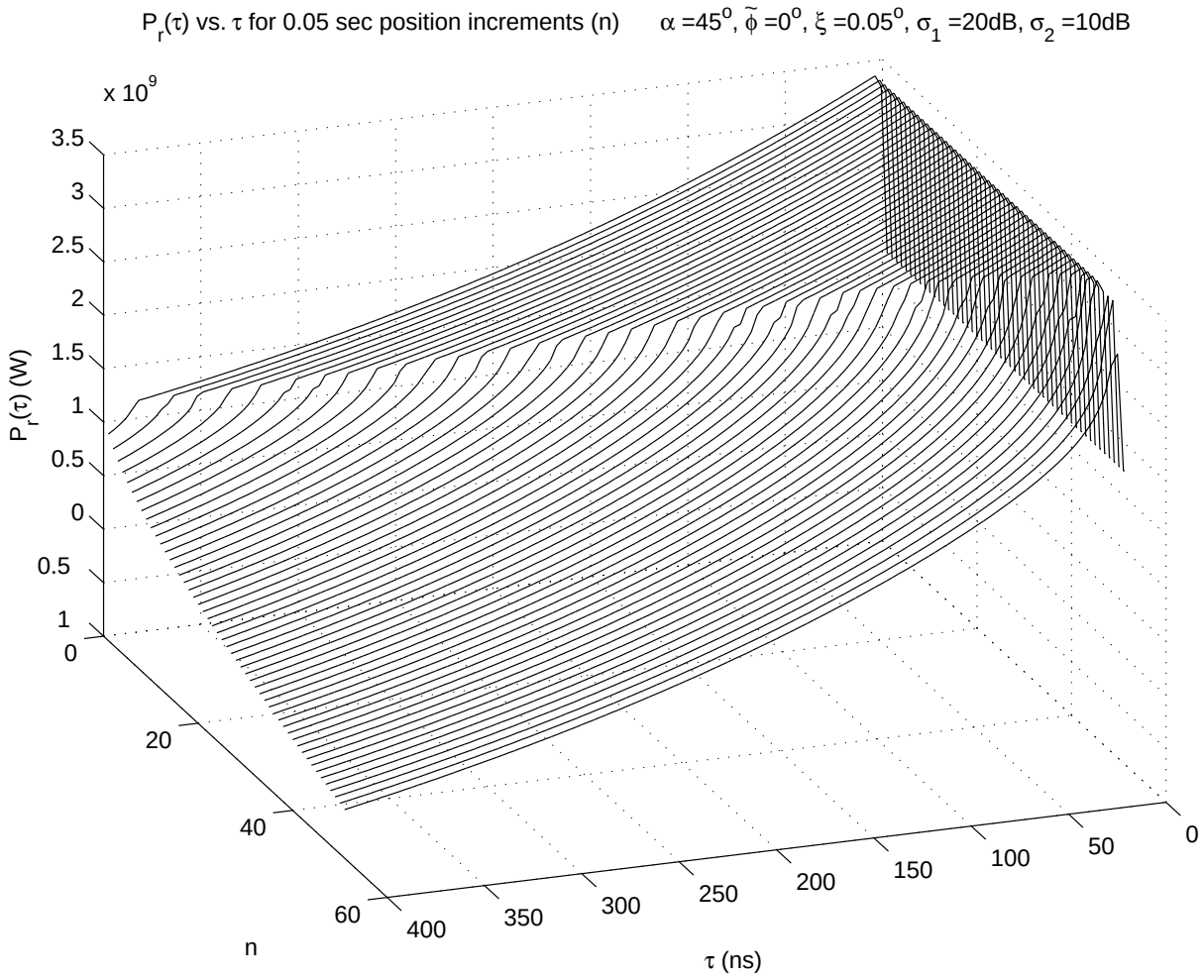

Figure 3.10. Simulated waveforms for $\Delta\sigma = -10$ dB without AGC effects or tracker induced shift

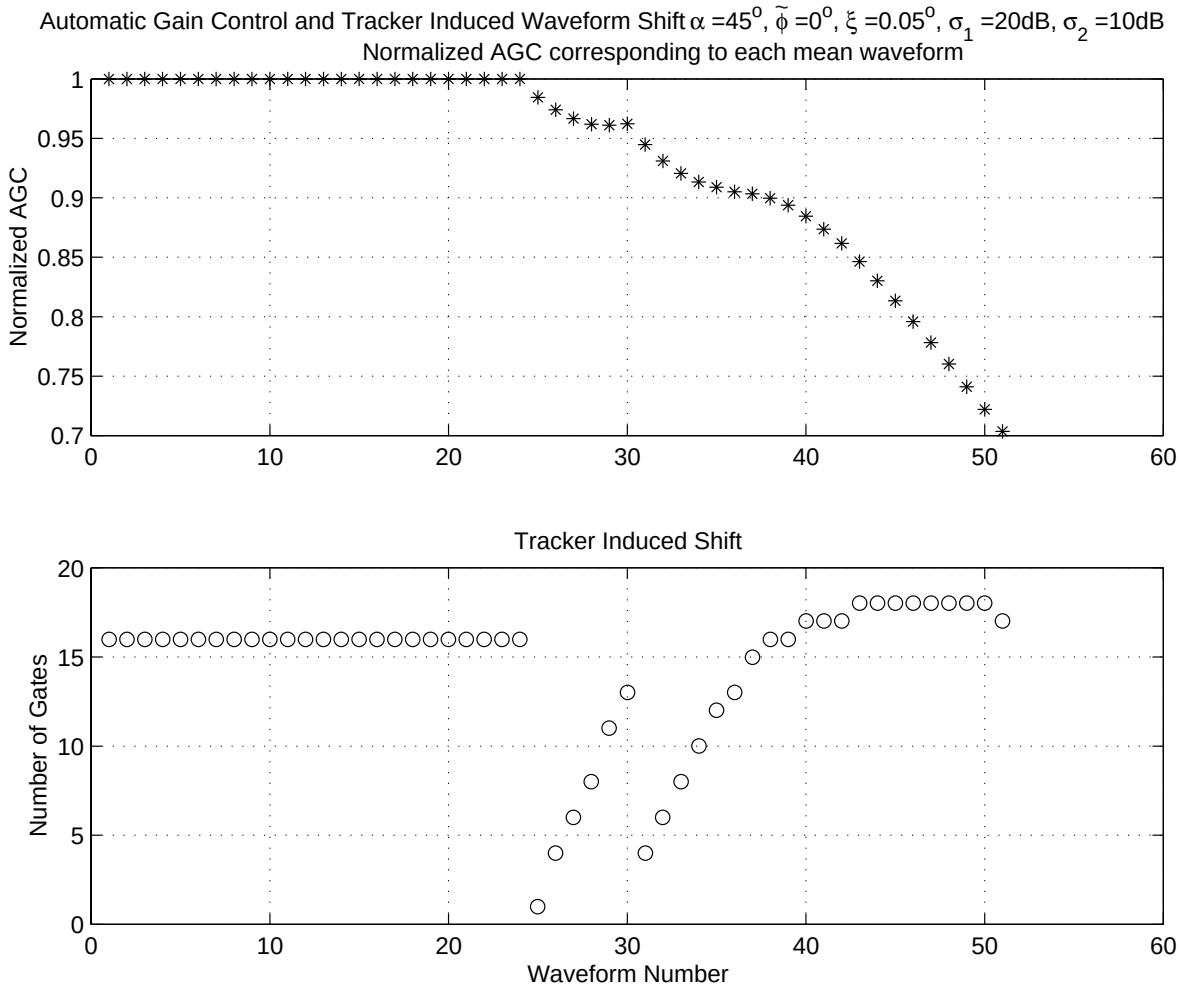

Figure 3.11. Normalized AGC and tracker induced shift for $\Delta\sigma = -10$ dB

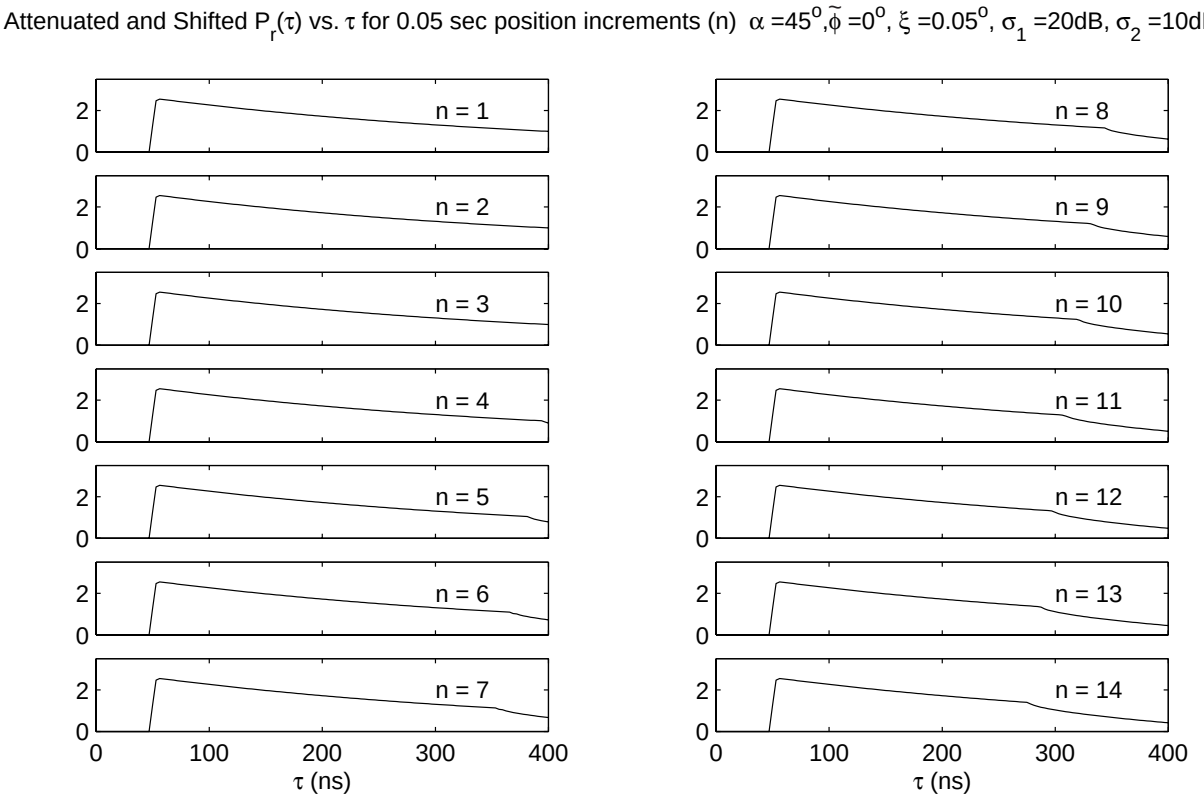

Figure 3.12. Attenuated and shifted waveforms for $\Delta\sigma = -10$ dB (1 - 14)

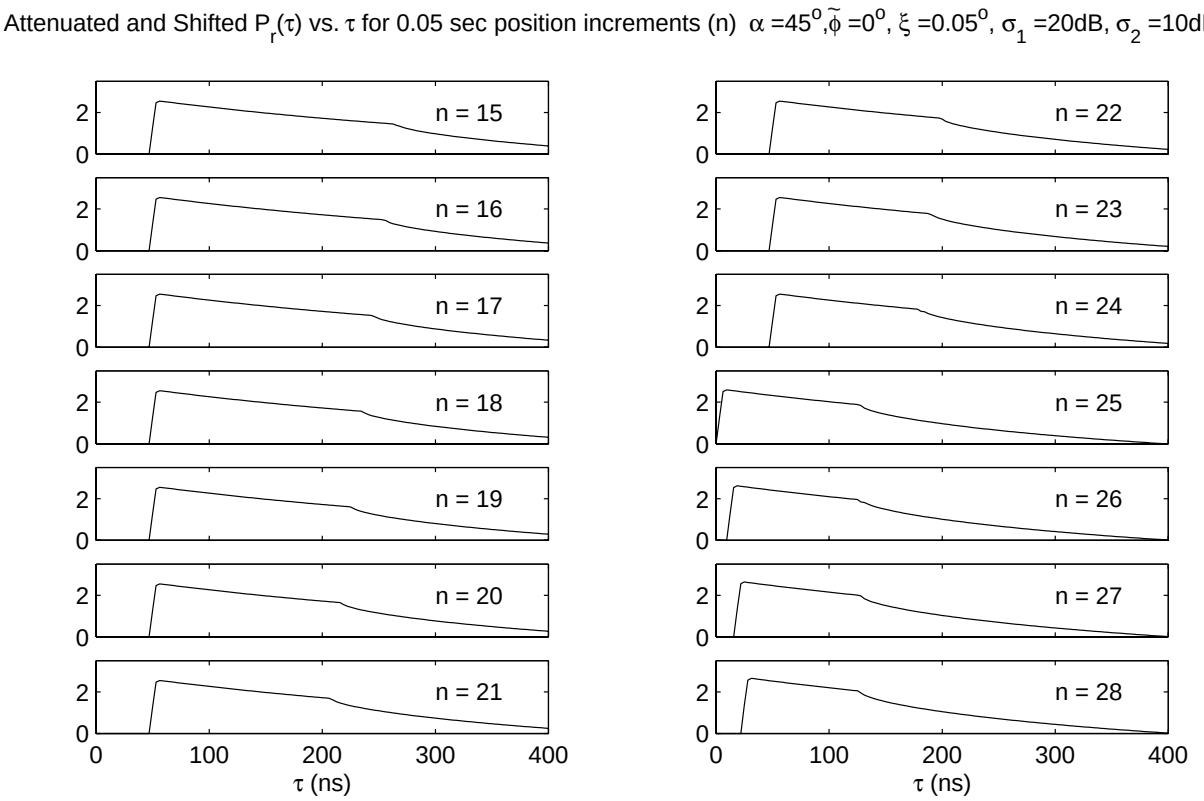

Figure 3.13. Attenuated and shifted waveforms for $\Delta\sigma = -10$ dB (15 - 28)

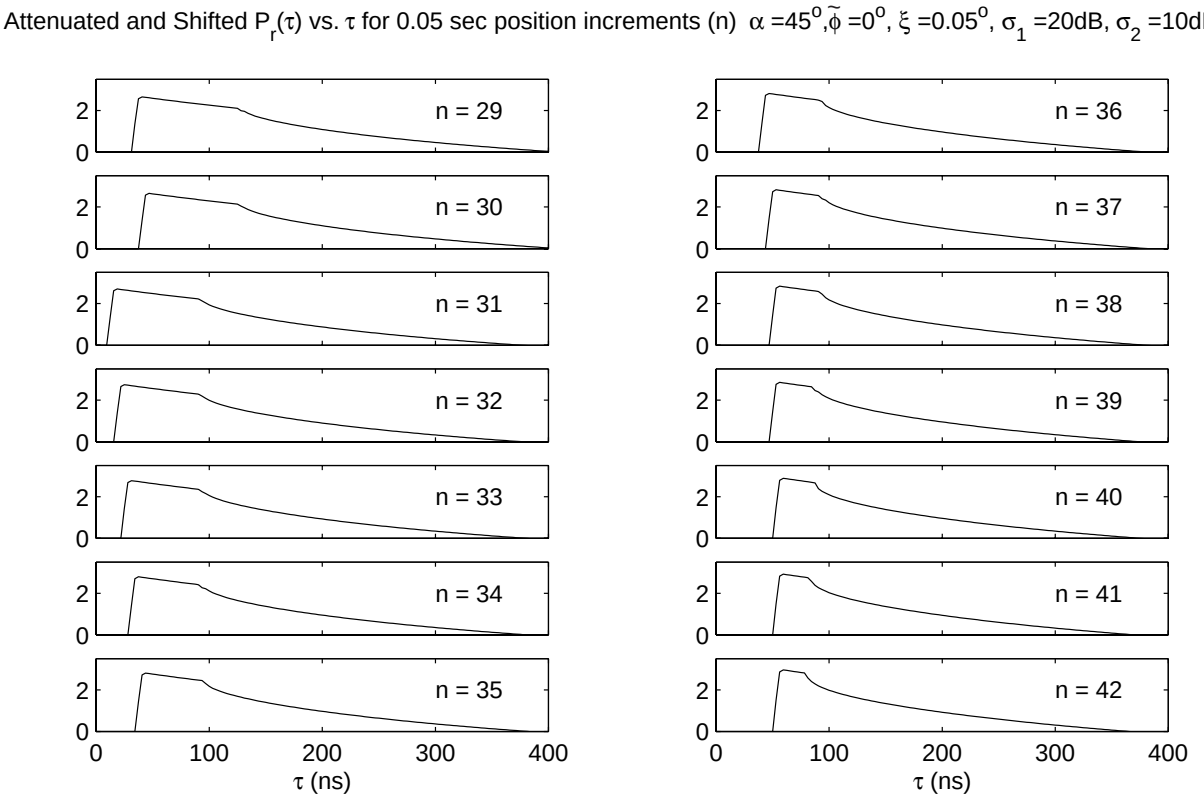

Figure 3.14. Attenuated and shifted waveforms for $\Delta\sigma = -10$ dB (29 - 42)

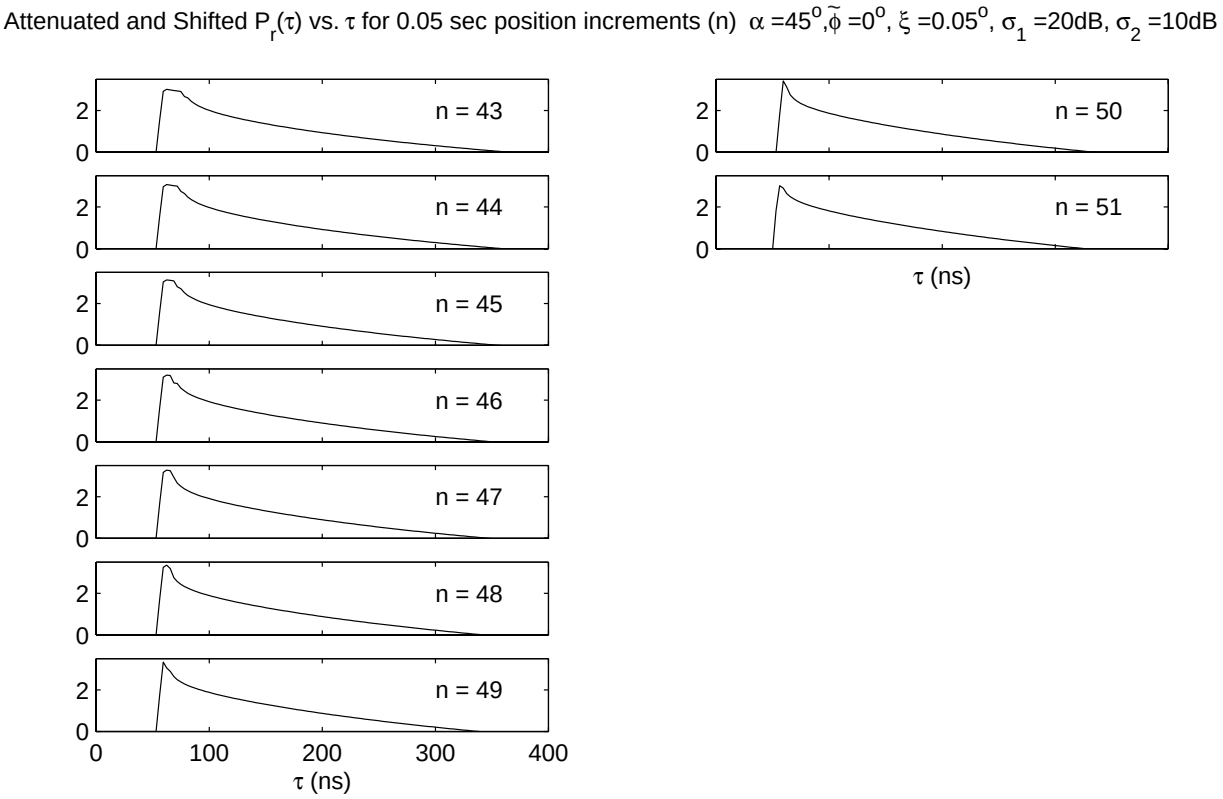

Figure 3.15. Attenuated and shifted waveforms for $\Delta\sigma = -10$ dB (43 - 51)

3.4.4 Simulation for a surface with $\Delta\sigma = -7$ dB

For the last simulation we calculate the average returned power waveforms from a surface with a net radar cross section discontinutity $\Delta\sigma = -7$ dB with $\sigma_1 = 15$ dB, an antenna pointing angle ξ of 0.05^o and an approach angle α of 0^o.

Figure 3.16 shows the average returned power waveforms as computed from Equation 2.18 without the effects of the AGC or the tracker induced shift. We have again reversed the viewing angle so that the waveform changes are more easily viewed. As in the previous simulation we can see how the negative contributions from the σ_2 part of the surface move across the waveforms as we get closer to the discontinutity. Here, since the net discontinuity is smaller, the depression in the waveforms is also smaller. As in the first simulation, the approach angle is 0^o so we will have only 36 waveforms in this set.

Figure 3.17 shows the normalized AGC and the tracker induced shift corresponding to this surface. The AGC remains unchanged for the first 17 waveforms and starts decreasing as the contributions from the σ_2 part of the surface begin to enter the AGC gate. We expected the normalized AGC corresponding to waveforms 18 to 36 to decrease smoothly. However, in this case the normalized AGC exhibits an unusual behavior. While still decreasing in two steps as in the previous simulation, at the end of the first step (n = 18 to 22) the normalized AGC increases slightly (n = 21, 22). This is again accompanied by a sudden jump in the tracker induced shift which indicates the tracker has momentarely lost track of the waveforms thus causing an abnormality in the normalized AGC. As expected, the remaining part of the normalized AGC decreases smoothly.

The tracker induced shift, as in the previous simulations, shows indications of confusion when the contributions from the σ_2 part of the surface begin to enter the AGC gate. Once these contributions fully enter the AGC gate the tracker begins to regain stability.

Figure 3.18 shows the attenuated waveforms corresponding to this surface. In this figure we can clearly see how the earlier waveforms in the set with higher AGC values are more attenuated than the latter.

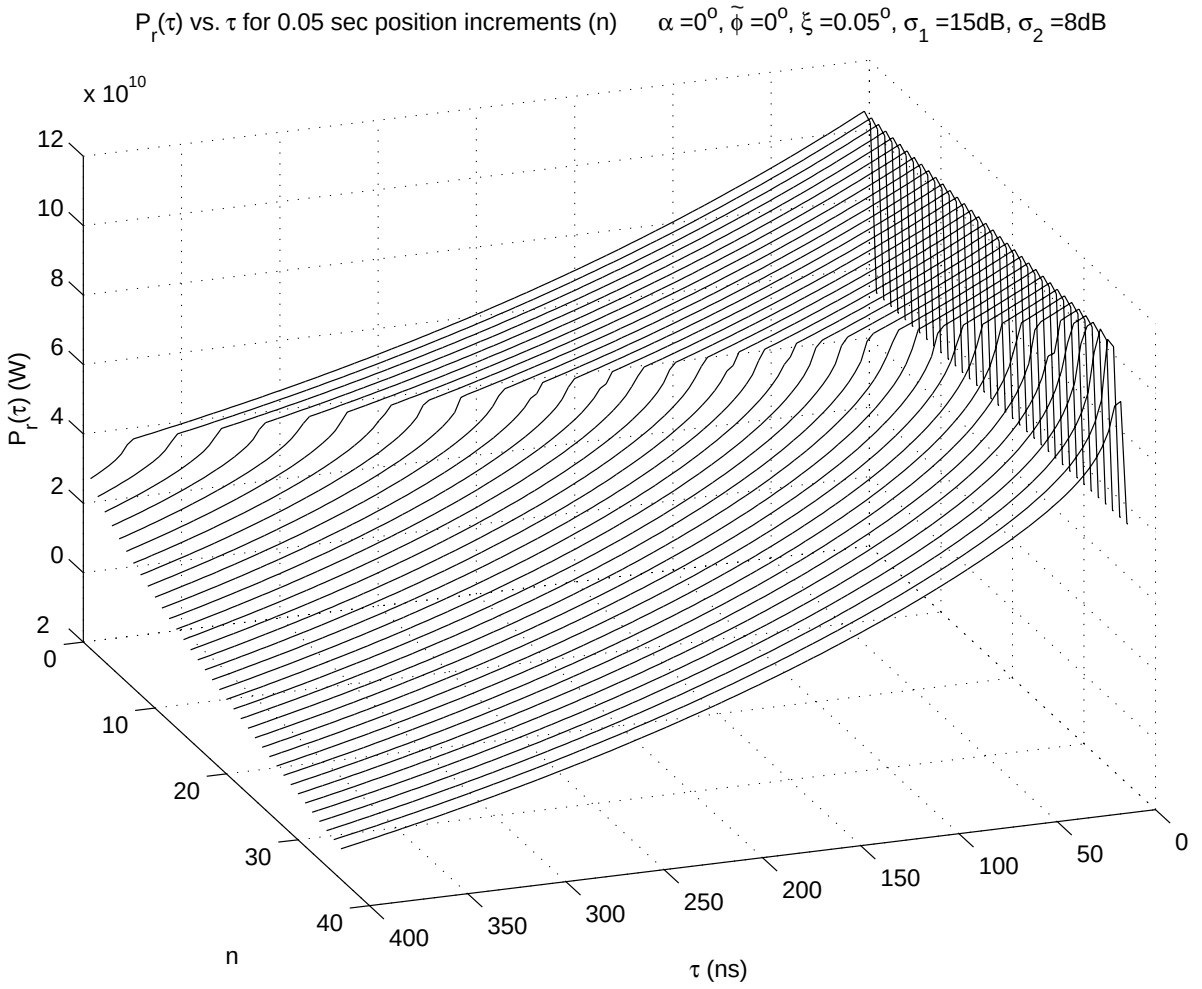

Figure 3.16. Simulated waveforms for $\Delta\sigma = -7$ dB without AGC effects or tracker induced shift

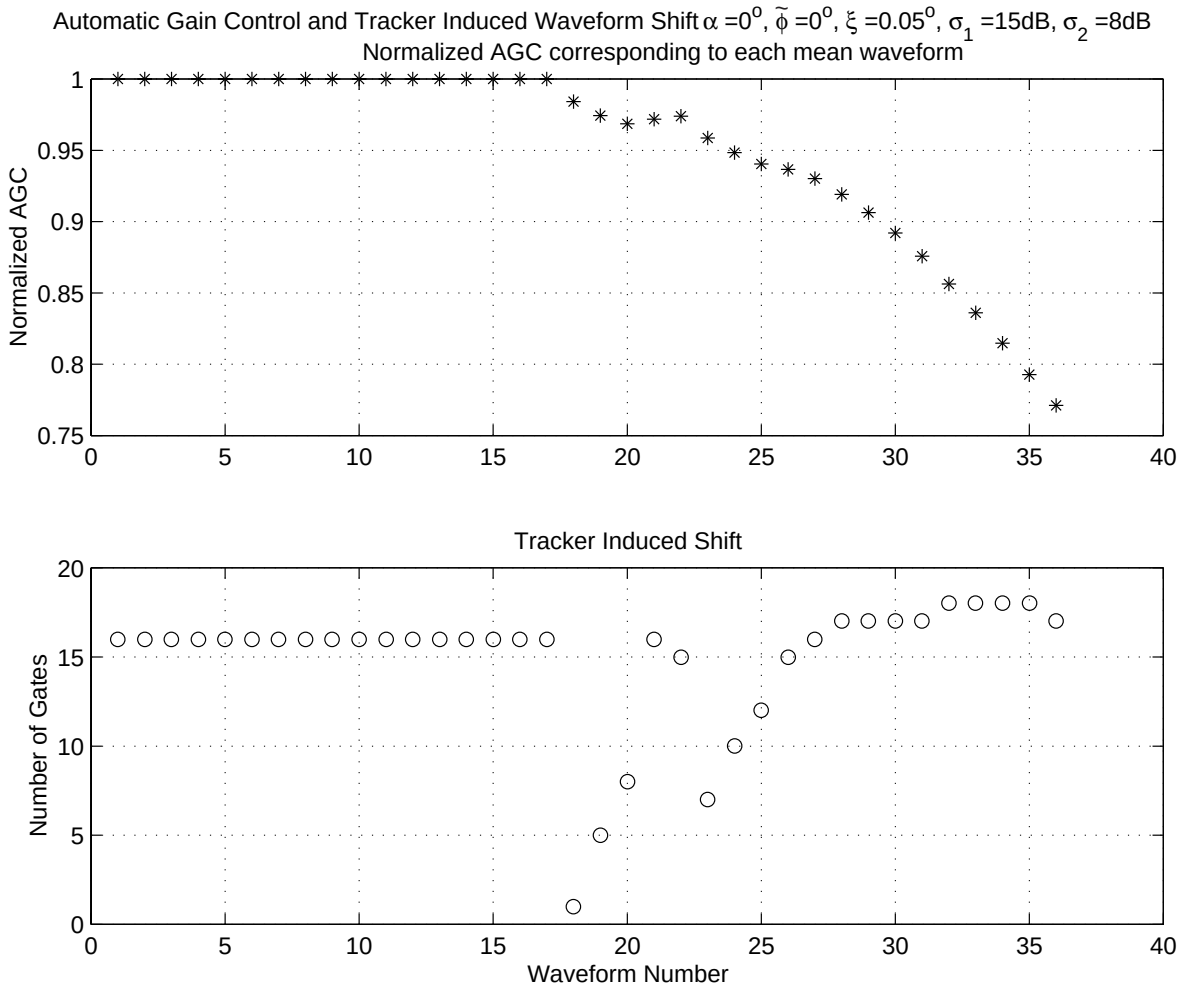

Figure 3.17. Normalized AGC and tracker induced shift for $\Delta\sigma = -7$ dB

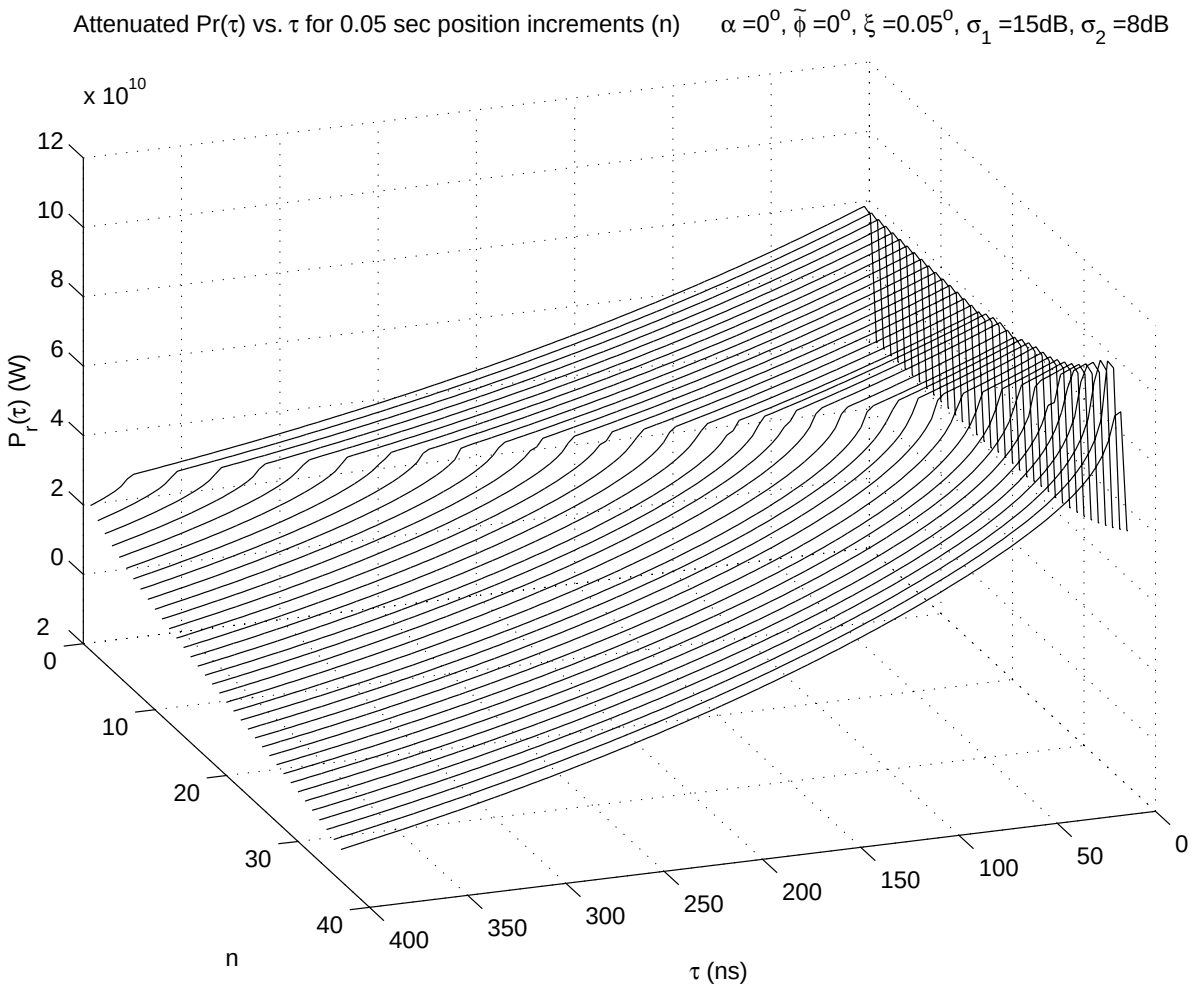

Figure 3.18. Attenuated waveforms for $\Delta\sigma = -7$ dB

3.5 Conclusion

From our simulations we can see that even though the level of the simulated waveforms increases (decreases) when approaching a surface containing an increasing (decreasing) σ^o discontinuity, the level of the entire waveform does not increase (decrease). Instead the contributions from the σ_2^o part of the surface move through the waveform as we approach the discontinuity. This waveform behavior does not match that of the waveforms seen during σ^o blooms as in Figure 1.2 where the level of the whole waveform appears to increase with no apparent change in the shape of the waveform. At the same time, the AGC corresponding to the simulated waveforms also increases and decreases fairly smoothly in contrast to the jumps in the surface's radar cross section, σ^o, observed in Figure 1.1. This comparison is valid since the AGC and the radar cross section σ^o are linearly dependent.

Considering these differences between our simulation results and the NASA data, we may conclude that a surface containing a σ^o step discontinuity cannot reasonably be the cause of the σ^o blooms.

Chapter 4

Derivation of the Average Power Returned from a Surface Containing Slick Areas

4.1 Introduction

After showing that a surface containing a σ^o discontinuity could not be the cause of the σ^o blooms, we learned that NASA (Vandemark, 1999) had found a correlation between calm oceans and σ^o blooms. That is, σ^o blooms seem to appear most often when the ocean has regions of calm water. We then decided to investigate the effects that a group of calm or slick areas with a radar cross section σ^o_F larger than the background's radar cross section σ^o_b would have on the average returned power.

A model was then derived for the average power returned from a surface containing slick or calm areas such as the waveform returns that might be expected from calmed oceans with very flat areas that are more reflective than their background. In this chapter we follow the approach used by Brown, 1977 as adapted to a surface containing slick or calm areas

with a radar cross section σ_n^o larger than the background's radar cross section σ_b^o. As in Chapter 2 we will start by deriving the flat surface impulse response corresponding to a surface containing slick or calm areas, and then we will derive the average power returned corresponding to this surface.

4.2 Derivation of $P_{FS}(t)$

The flat surface impulse response, $P_{FS}(t)$, represents the average power returned from a mean flat surface with small roughness with the same radar cross section, σ^o, as the ocean's surface when illuminated by an impulse. Given the problem geometry shown in Figure 4.1, the flat surface impulse response $P_FS(t)$ can be defined by

$$P_{FS}(t) = \frac{\lambda^2}{(4\pi)^3\, L_p} \int\limits_{IlluminatedArea} \frac{\delta(t - \frac{2r}{c})\, G^2(\theta,\omega)\, \sigma^o(\Psi,\phi)}{r^4}\, dA \tag{4.1}$$

where λ is the radar carrier wavelength, L_p is the two-way propagation loss over and above the free space loss, $G(\theta,\omega)$ is the gain of the radar antenna, and r is the range from the radar to the elemental scattering area dA on the surface (Brown, 1977).

The surface being modeled contains slick or calm areas with a radar cross section σ_n^o larger than the background's radar cross section σ_b^o. Thus to facilitate the compuation of $P_{FS}(t)$ we will divide the flat surface impulse response into two parts

$$P_{FS}(t) = P_{FS}^b(t) + P_{FS}^s(t) \tag{4.2}$$

where $P_{FS}^b(t)$ corresponds to the background flat surface impulse response and $P_{FS}^s(t)$ corresponds to the slick's flat surface impulse response. Then

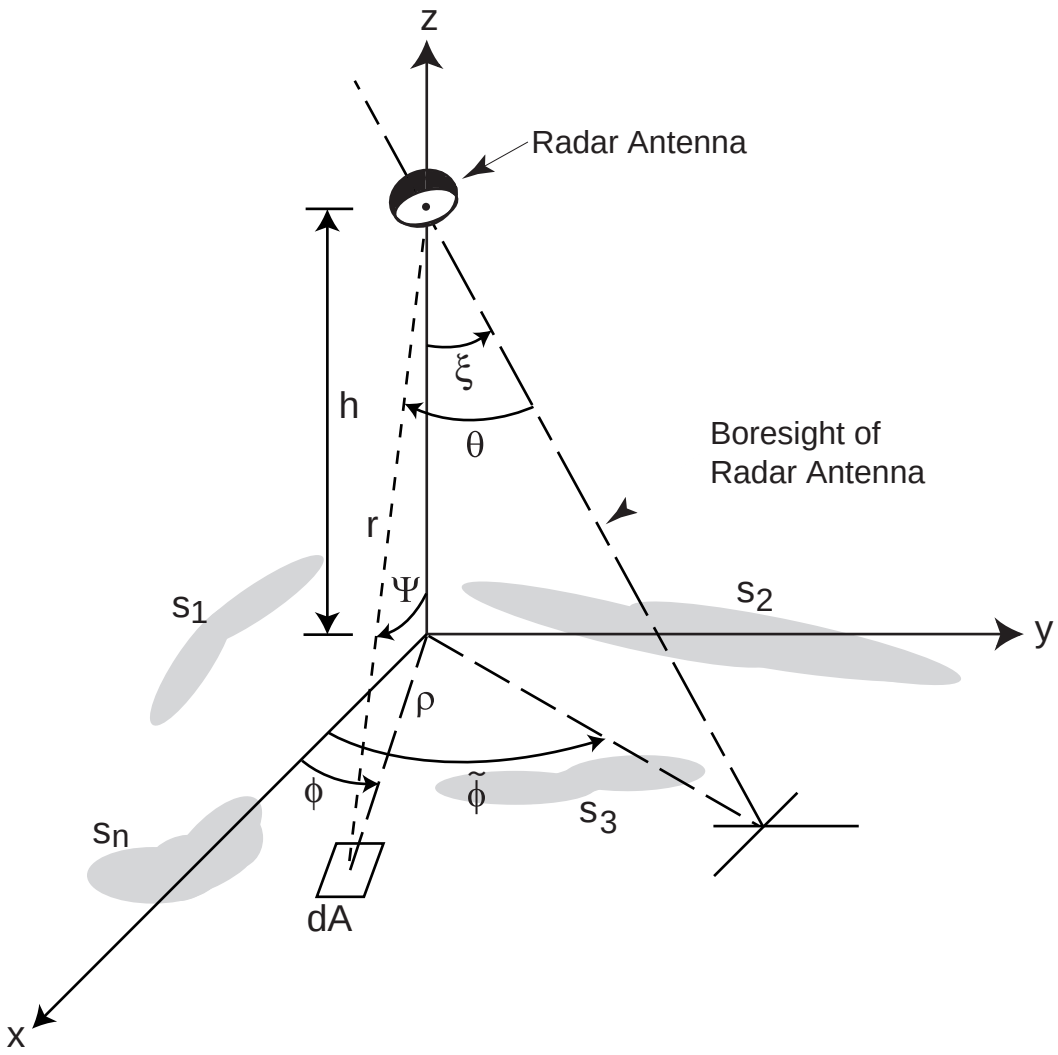

Figure 4.1. Problem geometry for surface containing slicks

$$P^b_{FS}(t) = \frac{\lambda^2}{(4\pi)^3\, L_p} \int\limits_{Plane} \frac{\delta(t - \frac{2r}{c})\, G^2(\theta,\omega)\, \sigma^o_b(\Psi,\phi)}{r^4}\, dA \tag{4.3}$$

and

$$P^s_{FS}(t) = \frac{\lambda^2}{(4\pi)^3\, L_p} \sum_{n=1}^{N} \int\limits_{S_n} \frac{\delta(t - \frac{2r}{c})\, G^2(\theta,\omega)\, [\sigma^o_n(\Psi,\phi) - \sigma^o_b(\Psi,\phi)]}{r^4}\, dA \tag{4.4}$$

where $S_n = S_n(\rho)$ is an area defined by $\rho_n \leq \rho \leq \rho_n + \delta_n$ and $\phi_n \leq \phi \leq \phi_n + \Delta_n$ where ϕ_n and Δ_n might depend on ρ_n. That is, the width of the ϕ-integration may depend on where a slick is located. $P^s_{FS}(t)$ consists of the flat surface impulse responses of N slick areas, hence the sumation term in Equation 4.4.

Integrating over S_n Equation 4.4 becomes

$$P^s_{FS}(t) = \frac{\lambda^2}{(4\pi)^3\, L_p} \sum_{n=1}^{N} \int_0^{\infty} \int_{\phi_n}^{\phi_n+\Delta_n} \frac{\delta(t - \frac{2r}{c})\, G^2(\theta,\omega)\, [\sigma^o_n(\Psi,\phi) - \sigma^o_b(\Psi,\phi)]}{r^4}\, \rho d\phi d\rho \tag{4.5}$$

We will assume the antenna gain to be Gaussian such that

$$G(\theta) \approx G_o\, e^{-(2/\gamma)\sin^2(\theta)} \tag{4.6}$$

where γ is a parameter dependent on the antenna beamwidth.
The solution to P^b_{FS} when $\frac{c\tau}{h} \ll 1$ and $\sqrt{\frac{c\tau}{h}}\, tan\xi \ll 1$, which is true for our problem, is well known to be

$$P^b_{FS}(\tau) = \frac{c\, G_o^2\, \lambda^2\, \sigma^o_b}{4(4\pi)^2\, L_p\, h^3} \exp\{-\frac{4}{\gamma}[\sin^2\xi + \frac{c}{h}\tau\cos 2\xi]\} I_o\left(\frac{4}{\gamma}\sqrt{\frac{c\,\tau}{h}}\sin 2\xi\right) \tag{4.7}$$

where $\tau = t - 2h/c$ represents the two-way incremental ranging time (Brown, 1977). For the slick or calm area return, we obtain

$$P^s_{FS}(t) = \frac{G_o^2 \lambda^2}{(4\pi)^3 \, L_p} \sum_{n=1}^{N} \int_0^{\infty} \frac{\delta(t - \frac{2h}{c}\sqrt{1+\varepsilon^2})}{[1+\varepsilon^2]^2} \, [\sigma^o_n(\Psi,\phi) - \sigma^o_b(\Psi,\phi)] \exp\left\{ -\frac{4}{\gamma}\left[1 - \frac{\cos^2\xi}{1+\varepsilon^2}\right] + b \right\}$$
$$\cdot \int_{\phi_n}^{\phi_n+\Delta_n} \exp\left\{ a\,\cos(\tilde{\phi}-\phi) - b\,\sin^2(\tilde{\phi}-\phi) \right\} \, d\phi \, \rho \, d\rho \tag{4.8}$$

where

$$\begin{aligned} \varepsilon &= \frac{\rho}{h} \\ a &= \frac{4\,\varepsilon}{\gamma} \, \frac{\sin(2\xi)}{1+\varepsilon^2} \\ b &= \frac{4\,\varepsilon^2}{\gamma} \, \frac{\sin^2(\xi)}{1+\varepsilon^2} \end{aligned} \tag{4.9}$$

At this point we will assume that both σ^o_n and σ^o_b are constant inside a slick or calm area since it is assumed to be very small. We can simplify Equation 4.8 with a change of variables such as $\eta = \phi - \phi_n$

$$P^s_{FS}(t) = \frac{G_o^2 \lambda^2}{(4\pi)^3 \, L_p} \sum_{n=1}^{N} \int_0^{\infty} \frac{\delta(t - \frac{2h}{c}\sqrt{1+\varepsilon^2})}{[1+\varepsilon^2]^2} \, [\sigma^o_n - \sigma^o_b] \exp\left\{ -\frac{4}{\gamma}\left[1 - \frac{\cos^2\xi}{1+\varepsilon^2}\right] + b \right\}$$
$$\cdot \int_0^{\Delta_n} \exp\left\{ a\,\cos(\tilde{\phi}+\phi_n-\eta) - b\,\sin^2(\tilde{\phi}+\phi_n-\eta) \right\} \, d\eta \, \rho \, d\rho \tag{4.10}$$

If we assume that ϕ_n is a uniformly distributed random variable between (0, 2π) such that

$$p(\phi_n) = \frac{1}{2\,\pi} \qquad 0 \leq \phi_n \leq 2\pi; \quad n = 1, 2, 3, ...N \tag{4.11}$$

we can average $P^s_{FS}(t)$ over all possible ϕ_n

$$\langle P^s_{FS}(t)\rangle_{\phi_n} = \frac{G_o^2 \lambda^2}{(4\pi)^3\, L_p} \sum_{n=1}^{N} \int_0^{\infty} \frac{\delta(t - \frac{2h}{c}\sqrt{1+\varepsilon^2})}{[1+\varepsilon^2]^2} \left[\sigma_n^o - \sigma_b^o\right] \exp\left\{-\frac{4}{\gamma}\left[1 - \frac{\cos^2\xi}{1+\varepsilon^2}\right] + b\right\}$$
$$\cdot \frac{1}{2\pi} \int_0^{\Delta_n} \int_0^{2\pi} \exp\left\{a\,\cos(\tilde{\phi} + \phi_n - \eta) - b\,\sin^2(\tilde{\phi} + \phi_n - \eta)\right\}\, d\phi_n d\eta\, \rho\, d\rho \tag{4.12}$$

From this point on, the computation of the integrals in Equation 4.12 is very similar to those solved by Brown, 1977. Because of the 2π range of the integration and the form of the integrand we can ignore the $(\tilde{\phi} - \eta)$ shift in the angle of Equation 4.12. Substituting

$$e^{-b\sin^2(\phi)} = \sum_{n=0}^{\infty} \frac{(-1)^n b^n \sin^{2n}\phi}{n!} \tag{4.13}$$

in Equation 4.12 and intergrating term by term yields

$$\begin{aligned}\left\langle P_{FS}^{s}(t)\right\rangle_{\phi_n} &= \frac{G_o^2\lambda^2}{(4\pi)^3\,L_p}\frac{1}{2\pi}\sum_{n=1}^{N}\sum_{l=0}^{\infty}\frac{(-1)^l\Gamma(l+1/2)}{\Gamma(l+1)}[\sigma_n^o-\sigma_b^o]\\ &\cdot\int_0^{\infty}\left(\frac{2b}{a}\right)^l I_l(a)\exp\left\{-\frac{4}{\gamma}\left[1-\frac{\cos^2\xi}{1+\varepsilon^2}\right]+b\right\}\frac{\delta(t-\frac{2h}{c}\sqrt{1+\varepsilon^2})}{[1+\varepsilon^2]^2}\rho\,d\rho\\ &\cdot\int_0^{\Delta_n}d\eta\\ &= \frac{G_o^2\lambda^2}{(4\pi)^3\,L_p}\sum_{n=1}^{N}\frac{\Delta_n}{2\pi}\sum_{l=0}^{\infty}\frac{(-1)^l\Gamma(l+1/2)}{\Gamma(l+1)}[\sigma_n^o-\sigma_b^o]\\ &\cdot\int_0^{\infty}\left(\frac{2b}{a}\right)^l I_l(a)\exp\left\{-\frac{4}{\gamma}\left[1-\frac{\cos^2\xi}{1+\varepsilon^2}\right]+b\right\}\frac{\delta(t-\frac{2h}{c}\sqrt{1+\varepsilon^2})}{[1+\varepsilon^2]^2}\rho\,d\rho \qquad (4.14)\end{aligned}$$

where $I_n(.)$ corresponds to the Bessel function of the second kind and the convergence of the series is sufficient to interchange the summation and integration (Brown, 1977). This integral only has a nonzero value when ϕ is such that a slick is encountered.

After a change of variables such as $x=\frac{2h}{c}\sqrt{1+\varepsilon^2}$, and evaluating the integral we obtain

$$\begin{aligned}\left\langle P_{FS}^{s}(t)\right\rangle_{\phi_n} &= \frac{G_o^2\lambda^2 c}{4(4\pi)^2\,L_p\,h^3}\sum_{n=1}^{N}\frac{\Delta_n}{2\pi}\left(\frac{2h}{c\,t}\right)^3(\sigma_n^o-\sigma_b^o)\exp\left\{-\frac{4}{\gamma}\left[\cos^2\xi-\frac{\cos 2\xi}{(\frac{c\,t}{2h})^2}\right]\right\}\\ &\cdot\sum_{l=0}^{\infty}\frac{(-1)^l\Gamma(l+1/2)}{\sqrt{\pi}\Gamma(l+1)}\left[\sqrt{(c\,t/2h)^2-1}\tan\xi\right]^l I_l\left(\frac{4}{\gamma}\frac{\sqrt{(\frac{c\,t}{2h})^2-1}}{(\frac{c\,t}{2h})^2}\sin 2\xi\right) \qquad (4.15)\end{aligned}$$

provided that t is in the n^{th} slick area.

We can further simplify Equation 4.15 by converting to the two-way incremental ranging time as before through $\tau=t-2h/c$. For our problem $\frac{c\tau}{h}\ll 1$, so we have

$$\langle P^s_{FS}(\tau)\rangle_{\phi_n} = \frac{G_o^2\lambda^2 c}{4(4\pi)^2\, L_p\, h^3}\sum_{n=1}^{N}\frac{\Delta_n}{2\pi}(\sigma_n^o - \sigma_b^o)\exp\left\{-\frac{4}{\gamma}\left[\sin^2\xi + \frac{c\tau}{h}\cos 2\xi\right]\right\}$$
$$\cdot\sum_{l=0}^{\infty}\frac{(-1)^l\Gamma(l+1/2)}{\sqrt{\pi}\Gamma(l+1)}\left[\sqrt{\frac{c\tau}{h}}\tan\xi\right]^l I_l\left(\frac{4}{\gamma}\sqrt{\frac{c\tau}{h}}\sin 2\xi\right) \tag{4.16}$$

for $\tau \geq 0$.

For our altimetry problem, the infinite series in Equation 4.15 may be considerably simplified. That is

$$\sum_{l=0}^{\infty}(.) = I_o(Y)\left\{1 + \sum_{l=1}^{\infty}\frac{(-1)^l\Gamma(l+1/2)}{\sqrt{\pi}\Gamma(l+1)}\frac{I_n(Y)}{I_o(Y)}\left[\frac{\gamma Y}{8\cos^2\xi}\right]^l\right\} \tag{4.17}$$

where

$$Y = \frac{4}{\gamma}\sqrt{\frac{c\tau}{h}}\sin 2\xi \tag{4.18}$$

When

$$\sqrt{\frac{c\tau}{h}}\tan\xi \ll 1 \tag{4.19}$$

which is true for our altimeter, the series above will be highly convergent due to the rapidly decreasing $[(\gamma Y)/(8\cos^2\xi)]^l$ term. Thus the infinite series in Equation 4.15 may be truncated at n = 0 with no effective loss of accuracy (Brown, 1977). Then

$$\langle P^s_{FS}(\tau)\rangle_{\phi_n} = \frac{G_o^2\lambda^2 c}{4(4\pi)^2\, L_p\, h^3}\sum_{n=1}^{N}\frac{\Delta_n}{2\pi}(\sigma_n^o - \sigma_b^o)\exp\left\{-\frac{4}{\gamma}\left[\sin^2\xi + \frac{c\tau}{h}\cos 2\xi\right]\right\} I_o\left(\frac{4}{\gamma}\sqrt{\frac{c\tau}{h}}\sin 2\xi\right) \tag{4.20}$$

for $\tau \geq 0$.

The magnitude of $\langle P^s_{FS}(\tau)\rangle_{\phi_n}$ will thus depend on the number of slick areas N, their radar

cross section σ_n^o, and their angular size Δ_n.

We can now combine $\langle P_{FS}^s(\tau)\rangle_{\phi_n}$ and $P_{FS}^b(t)$ to form $\langle P_{FS}(\tau)\rangle_{\phi_n}$

$$\langle P_{FS}(\tau)\rangle_{\phi_n} = \frac{G_o^2\lambda^2 c\,\sigma_b^o}{4(4\pi)^2\,L_p\,h^3}\exp\left\{-\frac{4}{\gamma}\left[\sin^2\xi + \frac{c\tau}{h}\cos 2\xi\right]\right\} I_o\left(\frac{4}{\gamma}\sqrt{\frac{c\tau}{h}}\sin 2\xi\right) \cdot\left\{1+\sum_{n=1}^{N}\frac{\Delta_n}{2\pi}\left(\frac{\sigma_n^o}{\sigma_b^o}-1\right)\right\} \tag{4.21}$$

4.3 Derivation of the Average Returned Power $P_r(\tau)$

$P_r(\tau)$ can now be derived in very much the same manner as in Chapter 2. If we assume the system point target response, $p_\tau(t)$, is well represented by a Gaussian function, and the ocean's surface height probability density function can also be represented by a Gaussian function, then the average returned power defined by a convolution in Equation 2.1 can be simplified to

$$P_r(\tau) \approx \eta P_T P_{FS}(\tau)\sqrt{2.\pi}\sigma_p\left[1+erf\left(\frac{\tau}{\sqrt{2}\sigma_c}\right)\right]/2 \qquad \text{for } \tau \geq 0 \tag{4.22}$$

where η is the pulse compression ratio, P_T is the peak transmitted power, σ_p is related to the point target 3dB width (T) by

$$\sigma_p = 0.425T \tag{4.23}$$

and

$$\sigma_c = \sqrt{\sigma_p^2 + \left(\frac{2\sigma_s}{c}\right)^2} \tag{4.24}$$

where σ_s is the rms sea height (Brown, 1977). In order to account for the curvature of the earth we will replace the altimeter's height h by h/0.826 in Equation 2.17 (Hayne, 1998).

Chapter 5

Data Fitting to the Average Power Returned from a Surface Containing Slick Areas

5.1 Introduction

Having derived a model for the average power returned from a suface containing slick areas with a radar cross section, σ_n^o, larger than the background radar cross section, σ_b^o, we next must validate the model. Our model depends on the number and size of the slick areas as well as their radar cross section. Because there are infinitely many combinations of these parameters that could contribute to a bloom, it is fruitless to carry out simulations similar to those completed in Chapter 3. Instead, we fit data received from the NASA Goddard Space Flight Center corresponding to Cycle 137, Pass 058, described in the problem statement, to our model. Our purpose in fitting this data to our model is not to obtain ranges for the parameters but to get a sense of the level of the contributions from the slick areas during a bloom are.

In this chapter, we describe the process used to prepare the Sensor Data Record (SDR) data provided by NASA and how we fit the data to the model. Data corresponding to the four regions A, B, C, and D described in the problem statement (Figure 1.1) will be used in a model fit. We will also investigate the relation between out of range off-nadir angles and the blooms.

5.2 Data Processing and Region Identification

We obtained both the Sensor Data Record (SDR) and the Geophysical Data Record (GDR) for regions A, B, C, and D of Cycle 137, Pass 058 from the NASA Goddard Space Fight Center. SDR files contain the waveform data computed and transmitted by the satellite. GDR files contain the data computed on the ground from the SDR; examples of GDR data include mean radar cross section of the ocean's surface σ^o, mean off-nadir angle, and mean SWH. Both Ku- and C-band waveform samples were provided at their full data rates of 10 and 5 Hz respectively.

Before fitting the waveform data to our model, three processes must be performed on the data; these processes are (1) correcting the data, (2) removing the AGC effects, and (3) expanding the time axis. Waveform data must first be corrected as described by Hayne et al., 1994. That is, noise spikes and leakage between samples known to be caused by the radar altimeter can be removed using the following algorithm

$$W_{c,i} = G_i \, (T_{s,i} + A_i) \tag{5.1}$$

where $T_{s,i}$ corresponds to each waveform telemetry sample, A_i corresponds to an additive factor, G_i corresponds to a multiplicative factor, and $W_{c,i}$ corresponds to the corrected telemetry sample i (1 to 64) (Hayne et al., 1994). The values for these factors are given in Table B.1. Even though the satellite uses 128 samplers to sample received waveforms, only

64 samples of data per waveform are transmitted. The contraction of 128 to 64 samples is not done uniformly, as shown in Figure 3.1. Waveform samples in the rising edge retain a 1:1 ratio in the telemetry samples whereas the remaining waveform samples have a 4:1 or 2:1 ratio with respect to the waveform samples since they do not usually contain as much information. Once the waveforms have been corrected, the AGC effects are removed using an AGC reference of 30.5 dB for Ku-band and 33.5 dB for C-band data as suggested by Dr. George Hayne (Hayne, 1999). The AGC values are provided in the SDR-SCI files at a 20 Hz rate, and thus the AGC values must be averaged accordingly. Finally, we convert back to a time axis for each waveform. When the waveforms were transformed from waveform samples to telemetry samples, telemetry samples were no longer spaced by 3.125 ns. Only the samples with a 1:1 ratio were spaced by 3.125 ns. The remaining samples are spaced by 6.25 ns or 12.5 ns.

5.3 Data Fitting

Once the waveform data have been corrected, the AGC effects removed, and the τ axis expanded, we can fit the waveform data to our model. Our goal is to obtain an estimate of the summation term in Equation 4.21. We hypothesize that the SDR waveform data corresponds to the average returned power waveforms from a surface containing slick areas, $P_r(\tau)$ (Equation 4.22).
Since

$$P_{FS}(\tau) = P^b_{FS}(\tau) + \langle P^s_{FS}(\tau) \rangle_{\phi_n} , \tag{5.2}$$

we can express the average power returned $P_r(\tau)$ as

$$P_r(\tau) = P^b_r(\tau) + \langle P^s_r(\tau) \rangle_{\phi_n} . \tag{5.3}$$

where $P^b_r(\tau)$ is the average returned power from the background and $\langle P^s_r(\tau) \rangle_{\phi_n}$ corresponds

to the average returned power from the slick areas. $\langle P_r^s(\tau)\rangle_{\phi_n}$ is defined by the substitution of Equation 4.20 into Equation 4.22. Then

$$\langle P_r^s(\tau)\rangle_{\phi_n} \approx \eta P_T \langle P_{FS}^s(\tau)\rangle_{\phi_n} \sqrt{2.\pi}\sigma_p \left[1 + erf\left(\frac{\tau}{\sqrt{2}\sigma_c}\right)\right]/2 \tag{5.4}$$

We assume that the properties of the background surface do not change for a given region, and that the average of the first 100 waveforms of a region is a representation of $P_r^b(\tau)$. Thus, by subtracting this average from the corrected and aligned waveform data we obtain an estimate for $\langle P_r^s(\tau)\rangle_{\phi_n}$. Furthermore, we assume the tracker has maintained a constant shift of 22 telemetry samples on the waveforms. That is, $\tau = 0$ corresponds to sample 22. We then compute an estimate of $\langle P_{FS}^s(\tau)\rangle_{\phi_n}$ for each waveform;

$$\langle P_{FS}^s(\tau)\rangle_{\phi_n} = \langle P_r^s(\tau)\rangle_{\phi_n}\ F\ /\eta P_T\sqrt{2\pi}\sigma_p \left[1 + erf\left(\frac{\tau}{\sqrt{2}\sigma_c}\right)\right] \tag{5.5}$$

where σ_c will be determined from the mean value of SWH over the entire region, and $F = 10^{14}$ counts/watt and is a factor that transforms counts to watts. This value was computed by comparing the power level of our simulations to the data obtained in counts for similar surface parameters.

By using the mean value of the pointing angle, ξ, over a bloom region in Equation 4.20, we can estimate the residual waveform data, RWD, which is defined to be

$$\begin{aligned} RWD &= \sum_{n=1}^{N} \frac{\Delta_n}{2\pi}\left(\frac{\sigma_n^o}{\sigma_b^o} - 1\right) \\ &= \langle P_{FS}^s(\tau)\rangle_{\phi_n} / \frac{G_o^2\lambda^2 c\,\sigma_b^o}{4(4\pi)^2\,L_p\,h^3} \exp\left\{-\frac{4}{\gamma}\left[\sin^2\xi + \frac{c\tau}{h}\cos 2\xi\right]\right\} I_o\left(\frac{4}{\gamma}\sqrt{\frac{c\tau}{h}}\sin 2\xi\right) \\ &= \frac{P_r(\tau) - P_r^b(\tau)}{K}. \end{aligned} \tag{5.6}$$

The value of σ_b^o is determined from the GDR data at the beginning of each region. We note that due to the approximations, the values of the residual waveform data, RWD, might be off by a constant. However, this does not affect our main concerns of trend and shape of the residual waveform data. K in Equation 5.6 is equal to the denominator in Equation 5.5.
We are interested in the residual waveform data, RWD, because it contains the most basic information about the slick areas, their number and size. While $P_r(\tau)$, $\langle P_r^s(\tau)\rangle_{\phi_n}$, and $\langle P_{FS}^s(\tau)\rangle_{\phi_n}$ also contain this information about the slick areas they do so in a more convoluted way which makes it harder to discern characteristics or patterns of the slick areas and consequently of the σ^o blooms.

5.3.1 Region A

As a reminder the bloom regions for Cycle 137, Pass 058 are defined in Figure 1.1. The mean SWH for region A is 1.771 m and 1.868 m for Ku- and C-band, respectively, and the mean off-nadir angle ξ is 0.06^o. Figure 5.1 shows the mean radar cross section, σ^o, corresponding to region A for both Ku- and C-band. Contaminated data is marked by a red asterisk and the lower limit of the bloom for the Ku- and C-band, 12 dB and 16 dB respectively, is marked with a green line. There are two blooms occurring in this region, a smaller bloom between GDR samples 30 and 65 and a larger bloom between GDR samples 122 and 160. The blooms appear to be very similar at both frequecies. Data for both frequencies is contaminated around GDR samples 43, 133 to 135, and 140 to 141. These samples correspond approximately to waveform numbers 416 to 426, 1317 to 1346, and 1386 to 1407. For simplification purposes, we will index waveforms with respect to the beginning of the region rather than in time.
Figure 5.2 shows the off-nadir or pointing angle, ξ, corresponding to region A. We can see that with one exception around GDR sample 95 all the out of range angles (2.55 degrees) occur during the bloom. Approximately half of these out of range values correspond to con-

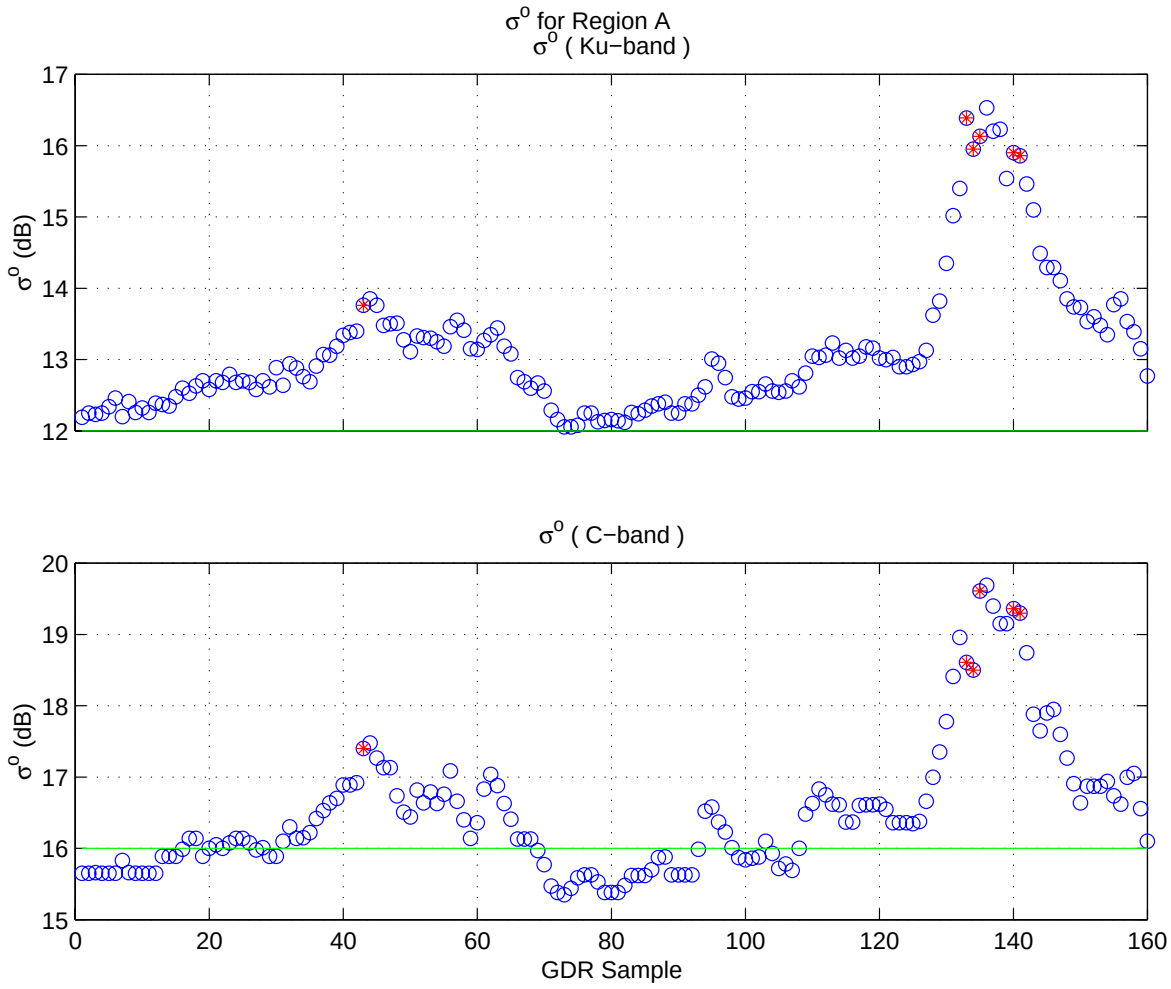

Figure 5.1. Ku- and C-band σ^o for region A

taminated data.

We will first examine the second and larger bloom of this region and show the data fitting steps for the Ku-band data.

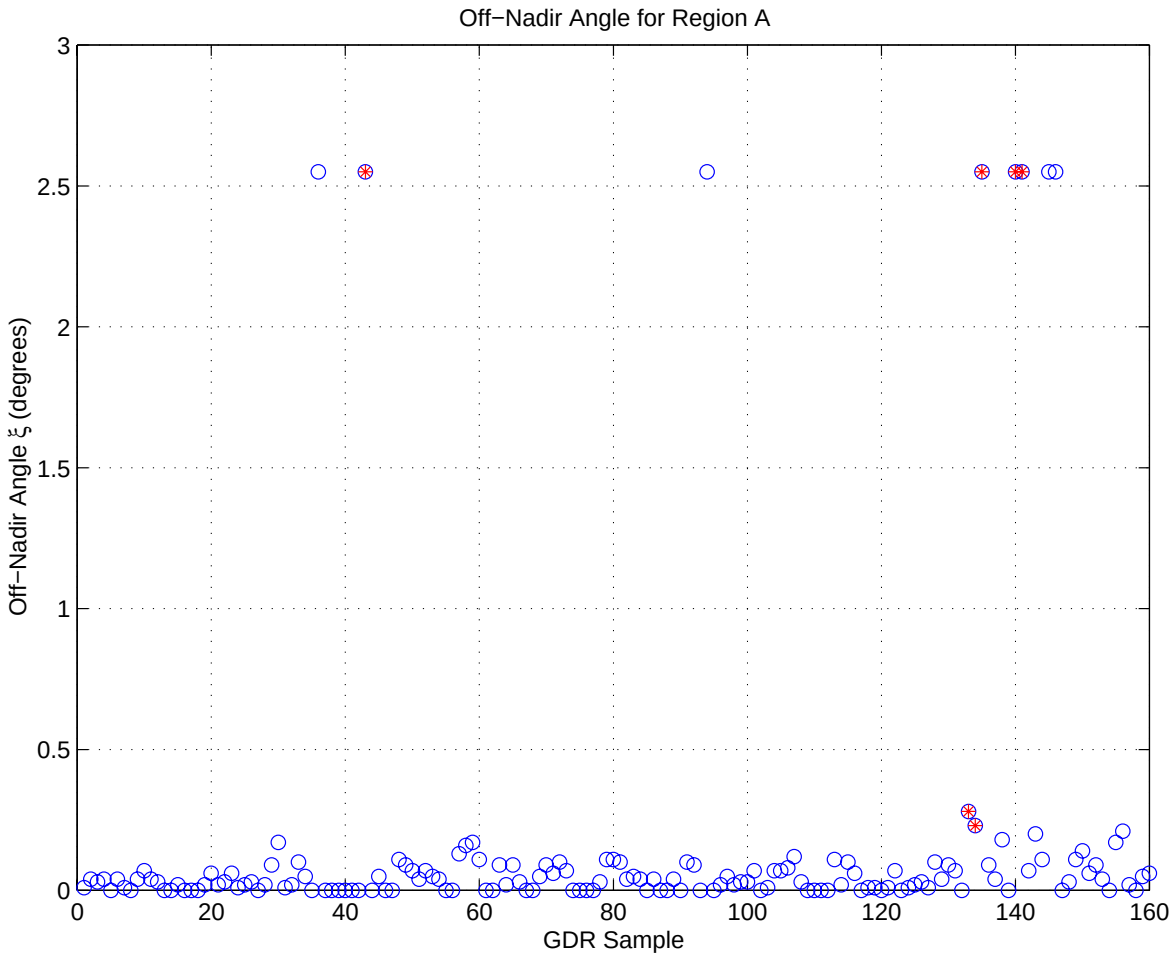

Figure 5.2. Off-Nadir angle ξ for region A

Figures 5.3 through 5.6 show the raw Ku-band SDR data after being corrected using Equation 5.1, having the AGC removed with respect to a reference of 30.5 dB, and expanding the τ axis. In these figures we can see the level of the waveforms increase up to the peak of the bloom in Figure 5.4 and then decrease as the bloom ends. At this point, we see no deviations from the expected waveforms that would cause the off-nadir angle to be out of range.

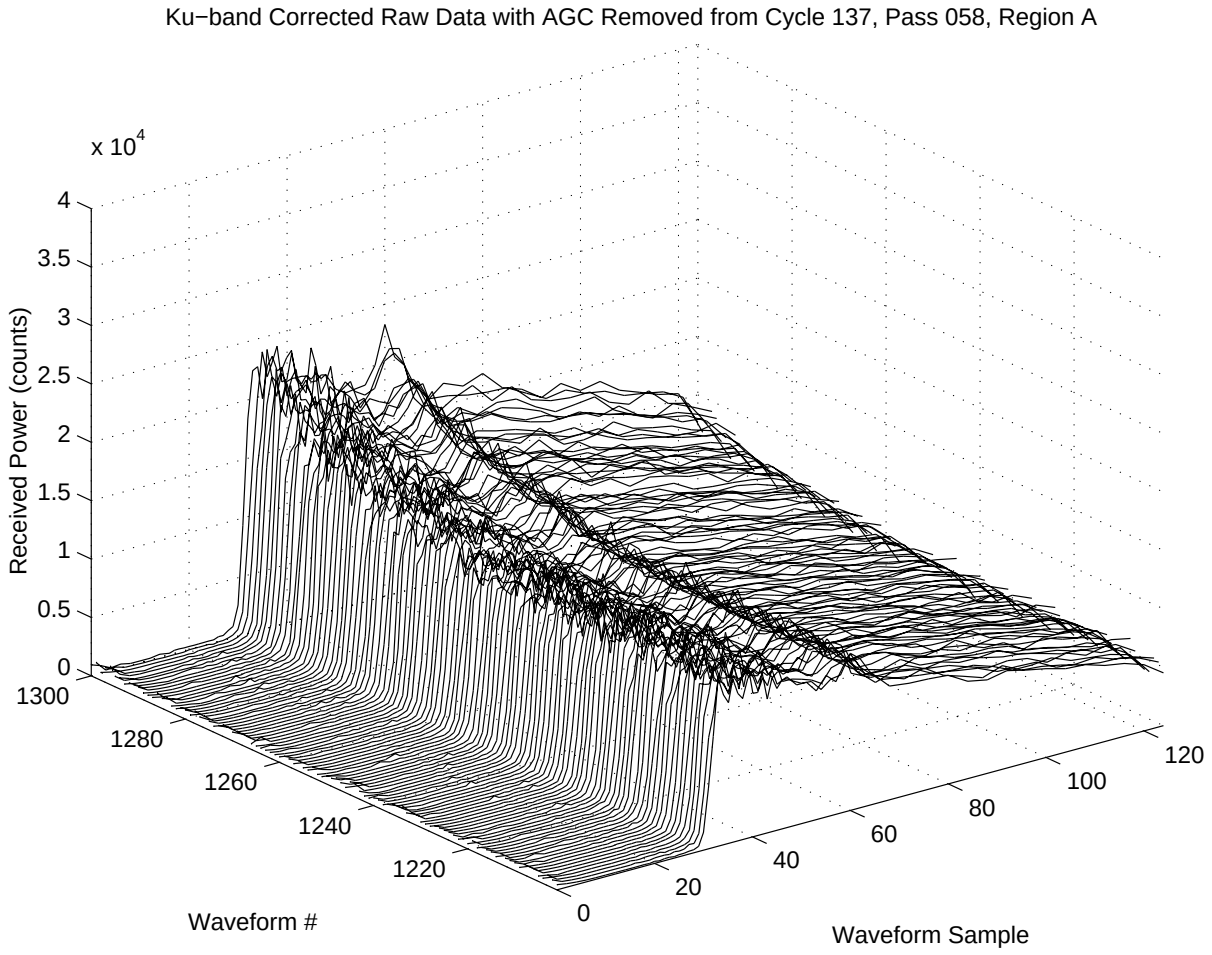

Figure 5.3. Ku-band corrected raw waveform data with AGC removed from region A, second bloom (i)

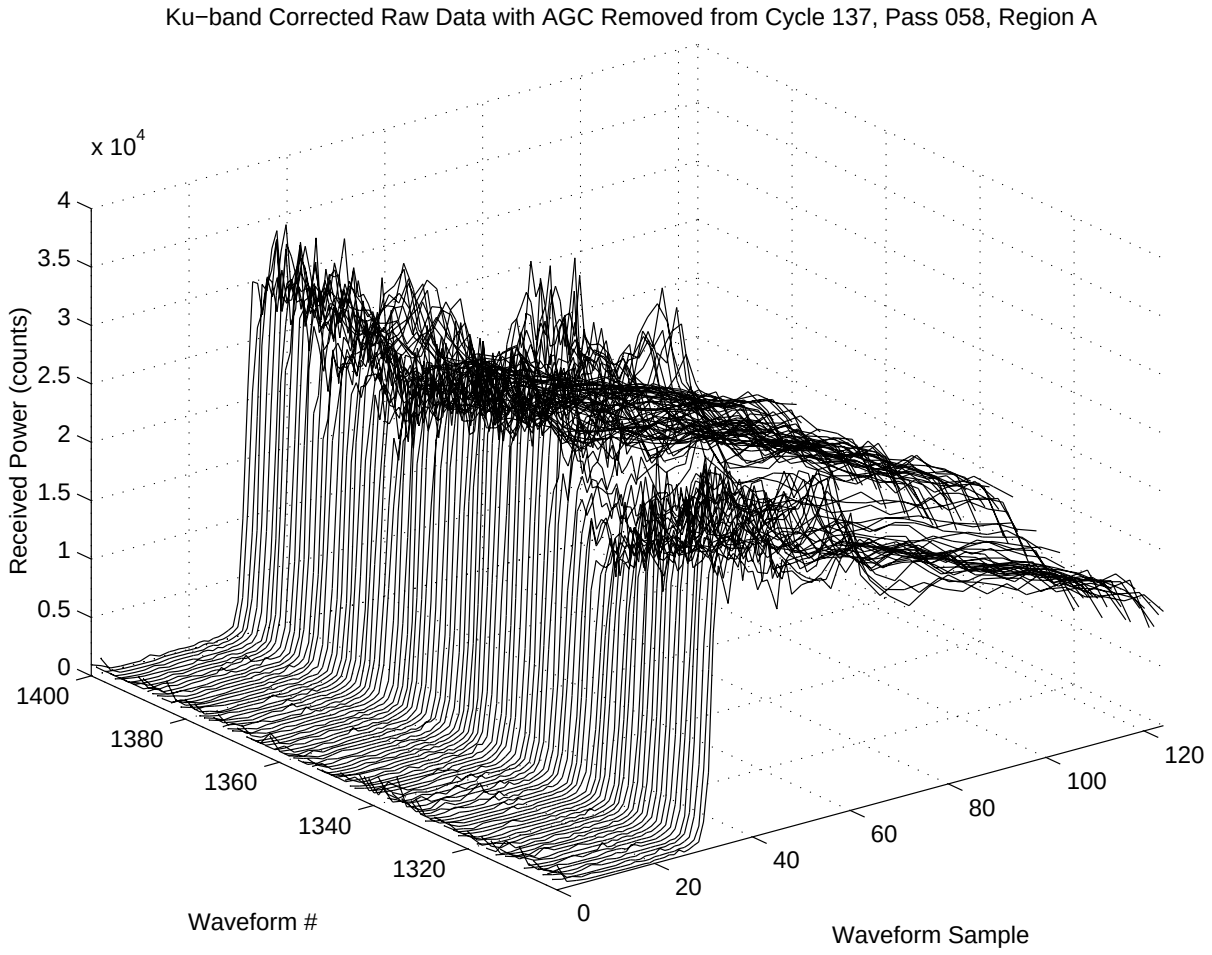

Figure 5.4. Ku-band corrected raw waveform data with AGC removed from region A, second bloom (ii)

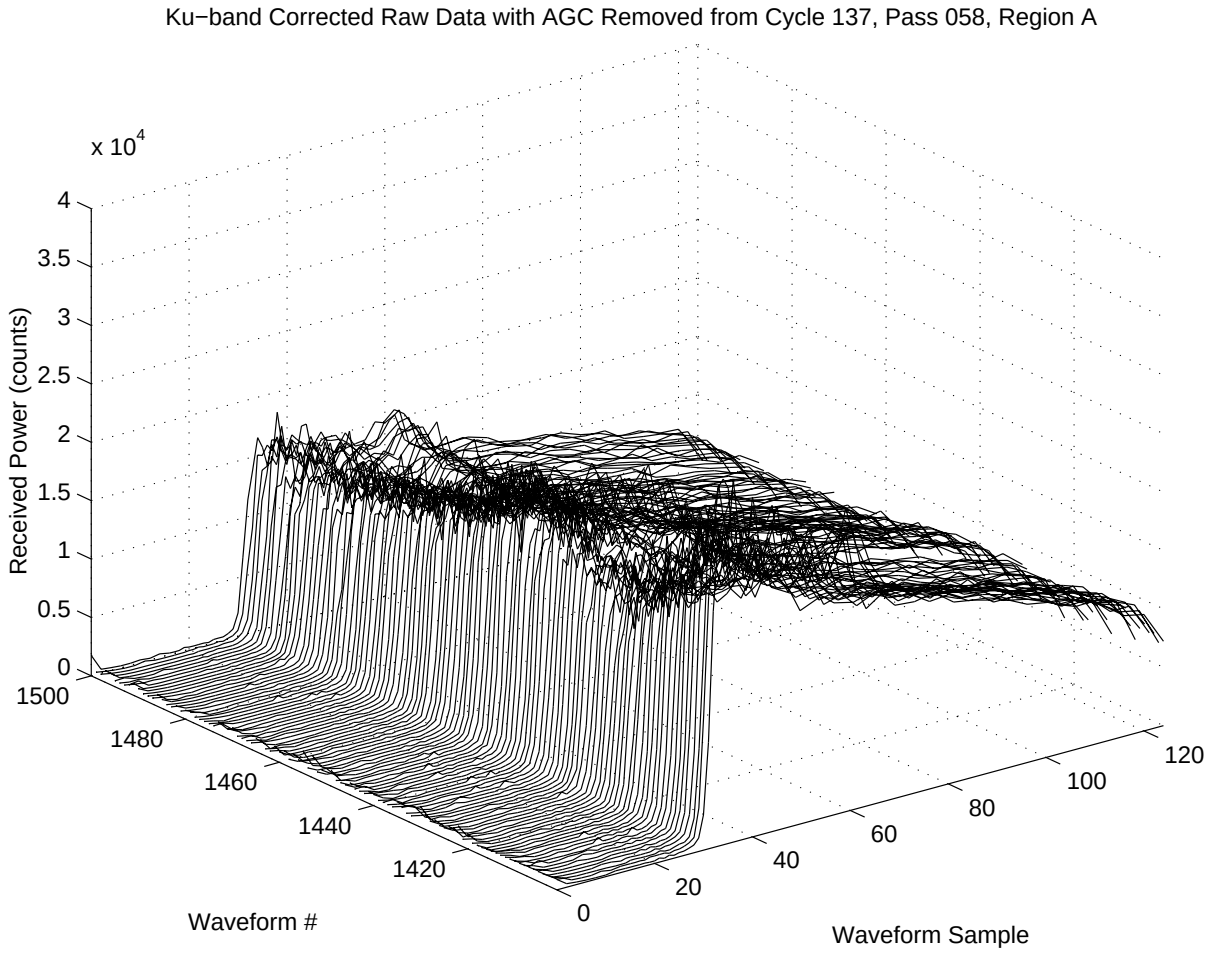

Figure 5.5. Ku-band corrected raw waveform data with AGC removed from region A, second bloom (iii)

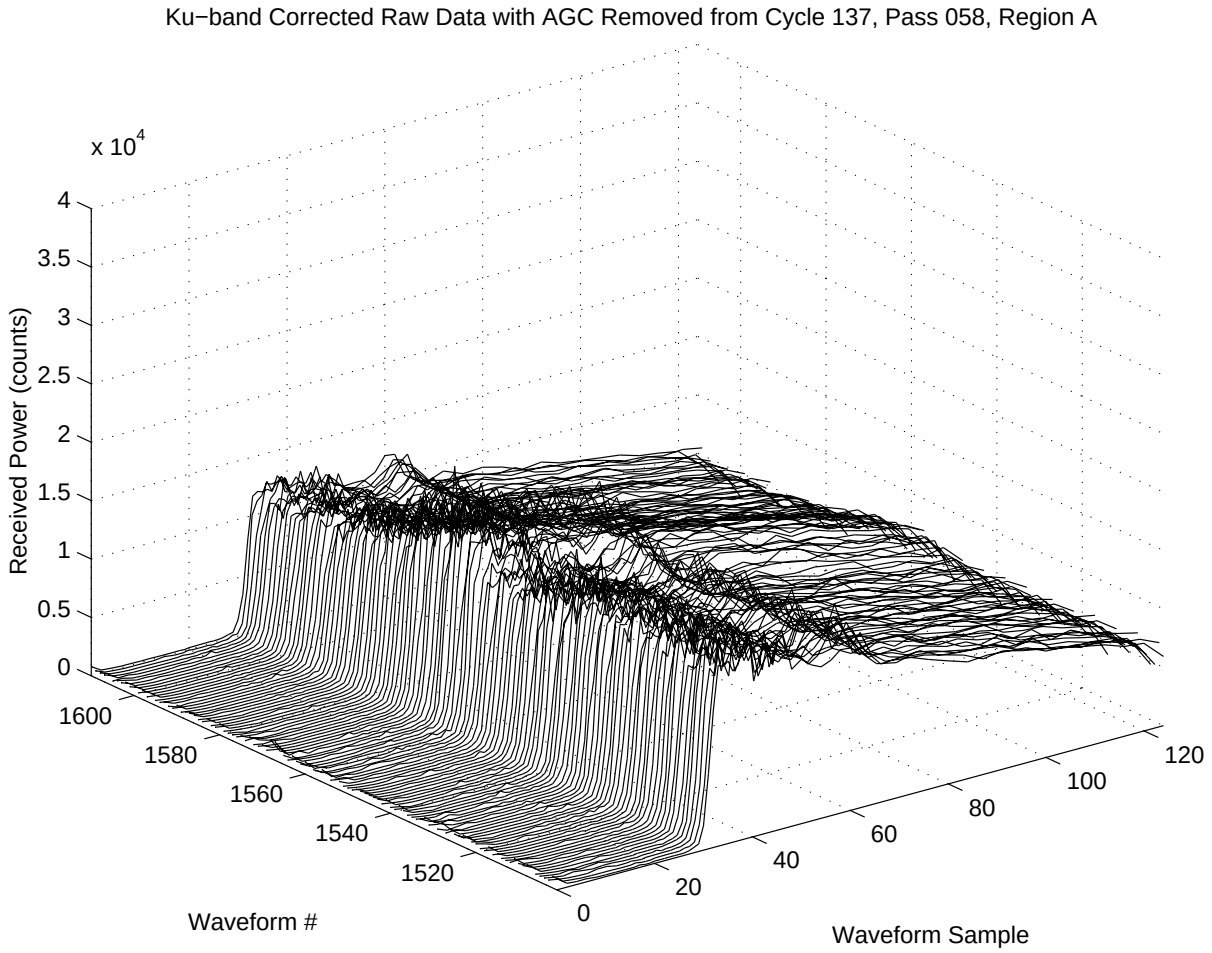

Figure 5.6. Ku-band corrected raw waveform data with AGC removed from region A, second bloom (iv)

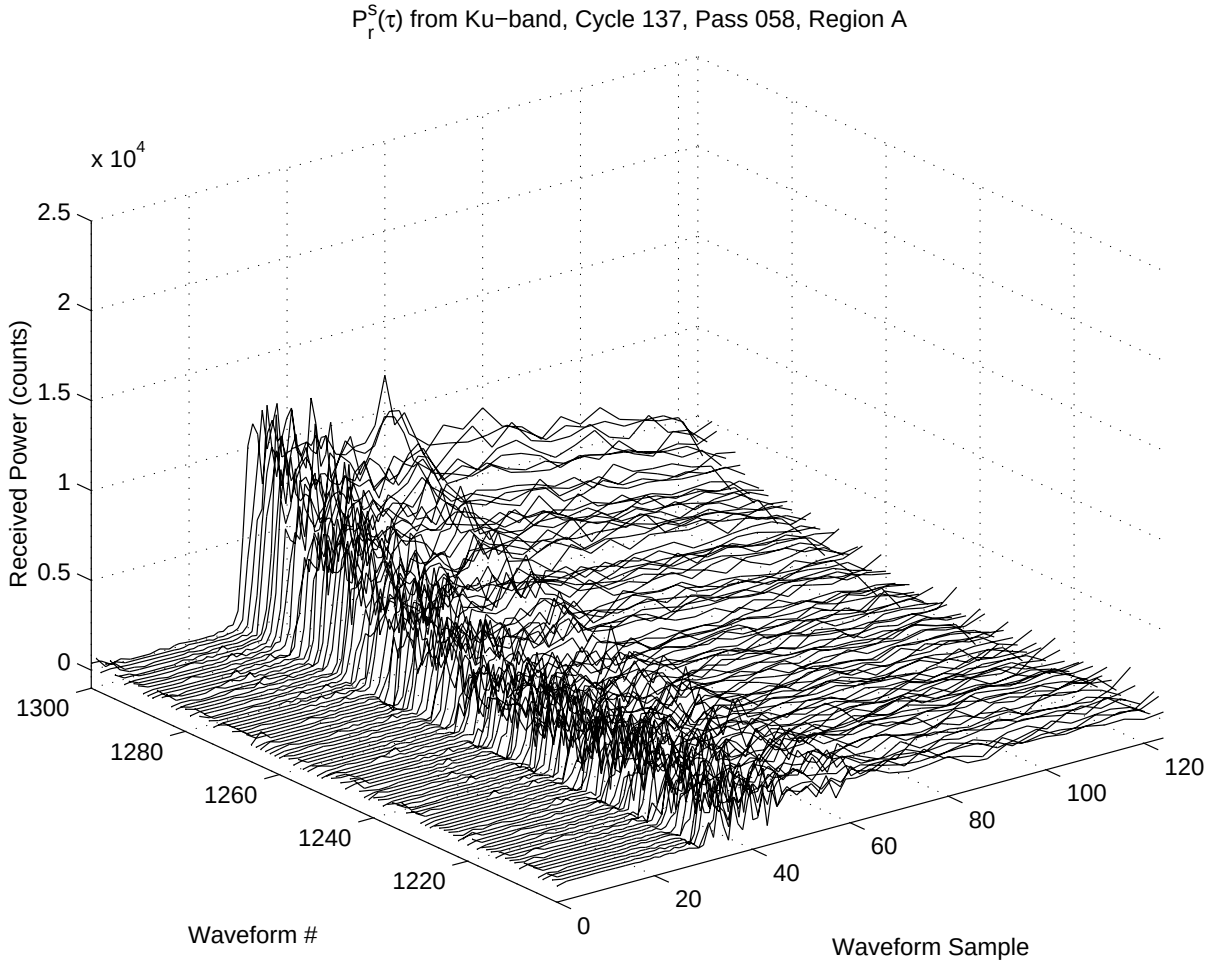

Figure 5.7. Ku-band $\langle P_r^s(\tau)\rangle_{\phi_n}$ from region A, second bloom (i)

Once the raw Ku-band SDR data has been corrected, the AGC effects removed, and the τ axis expanded, we can then compute an approximation of the average power returned from the slick areas $\langle P_r^s(\tau)\rangle_{\phi_n}$ for the bloom in question by subtracting the average of the first 100 waveforms from the waveforms in Figures 5.3 through 5.6.

$\langle P_r^s(\tau)\rangle_{\phi_n}$ is shown in Figures 5.7 through 5.10 corresponding to the corrected waveform data in Figures 5.3 through 5.6. Again, the bloom is apparent in these figures. We expected the waveforms in these figures to have near zero amplitudes at the beggining and ending of the bloom regions since there should not be any slick areas. As the radar's nadir point enters the area containing slicks, the sumation term in Equation 4.20 will increase thus increasing

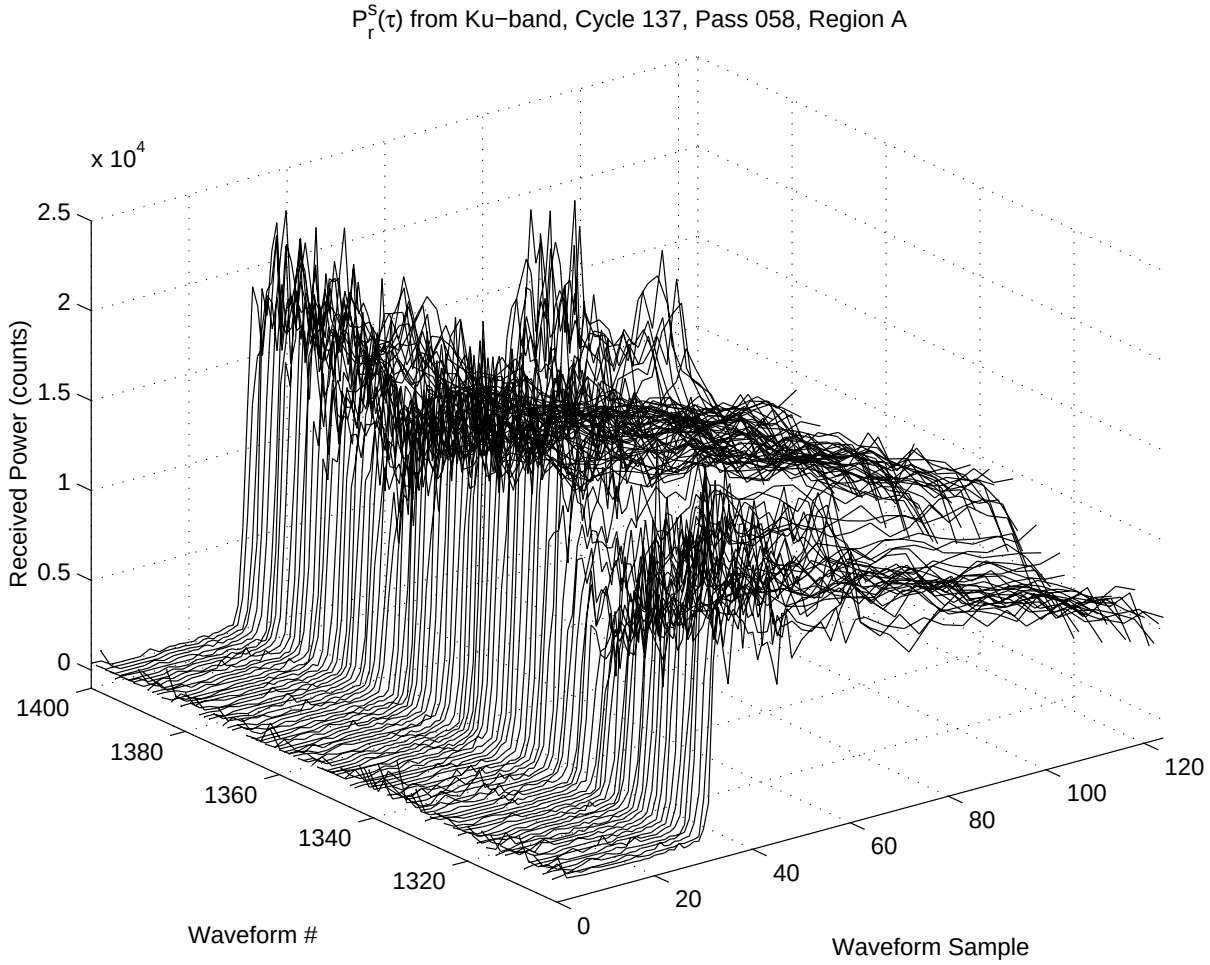

Figure 5.8. Ku-band $\langle P_r^s(\tau)\rangle_{\phi_n}$ from region A, second bloom (ii)

the the overall level of $\langle P_{FS}^s(\tau)\rangle_{\phi_n}$. Consequently, we expect the level of $\langle P_r^s(\tau)\rangle_{\phi_n}$ to also increase. Similarly, as the radar's nadir point exits the surface containing slick areas we expect the level of the waveforms to decrease. Figures 5.7 through 5.10 show no major deviations from these expectations.

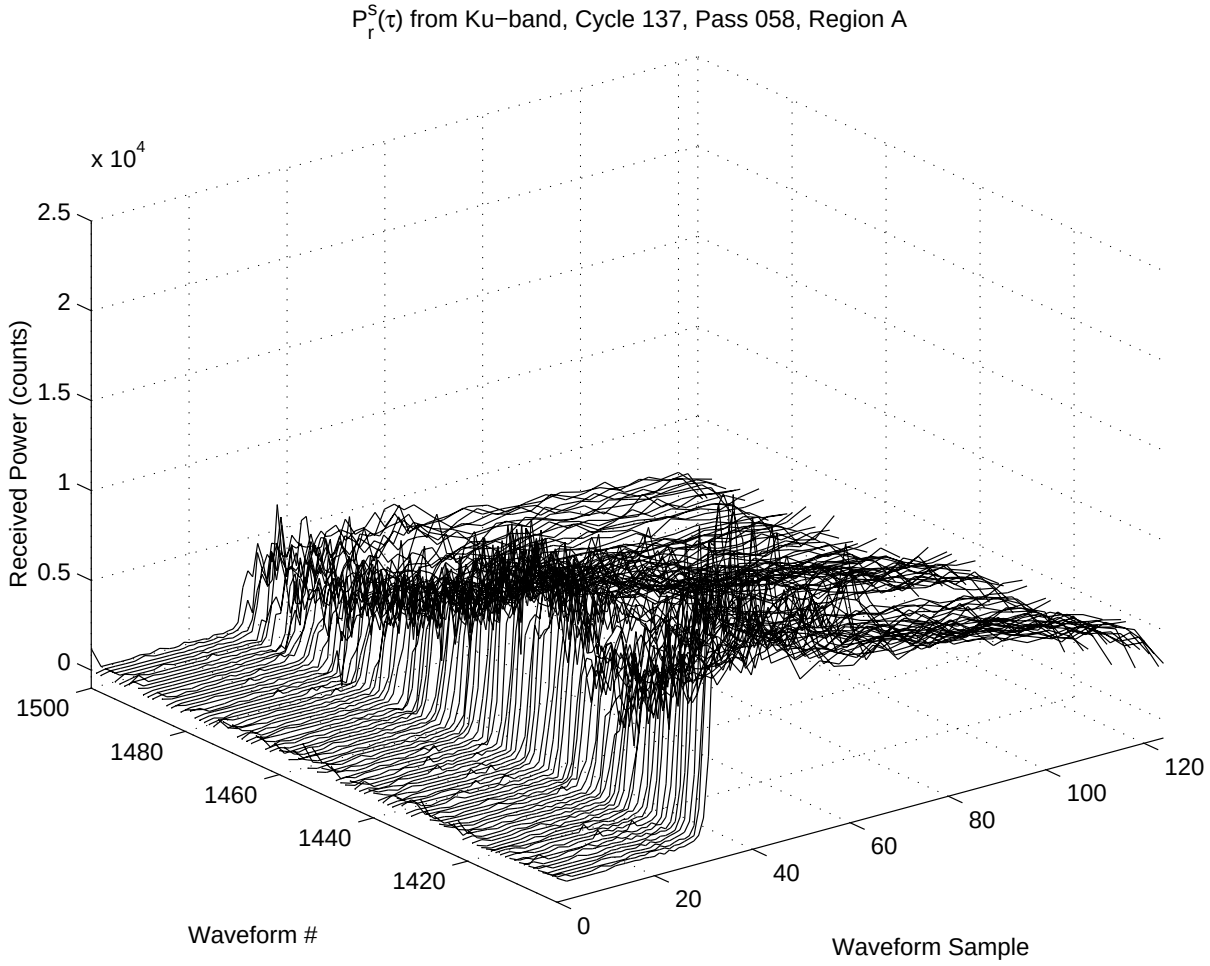

Figure 5.9. Ku-band $\langle P_r^s(\tau)\rangle_{\phi_n}$ from region A, second bloom (iii)

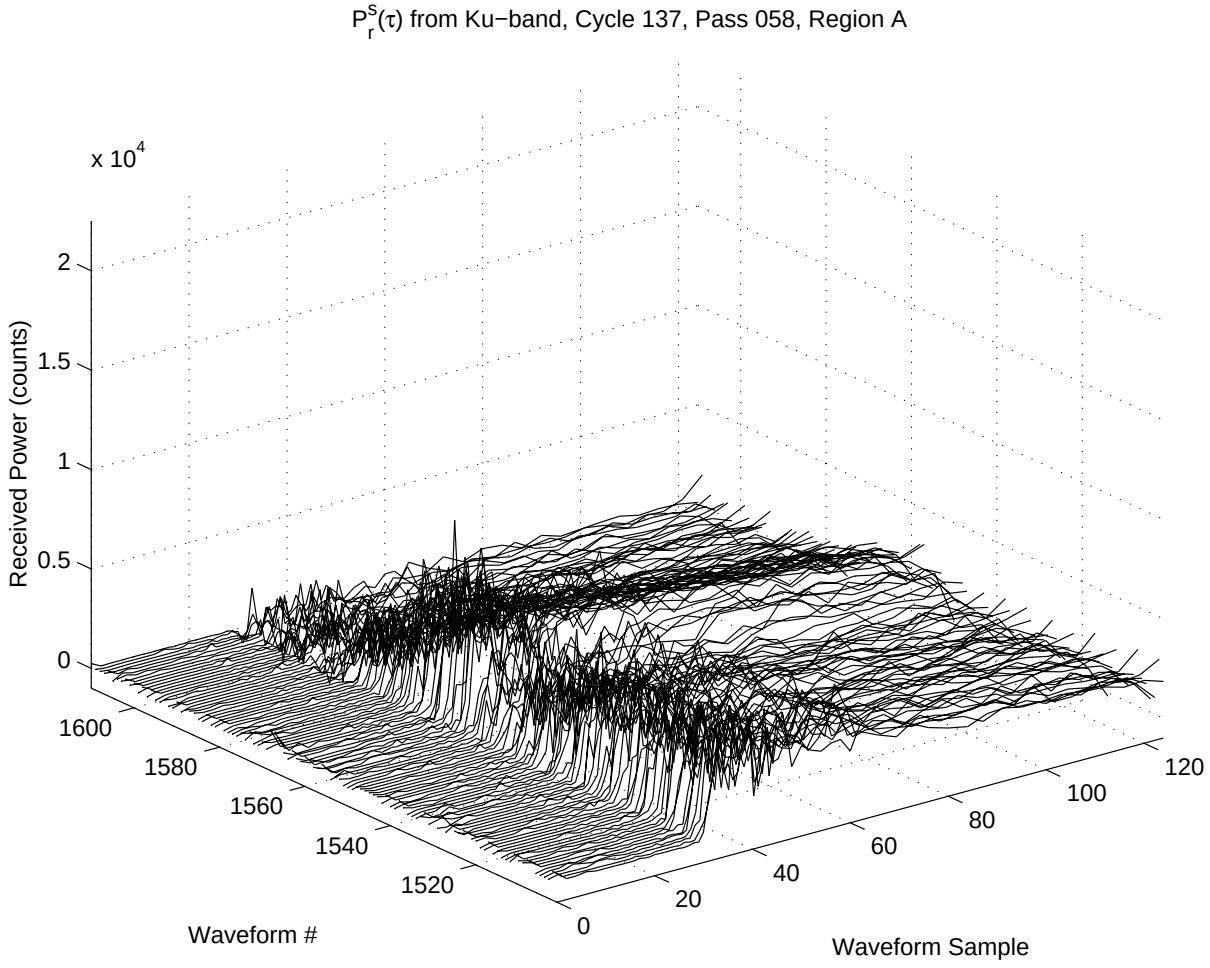

Figure 5.10. Ku-band $\langle P_r^s(\tau)\rangle_{\phi_n}$ from region A, second bloom (iv)

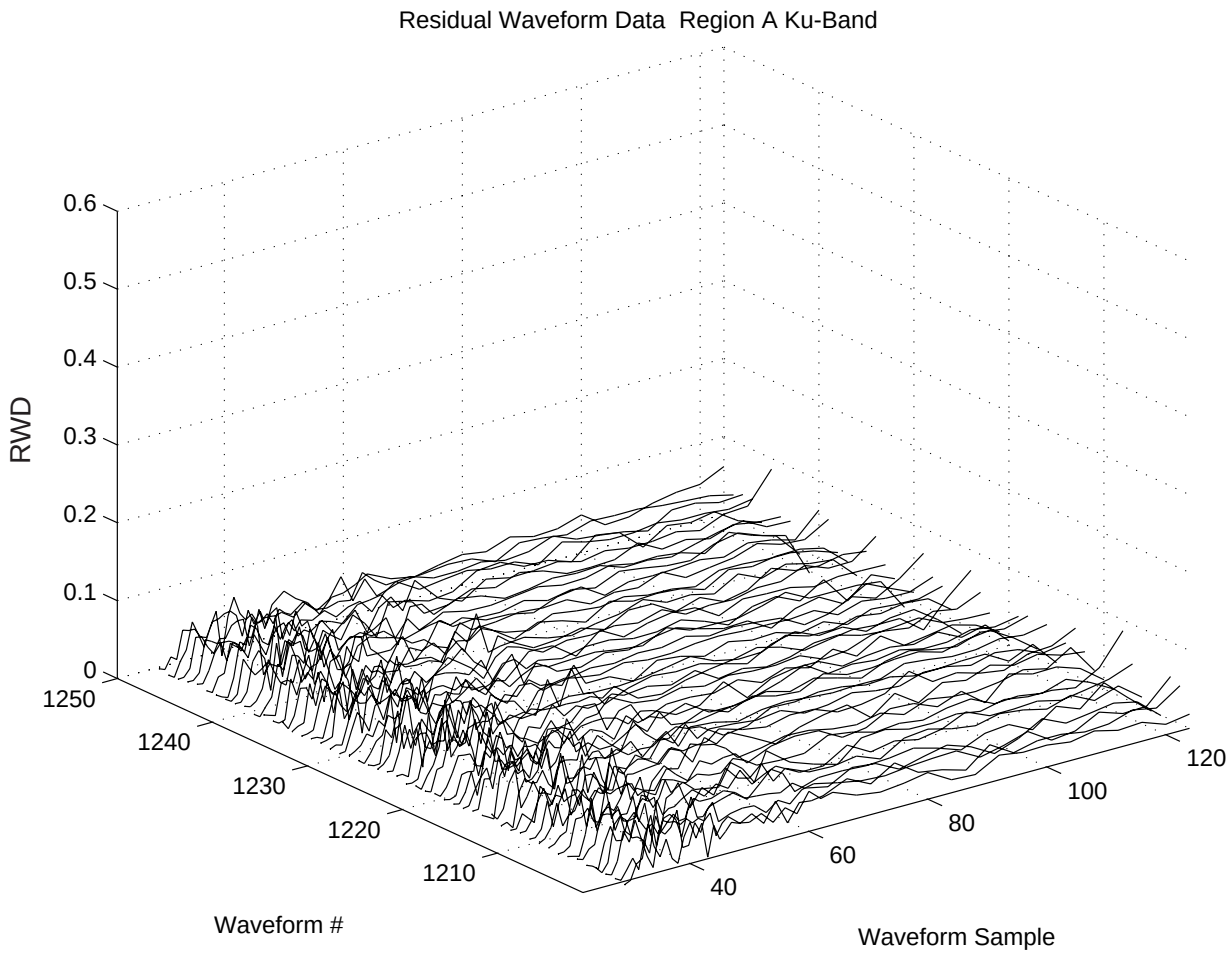

Figure 5.11. Ku-band residual waveform data from region A, second bloom (i)

Once an estimate of $\langle P_r^s(\tau)\rangle_{\phi_n}$ is computed, we can derive the residual waveform data, RWD, by using Equations 5.5 and 5.6. Figures 5.11 through 5.18 show the Ku-band residual waveform data for this bloom. We can see that as the bloom peaks, so does the level of the RWD. More importantly the waveforms are flat in shape which means that the slick areas are fairly uniform and homogeneus in radar cross section. Only half as many waveforms per plot are shown in Figures 5.11 through 5.18 as compared to the previous figures so that the RWD can be seen more clearly.

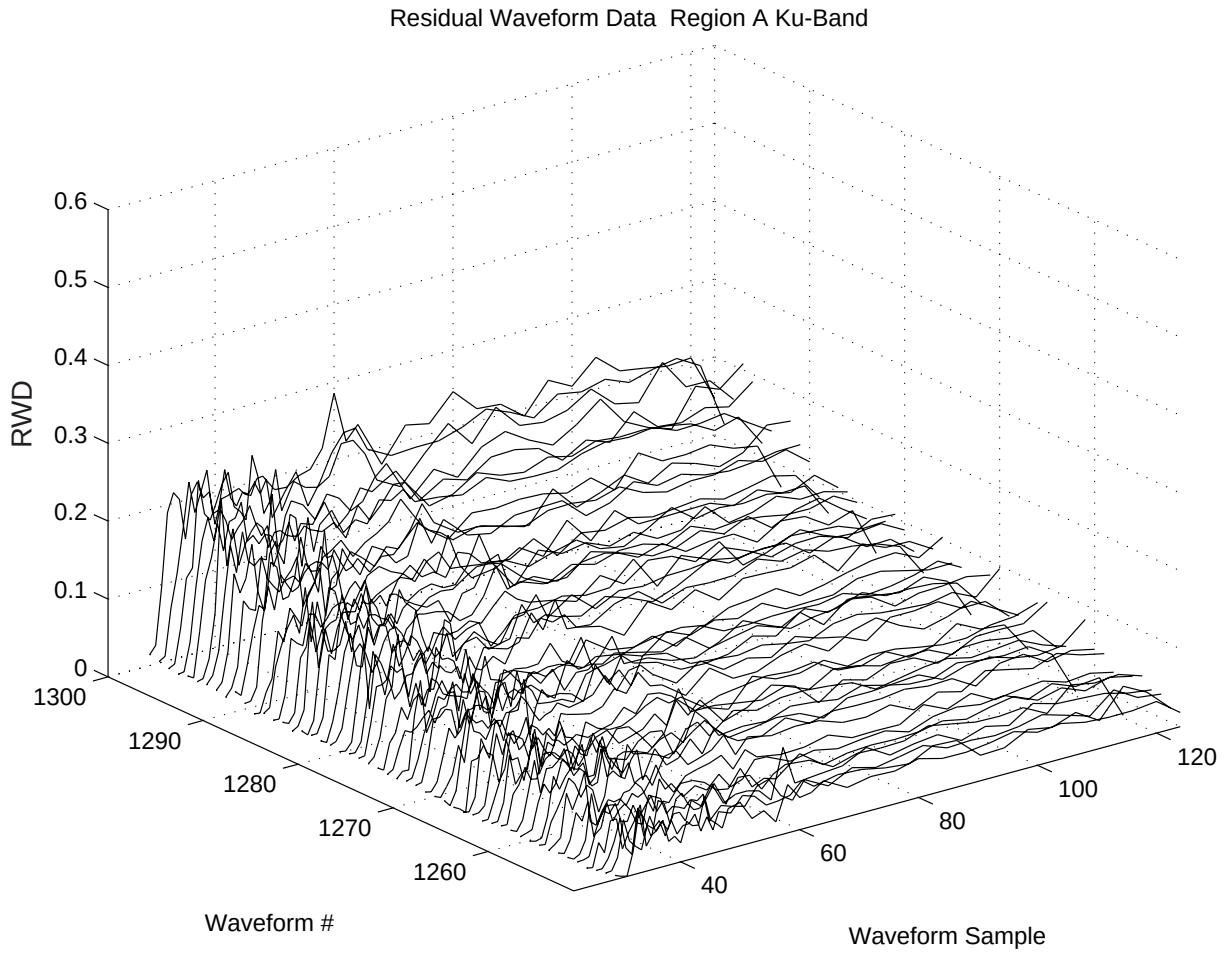

Figure 5.12. Ku-band residual waveform data from region A, second bloom (ii)

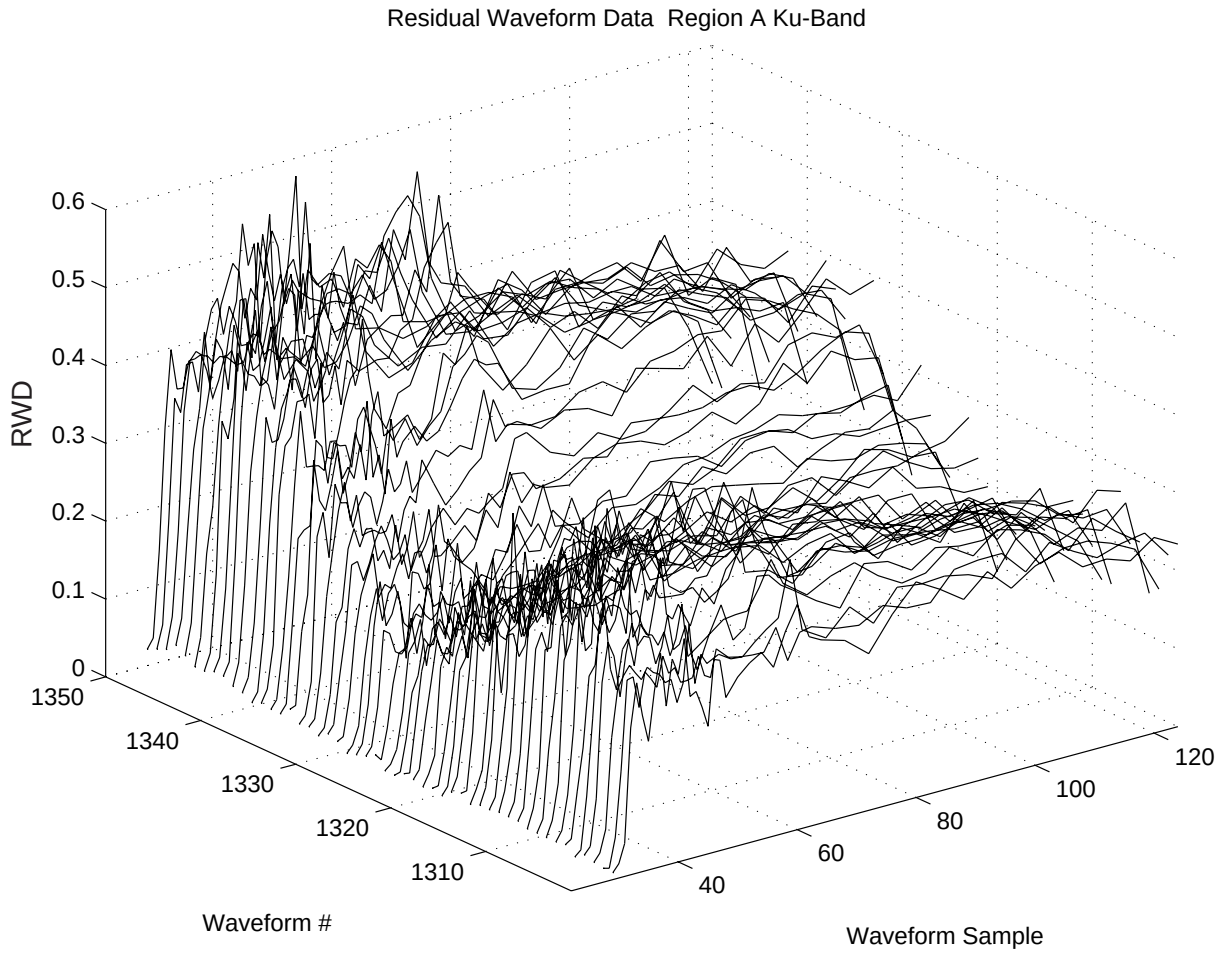

Figure 5.13. Ku-band residual waveform data from region A, second bloom (iii)

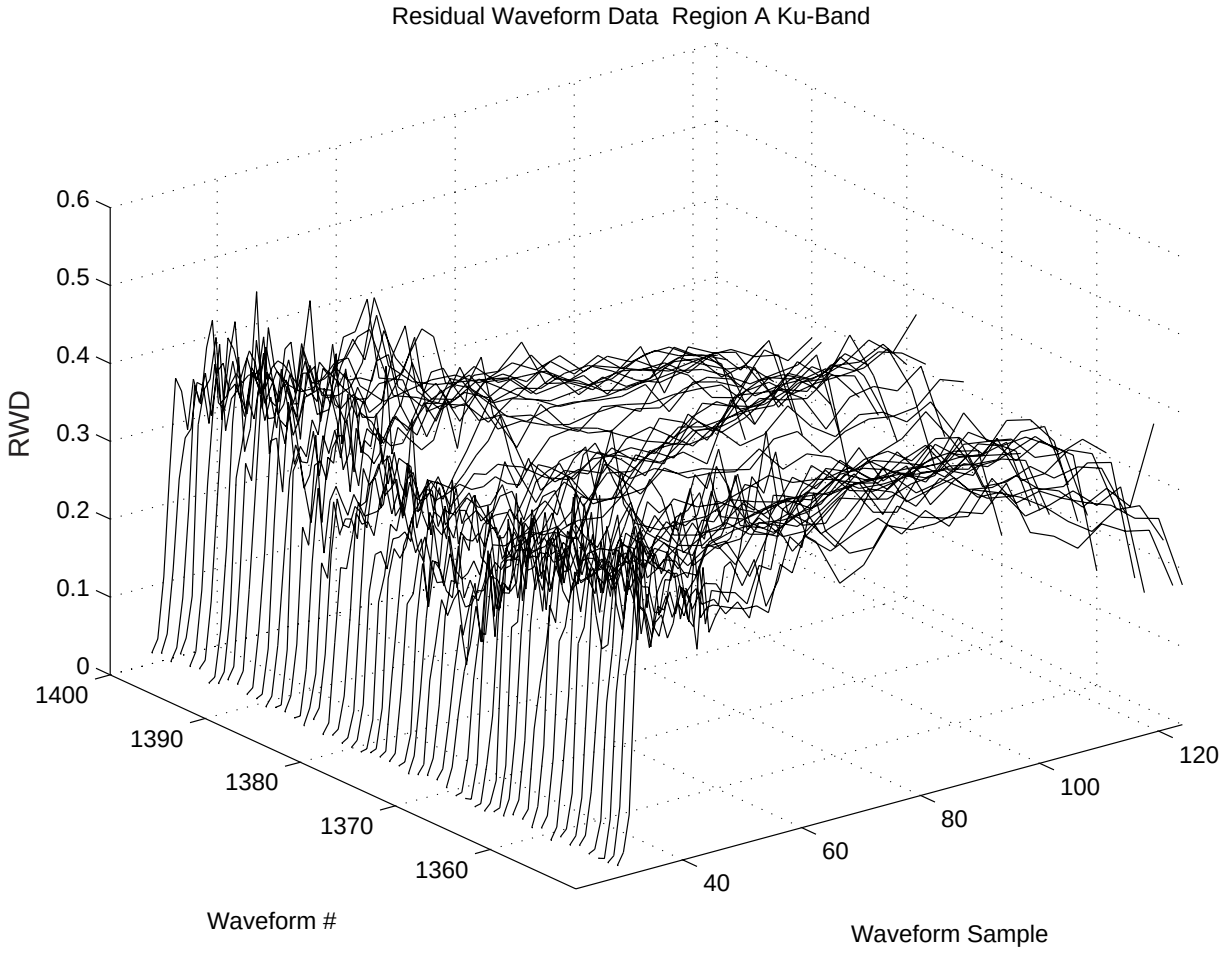

Figure 5.14. Ku-band residual waveform data from region A, second bloom (iv)

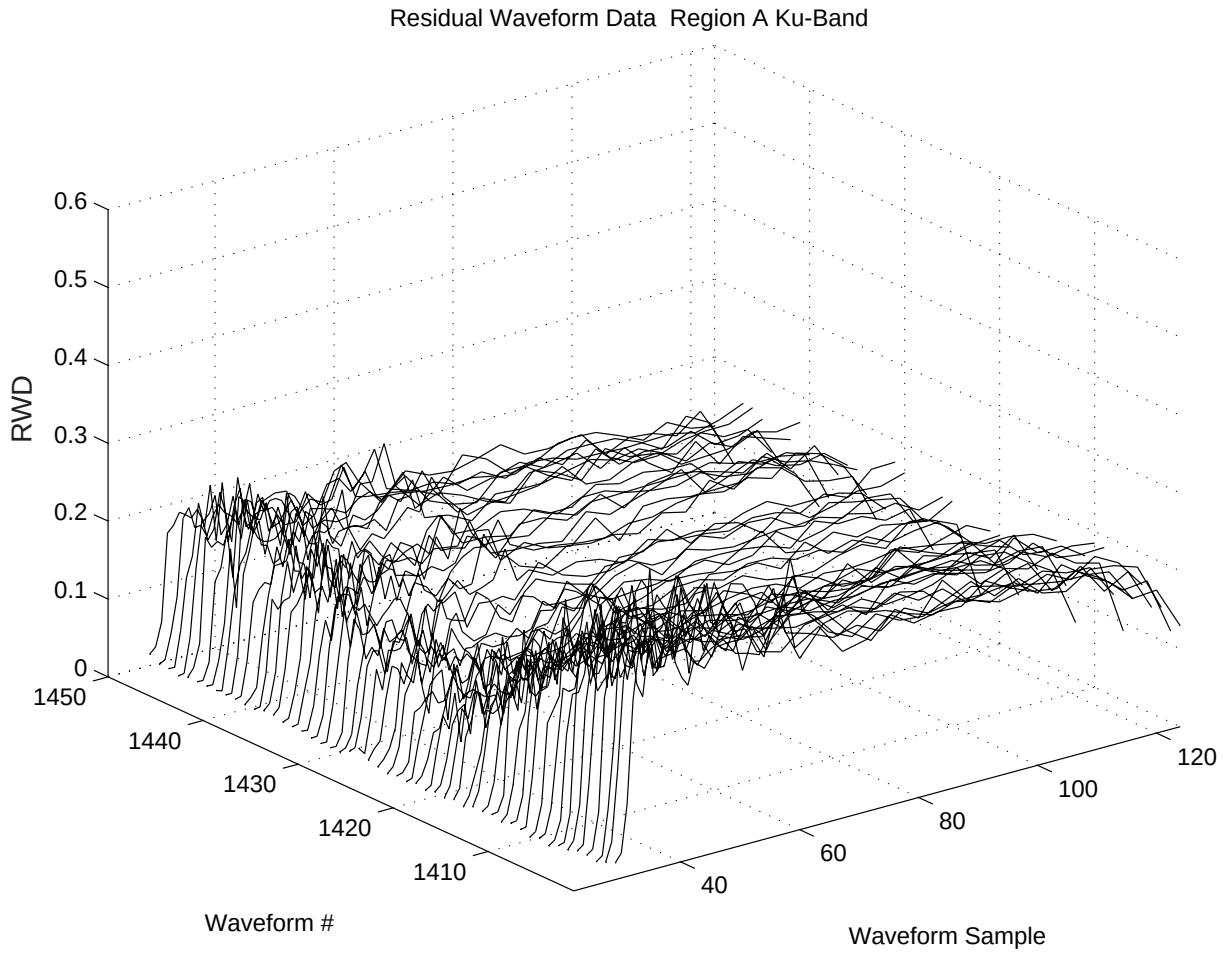

Figure 5.15. Ku-band residual waveform data from region A, second bloom (v)

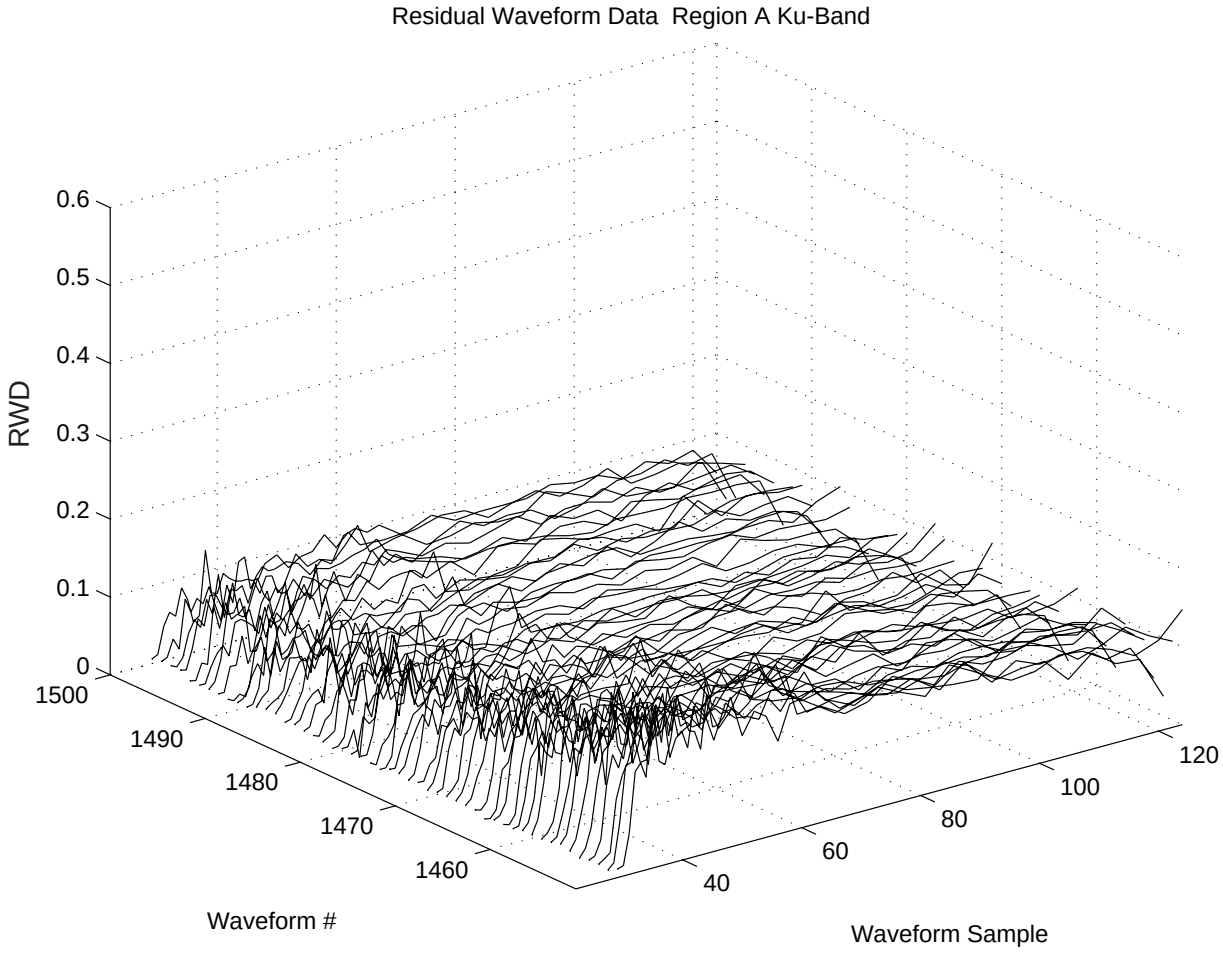

Figure 5.16. Ku-band residual waveform data from region A, second bloom (vi)

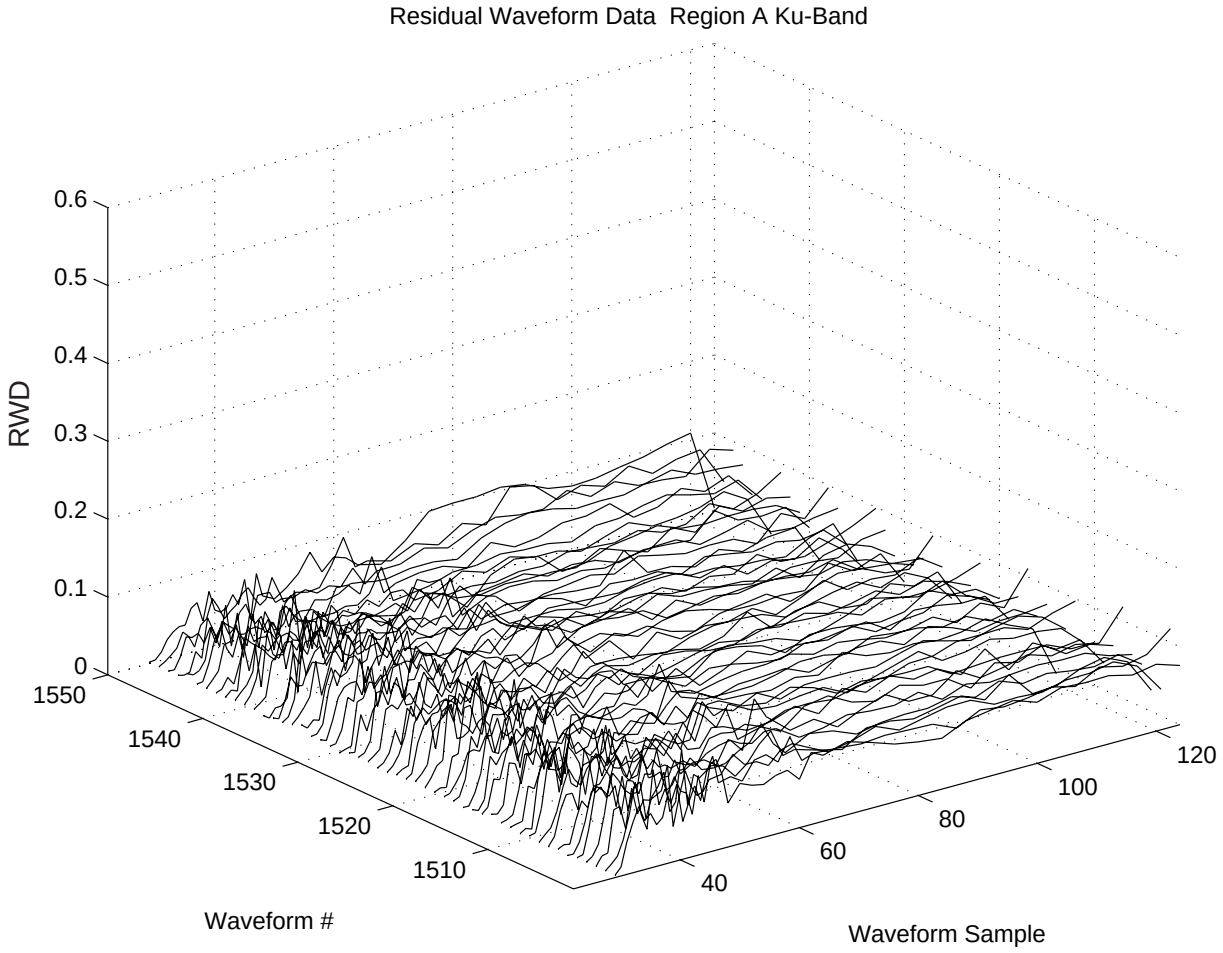

Figure 5.17. Ku-band residual waveform data from region A, second bloom (vii)

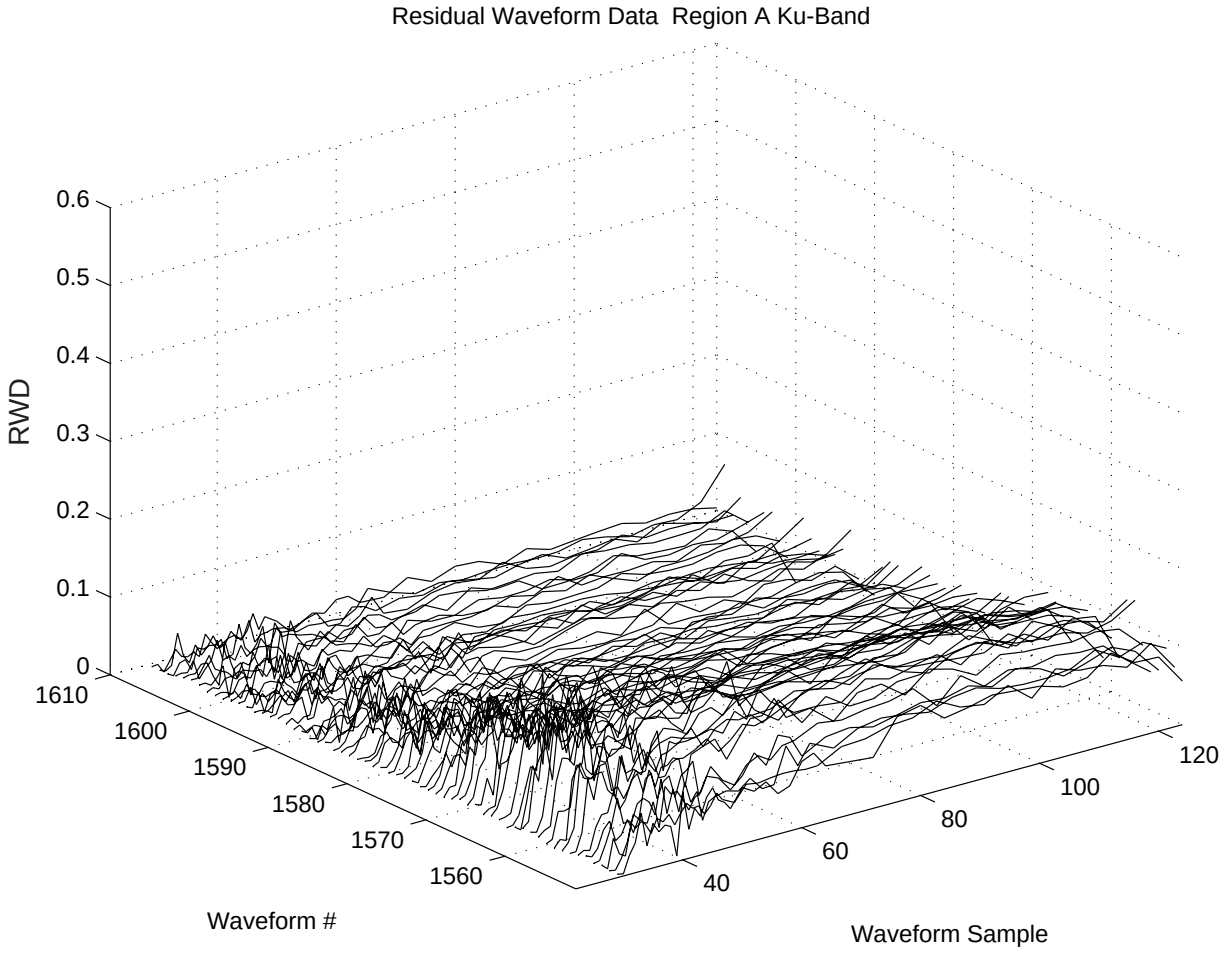

Figure 5.18. Ku-band residual waveform data from region A, second bloom (viii)

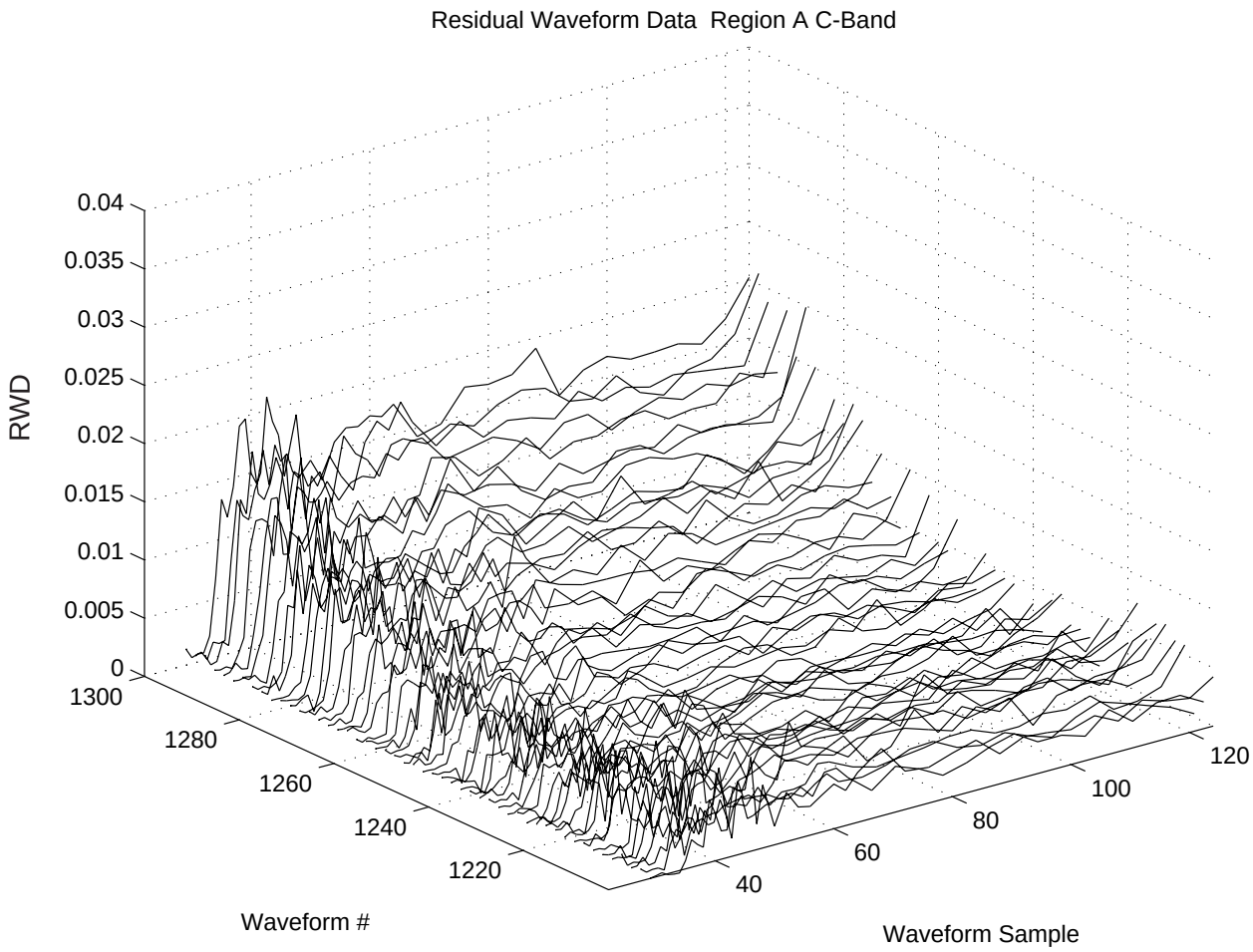

Figure 5.19. C-band residual waveform data from region A, second bloom (i)

Figures 5.19 through 5.22 show the C-band residual waveform data from the large bloom part of region A. These C-band waveforms appear to behave very similarly to their Ku-band counterparts, except for the difference in level. However, the tail of most of the waveforms is raised for no apparent reason. This leads us to beleive that this might be caused by the altimeter design.

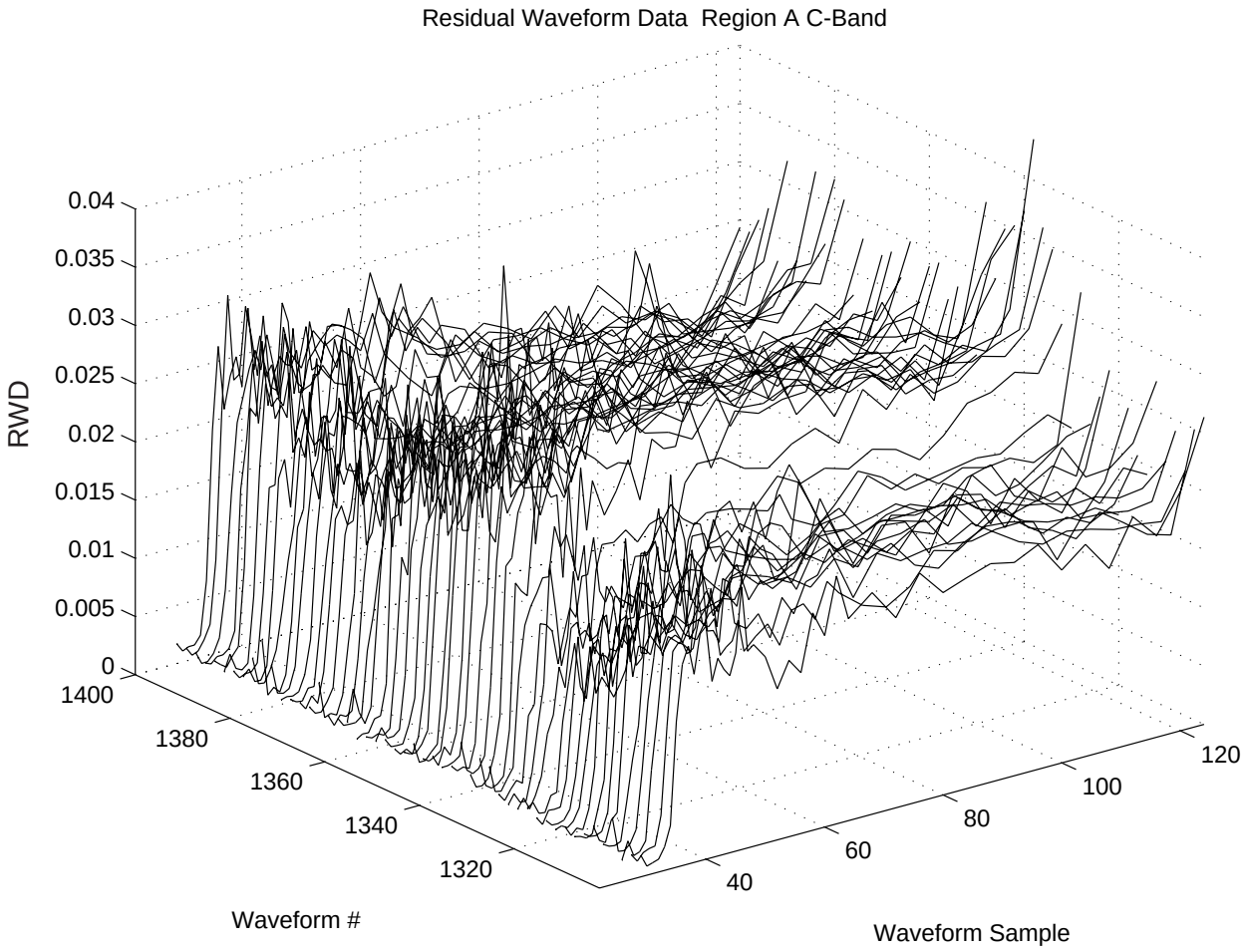

Figure 5.20. C-band residual waveform data from region A, second bloom (ii)

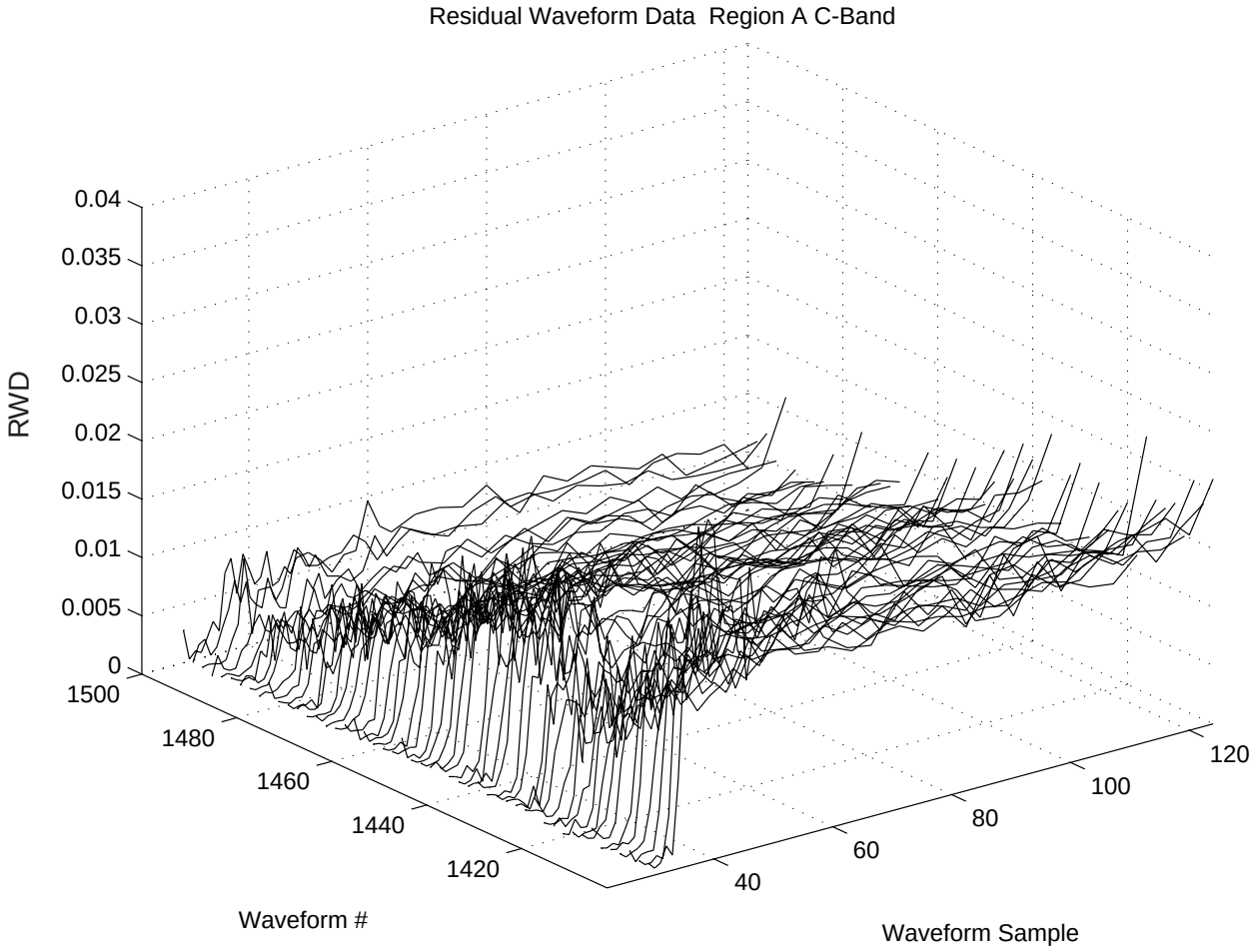

Figure 5.21. C-band residual waveform data from region A, second bloom (iii)

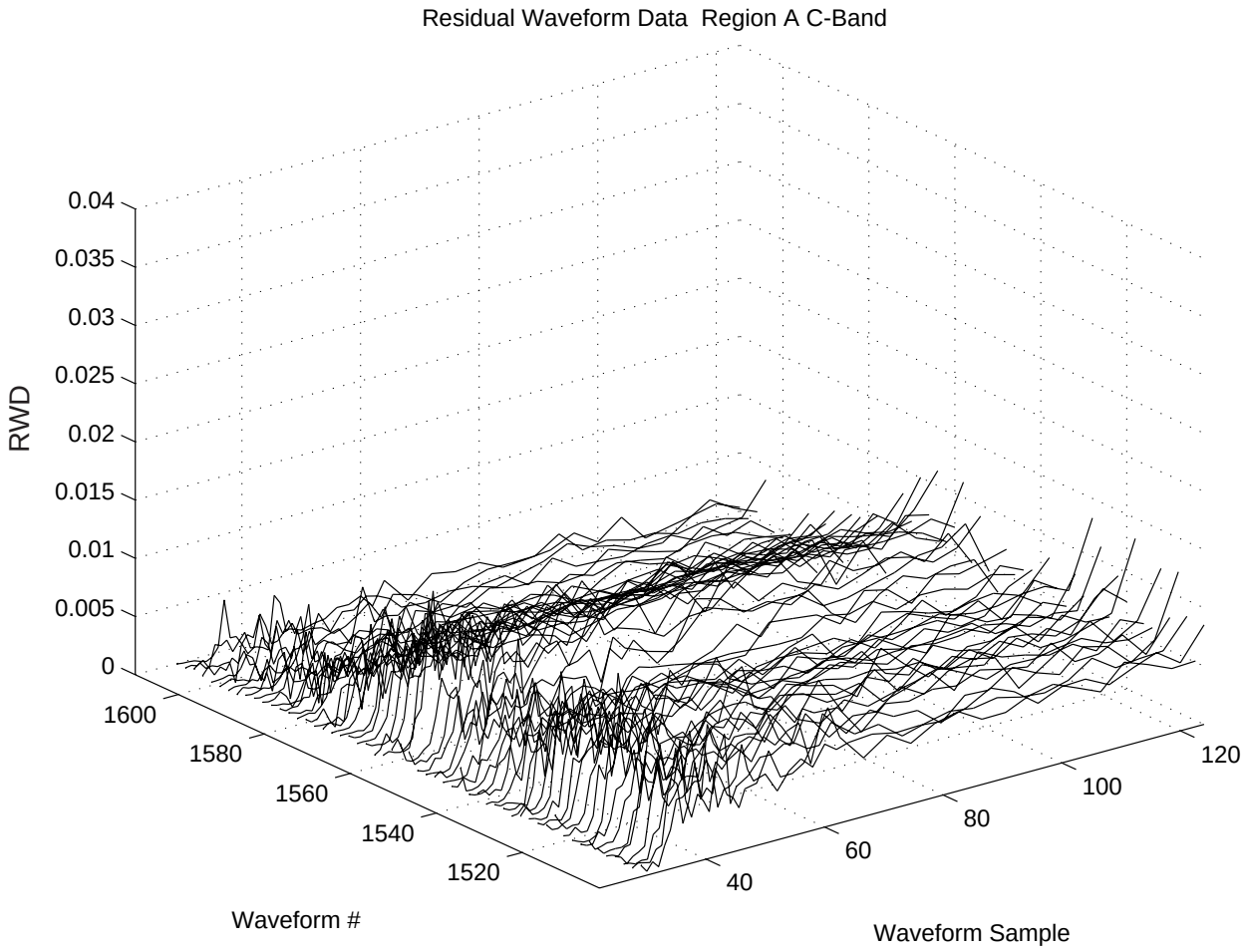

Figure 5.22. C-band residual waveform data from region A, second bloom (iv)

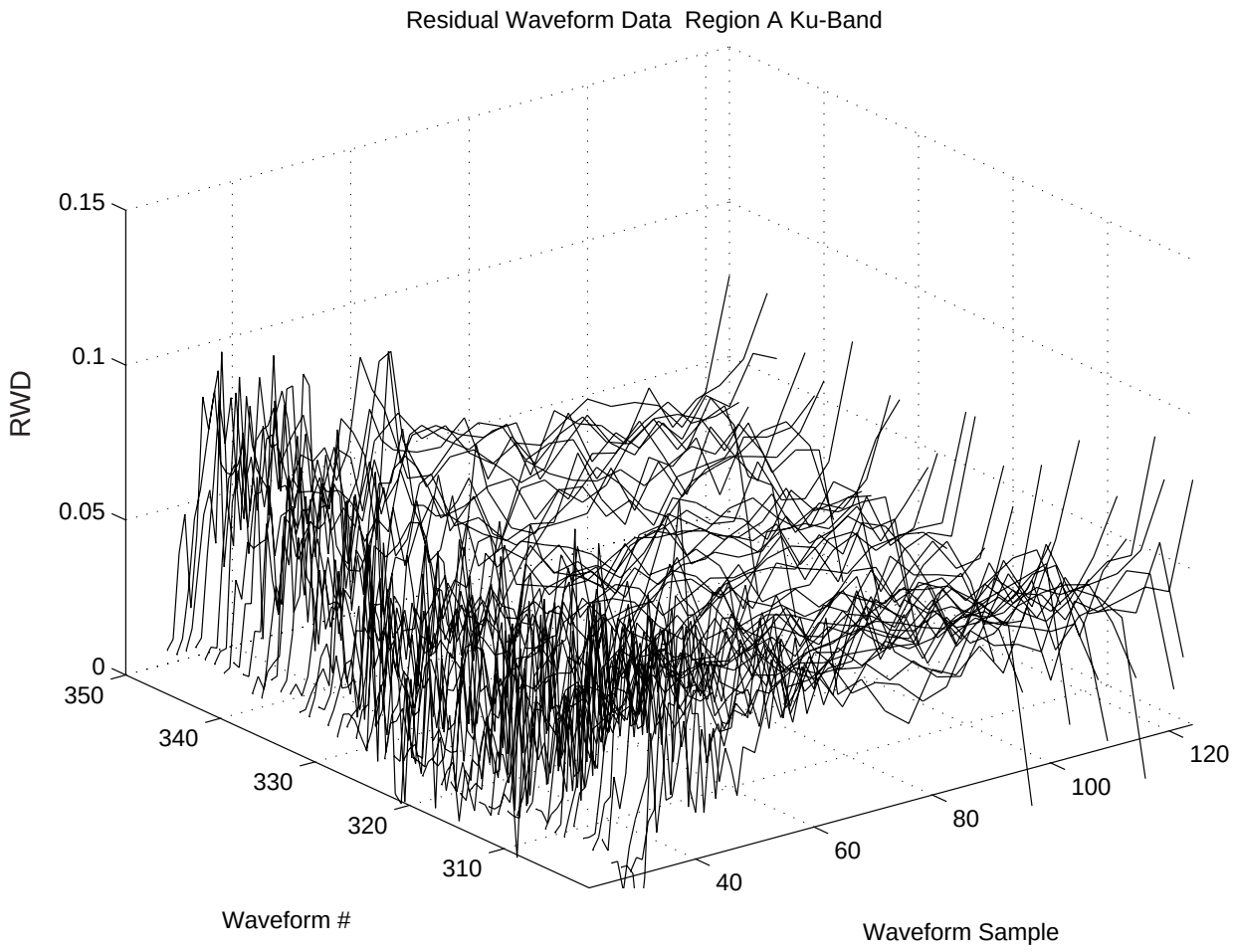

Figure 5.23. Ku-band residual waveform data from region A, first bloom (i)

We now examine the first and smaller bloom. Figures 5.23 through 5.29 show the Ku-band residual waveform data corresponding to the smaller bloom in region A. This bloom is smaller in amplitude and more constant in magnitude than the second larger bloom in the region. The RWD waveforms in this case appear more noisy, having more spikes than previous RWD data. These spikes could be caused by a less dense group of slick areas, thus explaining the smaller overall radar cross section of the bloom. It should be noted that the RWD values in these plots are very small. Again, the tails of some of the RWD waveforms seem to be raised.

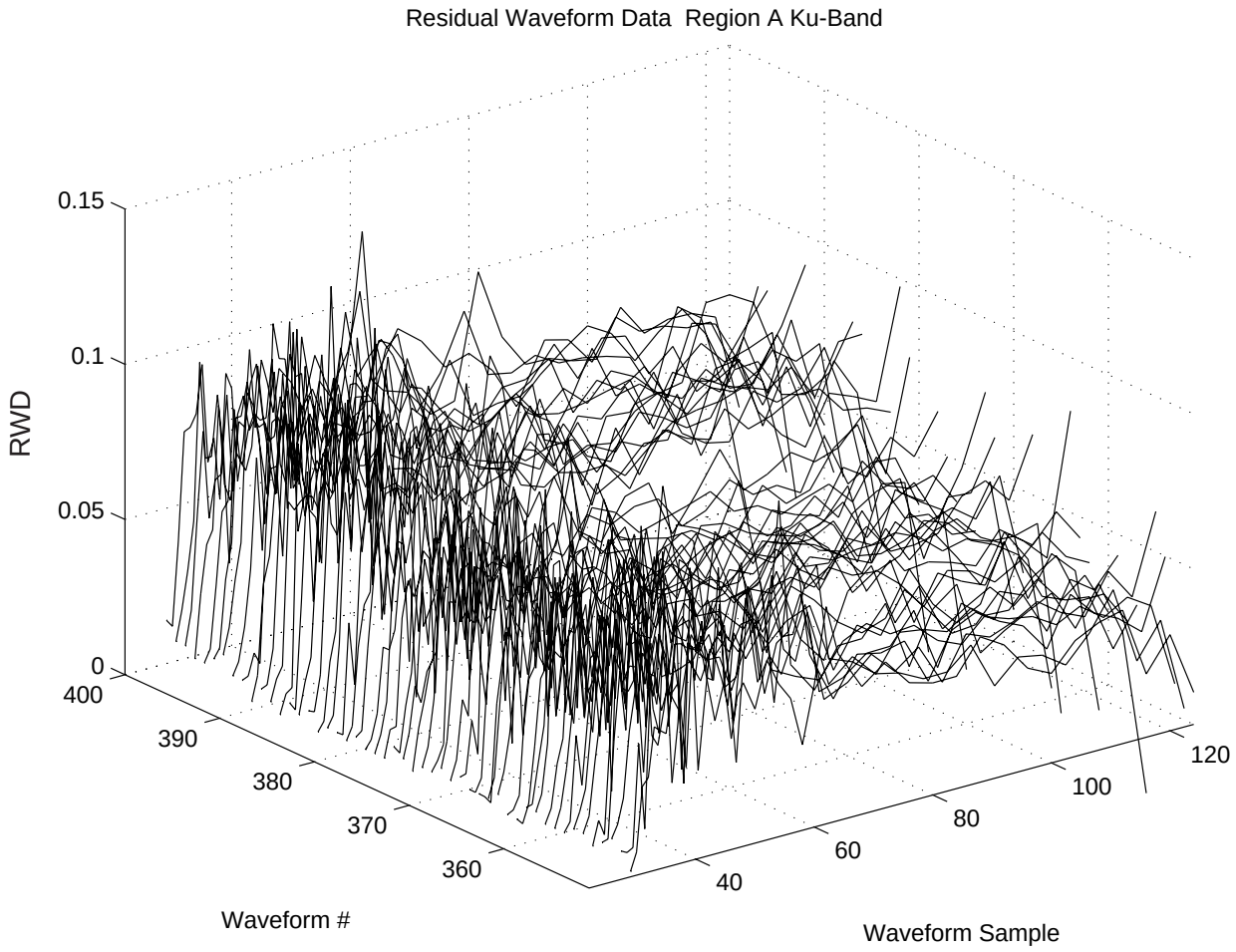

Figure 5.24. Ku-band residual waveform data from region A, first bloom (ii)

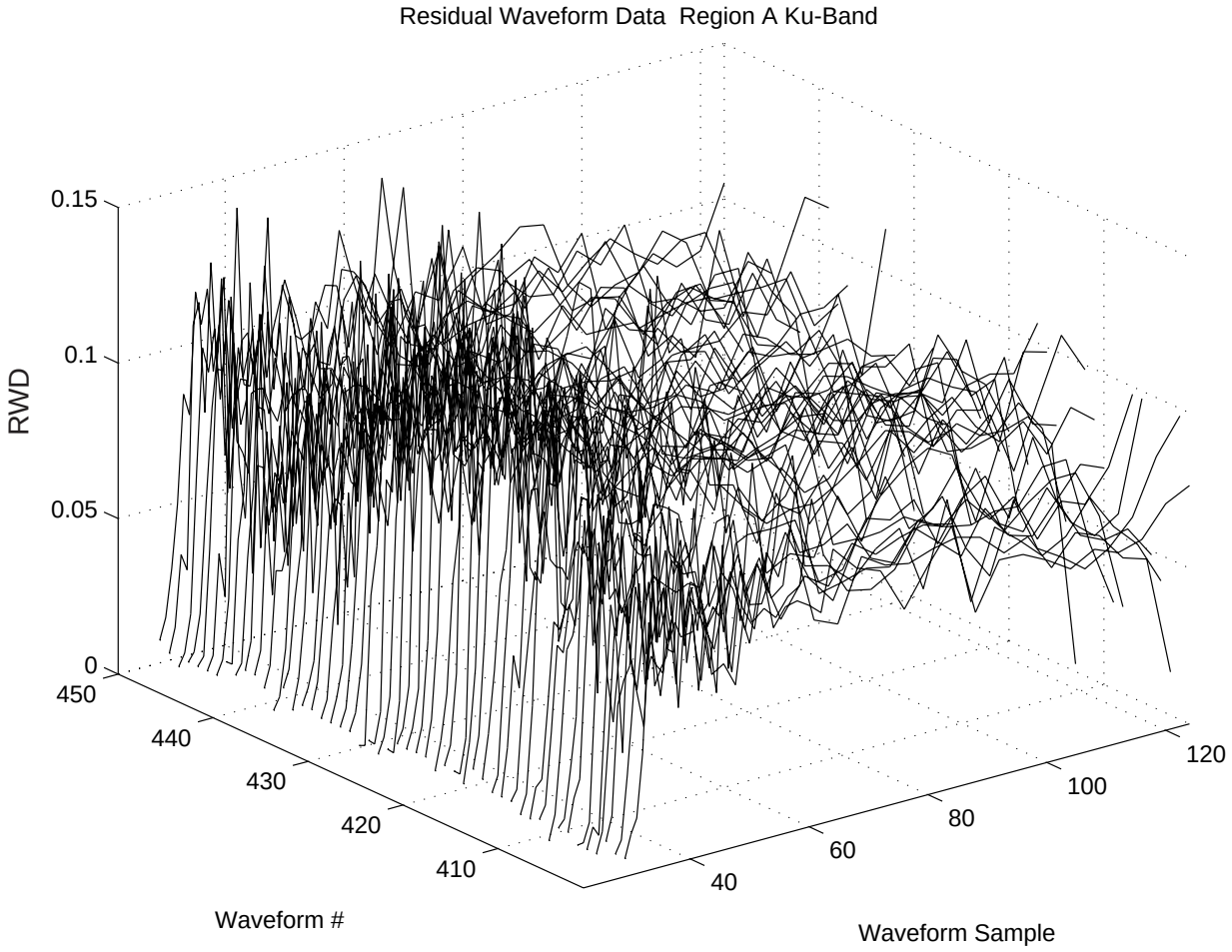

Figure 5.25. Ku-band residual waveform data from region A, first bloom (iii)

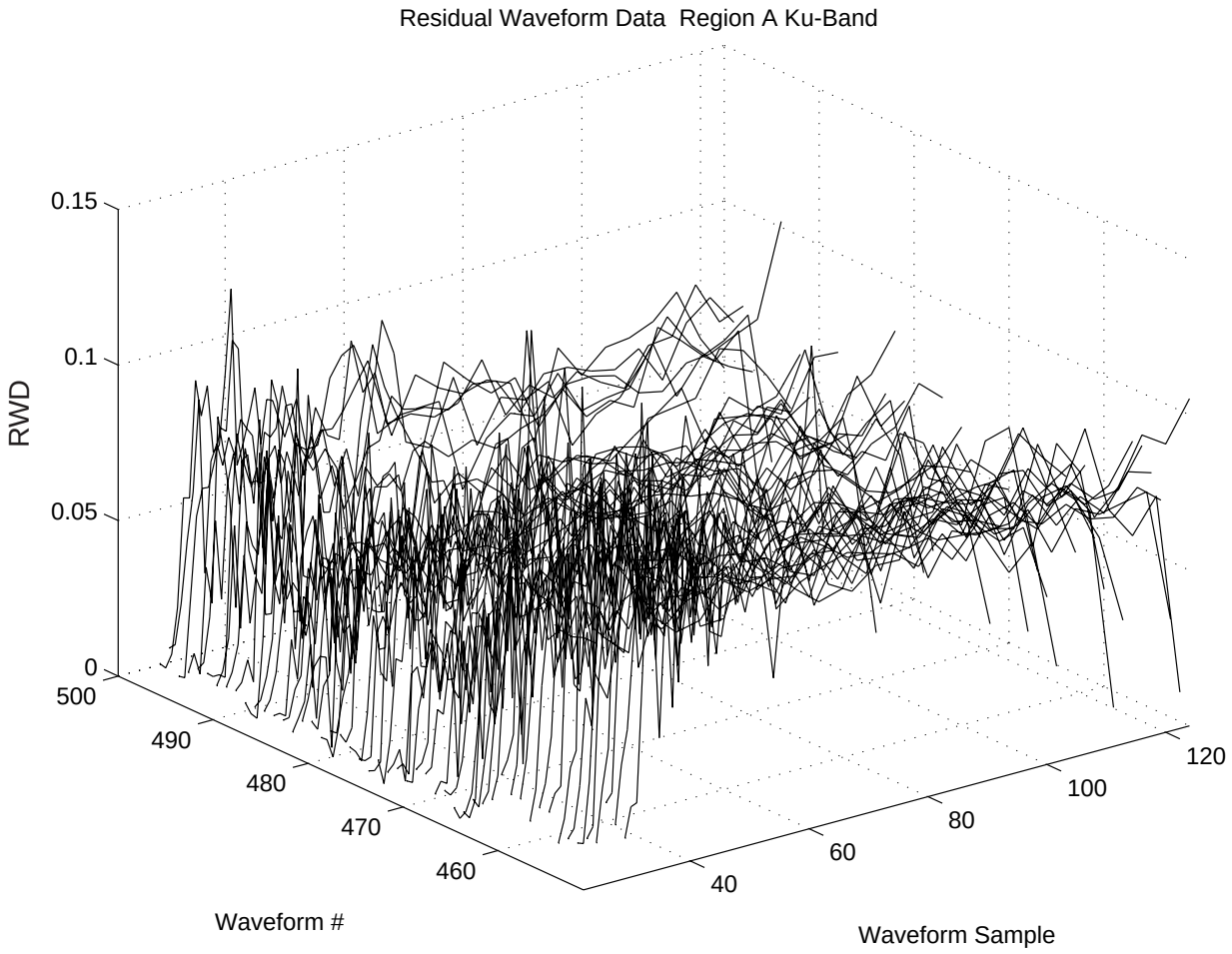

Figure 5.26. Ku-band residual waveform data from region A, first bloom (iv)

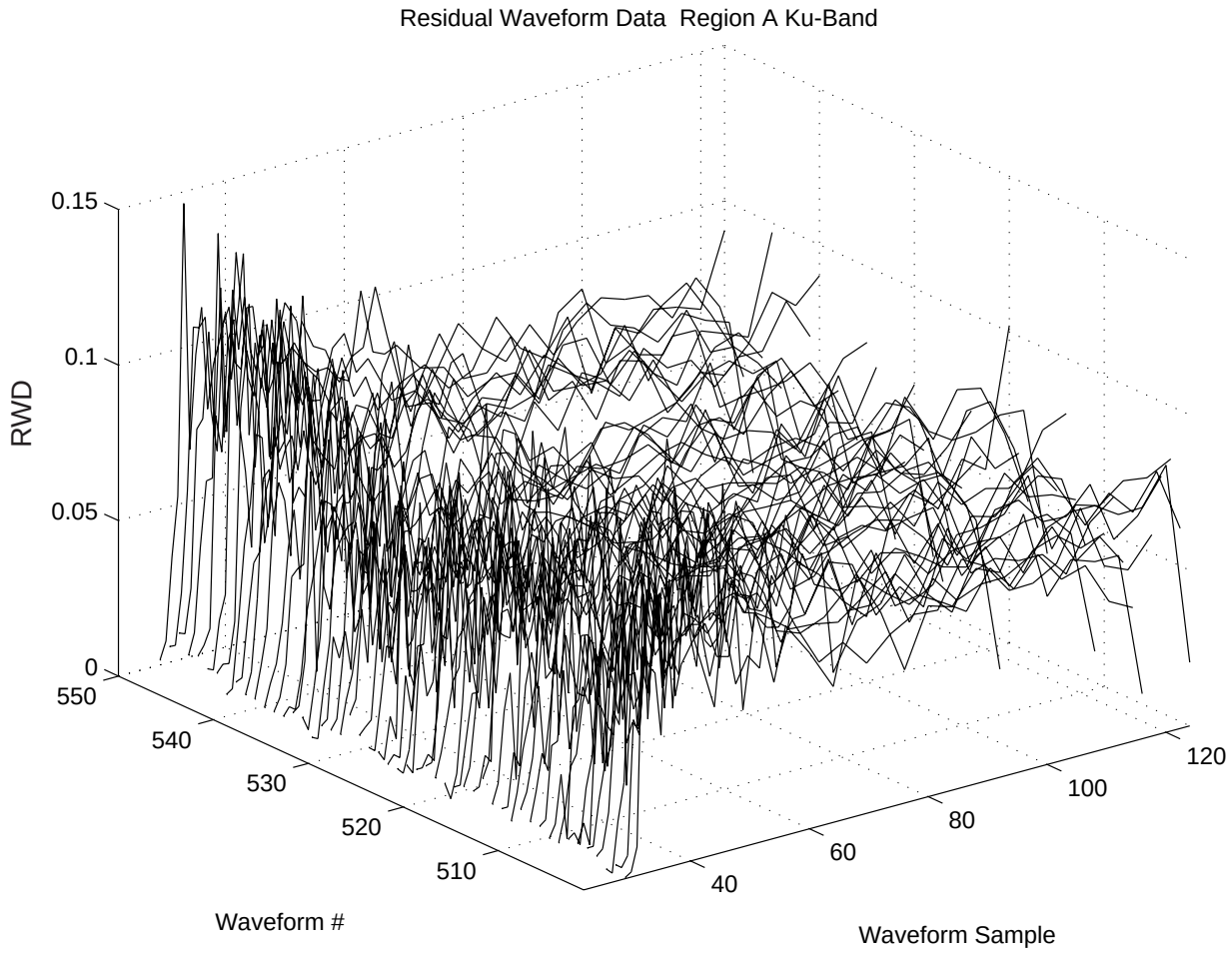

Figure 5.27. Ku-band residual waveform data from region A, first bloom (v)

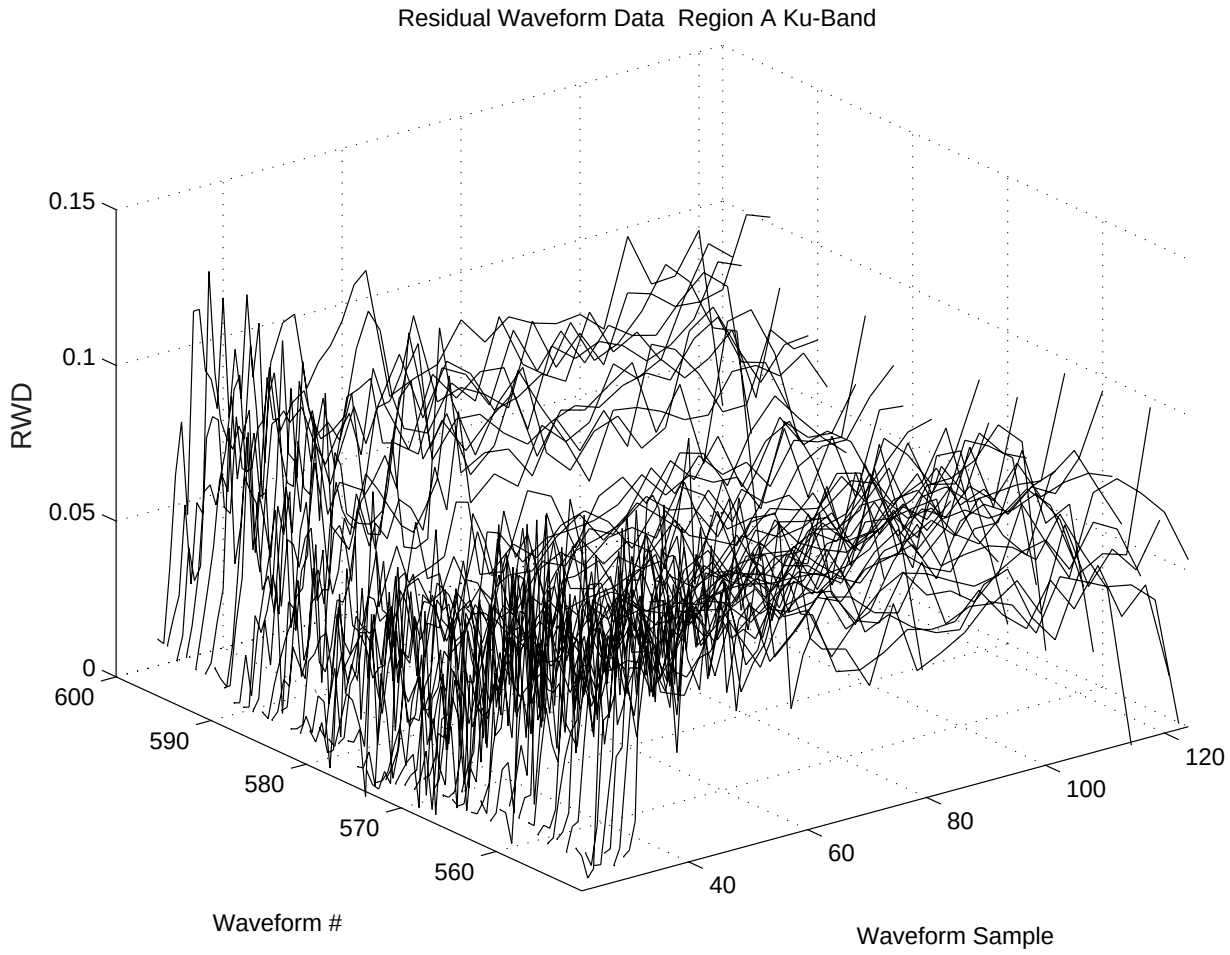

Figure 5.28. Ku-band residual waveform data from region A, first bloom (vi)

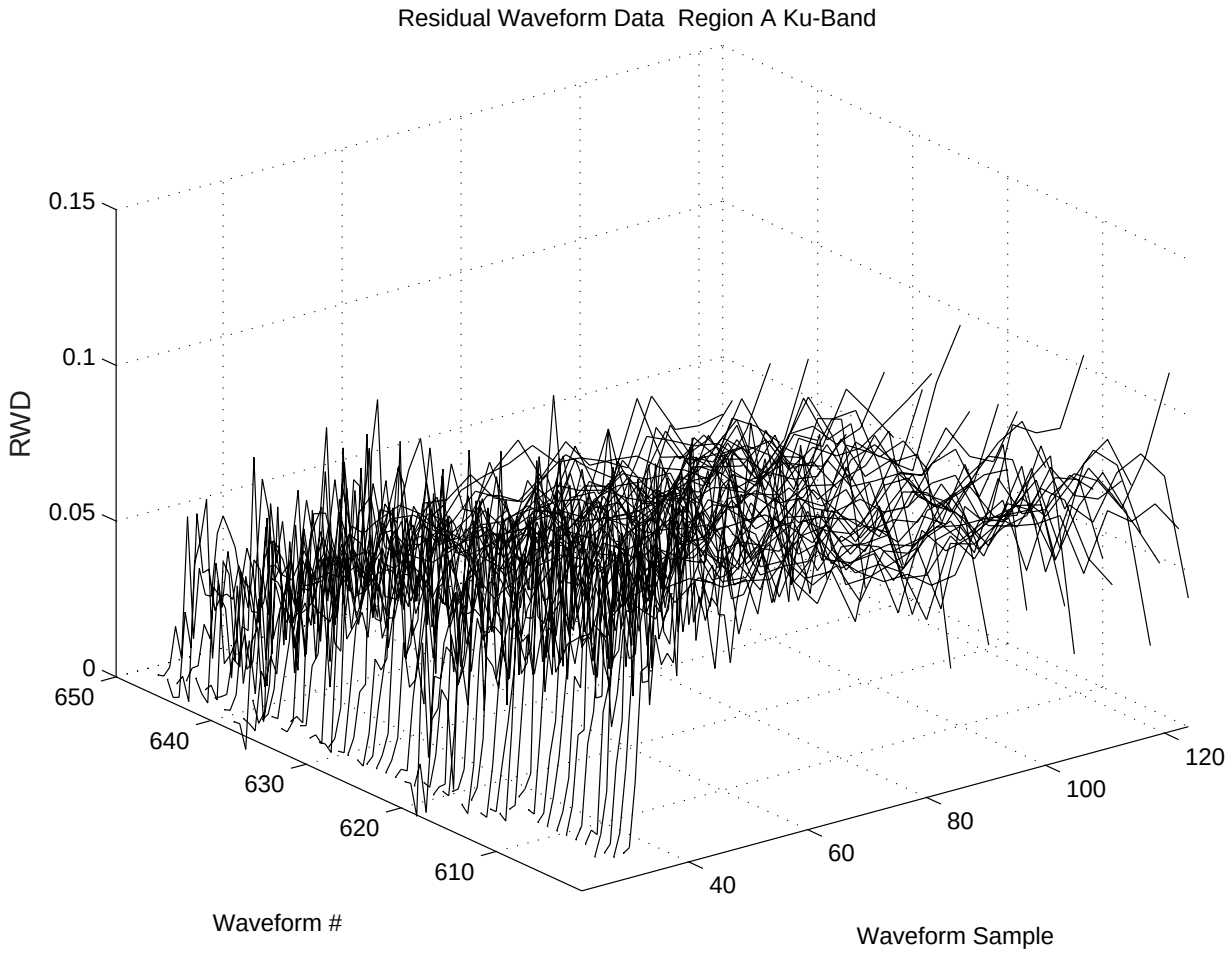

Figure 5.29. Ku-band residual waveform data from region A, first bloom (vii)

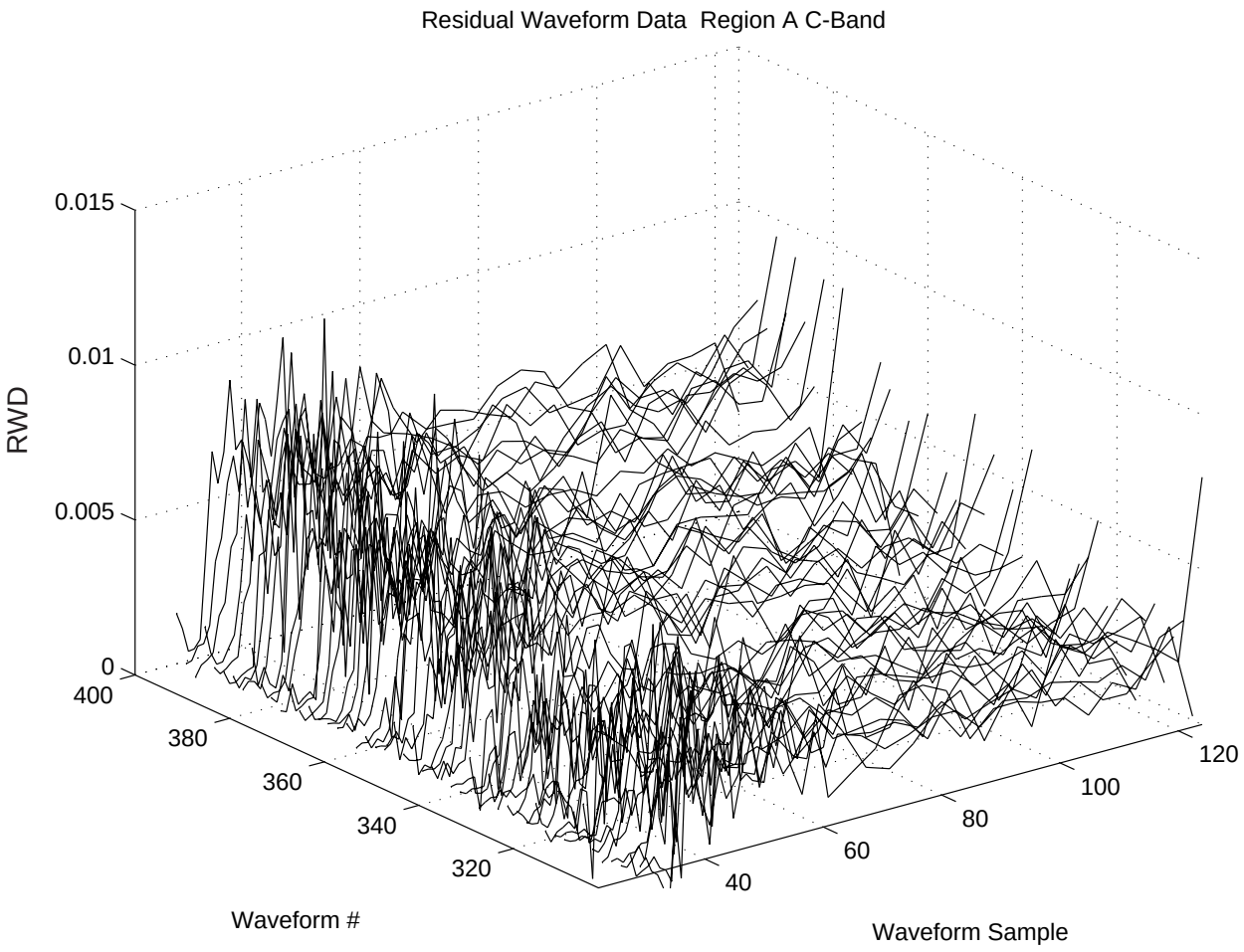

Figure 5.30. C-band residual waveform data from region A, first bloom (i)

Figures 5.30 through 5.33 show the C-band residual waveform data of the smaller bloom. Again, the RWD data appear noisier for this bloom than for the previous larger bloom (Figures 5.19 through 5.22). This increase in spikes could also be caused by less dense slick areas. In this case, the tails of the waveforms are raised in a much more noticeable way than in the previous sets of figures.

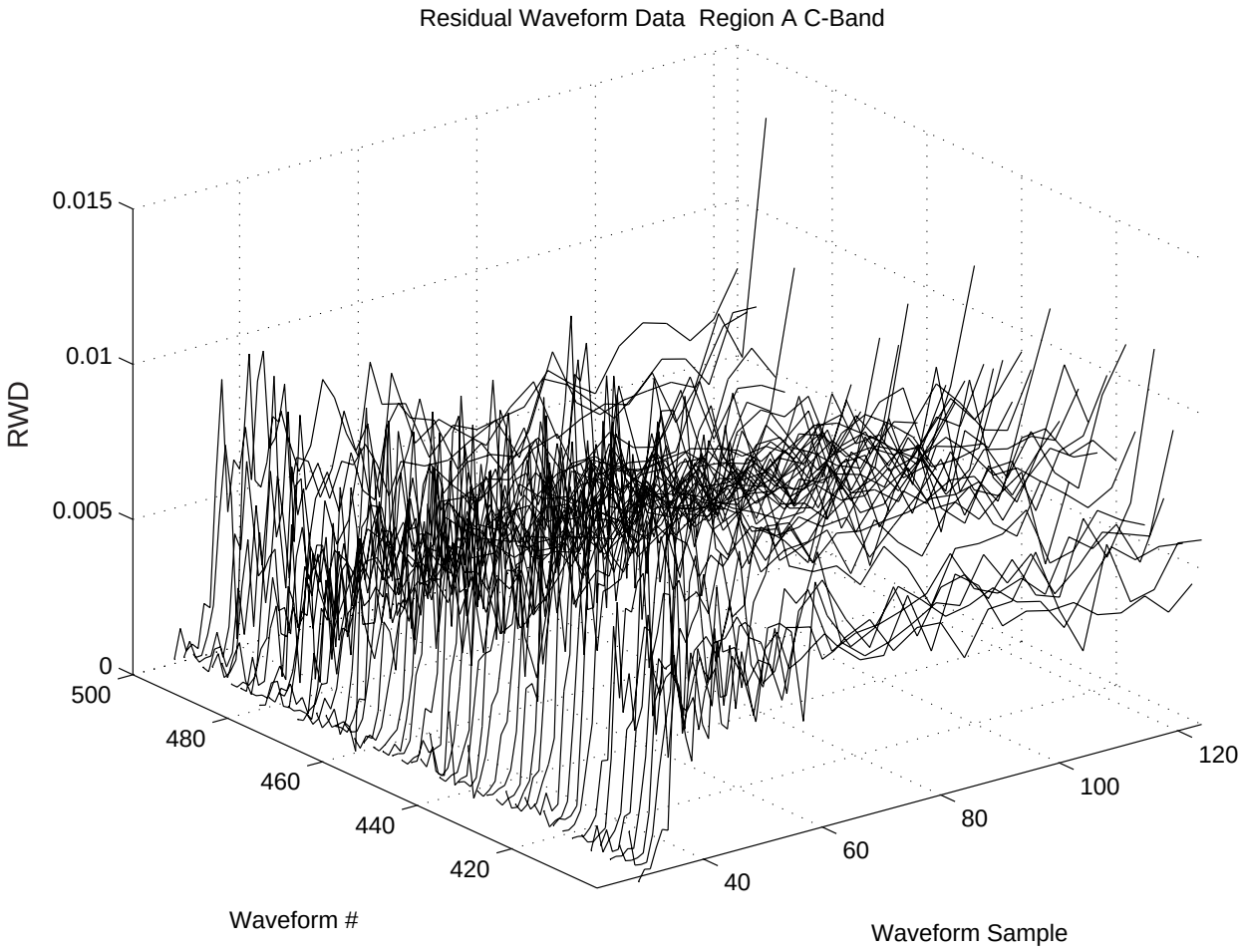

Figure 5.31. C-band residual waveform data from region A, first bloom (ii)

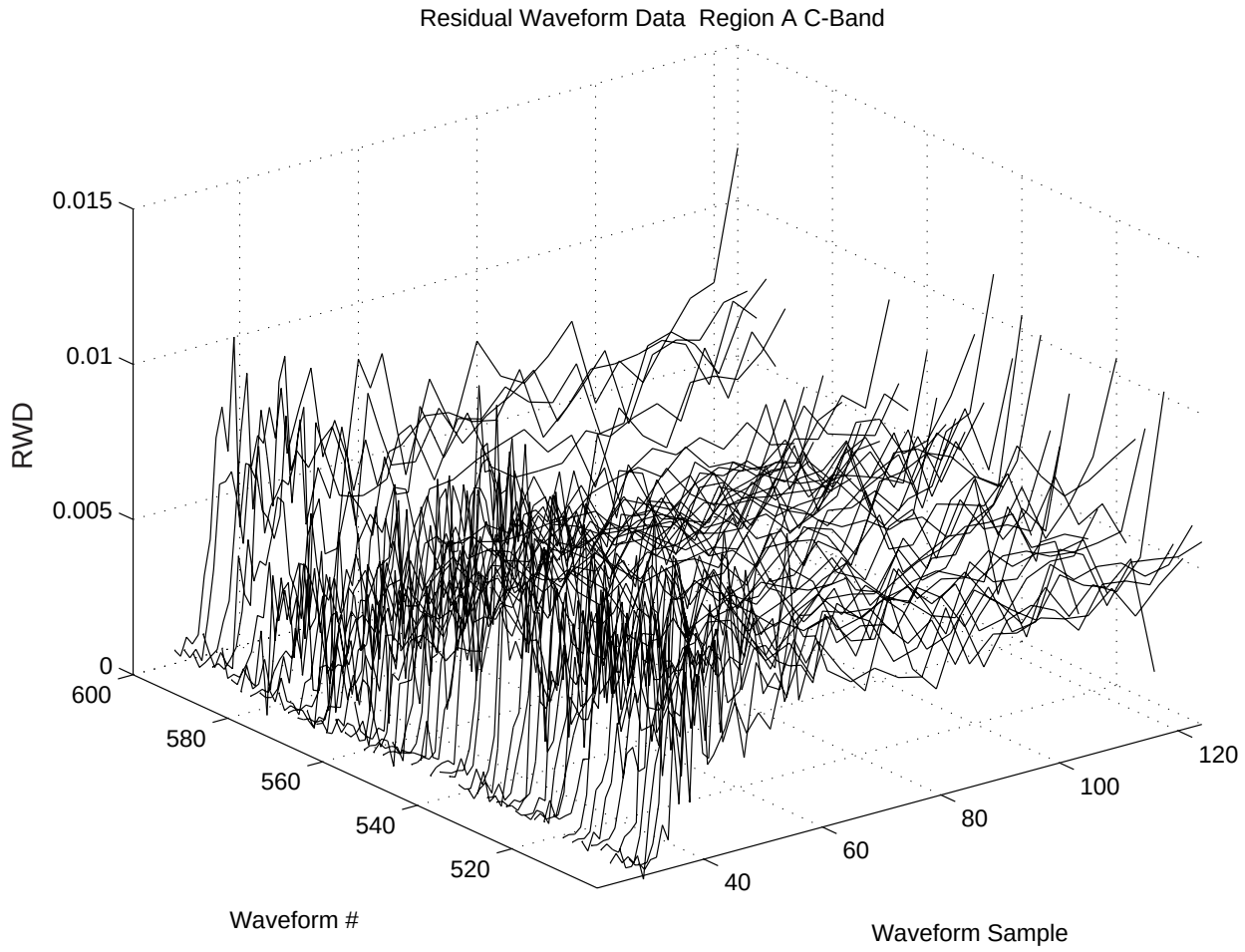

Figure 5.32. C-band residual waveform data from region A, first bloom (iii)

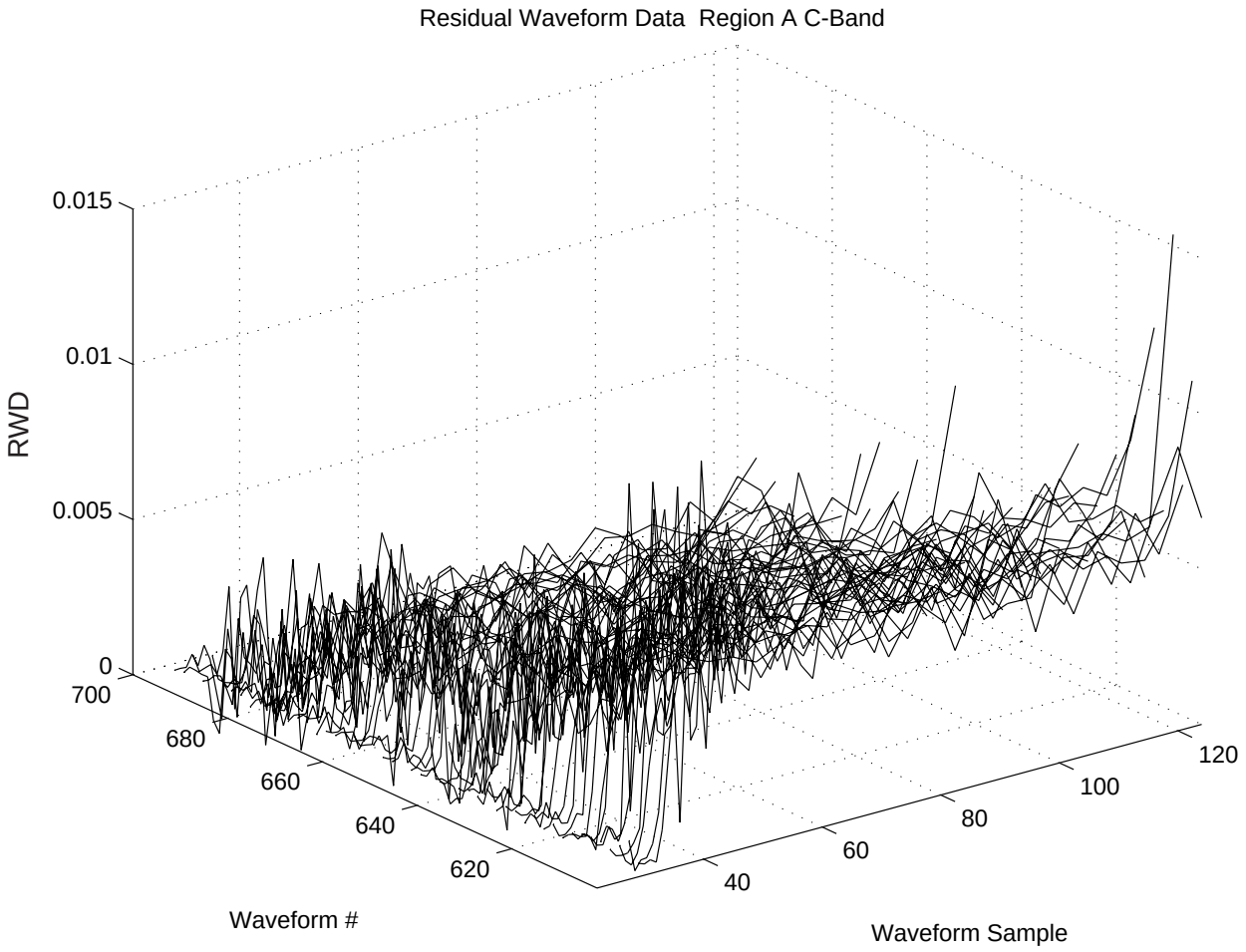

Figure 5.33. C-band residual waveform data from region A, first bloom (iv)

5.3.2 Region B

We found the mean SWH for region B to be 2.08 m and 2.203 m for Ku- and C-band respectively, and the mean off-nadir angle, ξ, to be 0.03^o. Figure 5.34 shows the mean radar cross section, σ^o, corresponding to region B for both Ku- and C-band. Contaminated data are marked by a red asterisk and bloom lower limits are marked with a green line.
Due to the high volume of contaminated data in this region no attemp was made to fit our model to the data because we do not fully understand the source of the contamination label and if the contamination is due to the blooms.

5.3.3 Region C

We found the mean SWH for region C to be 3.029 m and 3.139 m for Ku- and C-band, respectively, and the mean off-nadir angle, ξ, to be 0.073^o. Figure 5.35 shows the mean radar cross section, σ^o, corresponding to region C for both Ku- and C-band. Contaminated data are marked by a red asterisk, and bloom lower limits are marked with a green line. For both frequencies we see three blooms of decreasing magnitude. The first is contaminated, and hence we will not study it. The second bloom occurs between waveforms 2750 and 3050. The third occurs between waveforms 3400 and 3850. Data for both frequencies is contaminated around GDR samples 184, 218 to 221, 240, 293, 295 to 296, 299 to 301, and 371 to 376. These samples correspond approximately to waveform numbers 1826 to 1835, 2166 to 2205, 2386 to 2395, 2916 to 2925, 2936 to 2956, 2976 to 3005, and 3696 to 3755. Figure 5.36 shows the off-nadir angle for region C. As in region A, most of the out of range angles (2.55 degrees) correspond to contaminated data.

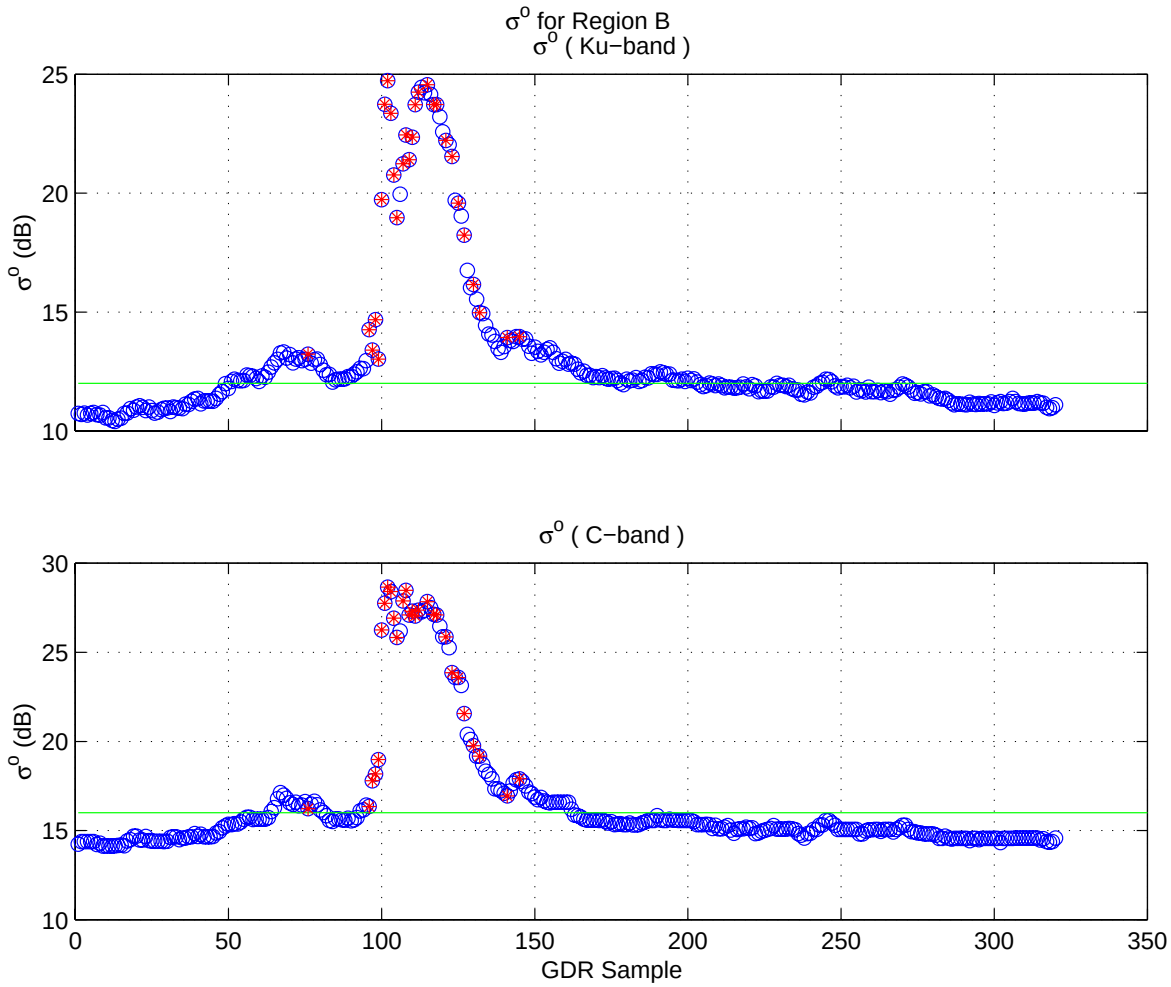

Figure 5.34. Ku- and C-band σ^o for region B

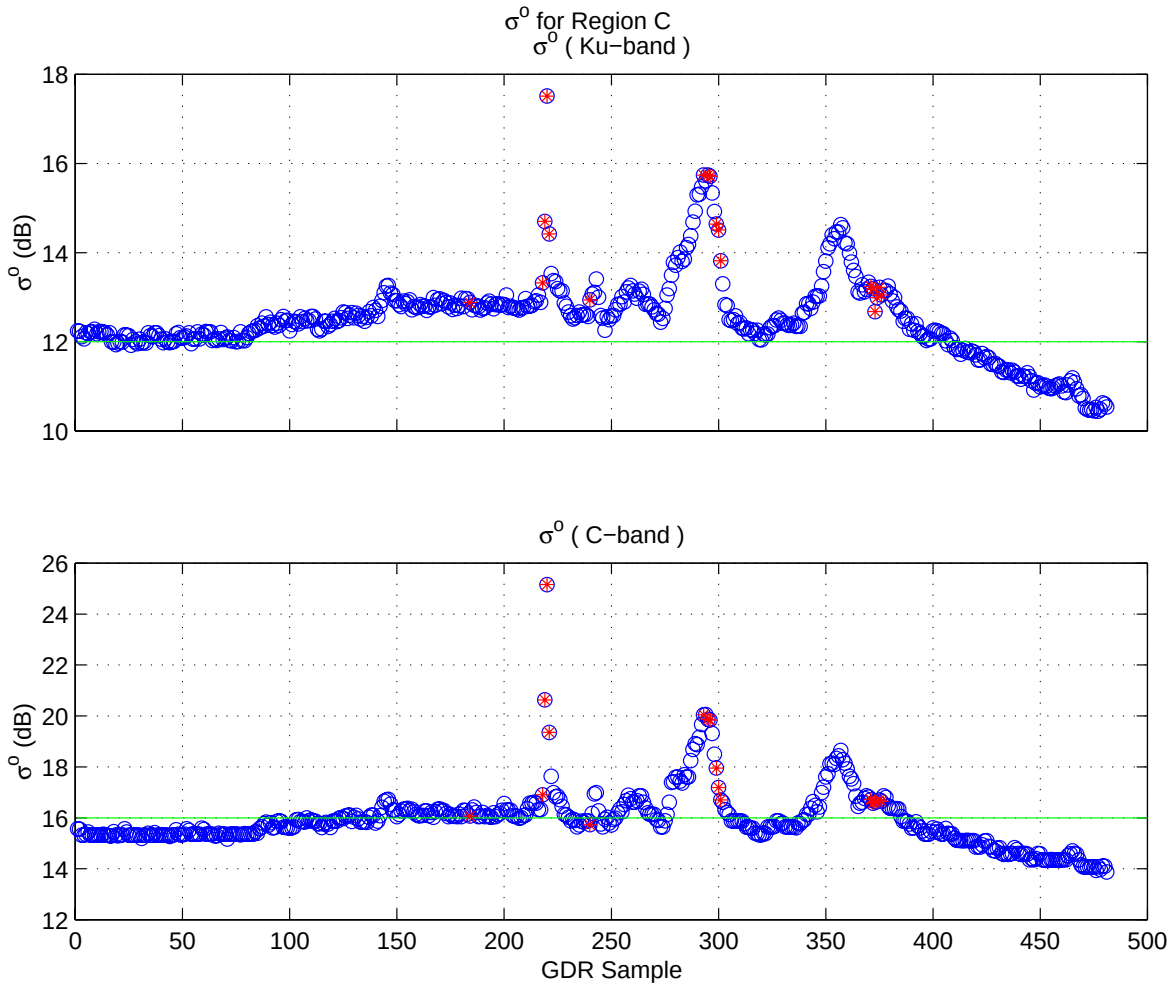

Figure 5.35. Ku- and C-band σ^o for region C

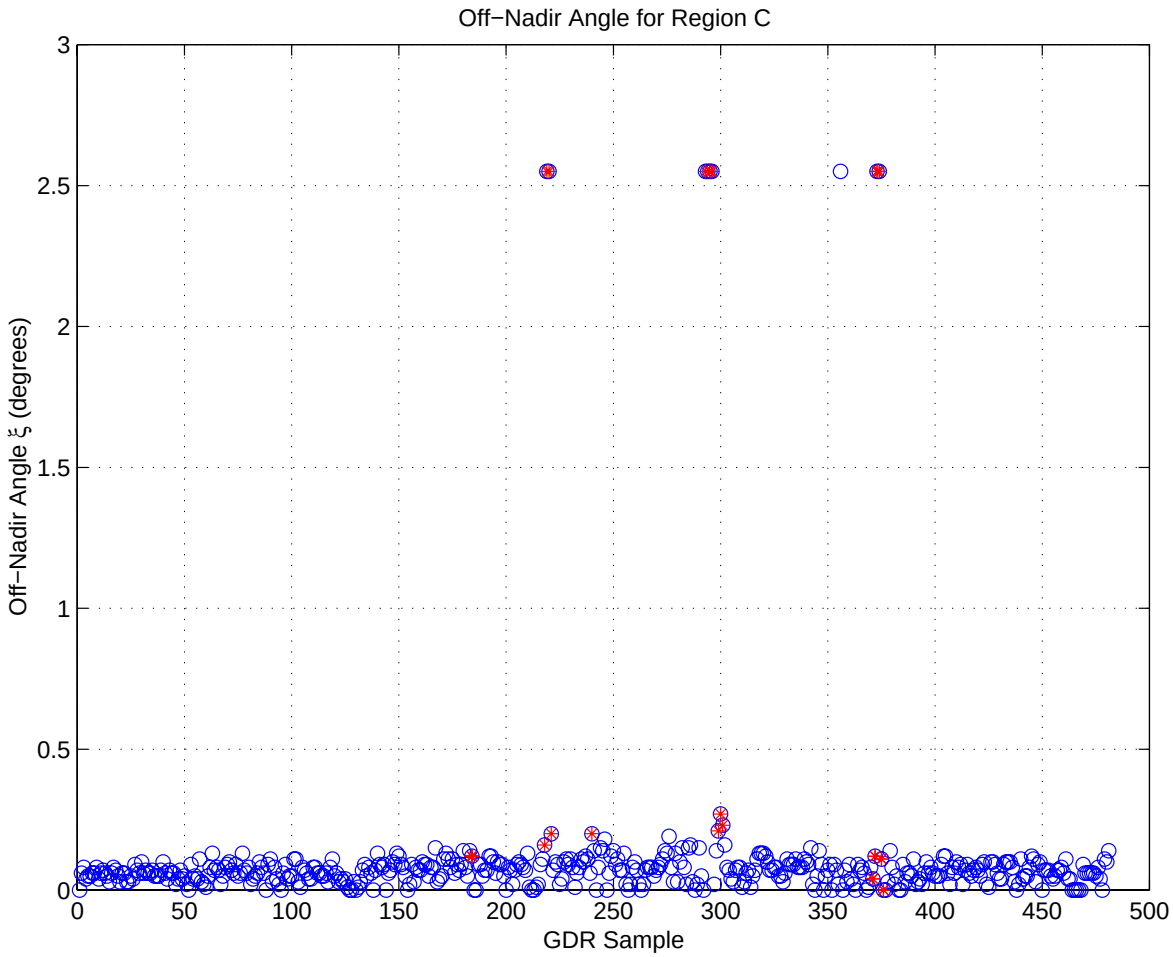

Figure 5.36. Off-Nadir angle ξ for region C

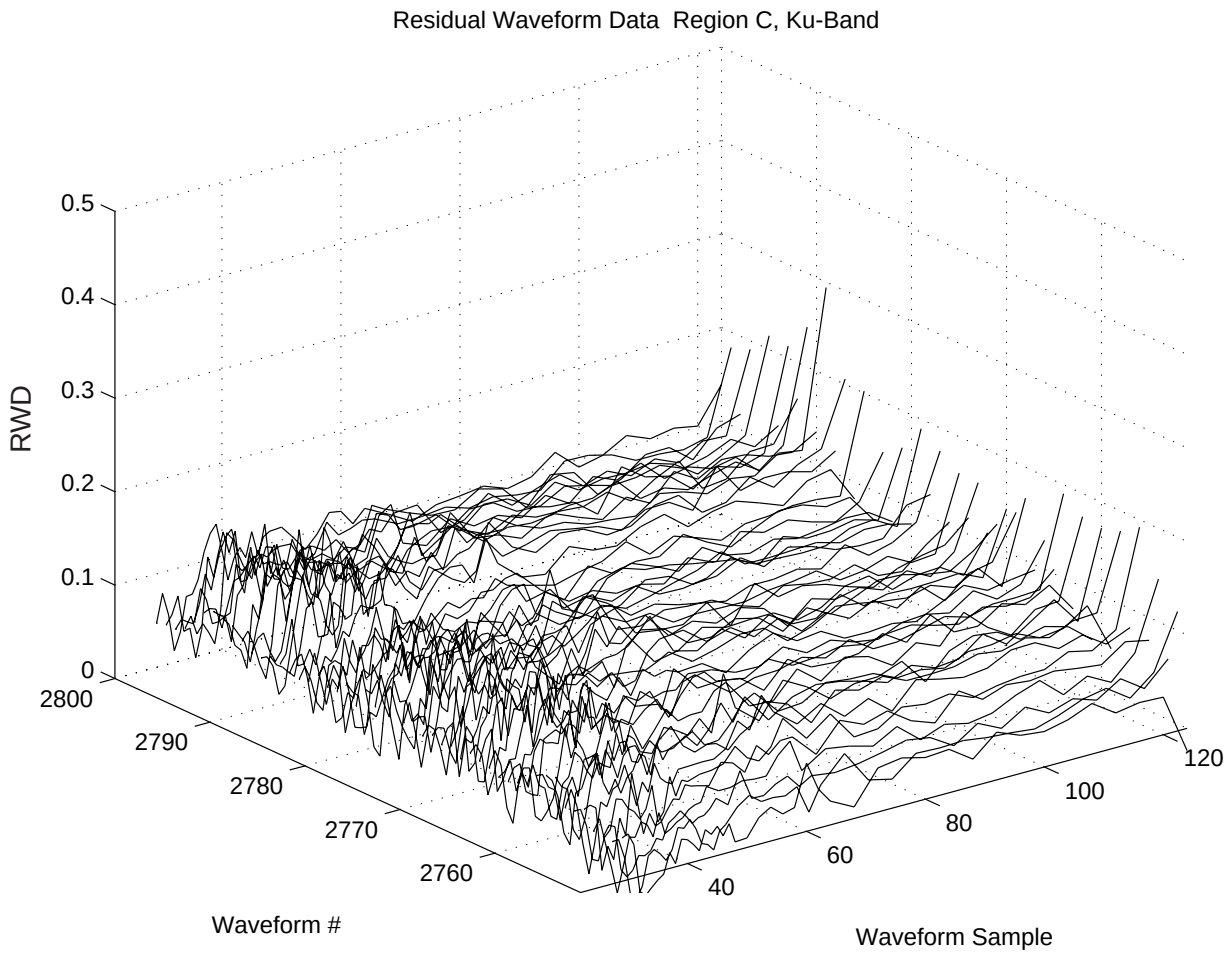

Figure 5.37. Ku-band residual waveform data from region C, second bloom (i)

Figures 5.37 through 5.42 show the Ku-band residual waveform data corresponding to the second bloom in region C. The bloom is clearly defined and the RWD waveforms appear flat and uniform with the exception of a slightly jagged rising edge and very obvious raised tails. The jaggedness in the rising edge of the RWD waveforms can be attributed to tracker movement which we have not accounted for in our simulation. However, the raising of the waveform tails is still unaccounted for.

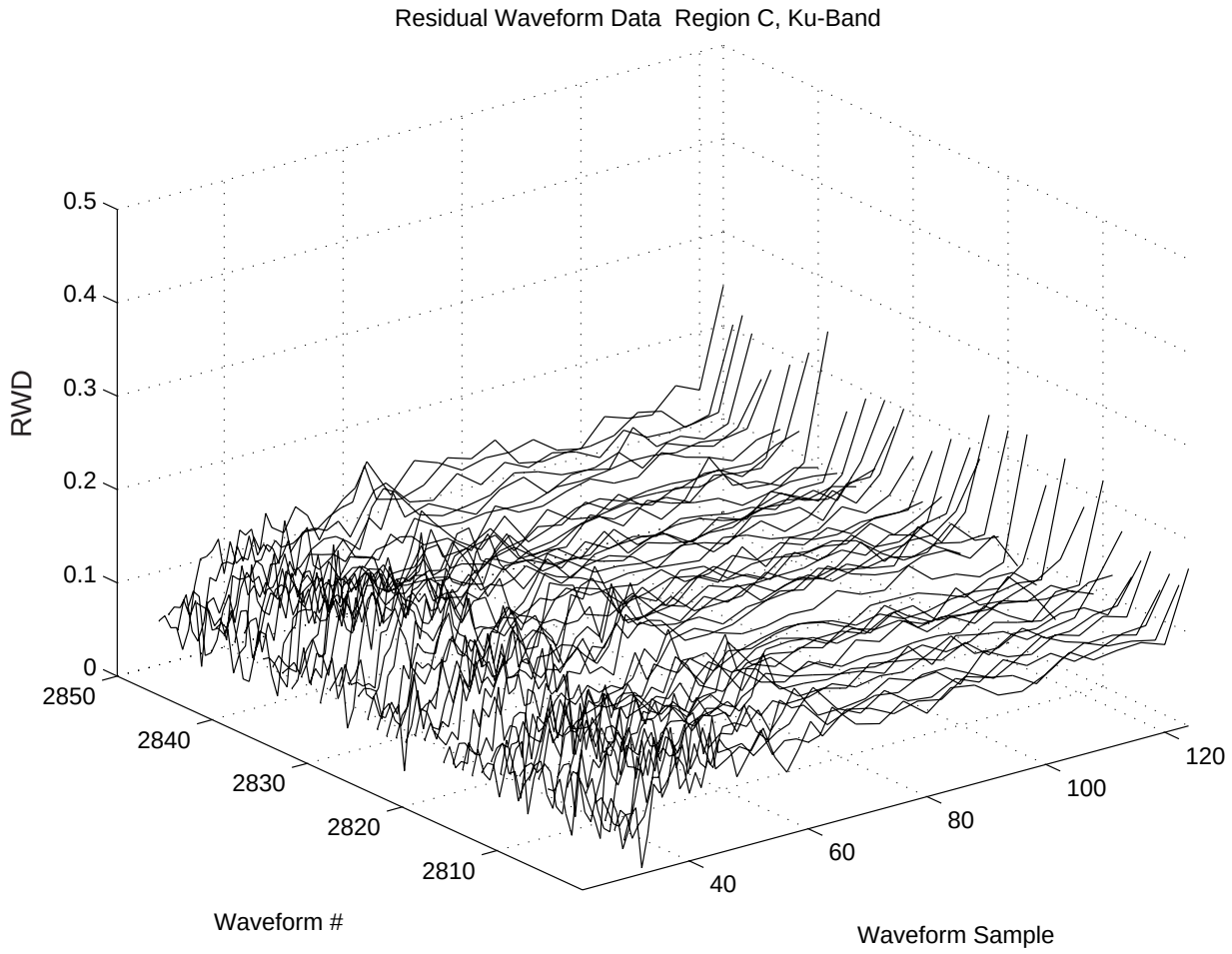

Figure 5.38. Ku-band residual waveform data from region C, second bloom (ii)

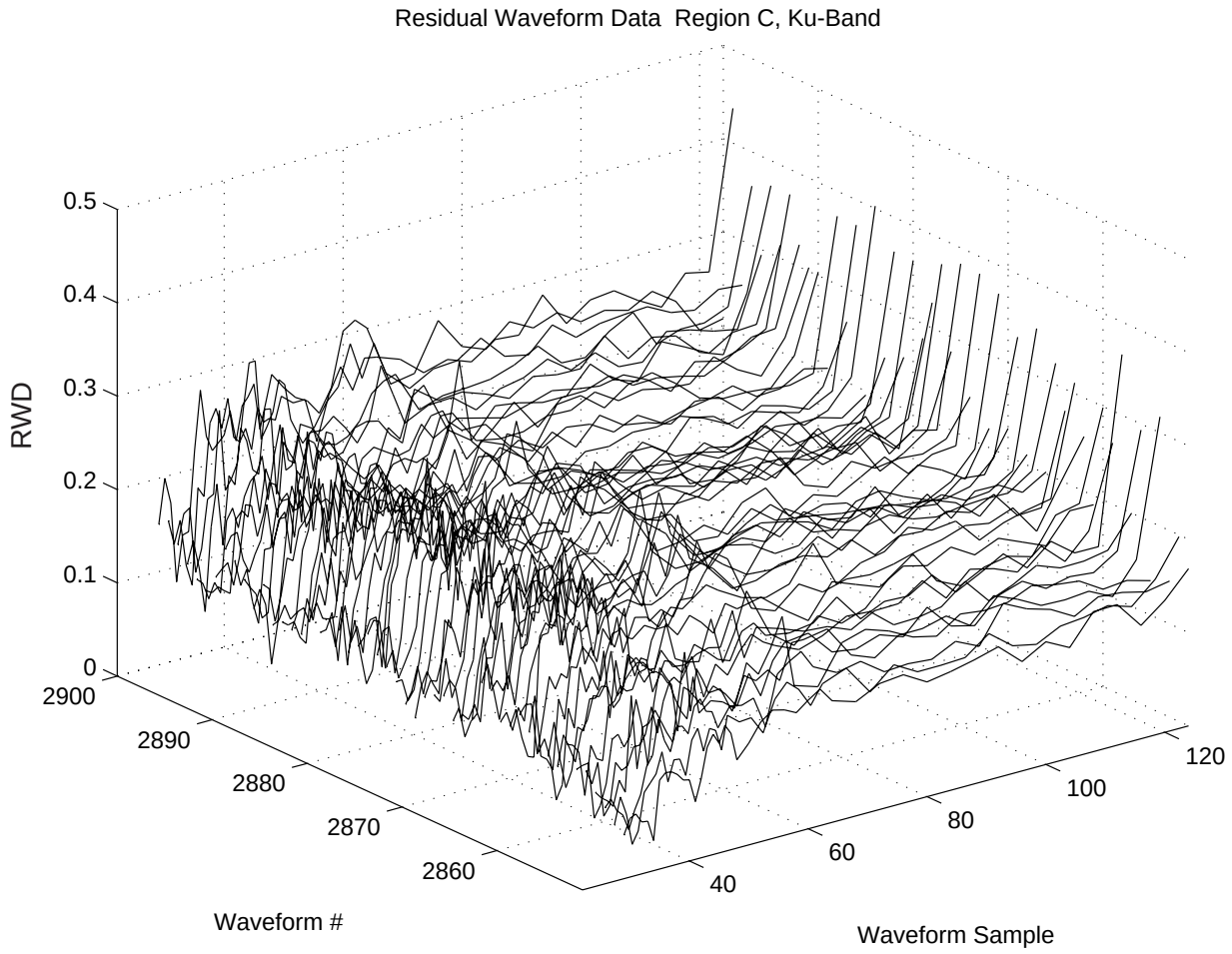

Figure 5.39. Ku-band residual waveform data from region C, second bloom (iii)

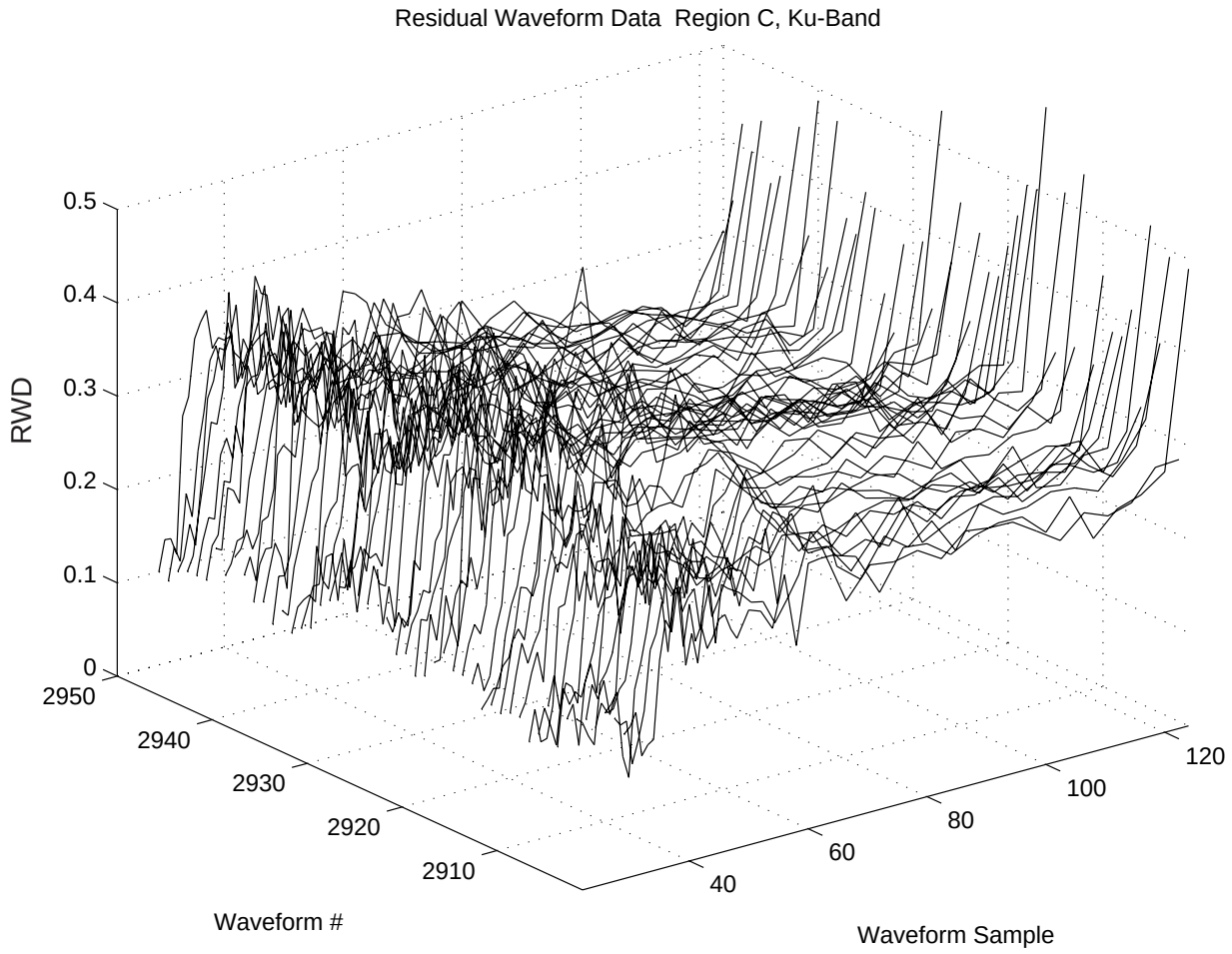

Figure 5.40. Ku-band residual waveform data from region C, second bloom (iv)

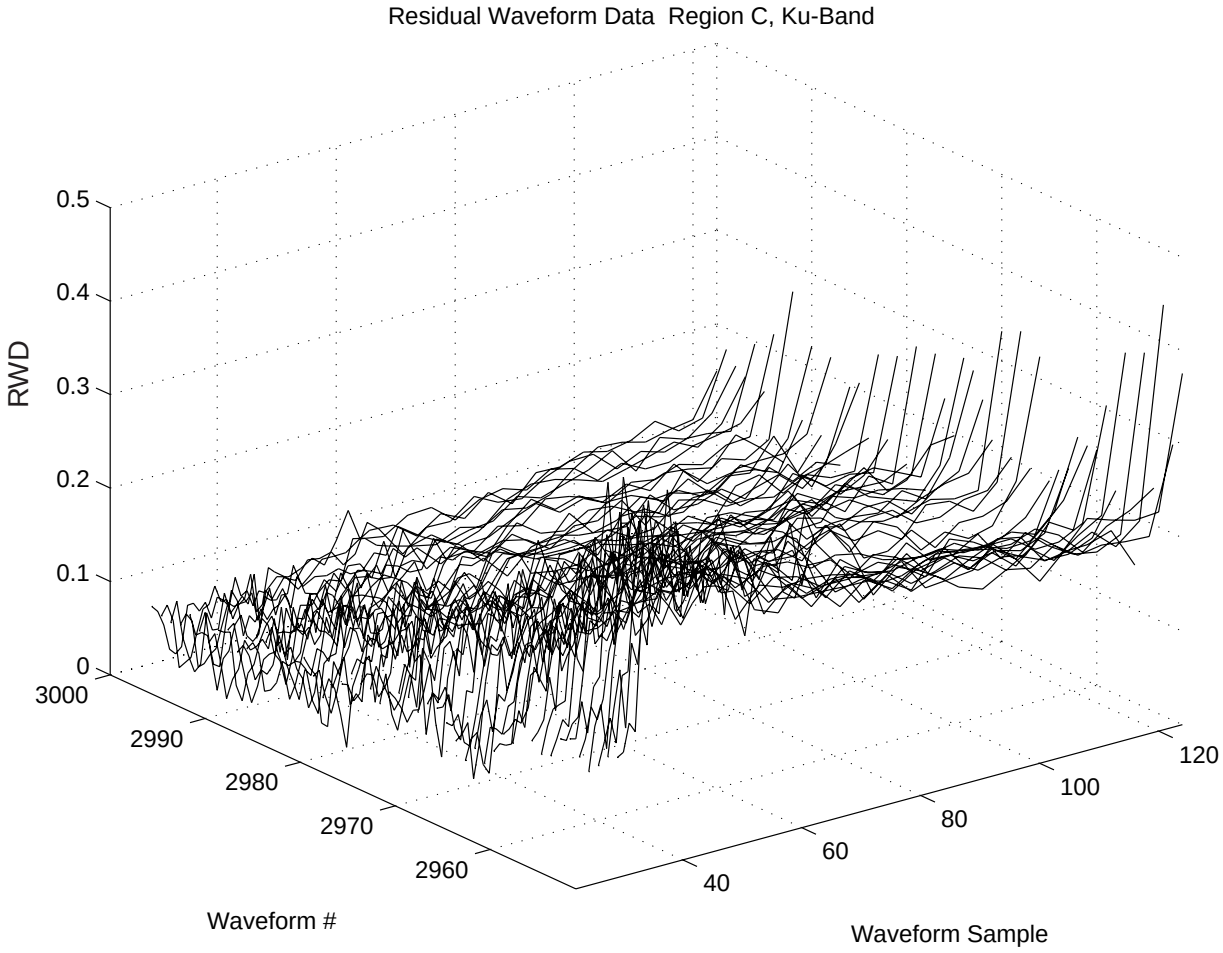

Figure 5.41. Ku-band residual waveform data from region C, second bloom (v)

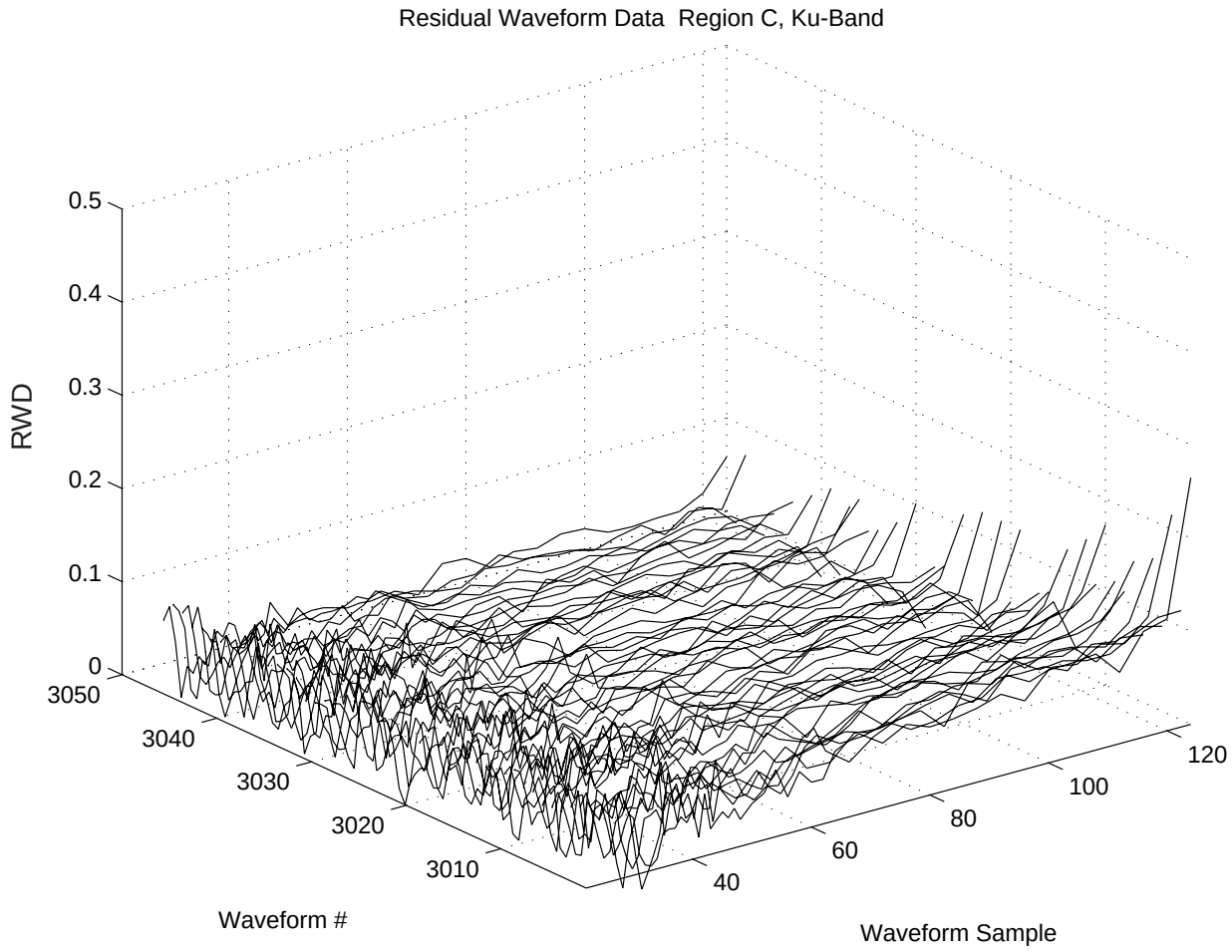

Figure 5.42. Ku-band residual waveform data from region C, second bloom (vi)

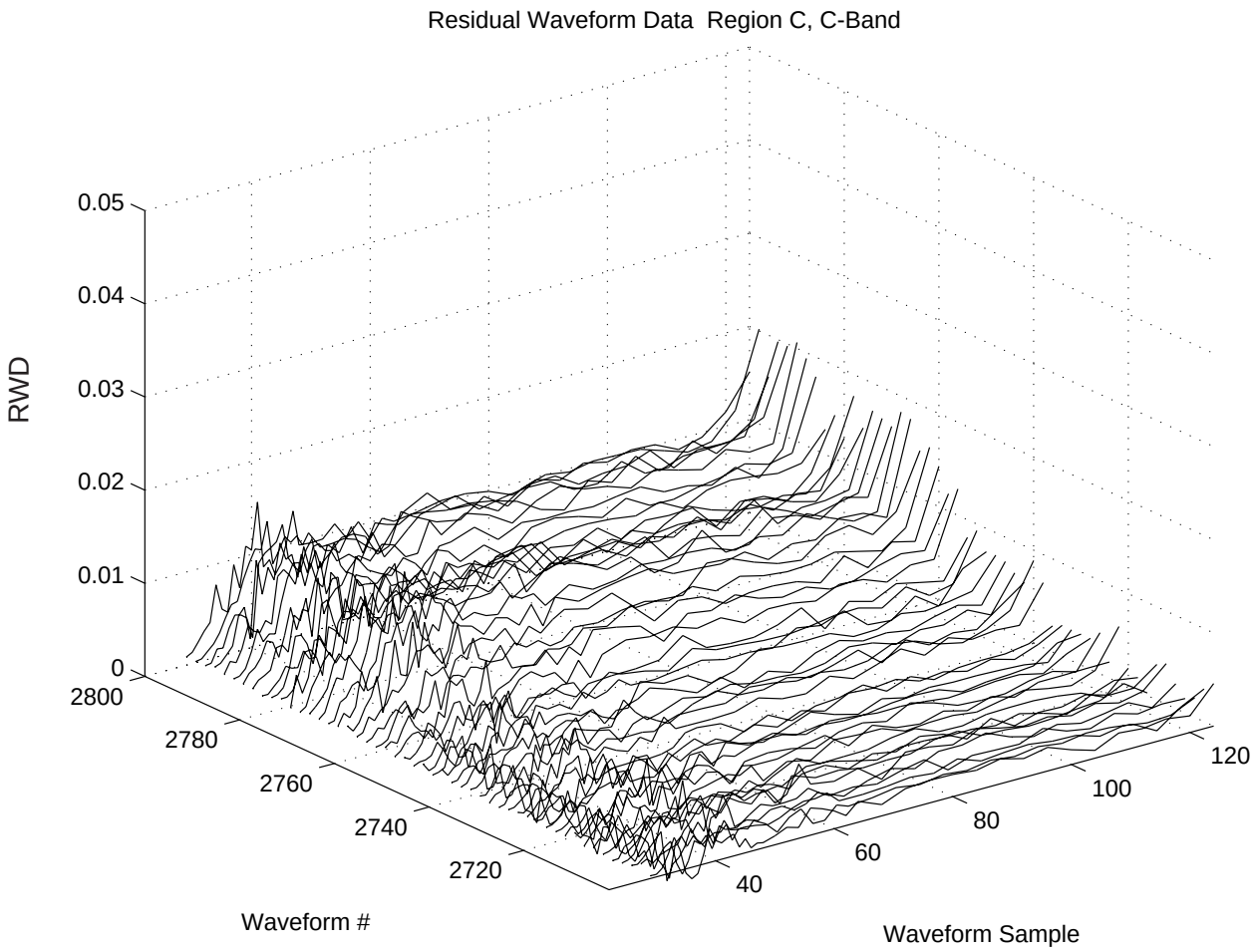

Figure 5.43. C-band residual waveform data from region C, second bloom (i)

Figures 5.43 through 5.46 show the C-band residual waveform data corresponding to the second bloom in region C. Again, the bloom is clearly defined and the RWD waveforms appear flat and uniform with the exceptions of a slightly jagged rising edge and very obvious raised tails.

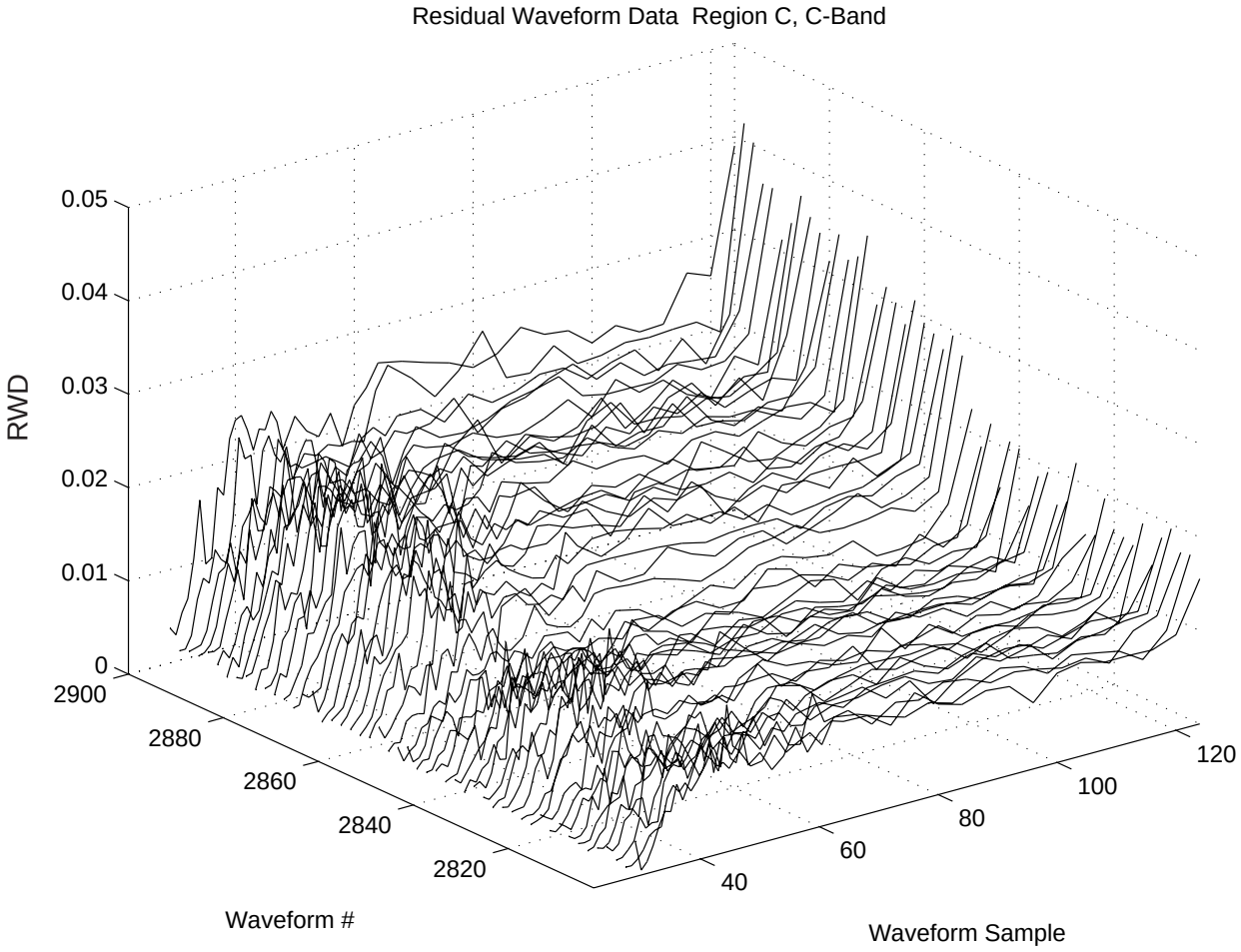

Figure 5.44. C-band residual waveform data from region C, second bloom (ii)

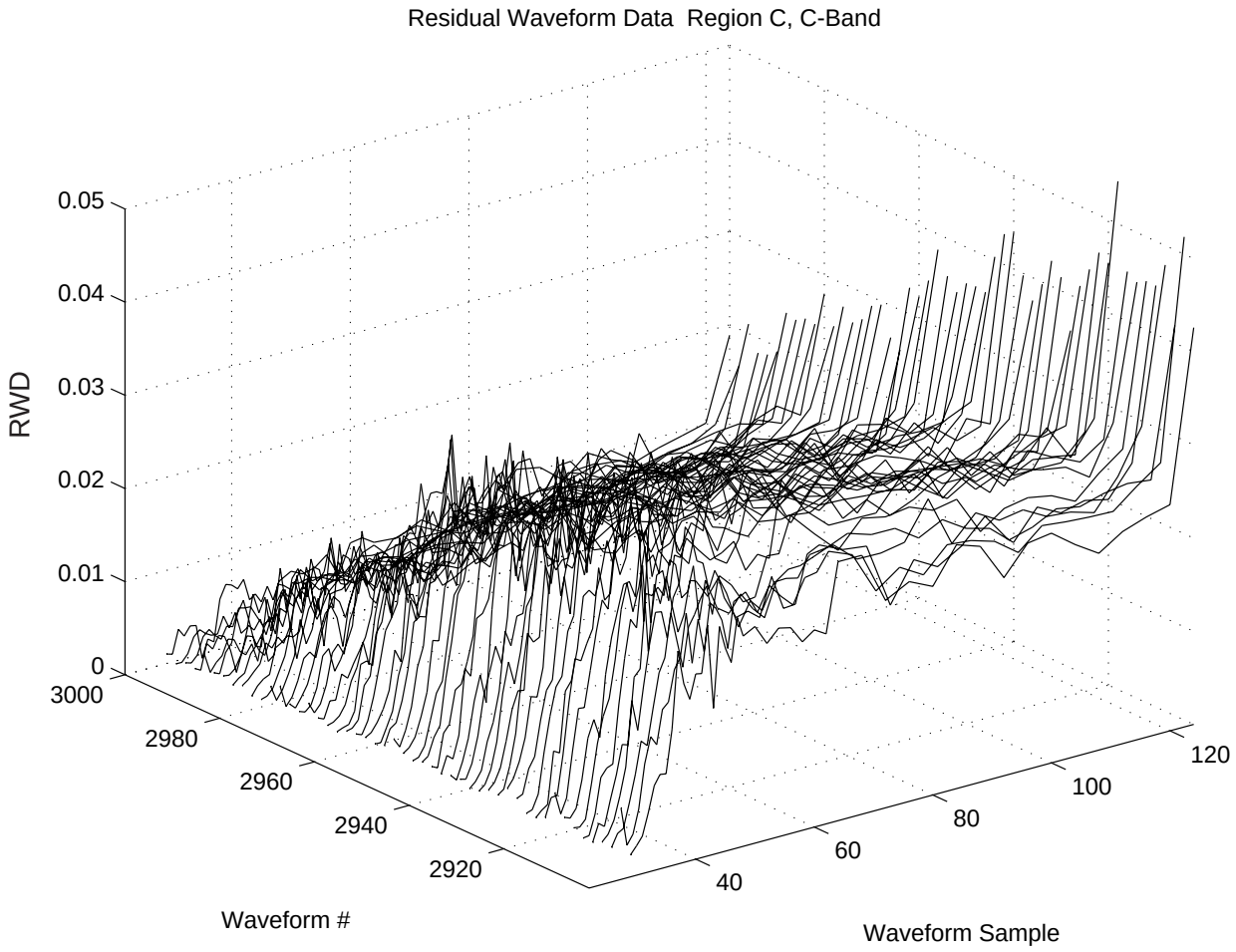

Figure 5.45. C-band residual waveform data from region C, second bloom (iii)

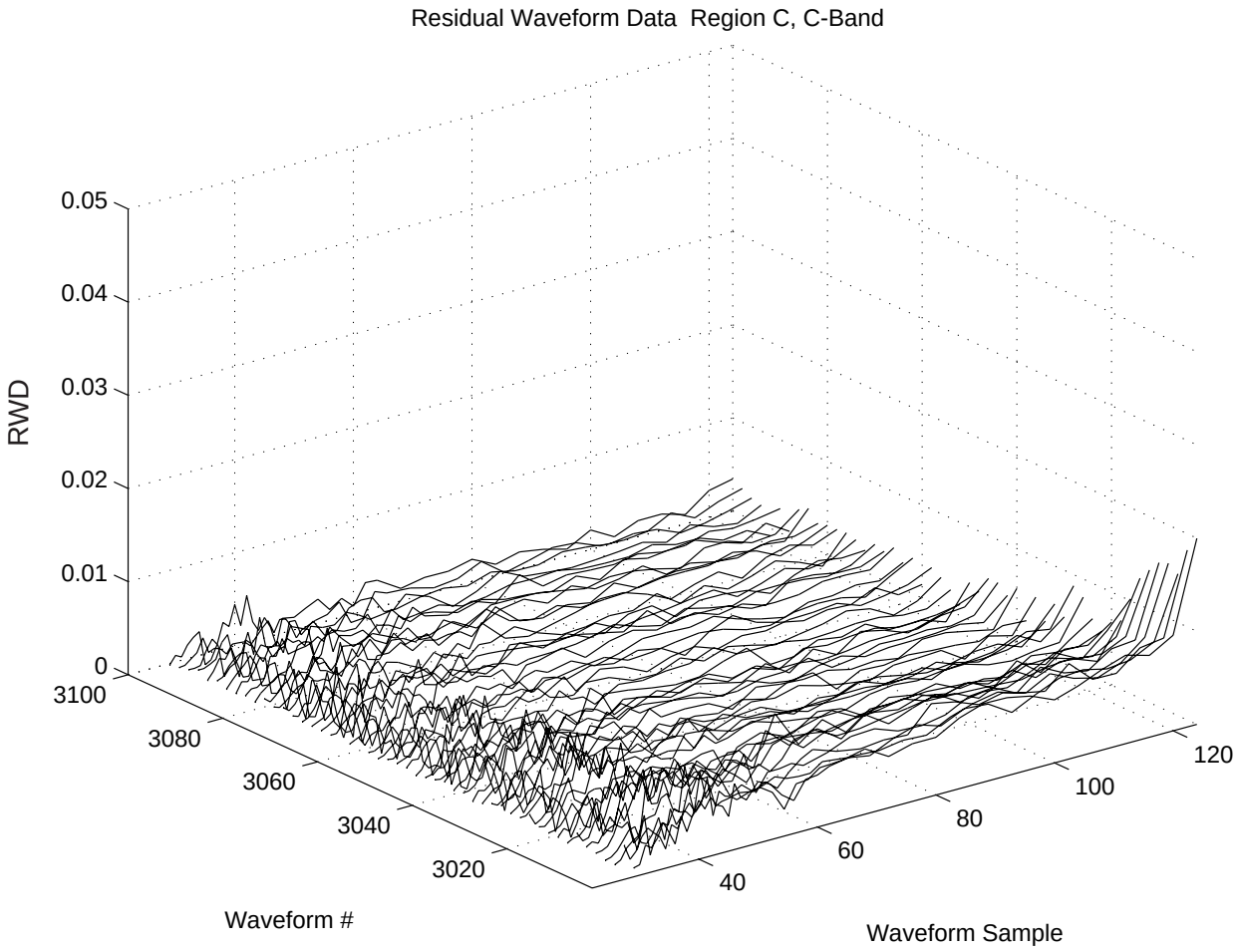

Figure 5.46. C-band residual waveform data from region C, second bloom (iv)

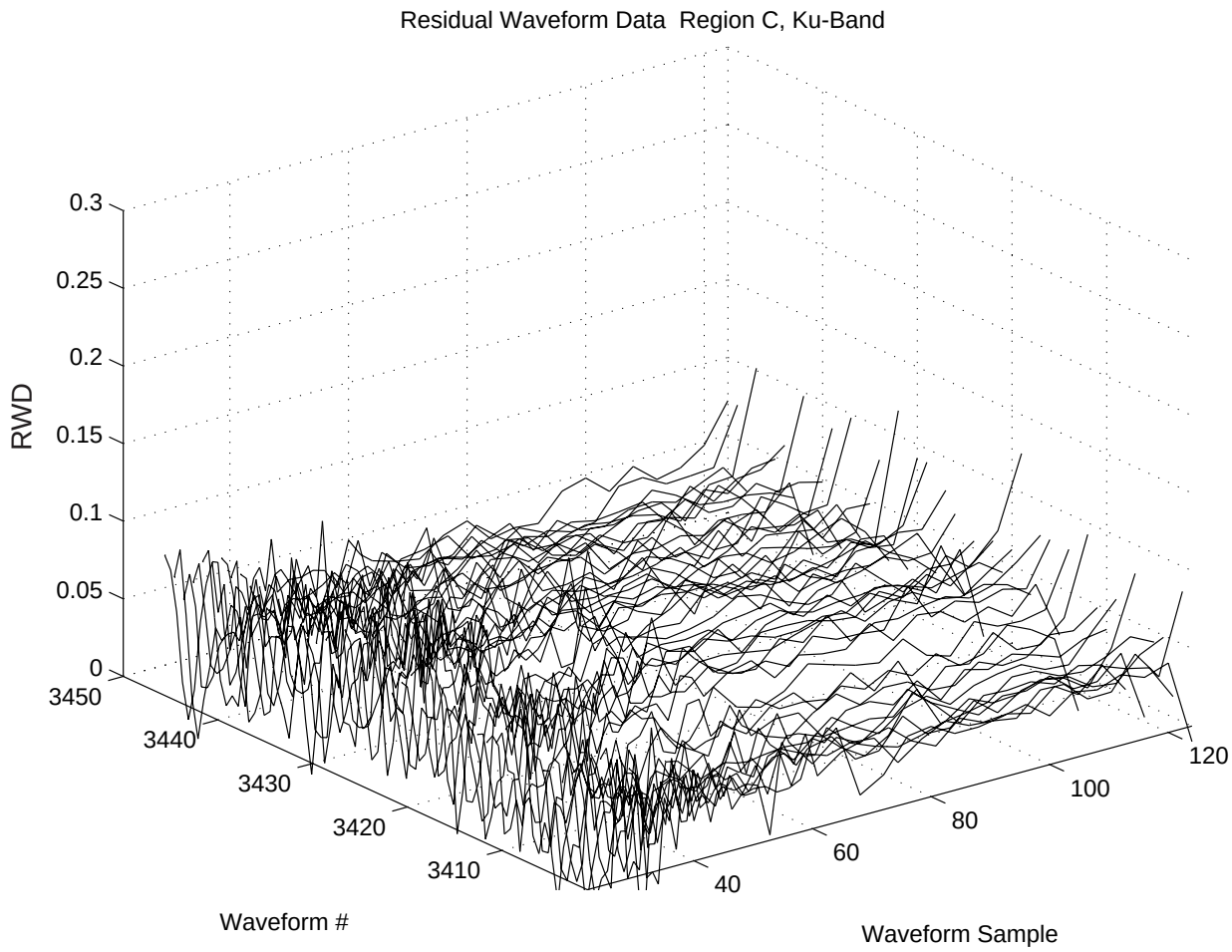

Figure 5.47. Ku-band residual waveform data from region C, third bloom (i)

Figures 5.47 through 5.55 show the Ku-band residual waveform data waveforms of the third and smallest bloom in region C. Again, the beginning part of the waveforms appears very noisy, and the tails of some waveforms are very raised. Note the low level of the RWD amplitude for this particular bloom.

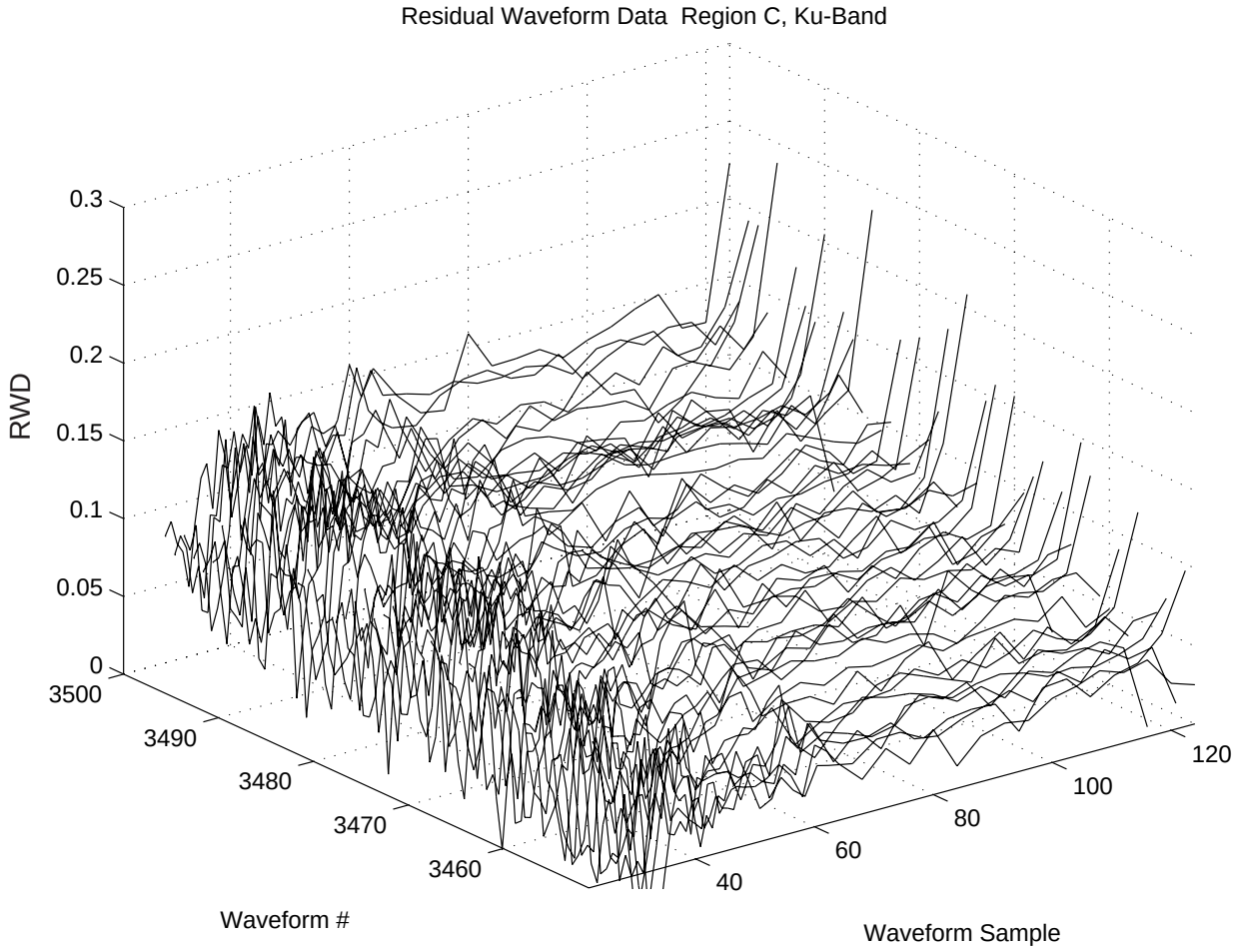

Figure 5.48. Ku-band residual waveform data from region C, third bloom (ii)

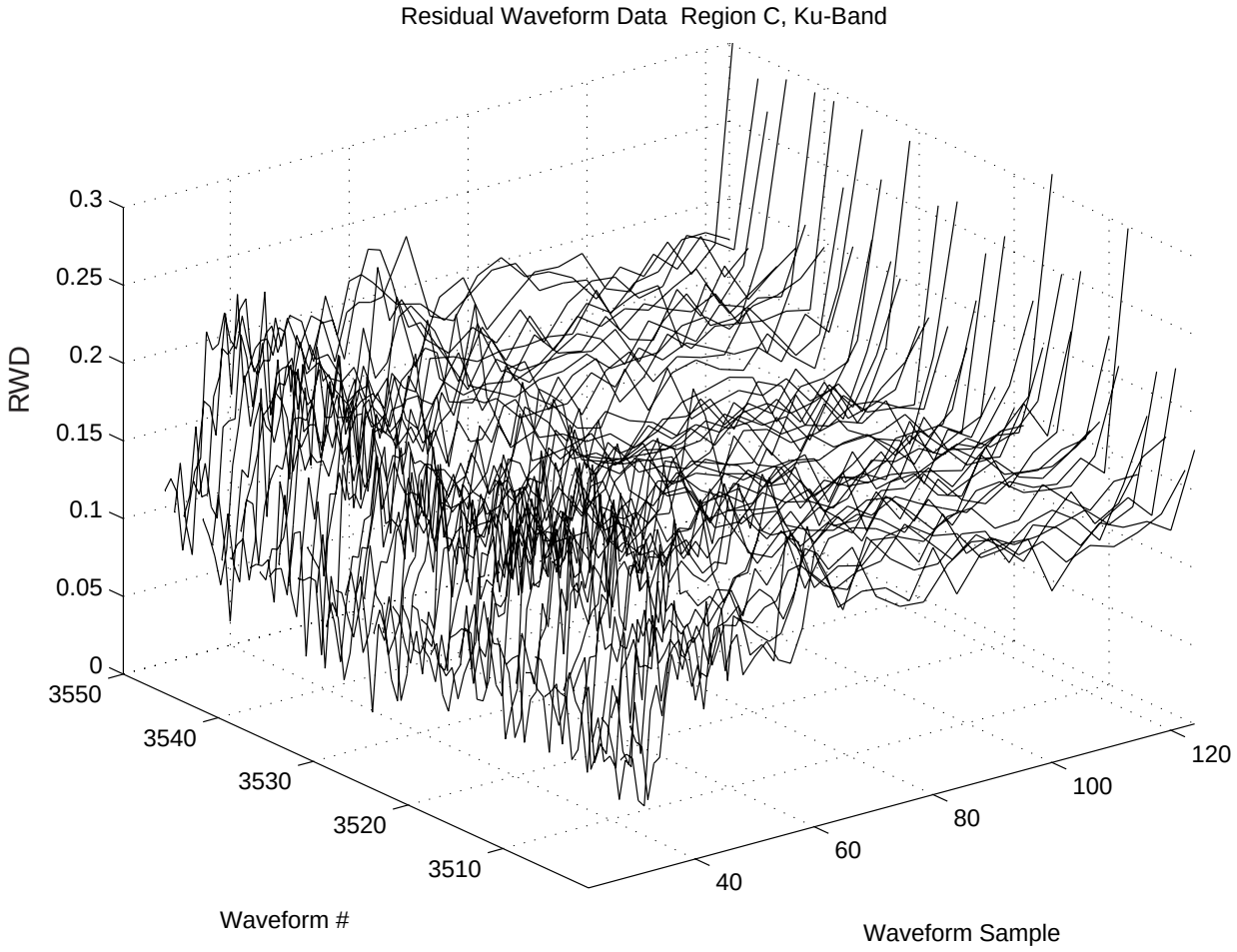

Figure 5.49. Ku-band residual waveform data from region C, third bloom (iii)

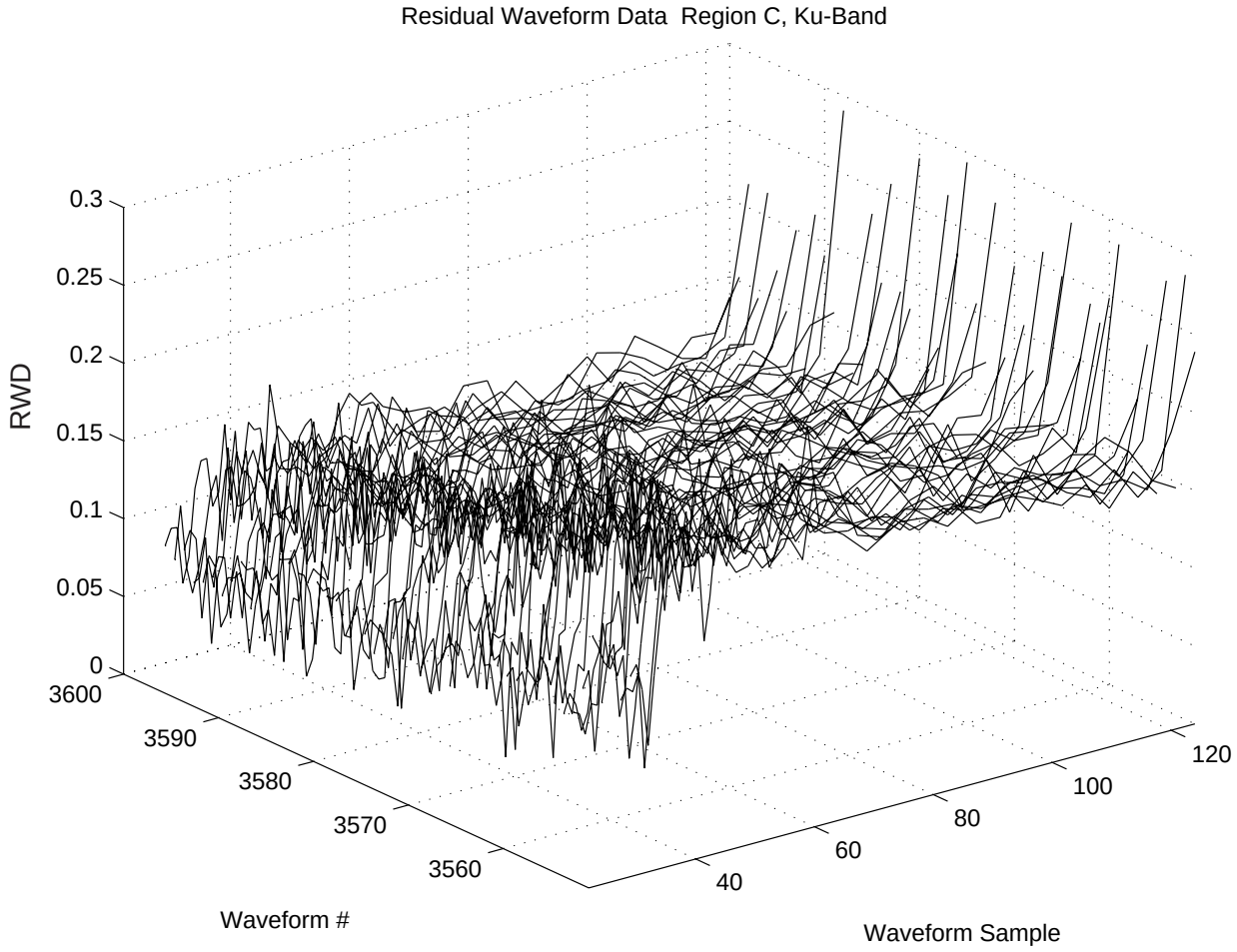

Figure 5.50. Ku-band residual waveform data from region C, third bloom (iv)

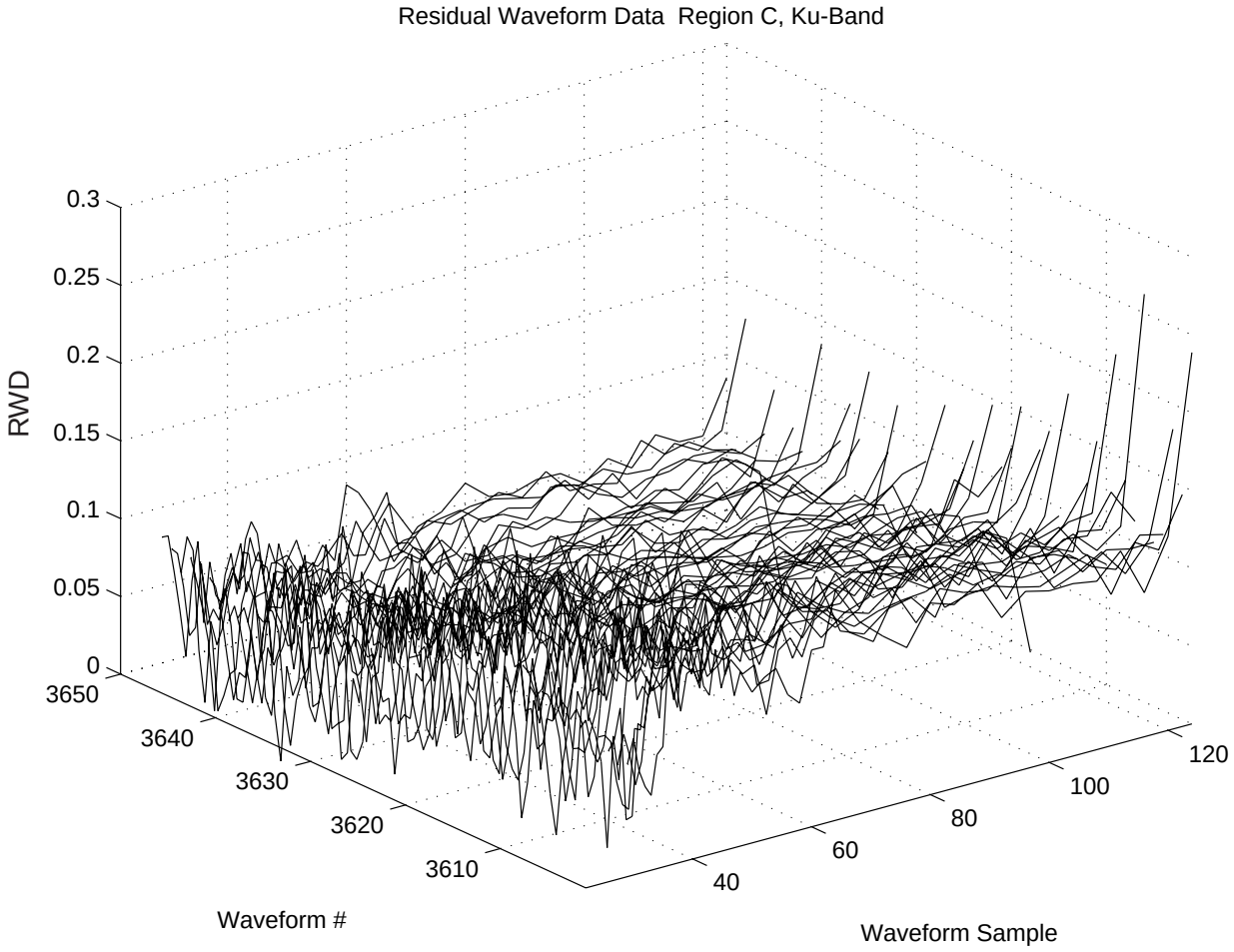

Figure 5.51. Ku-band residual waveform data from region C, third bloom (v)

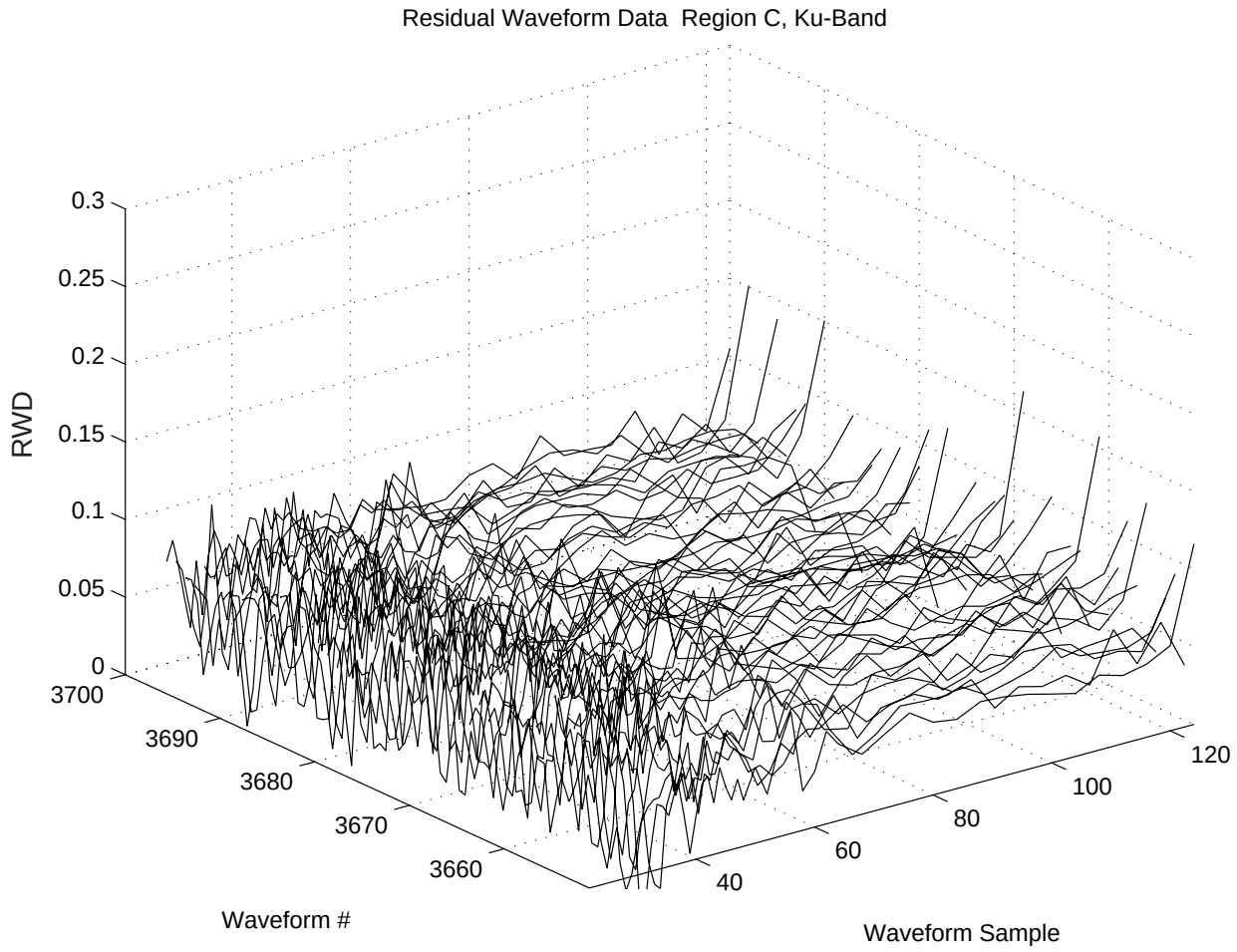

Figure 5.52. Ku-band residual waveform data from region C, third bloom (vi)

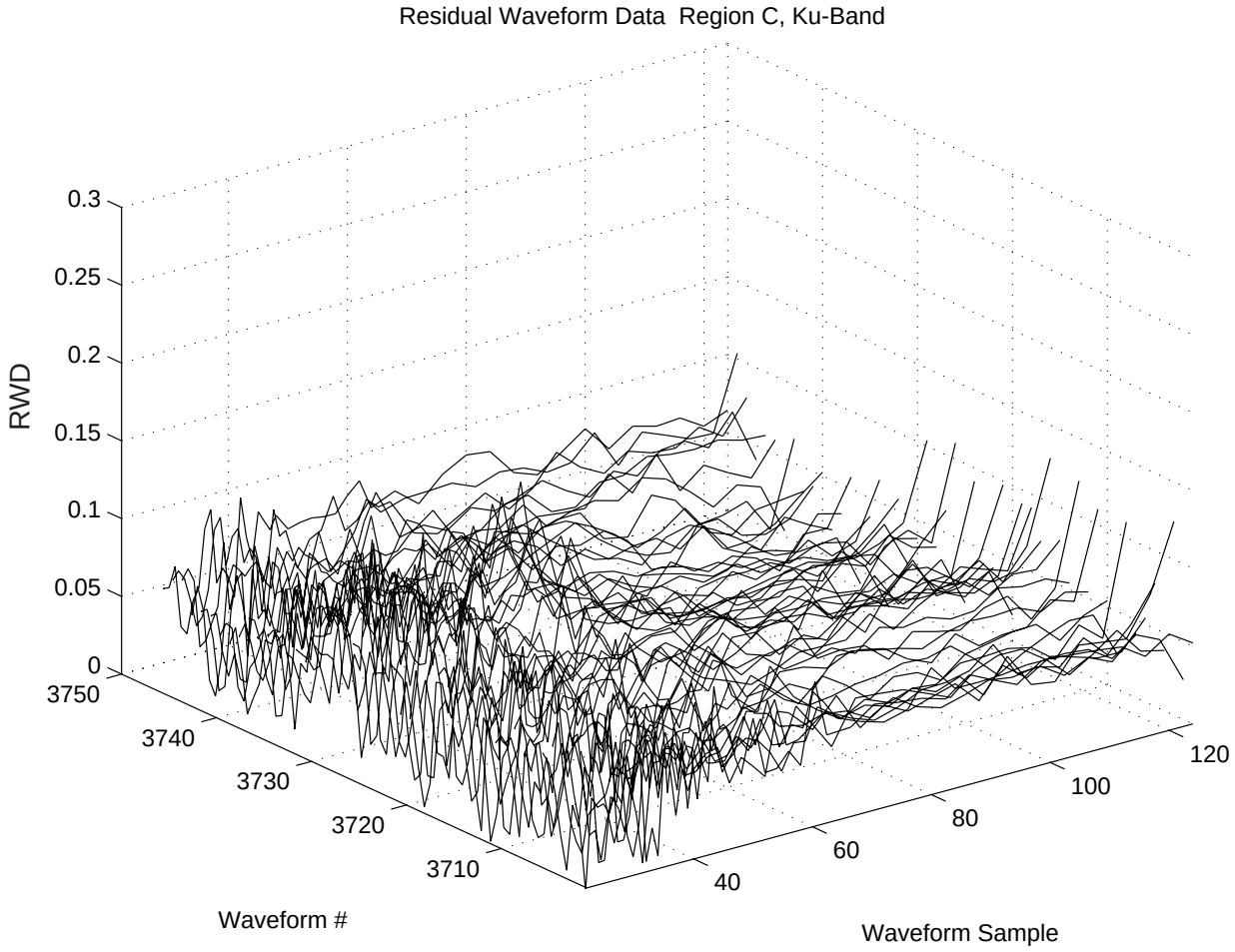

Figure 5.53. Ku-band residual waveform data from region C, third bloom (vii)

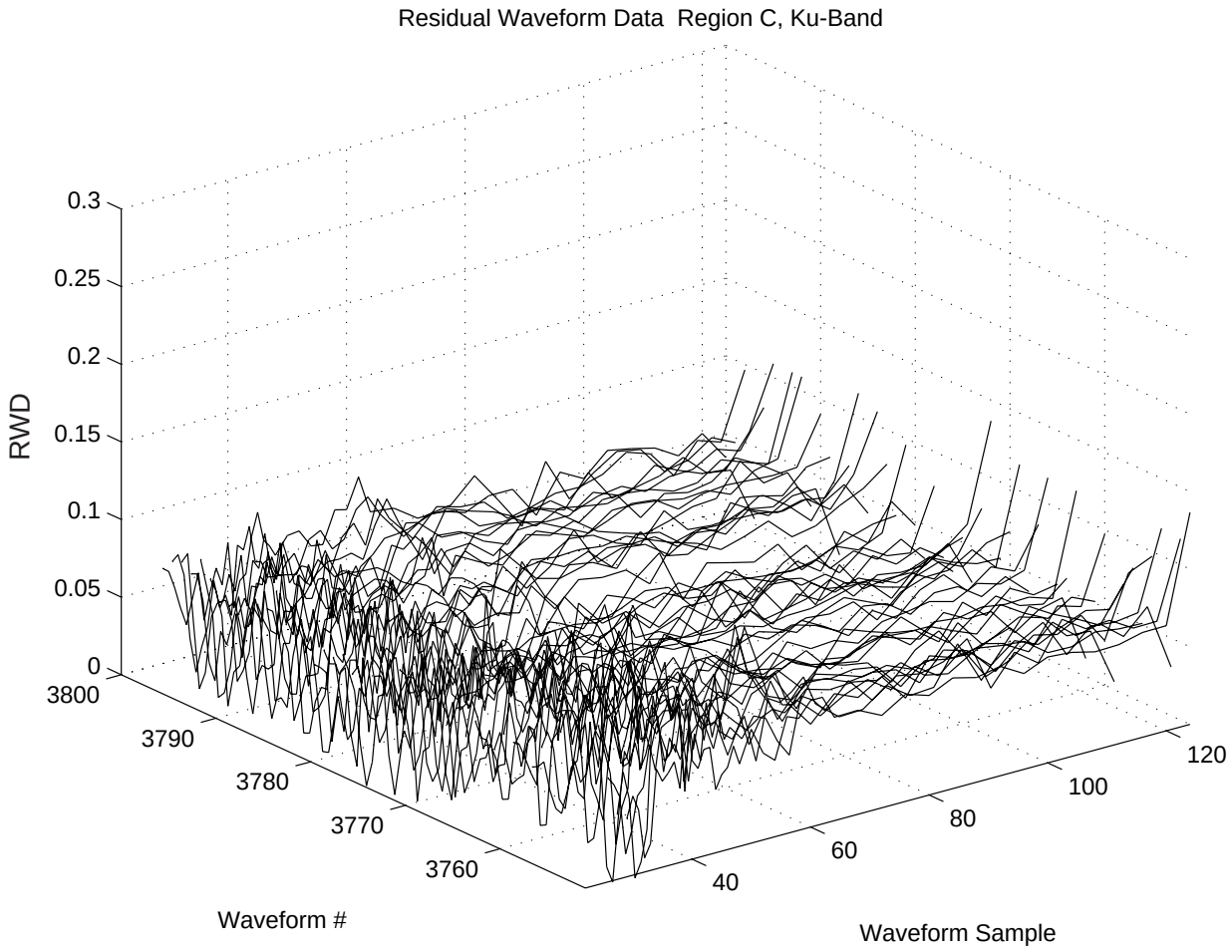

Figure 5.54. Ku-band residual waveform data from region C, third bloom (viii)

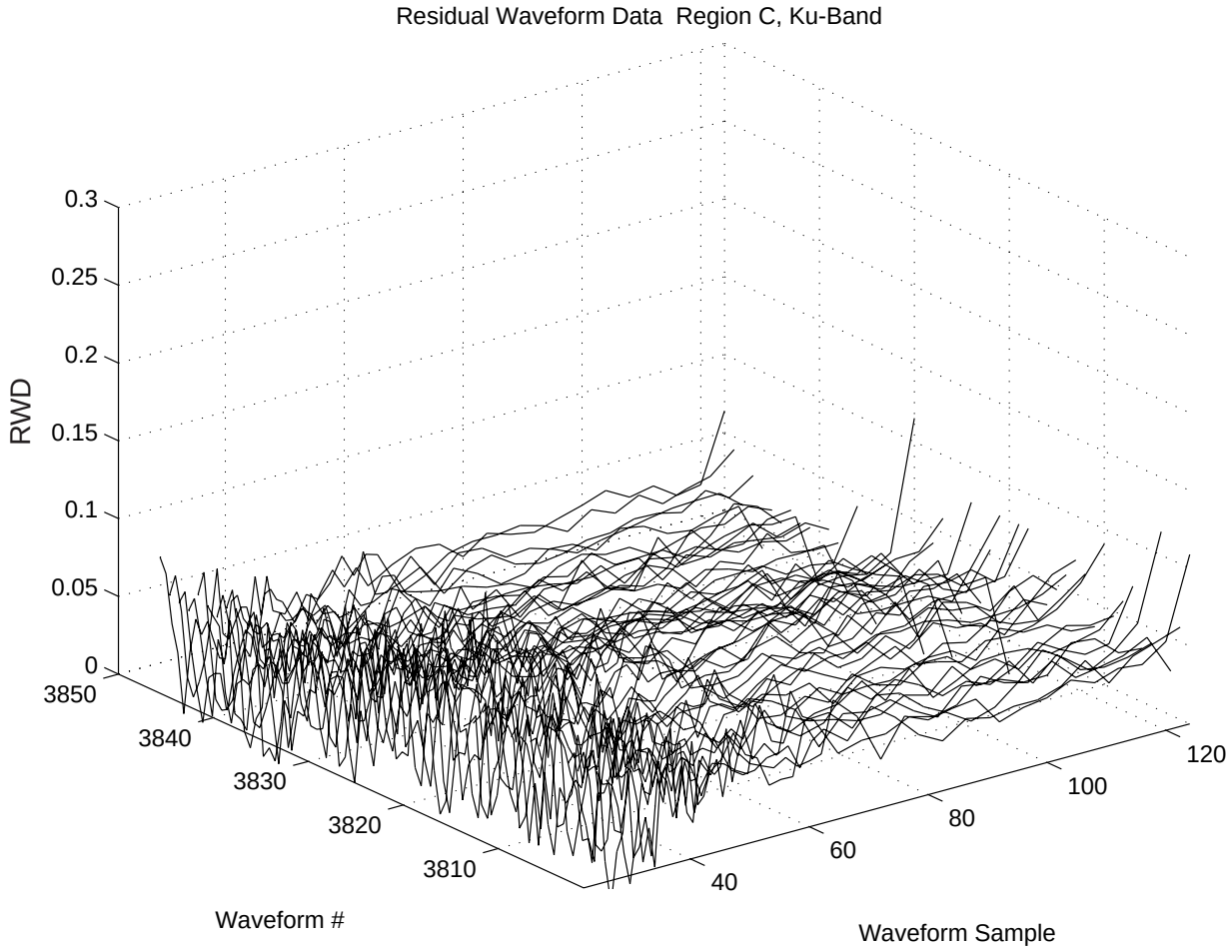

Figure 5.55. Ku-band residual waveform data from region C, third bloom (ix)

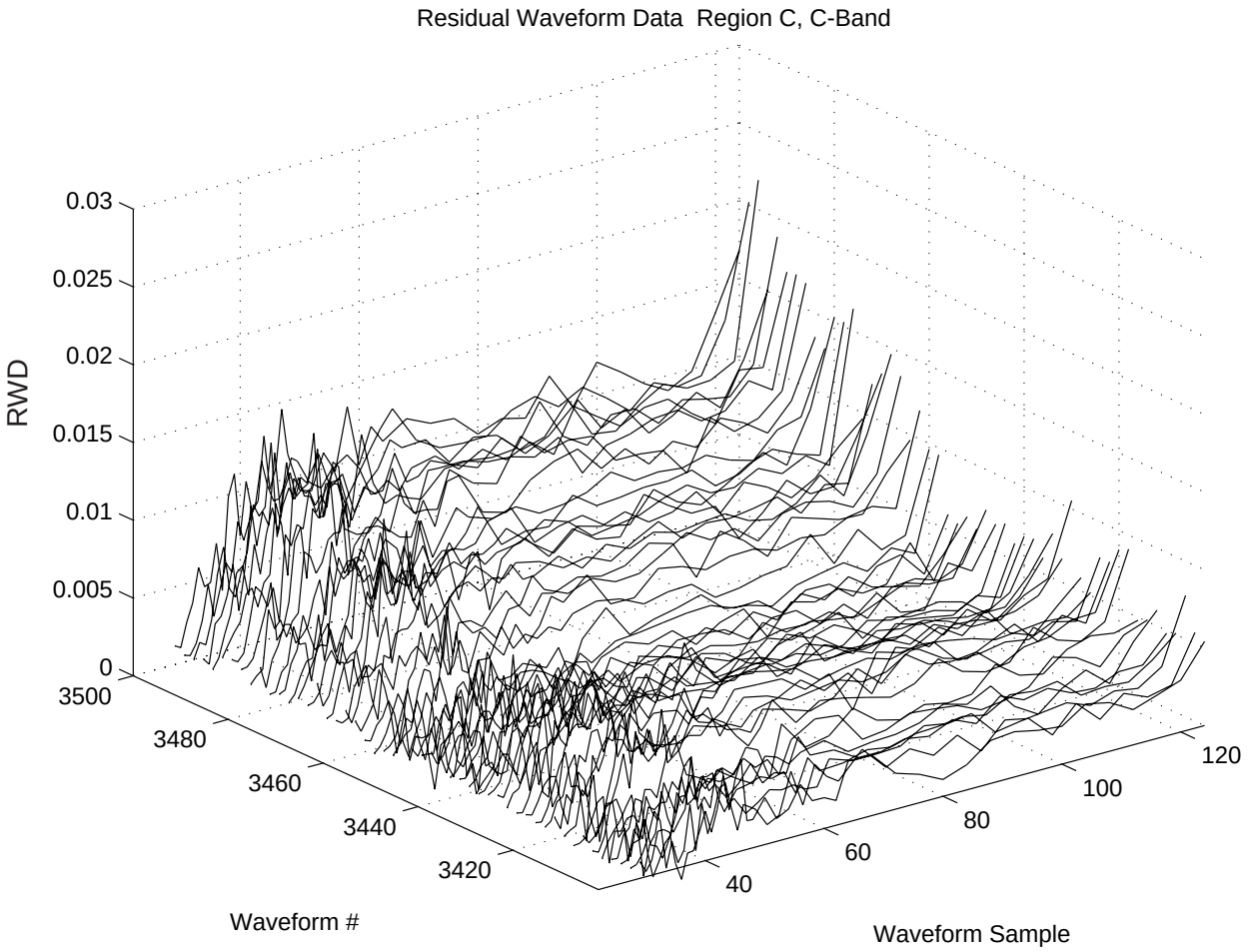

Figure 5.56. C-band residual waveform data from region C, third bloom (i)

Figures 5.56 through 5.59 show the C-band residual waveform data corresponding to the third and smallest bloom in region C. Again we notice that the tails of the RWD waveforms are extremely raised.

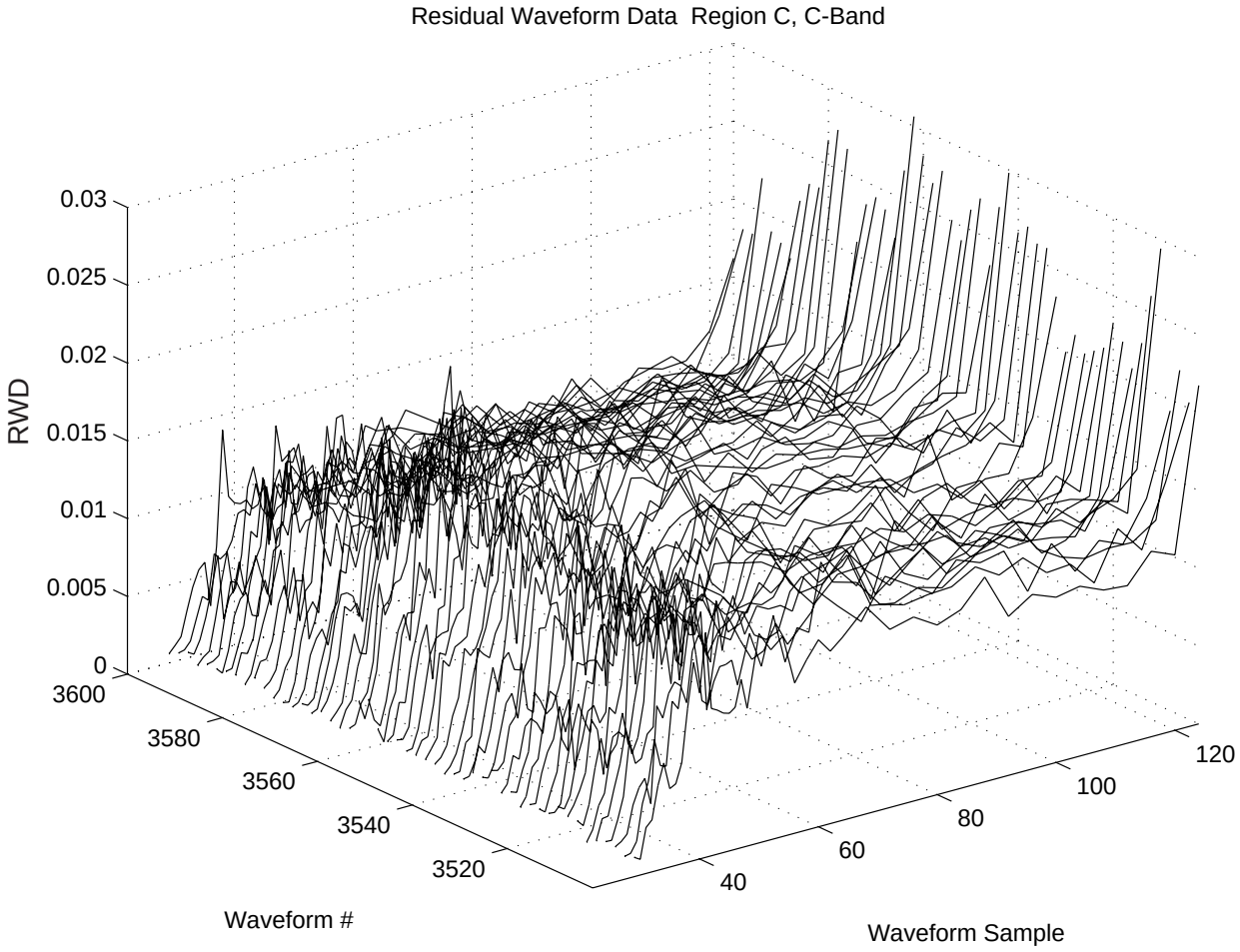

Figure 5.57. C-band residual waveform data from region C, third bloom (ii)

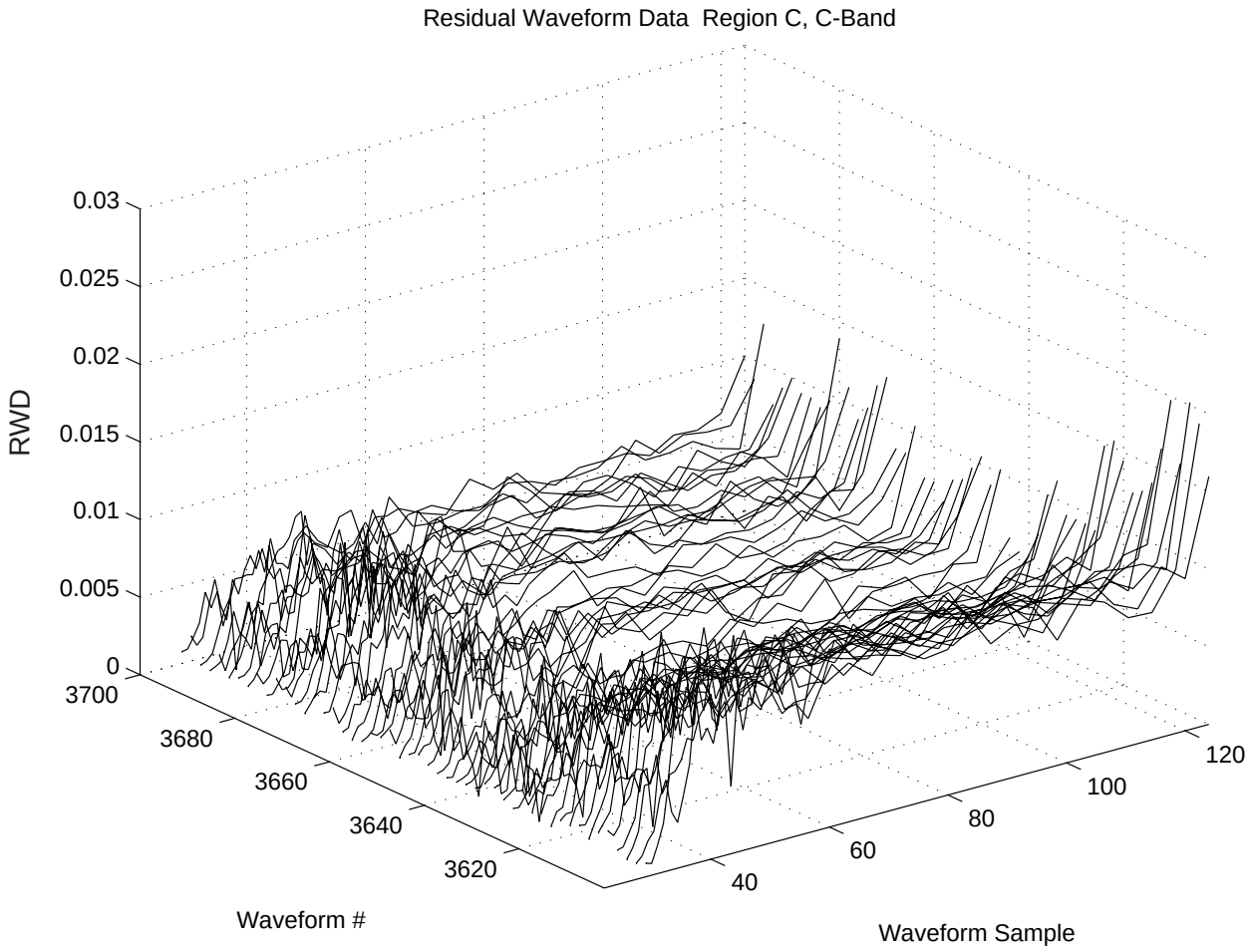

Figure 5.58. C-band residual waveform data from region C, third bloom (iii)

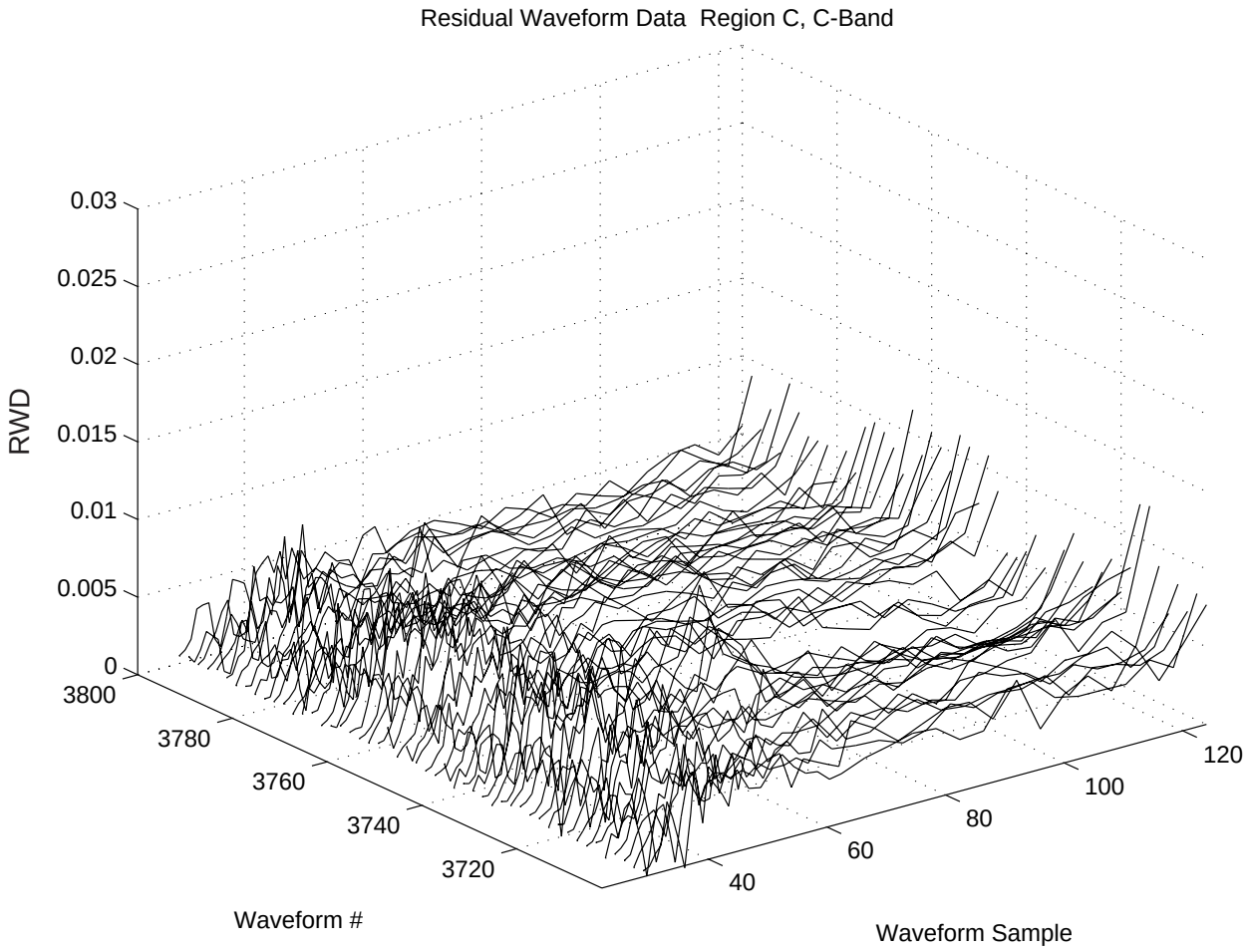

Figure 5.59. C-band residual waveform data from region C, third bloom (iv)

5.3.4 Region D

We found the mean SWH for region D to be 2.429 m and 2.495 m for Ku- and C-band respectively and the mean off-nadir angle, ξ, to be 0.075^o. Figure 5.60 shows the mean radar cross section σ^o corresponding to region D for both Ku and C-band. Contaminated data are marked by a red asterisk and the bloom lower limits are marked by a green line as before. We can see two blooms in this region. Due to high contamination of the second bloom, we will only study the first bloom. This first bloom occurs between GDR samples 40 and 70. Data for both frequencies is contaminated around GDR samples 58, 88, and 90 to 92. These samples correspond approximately to waveform numbers 566 to 576 (peak of the first bloom), 866 to 877, and 886 to 916.

Figure 5.61 shows the mean off-nadir angle, ξ. As seen in the other regions, approximately half of the out of range angles show contamination and appear during the peak of the blooms.

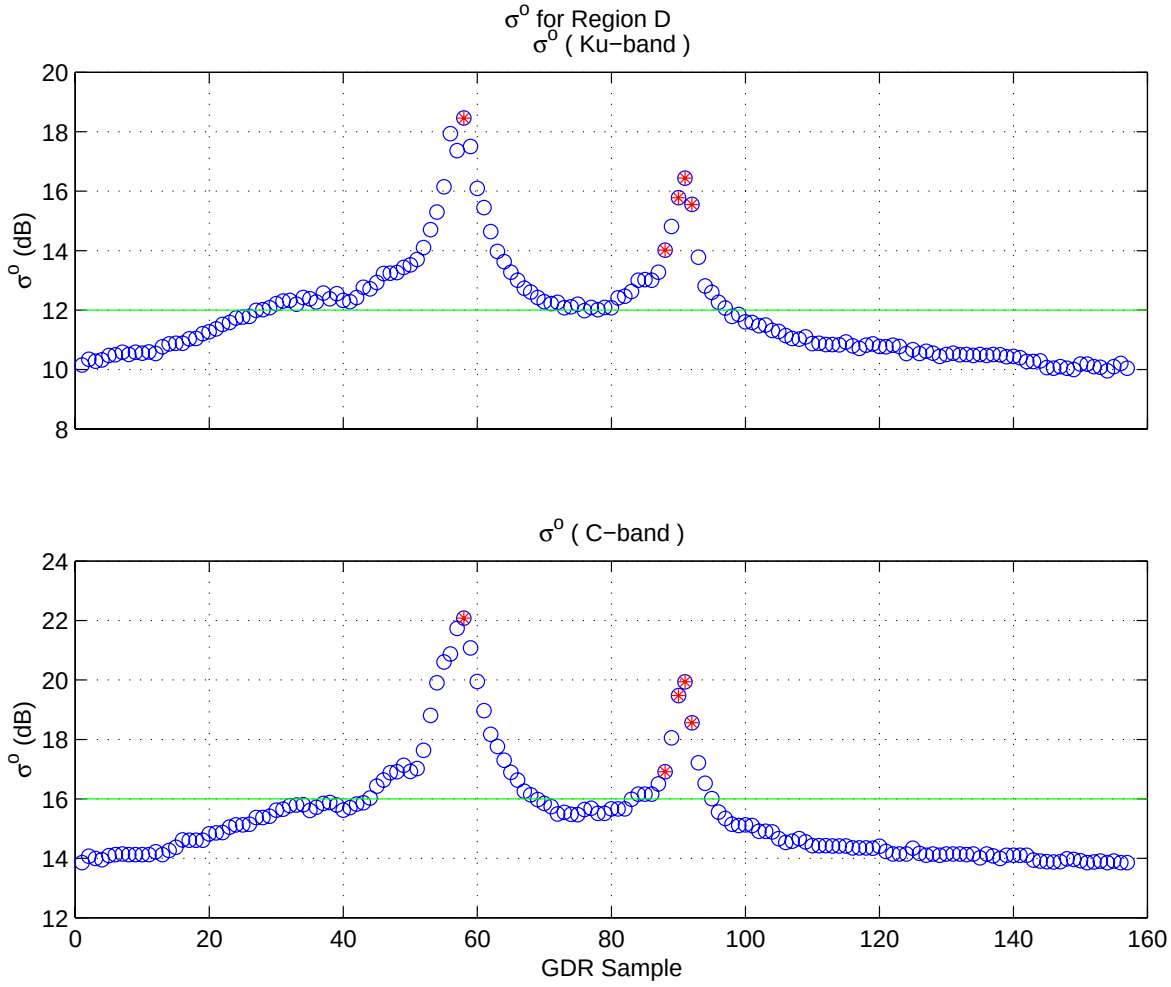

Figure 5.60. Ku- and C-band σ^o for region D

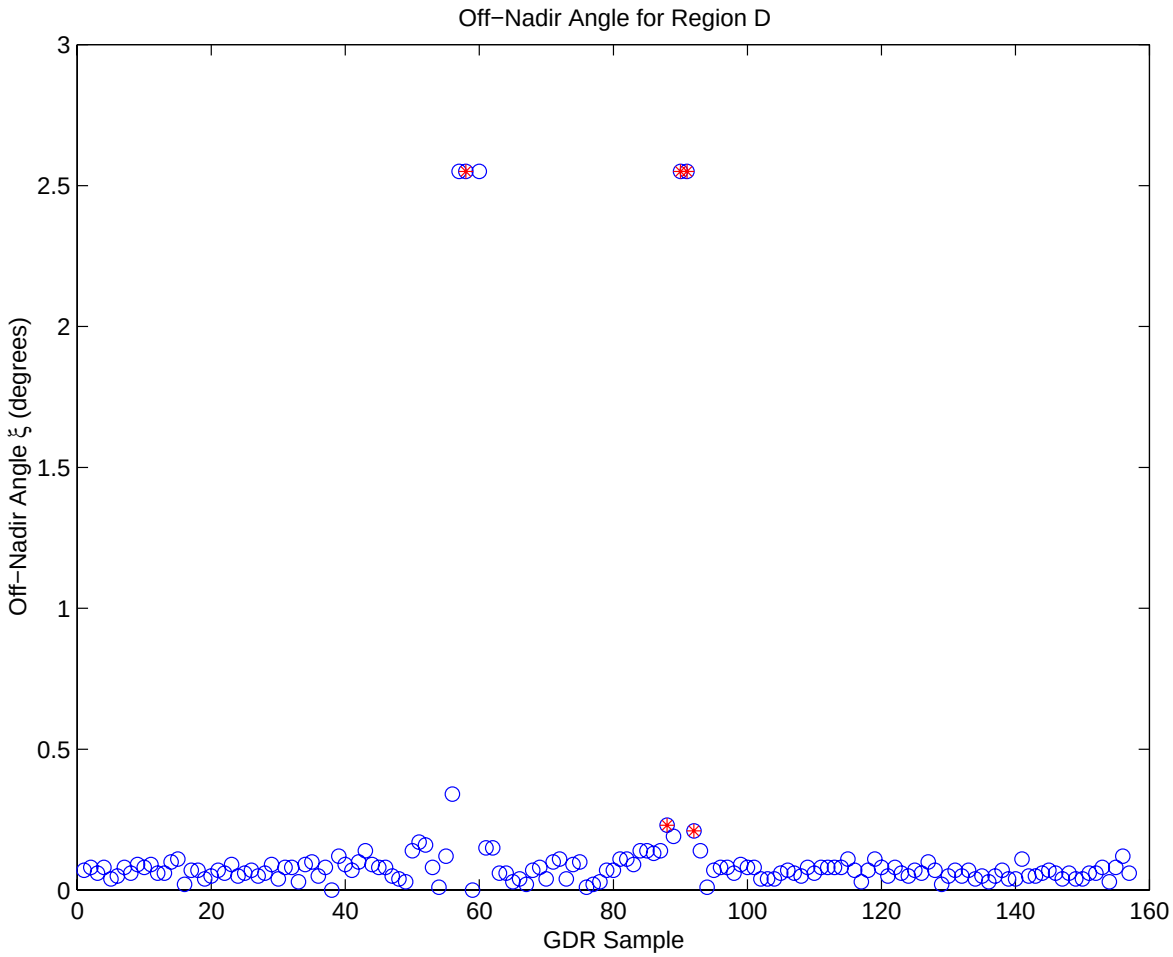

Figure 5.61. Off-Nadir angle ξ for region D

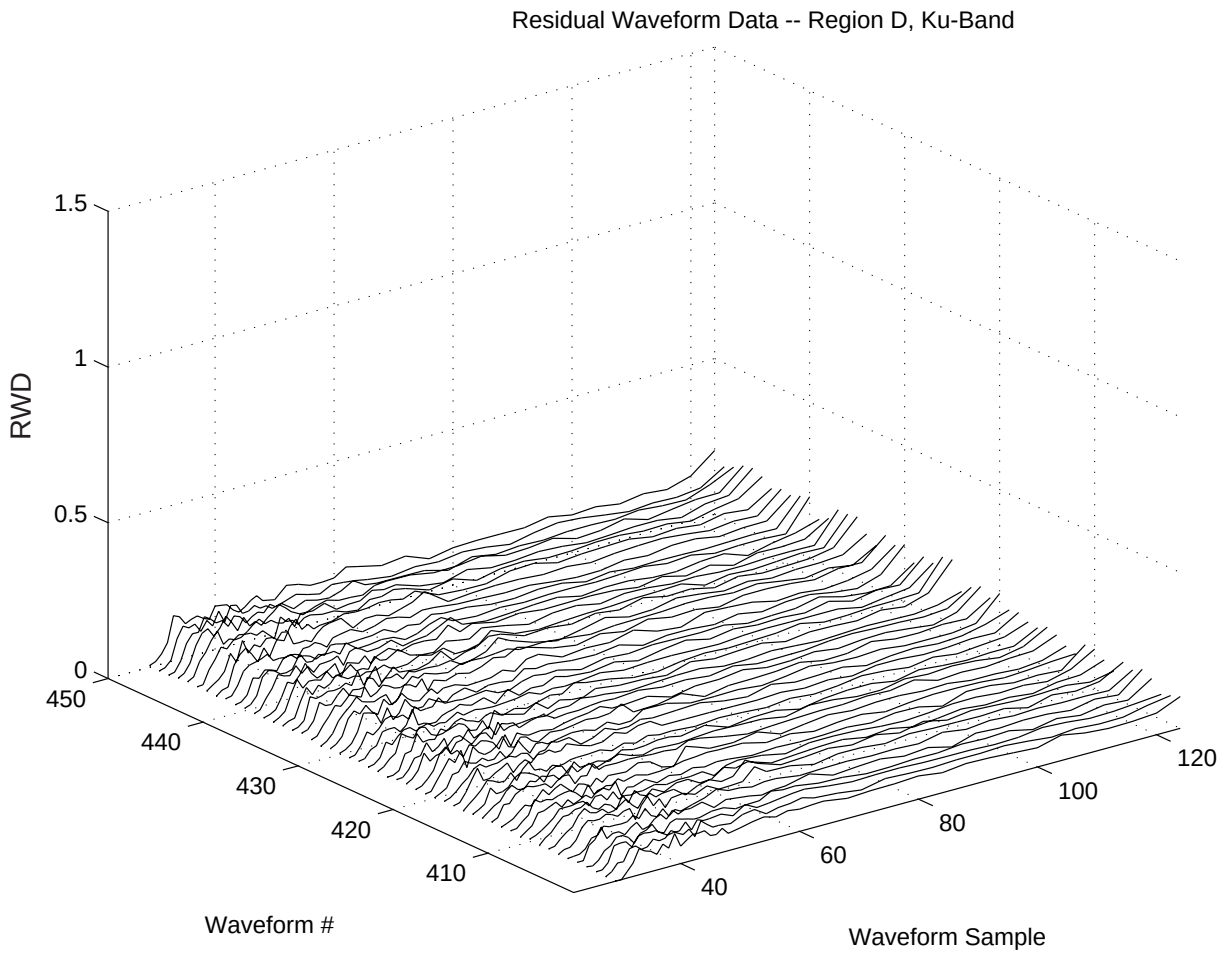

Figure 5.62. Ku-band residual waveform data from region D, first bloom (i)

Figures 5.62 through 5.67 show the Ku-band residual waveform data of the first bloom. This bloom is very large and progressive, and the RWD waveforms are very clean and uniform with the exception of the contaminated data. This bloom is probably caused by very dense and homogeneous slick areas. As in the previous cases, the tails of the waveforms are raised. In this case it seems highly unlikely that this tail behavior could be caused by the surface since the rest of each waveform lacks any indication of an abnormality in the surface.

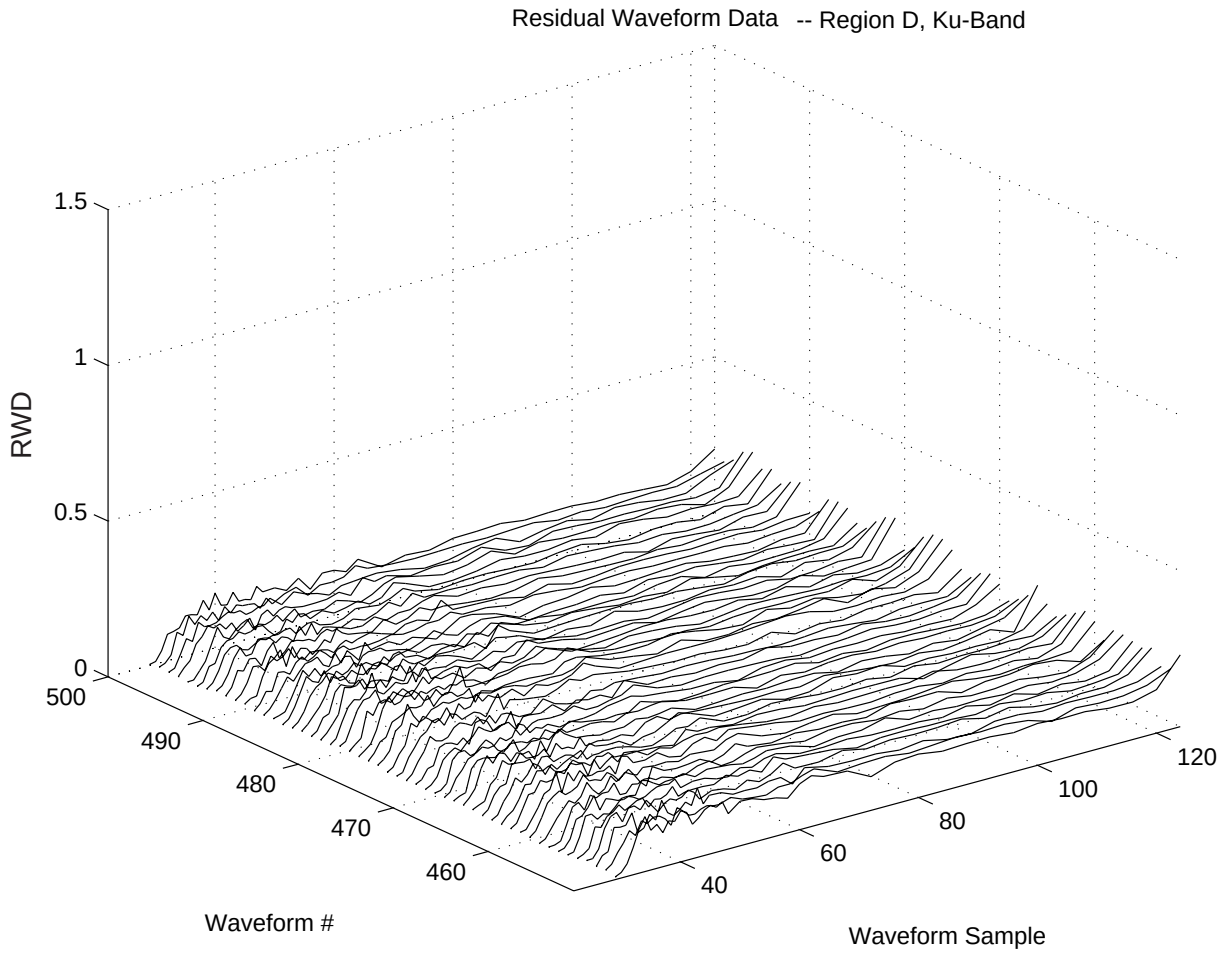

Figure 5.63. Ku-band residual waveform data from region D, first bloom (ii)

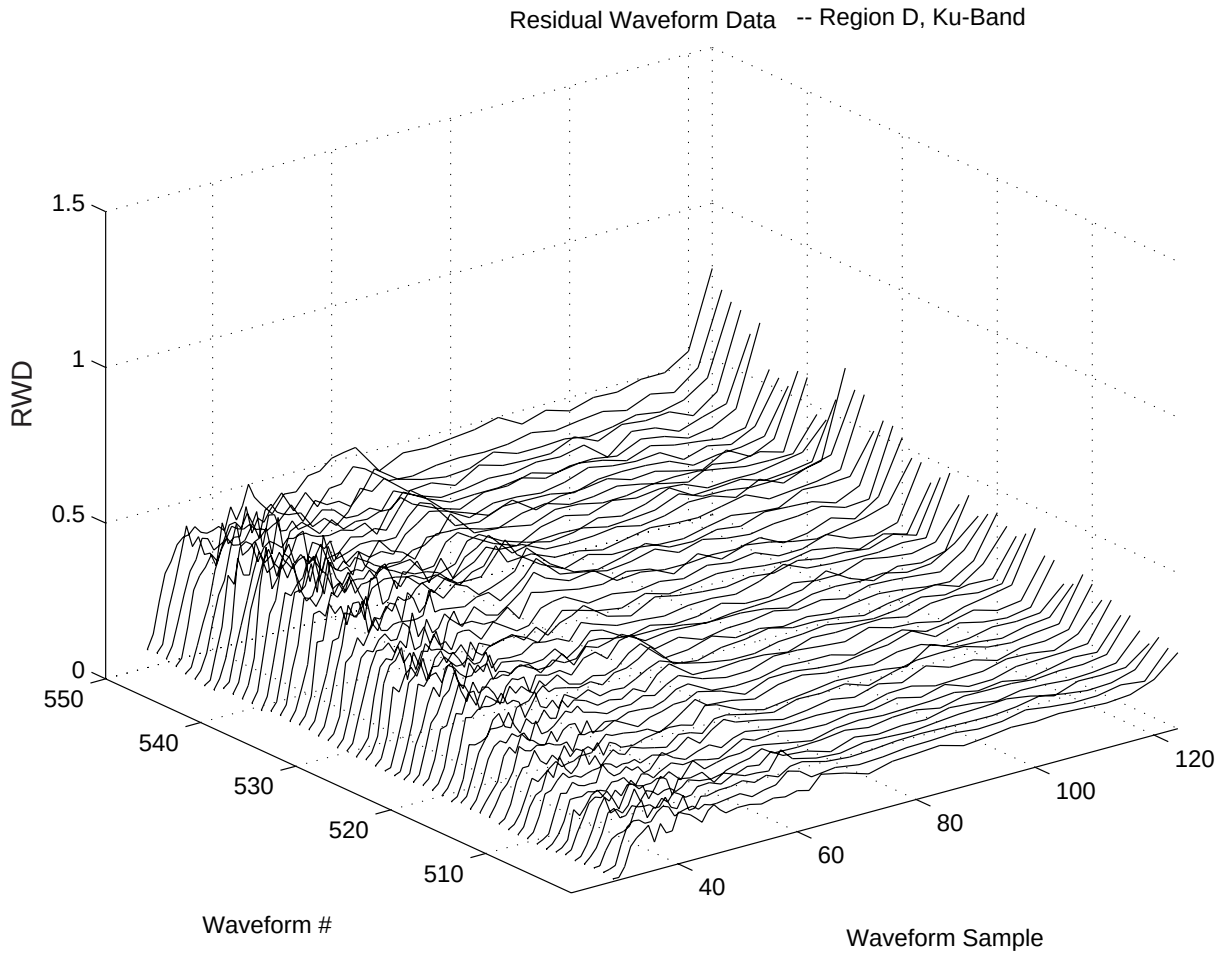

Figure 5.64. Ku-band residual waveform data from region D, first bloom (iii)

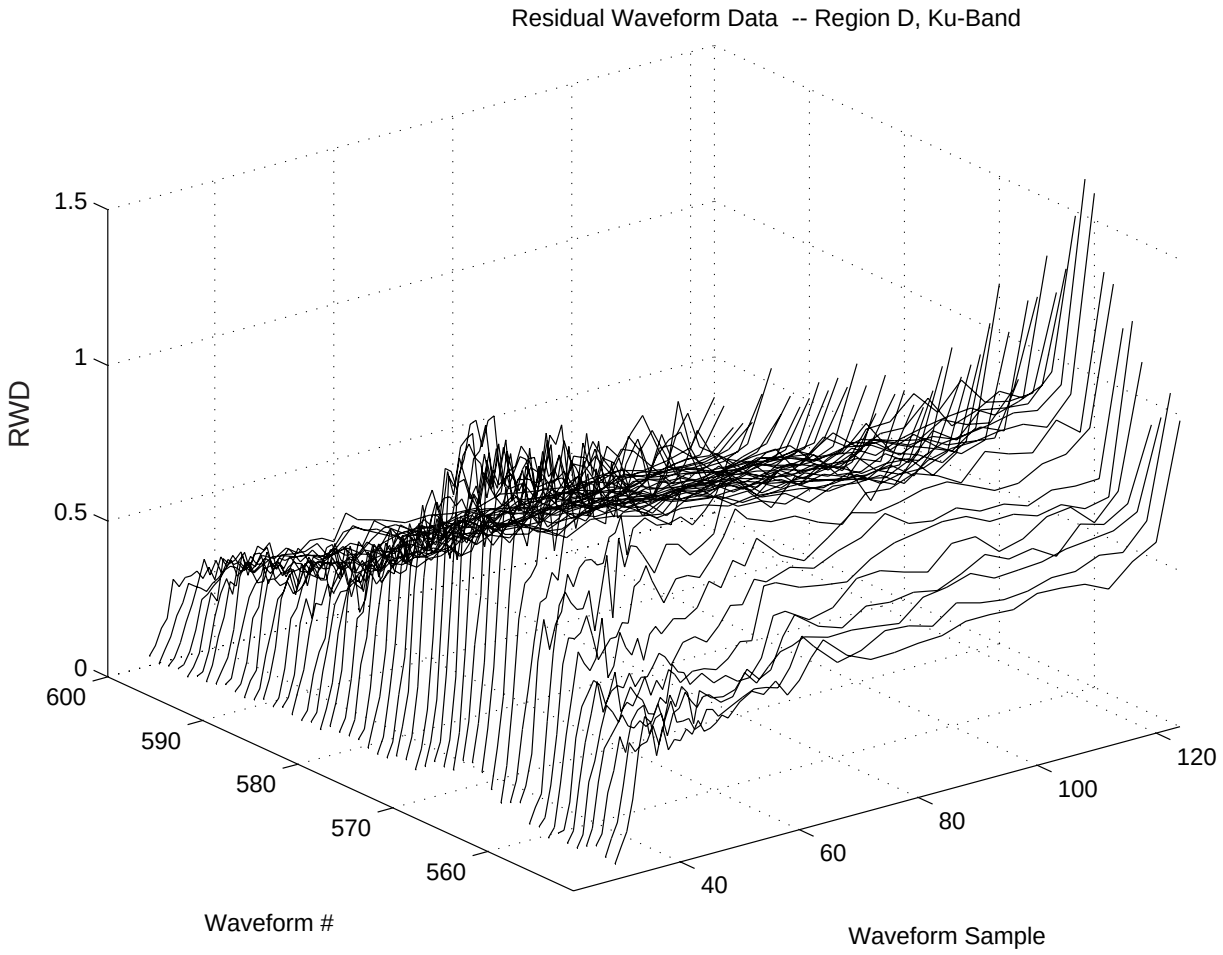

Figure 5.65. Ku-band residual waveform data from region D, first bloom (iv)

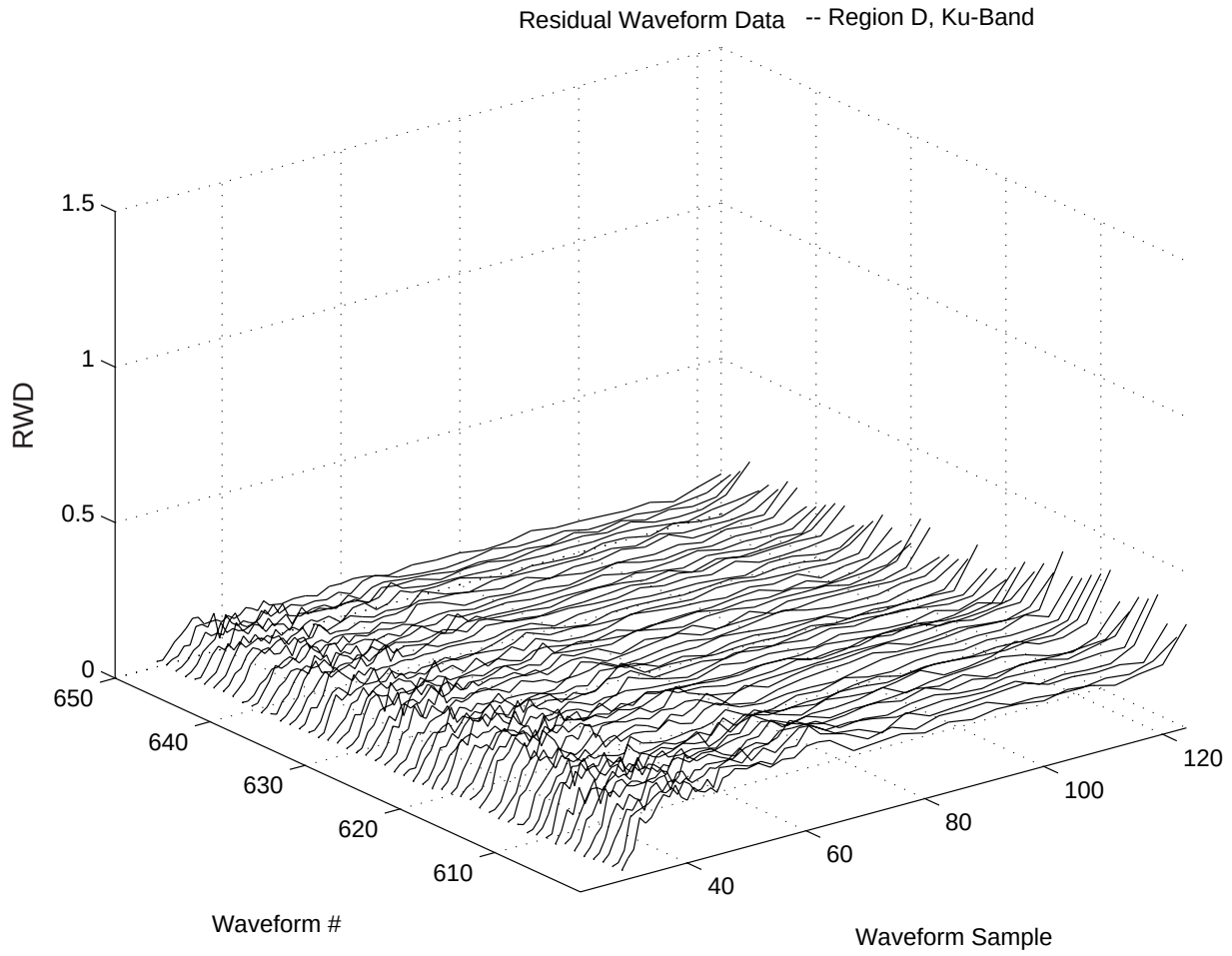

Figure 5.66. Ku-band residual waveform data from region D, first bloom (v)

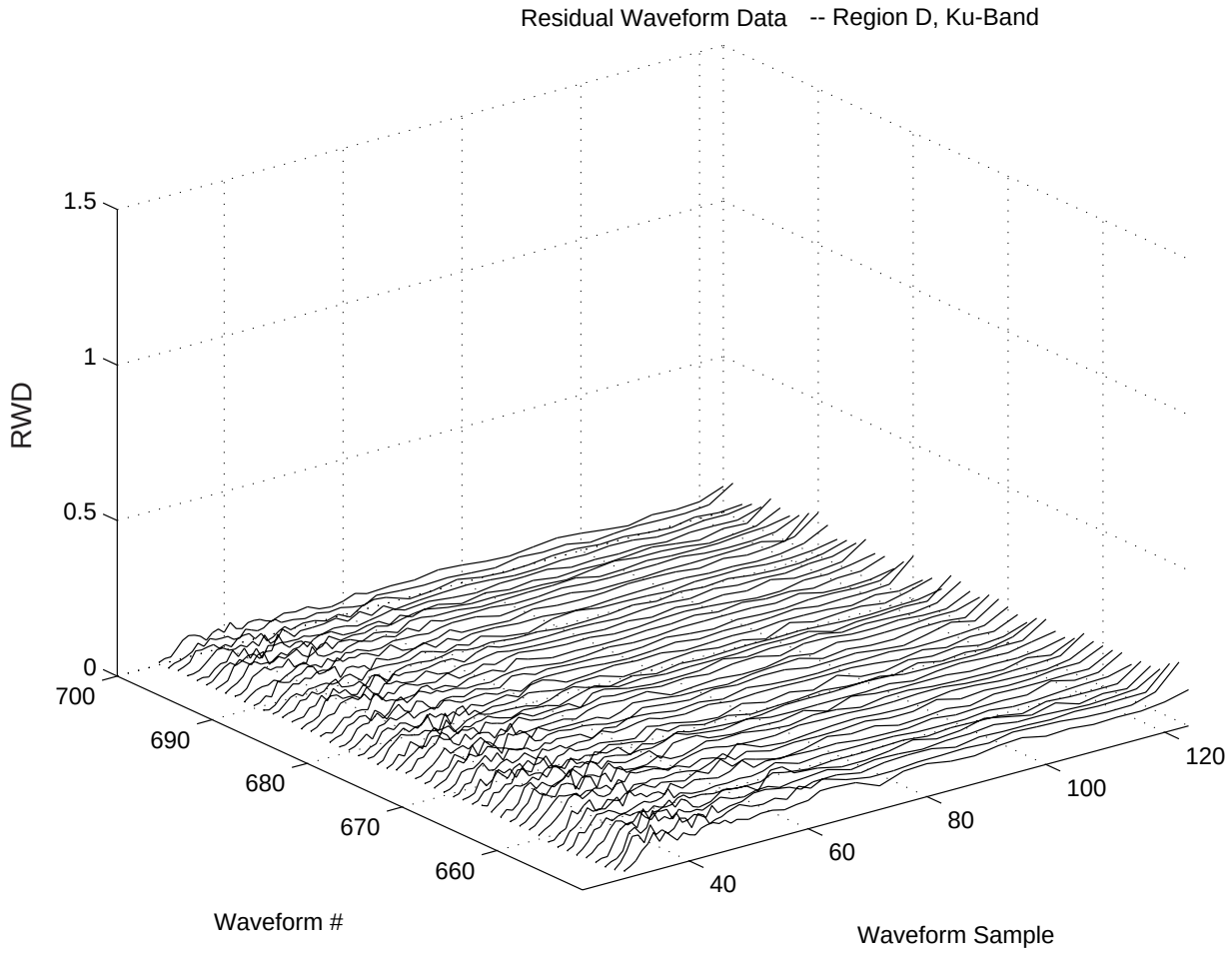

Figure 5.67. Ku-band residual waveform data from region D, first bloom (vi)

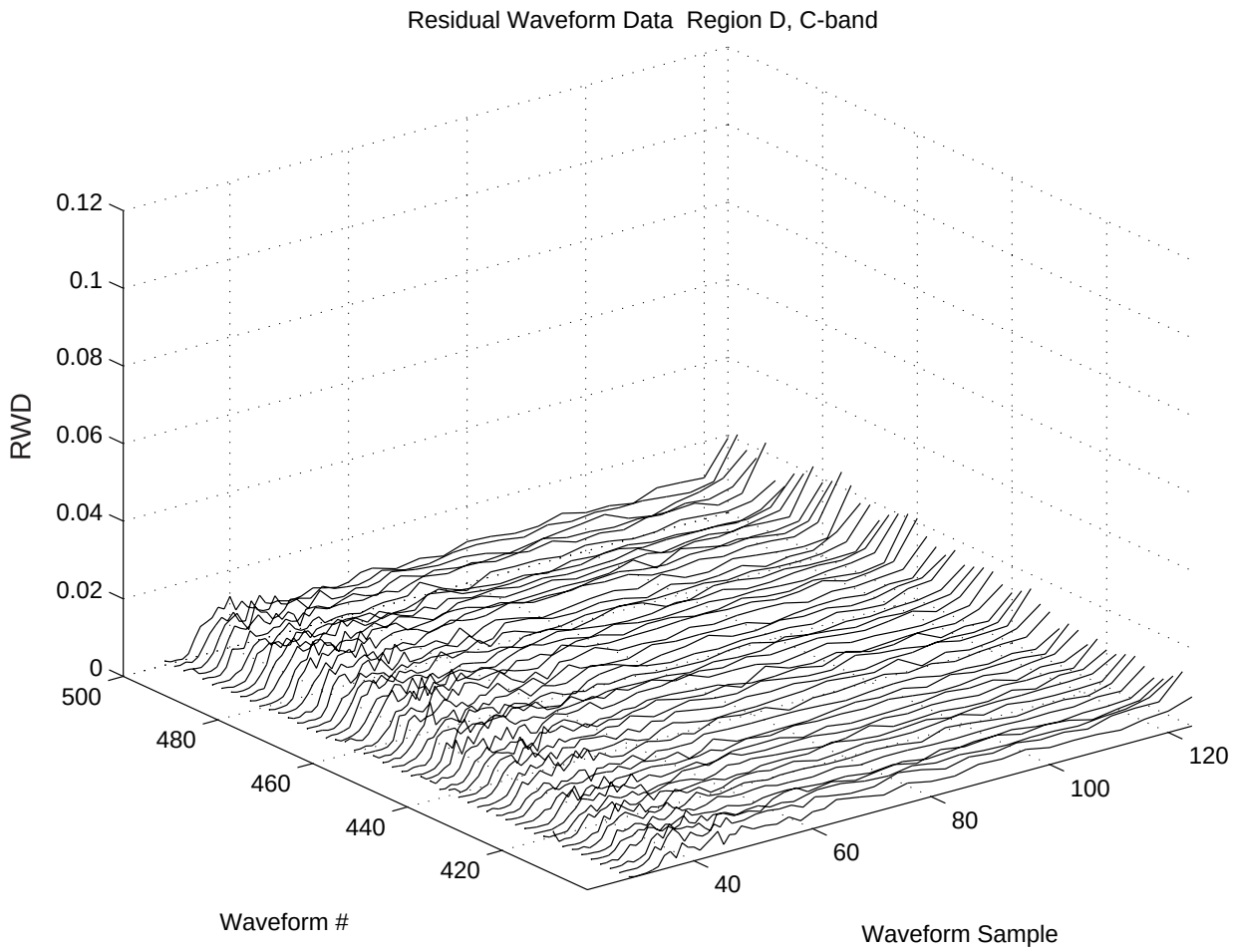

Figure 5.68. C-band residual waveform data from region D, first bloom (i)

Figures 5.68 through 5.71 show the C-band residual waveform data corresponding to the first bloom. These waveforms appear very similar to the Ku-band waveforms with a different magnitude. The tail behavior is also shown by these RWD waveforms.

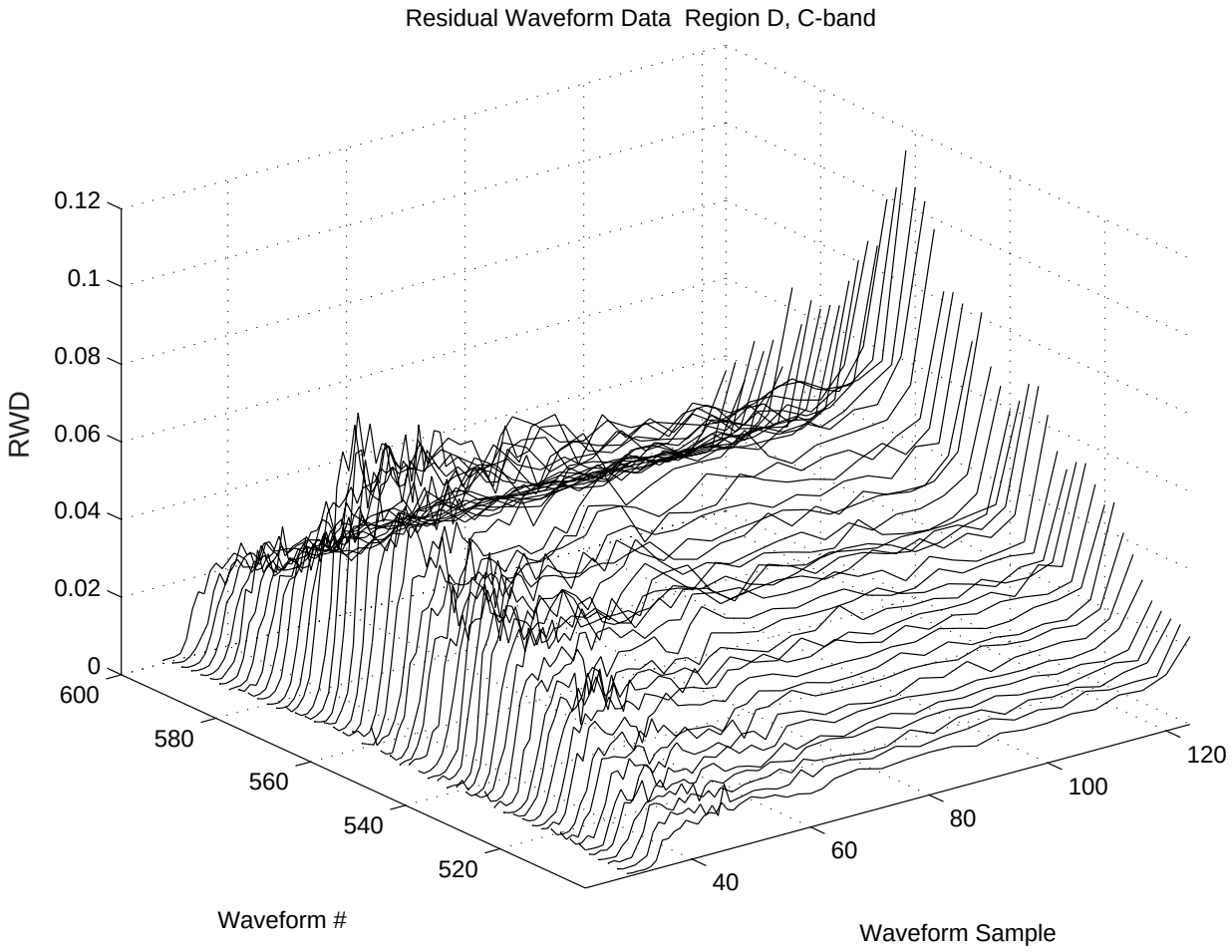

Figure 5.69. C-band residual waveform data from region D, first bloom (ii)

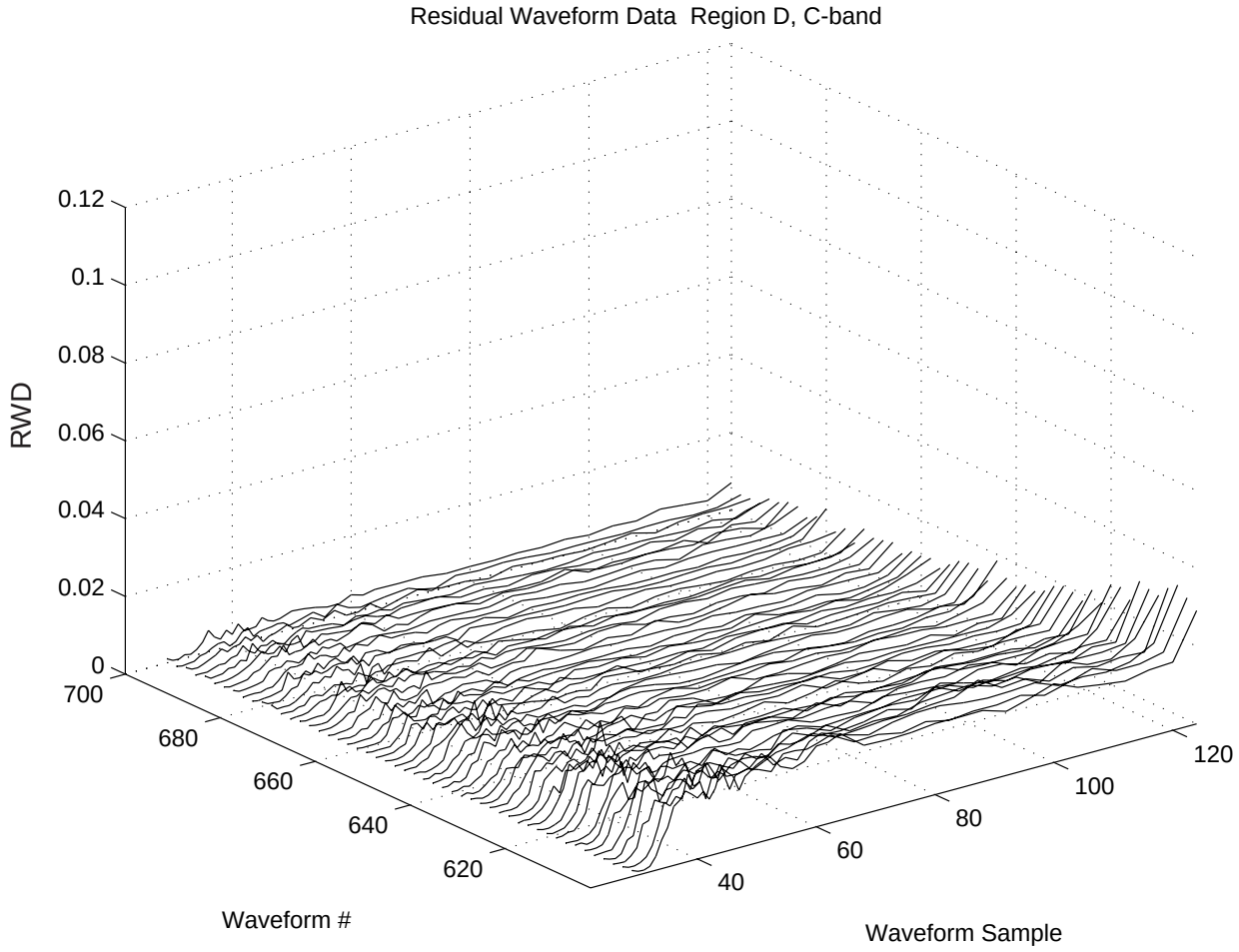

Figure 5.70. C-band residual waveform data from region D, first bloom (iii)

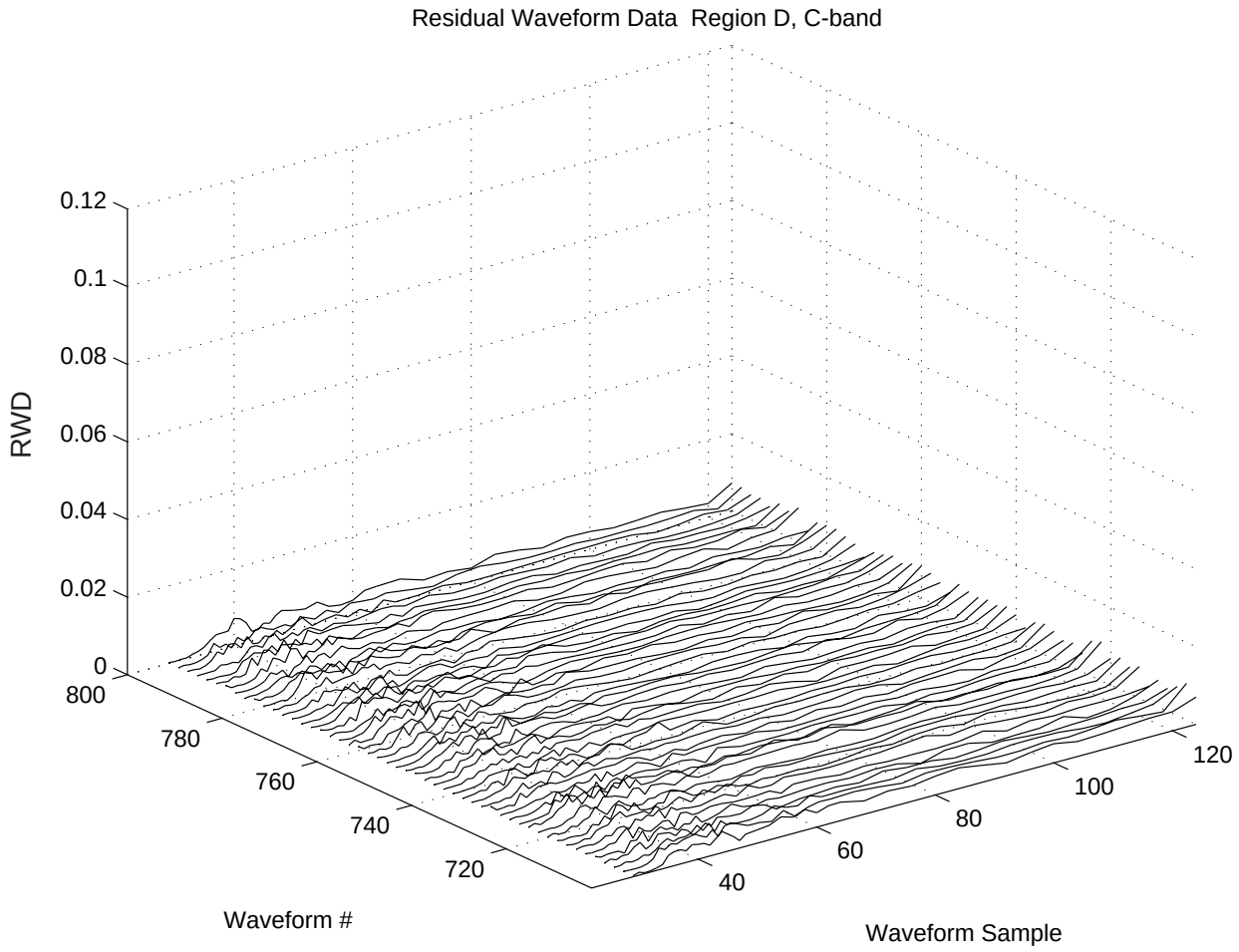

Figure 5.71. C-band residual waveform data from region D, first bloom (iv)

5.4 Summary

From the results shown in this chapter we conclude that our model for the average power returned from a suface containing slick areas with a radar cross section, σ_n^o, larger than the background radar cross section, σ_b^o, is valid. Through the fitting of the residual waveform data, RWD, to the blooms in regions A, C, and D, we showed that the contributions from slick or calm areas are a valid description of the σ^o blooms. The model can explain the uniform increase of the waveform's level during a bloom without any significant changes in the shape of the waveforms. This makes sense since as the satellite's nadir point enters a surface with uniformly distributed slick areas the level of the whole waveform will progressively increase. As shown in this chapter, the density and size variation as well as the σ_n^o homogeneity of the slick areas can affect the magnitude of the bloom and shape of the received waveforms.
Unfortunately, we still cannot account for out-of-range off-nadir angles that often accompany the blooms, nor for the raising of the waveform tails in the RWD. More research needs to be done in order to find a correlation between these anomalies and the σ^o blooms.

Chapter 6

Conclusions

6.1 Conclusion

In this thesis we studied two possible causes of the σ^o blooms, a surface containing a σ^o step discontinuity and a surface containing slick or calm areas with a radar cross section, σ_n^o, larger than the background's radar cross section, σ_b^o.

In Chapter 2 we derived a model for the average power returned from a surface containing a σ^o step discontinuity which we simulated in Chapter 3. We exercised this model for several surfaces and found that neither the resulting waveforms nor the automatic gain control computed from these waveforms exhibited the behavior found in the bloom waveforms and σ^o data obtained from the NASA Goddard Space Flight Center.

We then proceeded to derive a model for the average power returned from a surface containing slick or calm areas (based upon a suggestion of D. Vandemark of NASA) with a radar cross section, σ_n^o, larger than the background's radar cross section, σ_b^o, in Chapter 4. Since there are a high number of variations in the model that would produce the same results, we chose to fit the bloom data to our model instead of simulating the model for validation. In Chapter 5 we fitted our model to the bloom data to obtain the residual waveform data that corresponds to normalized contributions from the slick areas. We found the model to

provide a reasonable fit to the bloom data found in regions A, C,and D, of Cycle 137, Pass 058. Through our model, the uniform increase of the level of the waveforms during a bloom can be explained as well as the sometimes jagged behavior of the residual waveform data usually corresponding to smaller blooms. At this point, however, our model cannot explain the out-of-range off-nadir angles that often accompany the σ^o blooms nor the raising of the tails in the RWD waveforms.

Of particular importance to the design of future altimeters is the nature of these blooms. According to our model, the blooms are a consequence of relatively extensive areas of calm or slick regions on the surface of the ocean. Of specific interest is why these blooms did not appear in the data sets of earlier radar altimeters, e.g. Skylab, GEOS-3, and SEASAT. The answer probably has two parts. First, none of these altimeters produce the volume of data produced by TOPEX. Second, the resolution of these earlier altimeters was not even comparable to TOPEX. If our model is correct and our hypothesis is true, future altimeter designers must realize that increased altimetric resolution and precision are not obtained without a price to pay.

6.2 Future Work

More cases of σ^o blooms must be studied and fitt to our model to establish the level of correlations between the magnitude of the residual waveform data and the characteristics of the blooms. Furthermore, we must learn more about why data is considered contaminated so that we can determine if this data can be used to study the blooms, or if this contamination is caused by the blooms. We must also understand what mechanism produces out-of-range off-nadir angles associated with blooms and contaminated data.

Once correlations have been made between the size and shape of the residual waveform data and the characteristics of the blooms, it would be very useful to compare these results with studies of actual ocean slick areas.

Bibliography

[1] G. S. Brown. The average impulse response of a rough surface and its applications. *IEEE Transactions on Antennas and Propagation*, AP-25:67–74, 1997.

[2] Dudley B. Chelton, Edward J. Walsh, and John L. MacArthur. Pulse compression and sea level tracking in satellite altimetry. *Journal of Atmospheric and Oceanic Technology*, 6:407–438, 1989.

[3] David K. Cheng. *Field and Wave Electromagnetics*. Addison Wesley, Reading, Massachusetts, 1993.

[4] E. B. Dobson, F. M. Monaldo, D. L. Porter, A. R. Robinson, C. C. Kilgus, J. Goldhirsh, and S. M. Glenn. Radar altimetry and global climate change. *John Hopkins APL Technical Digest*, 13:431–443, 1992.

[5] G. S. Hayne, D. W. Hancock III, C. L. Purdy, and P. S. Callahan. The corrections for significant wave height and attitude effects in the topex radar altimeter. *Journal of Geophysical Research*, 99:24,941–24,955, 1994.

[6] George S. Hayne. Personal correspondence, 1997-1999.

[7] P. C. Marth, J. R. Jensen, C. C. Kilgus, J. A. Perschy, J. L. MacArthur, D. W. Hancock, G. S. Hayne, C. L. Purdy, L. C. Rossi, and C. J. Koblinsky. Prelaunch performance of the nasa altimeter for the topex/poseidon project. *IEEE Transactions on Geoscience and Remote Sensing*, 31:315–332, 1993.

[8] D. Vandemark. Personal communications, 1999.

[9] Alfred R. Zieger, David W. Hancock, George S. Hayne, and Craig L. Purdy. Nasa radar altimeter for the topex/poseidon project. *Proceedings of the IEEE*, 79:810–826, 1991.

Appendix A

TOPEX System Parameters

Parameter	Ku-Band	Common	C-Band
Mean Altitude (Km)		1334	
Frequency (GHz)	13.6		5.3
Peak RF Power (W)	20.0		20.0
Pulse width (μs)		102.4	
Pulse period (μs)		204.8	
Burst period at 1334 Km (μs)		8893	
Antenna Type		1.5 m parabola	
Antenna Gain (dB)	43.9		35.7
Antenna Beamwidth (deg)	1.1		2.7

Table A.1. TOPEX System Parameters (Zieger et at., 1991)

Appendix B

TOPEX Waveform Correction Factors

Telemetry Sample Number	Multiplicative Factors	Ku Additive Factors	C Additive Factors
1	3.355	0	0
2	2.327	0	0
3	1.638	0	0
4	1.178	0	0
5	1.120	-1.39	-0.35
6	1.083	-2.78	-0.69
7	1.065	-2.78	-0.69
8	1.047	-9.44	-2.36
9	1.070	-9.44	-2.36
10	1.025	-9.44	-2.36
11	1.041	-6.67	-1.67
12	1.025	-17.78	-4.44
13	1.036	-17.78	-4.44
14	1.012	-17.78	-4.44
15	1.029	-17.78	-4.44
16	1.009	-11.11	-2.78
17	1.037	-11.11	-2.78
18	0.999	-11.11	-2.78
19	1.023	-11.11	-2.78
20	1.002	-11.11	-2.78
21	1.006	0	0
22	0.992	-11.11	-2.78
23	1.005	-11.11	-2.78
24	0.987	-11.11	-2.78
25	1.027	-11.11	-2.78
26	0.987	-11.11	-2.78
27	0.997	-11.11	-2.78
28	0.981	-11.11	-2.78
29	0.990	-11.11	-2.78
30	0.979	-11.11	-2.78
31	0.997	0	0
32	0.969	0	0
33	1.007	0	0
34	0.958	0	0
35	0.981	0	0
36	0.956	0	0
37	0.976	0	0
38	0.960	0	0
39	0.986	0	0
40	0.953	0	0
41	0.966	0	0
42	0.955	0	0
43	0.955	0	0
44	0.947	0	0
45	0.945	0	0
46	0.941	-15.56	-3.89
47	0.913	-57.78	-14.44
48	0.882	-57.78	-14.44
49	0.868	-57.78	-14.44
50	0.909	-6.67	-1.67
51	0.934	0	0
52	0.932	0	0
53	0.937	0	0
54	0.932	0	0
55	0.945	-2.78	-0.69
56	0.948	-11.11	-2.78
57	0.954	-11.11	-2.78
58	0.936	-11.11	-2.78
59	0.949	-11.11	-2.78
60	0.957	-2.78	-0.69
61	0.983	0	0
62	1.103	0	0
63	1.158	0	0
64	2.273	0	0

Table B.1. TOPEX waveform correction factors (Hayne et al., 1994)

Vitae

Albert Garcia was born on November 20, 1975 in Barcelona, Spain. He attended La Salle Comtal school in Barcelona, Spain up to the 11th grade. Albert was an exchange student in Topeka West Highschool in Topeka, Kansas from where he graduated in May of 1993. Albert was awarded two Bachelors of Science degrees in Electrical Engineering and Applied Mathematics from Virginia Polytechnic Institute and State University in May of 1997. He began graduate work in August of 1997 at the Virginia Polytechnic Institute and State University working with Professor Gary Brown in the Electromagnetic Interactions Laboratory. After graduation Albert will join Scientific Atlanta Inc. in Atlanta, Georgia.